Distribution Agreement

In presenting this thesis or dissertation as a partial fulfillment of the requirements for an advanced degree from Emory University, I hereby grant to Emory University and its agents the non-exclusive license to archive, make accessible, and display my thesis or dissertation in whole or in part in all forms of media, now or hereafter known, including display on the world wide web. I understand that I may select some access restrictions as part of the online submission of this thesis or dissertation. I retain all ownership rights to the copyright of the thesis or dissertation. I also retain the right to use in future works (such as articles or books) all or part of this thesis or dissertation.

Signature:

_____ _____

Fengyi Zhao Date

Spectroscopic Investigation of Semiconductor Charge Carrier Dynamics and Semiconductor/electrolyte Catalytic Interface for Solar Energy Conversion

By

Fengyi Zhao

Doctor of Philosophy

Dr. Tianquan Lian

Advisor

Dr. Craig L. Hill

Committee Member

Dr. Michael Heaven

Committee Member

Accepted:

Kimberly Jacob Arriola, Ph.D, MPH

Dean of the James T. Laney School of Graduate Studies Date

Date

Spectroscopic Investigation of Semiconductor Charge Carrier Dynamics and Semiconductor/electrolyte Catalytic Interface for Solar Energy Conversion

By

Fengyi Zhao

B.S., Sun Yat-sen University, China, 2017

Advisor: Tianquan Lian, Ph.D.

An abstract of

A dissertation submitted to the Faculty of the

James T. Laney School of Graduate Studies of Emory University

in partial fulfillment of the requirements for the degree of

Doctor of Philosophy

In Chemistry

2023

Abstract

Spectroscopic Investigation of Semiconductor Charge Carrier Dynamics and Semiconductor/electrolyte Catalytic Interface for Solar Energy Conversion

By Fengyi Zhao

Utilizing semiconductor photoelectrode is a promising but challenging method to achieve direct energy conversion from solar energy to chemical energy stored in liquid fuels. A lot of fundamental questions need to be understood on semiconductor/electrolyte junction to achieve efficient energy conversion efficiency, for instance, how to understand the surface minority charge accumulation, the function of the surface co-catalyst and the catalytic interfacial electric field. In this thesis, we intend to investigate the semiconductor/electrolyte catalytic junction through time-resolved and *in situ* spectroscopic methods. In chapter 3 and 4, we introduced an *in-situ* bias-dependent Second Harmonic Generation (SHG) technique to investigate potential drop at the semiconductor electrode and solution double layer side without illumination and the minority charge accumulation at the surface under illumination condition for oxygen evolution reaction (OER). It is found that the TiO_2 crystal angle and light polarization will have significant effect on its bias-dependent SHG behavior. Under photoexcitation, screening of built-in potential is observed, which is correlated to the surface hole accumulation. Studying accumulated holes provides crucial understanding of water oxidation rate-determining species. In chapter 8, *in-situ* Raman spectroscopy is developed to study the properties of a novel semiconductor-catalyst/electrolyte junction SMA/CNT/CoPc-NH_2 during CO_2 photoreduction condition.

In chapter 5, the synthesis of TiO_2-**Co_9POM** hybrid photoanode material showed a three-fold OER photocurrent enhancement compared to unmodified nanoporous TiO_2, comprehensive transient absorption and photoelectrochemical characterization highlight the function of **Co_9POM** catalyst. Chapter 6 uses transient reflectance spectroscopy to study the photocathode material GaP/TiO_2, showcasing the importance of solution electrolyte concentration and potentiostat response in regulating interfacial recombination. Lastly, chapters 7 focused on the charge separation process of a CdS based CO_2 reduction catalyst, clearly revealing the initial rapid charge separation process and later charge accumulation on the catalyst through transient absorption spectroscopy, providing mechanistic insight of this novel hybrid photocatalyst.

Spectroscopic Investigation of Semiconductor Charge Carrier Dynamics and Semiconductor/electrolyte Catalytic Interface for Solar Energy Conversion

By

Fengyi Zhao

B.S., Sun Yat-sen University, China, 2017

Advisor: Tianquan Lian, Ph.D.

A dissertation submitted to the Faculty of the

James T. Laney School of Graduate Studies of Emory University

in partial fulfillment of the requirements for the degree of

Doctor of Philosophy

In Chemistry

2023

ACKNOWLEDGEMENT

First, I would like to express my sincere gratitude to my mentor Dr. Tianquan Lian, for his continuous guidance and support throughout my Ph.D. career. In research, his patience, motivation, and desire to understand scientific problems at a deeper level inspired and shaped me to become a better scientist. As a knowledgeable scientist, his collaboration with many great scientists from various fields taught me the importance of keeping an open mind when conducting interdisciplinary research. It is my great honor to work in your lab and train to be a qualified scientist. I would also like to express my gratitude to my committee members Dr. Hill and Dr. Heaven. Your insightful feedback on my research and encouragements throughout my six-year graduate journey make me a more open-minded and determined scientist.

I would also like to sincerely thank Dr. Zihao Xu for training and teaching me a lot about spectroscopy and semiconductor electrochemistry knowledge that set me up for my Ph.D. research. To Sa Suo for a lot of fruitful project discussions. Dr. Wenxing Yang, Dr. Tao Jin, Dr. Jinhui Meng, Dr. Sara T. Gebre, and Tao (Paul) Jin, for the fun time we spent together in and out of the labs that I enjoyed a lot. I would like to thank my past and current labmates, Dr. Aimin Ge, Dr. Laura Kiefer, Dr. Jia Song, Dr. Yawei Liu, Qiliang Liu, Dr. Shengxiang Wu, Dr. Dhriti Bhattacharyya, Dr. Chaoyu Li Dr. Brian Breeman, Dr. Nandan Ghorai, Dr. Lu Lin, Sheng He, Isaac Tangen, Zhicheng Yang, Yiwei Yang, Bo Dong, Chuchu Qiu, and Giorgi Petriashvili, your accompany and support that makes the lab a comfortable place. I would also like to my collaborator, Dr. Hailiang Wang, Dr. Paul Maggard, Dr. Jamal Musaev, Dr. Alexey Kalendin, Dr. Chungseok Choi, Bo Shang, Scott McGuigan, Dr. Qiushi Yin, Dr. Ting Cheng, Zhiyao Zhu.

Finally, I would like to express my love and appreciation to my family: my father, and my mother, for your continuous, unconditional caring and support. I would like to thank my partner Ruoya Ma, for the treasured moments we spent together in the past five years.

Table of Contents

1 Introduction 1

1.1. Description of semiconductor/electrolyte junction under equilibrium 1

1.2. Potential-current behavior of semiconductor/electrolyte junction under dark and illumination conditions 5

1.3. Progress of understanding semiconductor/electrolyte junctions 9

1.4. Challenges in studying the semiconductor/electrolyte junctions for oxygen evolution reaction, hydrogen evolution reaction and CO_2 reduction reactions 14

1.5. Reference 16

2 Experimental Methods 21

2.1. Transient absorption and reflectance spectroscopy 21

2.1.1. Transient absorption Spectroscopy 21

2.1.2. Transient reflectance spectroscopy 23

2.2. Second Harmonic Generation spectroscopy 24

2.3. *In situ* Raman spectroscopy 26

3 *In situ* Investigation of Electric Field Distribution on TiO_2(100)-electrolyte Junction by Azimuthal-Angle-Resolved Second Harmonic Generation 28

3.1. Introduction 28

3.2. Materials and Methods 30

3.2.1 Materials 30

3.2.2 Experimental Method 31

3.2.3 Bias-dependent SHG equation derivation 32

3.3. Results and discussion 35

3.4. Conclusion 48

Appendix Chapter 3 49

3.5. Reference 51

4 Direct *Operando* Observation of Surface Charge Build-up on TiO_2 Photoanode Under Water Oxidation Conditions by EFISH 57

4.1. Introduction 57

4.2. Materials and Methods 60

4.3. Results and Discussions 61

4.3.1 *Operando* EFISH of TiO_2 under illumination 61

4.3.2 Impedance spectroscopy investigation of light-induced Fermi-level pinning 67

4.3.3 Isotope effect on EFISH and Photocurrent 70

4.3.4 Effect of electrolyte on $\boldsymbol{\Delta Vbi}$ 72

4.3.5 Nature of surface charge and rate-determining step 74

4.3.6 Impact of $\boldsymbol{\Delta Vbi}$ to Incident Photon to Current Efficiency 78

4.4. Conclusion 80

Appendix Chapter 4 81

Appendix A4.1. EFISH and $\boldsymbol{\Delta Vbi}$acquired under negative and positive scan directions. 81

Appendix A4.2. Equivalent circuit of semiconductor/electrolyte junction and Gauss fitting of surface state capacitance. 81

Appendix A4.3. Effect of local pH change on $\boldsymbol{\Delta Vbi}$ 83

Appendix A4.4. Effect of electrolyte on $\boldsymbol{\Delta Vbi}$ and photocurrent and KIE values 85

Appendix A4.5. Effect of other solution adsorbate on $\boldsymbol{\Delta Vbi}$ 86

Appendix A4.6. Separation between flatband (V_{fb}) and photocurrent onset (V_{onset}) potential and calculation of IPCE 87

4.5. References 89

5 The Charge Transfer Mechanism on a Cobalt-Polyoxometalate-TiO_2 Photoanode for Water Oxidation in Acid 98

5.1. Introduction 98

5.2. Material and Methods 101

5.2.1 Sample synthesis 101

5.2.2 Generation Characterization Methods 102

5.2.3 Photoelectrochemical Characterizations 103

5.3. Results and Discussion 104

5.3.1 Characterization of TiO_2 and TiO_2-Co_9POM photoelectrodes 104

5.3.2 Photoelectrochemical Oxygen Evolution Reaction Performance of TiO_2-Co_9POM 107

5.3.3 Transient Absorption Spectroscopy Probing Charge Transfer Dynamics in TiO_2-Co_9POM112

5.4. Conclusions 115

Appendix Chapter 5 116

Supplementary General Characterization 116

Supplementary PEC Characterization and AC Impedance Fitting Parameters 118

Supplementary Transient Absorption Spectroscopy 120

5.5. References 122

6 Semiconductor Photocatalysis Quantum Efficiency Limited by Electrolyte Concentration 128

6.1. Introduction 128

6.2. Material and Method 129

6.2.1. Material preparation 129

6.2.2. Photoelectrochemistry 130

6.2.3. Transient Reflectance Spectroscopy 130

6.3. Results and Discussions 130

6.4. Conclusion 142

Appendix Chapter 6 143

6.5. References 147

7 Synergizing Electron and Heat Flows in Photocatalyst for Direct Conversion of Captured CO_2 150

7.1. Introduction 150

7.2. Materials and Methods 152

7.2.1. Materials 152
7.2.2. General Characterization Methods 153
7.2.3. Measuring work function and valence band maximum (VBM) with UPS 154
7.2.4. TA measurement conditions 155
7.2.5. Photochemical CO_2 reduction measurements 156
7.2.6. In situ Raman spectroscopy and in situ UV-visible spectroscopy 156
7.2.7. Modeling of CNT local heating 157
7.3. Results and Discussion 158
7.4. Conclusion 173
Appendix Chapter 7 173
Bleach decay kinetics fitting 173
Supplementary Figures and Tables 177
7.5. Reference 192
8 Enhanced Methanol Production from Photoelectrochemical CO_2 Reduction via Interface and Microenvironment Tailoring 197
8.1. Introduction 197
8.2. Material and Methods 199
8.2.1. Materials 199
8.2.2. Preparation of catalyst ink 199
8.2.3. Fabrication of SMA-CF_x 200

8.2.4. Fabrication of photocathode 200

8.2.5. PEC measurement 201

8.2.6. Characterization 201

8.2.7. Numerical Modeling 202

8.3. Results and Discussion 203

8.4. Conclusion 214

Appendix Chapter 8 215

Supplementary Results 215

8.5. References 226

9 Conclusions and Outlook 229

List of Figures

Figure 1.1 Energy diagram between a n-type semiconductor/electrolyte junction (a) before and (b) after equilibrium with redox couple (A/A^-) in solution. Here distant x describes the position of semiconductor/electrolyte junction, x=0 is the interface, x>0 describes the semiconductor phase, and x<0 describes the liquid phase. 2

Figure 1.2 n-type semiconductor electrode under (a) electrochemical with no light illumination and (b) photoelectrochemical with monochromatic light excitation conditions. A simple regenerative cell condition is assumed, where [A] is the only oxidative species and [A^-] is the only reductive species, both will interact with semiconductor conductor band electrons and valance band holes.[22] 6

Figure 1.3. Transient absorption kinetic of hematite photoanodes measured under applied bias of -0.1 V *vs* Ag/AgCl in 0.1 M NaOH (aq) (blue), +0.4 V *vs* Ag/AgCl with methanol in 0.1 M NaOH (aq) (red), +0.4 V *vs* Ag/AgCl in 0.1 M NaOH (aq) as a function of time. Kinetics are obtained upon pump excitation at 355 nm and probe at 580 nm. Reproduced with permission from Stephanie R. Pendlebury, Monica Barroso, Alexander J. Cowan, Kevin Sivula, Junwang Tang, Michael Gratzel, David Klug, and James R. Durrant, *Chemical Communication*, 2011, 47, 716-718. Copyright Royal Society of Chemistry 2011.[32] 11

Figure 1.4. (a) Proposed water oxidation kinetic model at hemitite surface (b) change of water oxidation reaction order, dertemined by different experimental techniques, as a function of surface hole density. Reproduced with permission from Florian Le Formal, Ernest Pastor, S. David Tilley, Camilo A. Mesa, Stephanie R. Pendlebury, Michael Gratzel, and James R. Durrant,

Journal of the American Chemical Society, 2015, 137, 6629-6637. Copyright 2015 American Chemical Society.[33] 12

Figure 2.1. TA spectroscopy operation process using visible or near-IR as probe. 22

Figure 2.2. Schematic of transient reflectance spectroscopy. 24

Figure 2.3. Second Harmonic generation spectroscopy with sample in a typical three-electrode electrochemical setup. 26

Figure 2.4. *In situ* Raman spectroscopy with sample in a typical three-electrode electrochemical setup. 27

Figure 3.1. An Argand diagram of Equation 3.6 and 3.7, demonstrates the contribution of each term to the total SHG susceptibility in (a) the semiconductor accumulation region and (b) the semiconductor depletion region. 35

Figure 3.2. Azimuthal angle dependence of SHG signal of rutile TiO_2 (100) with (a) p in p out, (b) p in s out, (c) s in p out and (d) s in s out fundamental and SHG polarization combination. (e) SHG signal summarizing (a)-(d) polarization combination. (f) Illustration of experimental condition, where azimuthal angle Φ is defined as the angle between incident plane and [001] crystal axis. 35

Figure 3.3. Schematic of *in situ* azimuthal-angle-resolved SHG setup. Inset illustrates the band alignment of semiconductor-electrolyte junction under semiconductor flatband (black), depletion (red), and accumulation (green) region conditions. 37

Figure 3.4. (a) Mott-Schottky experiment of rutile TiO_2 (100) electrode using 550 Hz AC frequency and 7 mV amplitude of AC bias perturbation under negative scan direction. (b)

Representative cyclic voltammetry during SHG process with a scan rate of 3.5 mV/s in 0.1 M pH 7 phosphate buffer solution containing 1 M Na_4ClO_4 supporting electrolyte. 39

Figure 3.5. Azimuthal angle dependent SHG response as a function of applied potential in pH 7 buffer solution with (a) p in p out; (b) p in s out; (c) s in s out and (d) s in p out polarization combination. The green and red part indicate the semiconductor accumulation and depletion region, respectively, using the V_{fb} extracted from impedance measurement. 41

Figure 3.6. Summary of (a) relative phase difference and (b) amplitude ratio between $\chi sc3$ and bias-independent non-linear susceptibility. Dash line in (a) indicates $\gamma = 90^o$ values. 43

Figure 3.7. pH dependent (a) cyclic voltammetry and (b) Mott-Schottky of rutile TiO_2 (100). (c) Oxidation and reduction peak potential plotted as a function of pH extracted from (a). (d) Summary of flat-band potential (V_{fb}) extracted from (b) and potential of minimum (V_{min}) extracted from Figure A3.2 plotted as a function of pH. Cyclic voltammetry is measured under scan rate of 3.5mV/s, capacitance is measured under 550 Hz 7mV AC voltage perturbation. Experiments are done in citric-phosphate buffer with pH varying from around 2 to 9. 46

Figure 3.8. (a) SHG intensity of TiO_2 measured under different power densities of 360 nm CW light illumination with electrode held at open circuit condition. (b) Illumination power density dependent OCP values measured by potentiostat (red) and by SHG (blue) calculated from the dark response fitting curve as shown in Figure A3.3. OCP experiments are conducted in a pH 7 1 M $NaClO_4$ solution as electrolyte. 48

Figure A3.1. Current density derivatives as a function of applied potential at TiO_2-electrolyte junction at different pH. Reduction/oxidation peak positions are determined either from the dJ/dV=0 potential (when there is a peak) or from the d^2J/dV^2=0 potential (shoulder peak). 50

Figure A3.2. Bias-dependent SHG of TiO_2-electrolyte junction in different pH solutions at (a) pp $\Phi = 90^o$ and (b) sp $\Phi = 0^o$ light polarization and TiO_2 azimuthal angle..... 50

Figure A3.3. Bias-dependent SHG of TiO_2-electrolyte junction in pH 7 1 M $NaClO_4$ solution without 360 nm CW illumination. The quadratic fitting curve is used as a calibration curve to calculate the OCP potential from the SHG intensity change at different illumination power density depicted in Figure 3.8. The SHG is measured at sp $\Phi = 0^o$ light polarization and TiO_2 azimuthal angle. 51

Figure 4.1. Schematic of steady-state EFISH setup. The zoom-in panel indicates the second harmonic generation uses an s-in-p-out polarization and the adopted crystal azimuthal angle. 1 kHz 35 fs 800 nm pulses are used as the fundamental light. 63

Figure 4.2. (a) EFISH intensity as a function of applied potential on rutile TiO_2 (100) under UV illumination with different power densities. Also shown is an example of determining ΔVbi under 15 mW/cm^2 illumination using the applied potential $Vapp$ and calculated actual Vbi calibrated by quadratic fitting (Equation 3.8b) of dark EFISH response. (b) The change of semiconductor built-in potential ΔVbi as a function of applied potential. (c) Current densities as a function of applied potential under different UV power densities measured by CV with a scan rate of 3.53 mV/s. (d) Comparison of initial photocurrent densities $J0$ (pink open circles) and steady state photocurrent density $Jinf$ (red open circles) measured by chopped chronoamperometry measurement, current density (J) measured by CV, and ΔVbi under 10 mW/cm^2 illumination. Inset: a representative transient current curve and J_0 and J_{inf} values obtained from chopped chronoamperometry measurement at -0.1 V vs Ag/AgCl. All the above experiments are done in 1 M $NaClO_4$ electrolyte under stirring conditions. 66

Figure 4.3. (a) Mott-Schottky plot of TiO_2 electrode. (b) Effect of screened potential measured by Mott-Schottky (blue trace) and by EFISH (red trace, extracted at 1 V vs Ag/Ag Cl) as a function of illumination power density. (c) Surface state capacitance as a function of applied potential under different illumination power densities, fitted from (V_{fb} + 0.2) V to 1.2 V vs Ag/AgCl. A fitting example at 0.5 mW cm^{-2} is plotted. All fitting details summarized in Table A4.1. All the above experiments are done in 1 M $NaClO_4$ electrolyte under stirring conditions. 67

Figure 4.4. (a) ΔVbi (collected at 1V vs Ag/AgCl) as a with illumination power density in H_2O and D_2O. (b) ΔVbi-V plot and (c) *J*-V plot in H_2O and D_2O under 10 mW/cm^2 illumination power density. (d) KIE value calculated from Equation 4.4, measured by light on-off amperometric measurement. All above experiments used 1 M $NaClO_4$ as the electrolyte, H_2O or D_2O as the solvent, and under stirring conditions..... 72

Figure 4.5. Bias-dependence EFISH measured in (a) pH 7 with 0.1 M phosphate buffer, and (b) pH 12.7 buffered; All experiments are conducted under no stirring conditions as surface pH is stabilized by buffer solution..... 74

Figure 4.6. Energy diagram of rutile TiO_2 (100) immersed in pH 7 1 M $NaClO_4$ aqueous solution with applied potential at 1 V vs Ag/AgCl in the dark (black) and under illumination (red) with electron energy presented in the absolute energy scale vs vacuum level, and potential in the electrochemical scale, with respect to Ag/AgCl. E_c, E_f, E_c stands for the energy of the conduction band, Fermi-level, and valance band level of TiO_2, E_{vac} stands for the energy of local vacuum level, ΔVH and ΔVbi stands for the change of potential drop in solution and in semiconductor, respectively. The insert panel illustrates the proposed PCET rate-determining species during OER..... 75

Figure A4.1. (a) TiO_2 EFISH intensity as a function of applied potential under 0 (open circle) and 10 (open triangle) mW/cm^2 360 nm illumination at negative (grey) and positive (red) potential scan direction. (b) ΔVbi as a function of applied potential under 10 mW/cm^2 illumination under negative (grey) and positive (red) potential scan direction. 81

Figure A4.2. Simplified equivalent circuit of semiconductor/electrolyte with and without illumination, only showing the capacitance component. 81

Figure A4.3. EFISH and impedance measurement of TiO_2/electrolyte junction under no solution stirring condition. (a) EFISH intensity, (b) ΔVbi, (c) current densities, (d) Mott-Schottky plot, and (e) surface state capacitance Css as a function of applied potential under different illumination power densities. (f) Effect of screened potential measured by Mott-Schottky (blue) and by EFISH (red, extracted at 1 V vs Ag/AgCl) as a function of illumination power density. 1 M $NaClO_4$ is used as electrolyte. 83

Figure A4.4. (a) J-V plot measured in pH 7 1 M $NaClO_4$ solution with (red) and without (green) stirring conditions, and in 0.1 M pH 7 sodium phosphate buffer without stirring (blue) under 10 mW/cm^2 illumination. (b) ΔVbi plot as a function of applied potential with (red) and without (green) stirring under 10 mW/cm^2 illumination. (c) ΔVbi (collected at 1V vs Ag/AgCl) plotted as a function of illumination intensity with (red) and without (green) stirring. 83

Figure A4.5. Mott-Schottky plot in (b) pH 7 with 0.1 M phosphate buffer, and (e) pH 12.7 buffered; J-V curve in (c) pH 7 with 0.1 M phosphate buffer, and (f) pH 12.7 under different illumination power densities. All experiments are conducted under no stirring conditions as surface pH is stabilized by buffer solution. 85

Figure A4.6. (a) Steady (solid symbol) and transient (open symbol) photocurrent density as a function of applied potential measured in pH 7 unbuffered (red), pH 7 buffered (blue), and pH 12.7 buffered (yellow) solution extracted from light on-off amperometric measurement. (b) KIE values in pH 7 unbuffered (red), pH 7 buffered (blue), and pH 12.7 buffered (yellow) solution as a function of applied potential. All experiments are performed under stirring conditions. 86

Figure A4.7. Power dependent ΔVbi comparison collected between (a) 1 M $NaClO_4$ (red) and 1 M NaCl (purple), (b) 1 M $NaClO_4$ and 1M $NaClO_4$ containing 5% H_2O_2 (blue) electrolyte, and (c) 1 M $NaClO_4$ and 1 M $NaClO_4$ containing 0.1 M HCOOH (light blue). ΔVbi is measured at 1V vs Ag/AgCl applied potential under stirring conditions..... 87

Figure A4.8. Photocurrent comparison in different electrolytes under 1.6 V vs RHE. IPCE can be calculated from the slope of the fitting following Equation A4.2..... 88

Figure 5.1. (a) Diffuse-reflectance of TiO_2, TiO_2-APS, and TiO_2-**Co_9POM** samples on sapphire substrates. (b) *ex-situ* Raman spectroscopy of TiO_2, solid **Co_9POM**, and TiO_2-**Co_9POM** on FTO substrates, where diamonds and stars represent the characteristic Raman peaks of anatase TiO_2 and **Co_9POM**, respectively. (c-f) Co 2p, W 4f, Ti 2p, and O 1s are the X-ray photoelectron spectra of the as-prepared TiO_2-**Co_9POM** sample..... 105

Figure 5.2. (a) J-V curve of TiO_2, TiO_2-APS, and TiO_2-**Co_9POM** in the dark (dash curve) and under 100 mW/cm^2 365 nm UV illumination (solid curve). (b) Open circuit potential (OCP) of TiO_2 and TiO_2-**Co_9POM** under dark and 100 mW/cm2 365 nm UV illumination. (c) Mott-Schottky analysis of TiO_2, TiO_2-APS, and TiO_2-**Co_9POM** photoanode under dark conditions. (d) Nyquist plot for electrochemical impedance spectroscopy conducted on TiO_2 and TiO_2-**Co_9POM** at 1.23 V under 12.8 mW/cm^2 UV illumination. Inset shows the equivalent circuit to fit the plot.

(e) Band structure schematic of TiO_2 and TiO_2-**Co_9POM** under illumination and dark OCP process. All experiments are performed under pH 2 sulfate buffer solution. 108

Figure 5.3. Excitation fluence-dependent (a) photocurrent and (b) incident photo-to-current efficiency (IPCE) of TiO_2, TiO_2-APS, and TiO_2-**Co_9POM** measured at 1.23 V_{RHE} under 365 nm UV illumination. 110

Figure 5.4. (a) FOXY Forspor oxygen probe during chronoamperometry and (b) chronoamperometric stability test of TiO_2-**Co_9POM** photoanode collected at 0.73 V under 20 mW/cm^2 365 nm UV illumination in pH 2 sulfate buffer. 111

Figure 5.5. Transient absorption spectra of TiO_2-**Co_9POM** films under 350 nm pump and (a) visible (c) mid-IR probe. Normalized transient absorption decay kinetics on TiO_2 and TiO_2-**Co_9POM** probed at (b) 460-520 nm in the visible and (d) 2020-2040 cm^{-1} in the mid-IR following 350 nm excitation. (e) Schematic illustration of charge transfer mechanism between TiO_2 and **Co_9POM**. Samples for TA-vis experiments are deposited on FTO substrates, samples for TA-IR experiments are deposited on a sapphire window to avoid extensive absorption by tin oxide. An excitation power density of 462 $\mu J/cm^2$ is used in all TA experiments. 113

Figure A5.1. (a) FT-IR spectroscopy and (b) TGA of **Co_9POM**. 116

Figure A5.2. (a) Full XPS of TiO_2-**Co_9POM** before bulk electrolysis. XPS of (b) W 4f, (c) Co 2p, and (d) O 1s of TiO_2-**Co_9POM** after bulk electrolysis. 117

Figure A5.3. XPS of (a) Co 2p and (b) O 1s in Co_3O_4 solids. 117

Figure A5.4. Raman spectroscopy of TiO_2-**Co_9POM** on FTO substrates after passing around 3.0 C of charge on the electrode for OER reaction as described in Figure 5.4b. Black diamonds and red stars represent the feature Raman peaks for anatase TiO_2 and **Co_9POM**, respectively.....118

Figure A5.5. (a) Cyclic voltammetry of **Co_9POM** in pH 2 buffer solution (b) J-V curve of $H_3PW_{12}O_{40}$ modified TiO_2 and (c) J-V photocurrent of Co-Pi modified TiO_2 under 100 mW cm^{-2} 365 nm LED light illumination. 118

Figure A5.6. FOXY Forspor oxygen probe setup during OER condition. Right panel shows the zoom-in of probe and electrode relative position. 119

Figure A5.7. Transient absorption spectroscopy of TiO_2 on FTO pumped by 350 nm pulses and probed by visible white light: (a) TA-vis spectra; excitation fluence dependent of (b) kinetic decay and (c) maximum signal amplitude, half lifetime and signal residual as a function of power density; (d) kinetic decay in DI water, 0.1 M $Na_2S_2O_8$, and 30% methanol; (e) normalized hole decay kinetics on of TiO_2 and TiO_2-APS. All signal kinetics decays are extracted by averaging 460-520 nm, excitation power density of 462 μJ/cm^2 are used in (a), and 231 μJ/cm^2 are used in (d) and (e). 120

Figure A5.8. TA-IR spectra on (a) TiO_2, (b) TiO_2-APS, and (c) TiO_2-**Co_9POM** samples. (d) Kinetics comparison of three samples from 2020-2040 cm^{-1}. TA-IR experiments are conducted under 462 μJ/cm^2 350-nm pump, with all samples deposited on sapphire windows. 121

Figure 6.1. Schematic diagram of the *p*-GaP/*n*-TiO_2 water reduction photocathode in a 3-electrode photoelectrochemical cell. (a) The setup allows pulsed (femtosecond 1 kHz ultrafast laser) and continuous wave (CW, LED) illumination. Working electrode: GaP/TiO_2, counter electrode: Pt wire, reference electrode: Ag/AgCl in 1 M KCl. (b) Light on-off measurement of photocurrent for the GaP/TiO_2 in 0.9 M $NaNO_3$ aqueous solution at -1.5 V vs Ag/AgCl under 0.5 mW/cm^2 405 nm LED CW illumination with iR compensation. The dashed line indicates the dark current. (c) Incident photon to current efficiency (IPCE) under 0.5 mW/cm^2 CW 405 nm

LED illumination at -1.5 V vs Ag/AgCl in aqueous solution with various $NaNO_3$ concentrations with and without iR compensation by potentiostat. 132

Figure 6.2. (a) Transient reflectance spectra of GaP/TiO_2 at various delay times under 300x pump beam size, 4.4 mW/cm^2 excitation density, -1.5 V vs. Ag/AgCl applied bias, in 0.03 M $NaNO_3$ aqueous solution. (b) FKO kinetics probed at 2.78 eV under -1.5 V applied bias, in various $NaNO_3$ concentrations. The full FKO kinetics 400 μs is shown in Figure A6.3. (c) FKO decay rate plotted as a function of $NaNO_3$ concentration. The linear fit (solid blue line) shows the rate constant of 0.62 $\mu s^{-1}M^{-1}$. (d) Numerical solutions to fit the FKO kinetics from 0.03 to 1.5 M concentration. 134

Figure 6.3. (a) Schematic diagram of interfacial recombination suppressed by the potentiostat removing hole in GaP. (b) IPCE at various $NaNO_3$ concentration under -1.5 V applied bias and 4.4 mW/cm^2 pulsed 400 nm excitation (red circle, left axis). The numerical simulation of the IPCE is shown in purple line and triangles. In comparison, the IPCE under -1.5V applied bias and 0.5 mW/cm^2 405 nm LED illumination is also shown (blue box, right axis). 138

Figure 6.4. FKO kinetics under 300x pump beam size, 400 nm, 4.4 mW/cm^2 excitation, 0.9 M $NaNO_3$ aqueous solution and various applied bias. (a) The raw FKO kinetics. (b) The E_{AC} and its numerical fitting shown in black solid lines. (c) The simulated electron concentration over a 100 μs time window. (d) The IPCE measured *in-situ* under pulsed illumination, steady state CW illumination, and the $[e^-]_{100\mu s}$ from the simulation shown in panel c. 141

Figure A6.1. (a) Transient reflectance spectra of GaP/TiO_2 at various delay time under -1.5 V vs Ag/AgCl applied bias, in 0.1 M Na_2SO_4 aqueous solution. The sample is excited by 400 nm with an excitation density of 4.4 μJ/cm^2. The relative pump to probe beam size is 300 times. (b) FKO

kinetics probed at 2.78 eV with various pump beam sizes. The legend indicates the relative pump to probe size. The excitation power is increased accordingly to maintain the same excitation density of 4.4 μJ/cm^2. Other experimental conditions are kept the same. (c) FKO kinetics comparison of different pump beam sizes of GaP/TiO_2 (5 nm) dry film. The excitation density is the same. (d) Schematics of carrier diffusion at indicated x-y (lateral) direction coupled with cations. 143

Figure A6.2. FKO kinetics with 300x and 1300x pump beam size with 400 nm 4.4 μJ/cm^2 excitation, -1.5 V vs Ag/AgCl applied bias, and 1.5 M $NaNO_3$ aqueous solution. The similar kinetics show that the x-y diffusion can be neglected even at highest electrolyte concentration. 144

Figure A6.3. Exponential-exponential plot of Figure 6.1b and corresponding multiexponential fit. 144

Figure A6.4. Numerical simulation to fit the FKO decay kinetics in Figure 6.2d. (a) hole concentration, (b) electron concentration. 146

Figure A6.5. Normalized FKO kinetics at 1 ns for Figure 6.4a. 146

Figure 7.1. CdS/CNT/CoPc hybrid material. (a) STEM-HAADF image of CdS/CNT/CoPc. (b) XRD of CdS/CNT/CoPc. (c) UV-visible spectroscopy of CdS/CNT/CoPc. (d)-(g) STEM-HAADF image and EELS elemental mapping of CdS/CNT/CoPc. (h) High-resolution STEM-HAADF image of CdS/CNT/CoPc. (i) Schematic illustration of CdS/CNT/CoPc structure. 160

Figure 7.2. Electronic energy level diagram of CdS/CNT/CoPc. 162

Figure 7.3. Electron transfer kinetics. TA spectra (400 nm excitation) probing CdS exciton bleach signal for (a) CdS QDs and (b) CdS/CNT at varied time delays. (c) Comparison of normalized

exciton bleach signal decay between CdS/CNT and CdS QDs. Signal was averaged from 468 nm to 483 nm. Black curves are fitting results using Equations A7.1 and A7.2. (d) Near-IR TA spectra (400 nm excitation) probing CNT bleach signal for CdS/CNT. (e) CNT bleach kinetics of CdS/CNT and CdS/CNT/CoPc. Signal was averaged from 880 nm to 950 nm. (f) Proposed electron transfer pathway. 163

Figure 7.4. Photocatalytic CO_2 reduction performance measured in TEOA-acetonitrile (1:4). (a) Photocatalytic reaction rate of CdS/CNT/CoPc compared to CdS/CNT, CNT/CoPc, and CdS/CoPc under AM1.5G-filtered 150 W Xe lamp illumination (216 mW cm^{-2} beam power). (b) Long-term photocatalytic CO production rate of CdS/CNT/CoPc under 405 nm LED illumination (47 mW cm^{-2} beam power). 168

Figure 7.5. *In situ* Raman spectroscopy measurements to uncover catalytic sites and electron transfer. *In situ* Raman spectra of CdS/CNT/CoPc in TEOA-acetonitrile (1:4) under photochemical conditions (405 nm LED illumination) (a) with MV^{2+} or (b) CO_2 as electron acceptor. 169

Figure 7.6. *In situ* UV-visible spectroscopy measurements to uncover catalytic sites and electron transfer. *In situ* UV-visible spectra of CdS/CNT/CoPc in TEOA-acetonitrile (1:4) under photochemical conditions (405 nm LED illumination), (a) with Ar purging, (b) with CO_2 purging, and (c) with first Ar and then CO_2 purging. 170

Figure 7.7. Photocatalytic conversion of captured CO_2. Photochemical CO and H_2 production from CO_2 captured by MEA solution (a) from a pure CO_2 source and (b) from air catalyzed by CdS/CNT/CoPc. (c) Modeling of local heating effect near CNT. (d) Proposed mechanism for direct photocatalytic reduction of MEA-captured CO_2. 172

Figure A7.1. (a)-(d), TEM images of CdS/CNT/CoPc taken with different magnifications. 177

Figure A7.2. (a) Carbon and (b) Cobalt EDX spectrum of CdS/CNT/CoPc in comparison with that of bare CNTs. 177

Figure A7.3. (a) Cyclic voltammograms of CNT/CoPc measured in CO_2-saturated 0.1 M aqueous $KHCO_3$ at 100 mV s^{-1}. (b) Cyclic voltammograms of CdS/CNT/CoPc measured in CO_2-saturated 0.1 M aqueous $KHCO_3$ at 100 mV s^{-1}. CNT/CoPc and CdS/CNT/CoPc show the first reduction peak of CoPc at similar electrode potentials, suggesting that CdS QDs have no effects on the reduction potential of CoPc. The standard electrode potential of CO_2 reduction to CO is -0.11 V vs RHE or 4.33 V below the vacuum level.[48] 178

Figure A7.4. Determining orbital gap of CoPc from Tauc plot measured by UV-visible spectroscopy. 179

Figure A7.5. Determining work function of (a)-(c) gold standard, (d)-(f) CNT. 179

Figure A7.6. (a) Valence bands of CNTs and CdS/CNT measured by UPS. CNTs show the characteristic valence band features of multiwalled CNTs at 0.7 eV, 3 eV, and 6 eV (labeled as A, B, and C)[49]. CdS/CNT shows no clear CNT features but CdS valence band features from Cd 5s and S 3p mixed orbitals at 3.5 eV and 6.9 eV (labeled as D and E)[50], which indicates that CdS (~70 wt.% in the material and covering most of the CNT surfaces) dominates the valence band structure probed by UPS. (b) Determination of valence band maximum (VBM) of CdS and Fermi energy (Ef) of CNT in CdS/CNT from the UPS result. 179

Figure A7.7. (a)-(b) TEM images of CdS taken with different magnifications. (c) XRD of CdS. (d)-(e) UV-visible spectroscopy of CdS/CoPc and CdS/CNT. 180

Figure A7.8. Determining band gap of CdS QDs from Tauc plot measured by UV-visible spectroscopy. 181

Figure A7.9. (a) UV-visible spectra of CdS, CdS/CNT, and CdS/CNT/CoPc in toluene. (b) TA spectra of CdS/CNT/CoPc. Pump beam was 400 nm. Probe signal was averaged from 468 nm to 483 nm. 181

Figure A7.10. Maximum exciton bleach signal recorded at 1 ps time delay as a function of 400 nm excitation power density for (a) CdS QDs and (b) CdS/CNT. 182

Figure A7.11. Comparison of CdS exciton bleach signal decay kinetics (a) between CdS/CNT and CdS/CNT with TEA, and (b) between CdS/CNT and CdS/CNT/CoPc. Pump beam was 400 nm. Probe signal was averaged from 468 nm to 483 nm. 182

Figure A7.12. (a) Near-IR TA spectra of CNTs under 400 nm excitation. (b) CNTs bleach signal decay kinetics with varied excitation wavelength. Signal was averaged from 880 nm to 950 nm. 183

Figure A7.13. (a) CNT bleach signal decay kinetics of CdS/CNT under 400 and 800 nm pump excitation. The signal was averaged from 880 nm to 950 nm. (b) Fitting of CdS bleach decay kinetics of CdS/CNT (same data as Figure 7.3c) using model proposed in Equation A7.6. (c) Schematic of proposed charge transfer mechanism in CdS/CNT/CoPc. 183

Figure A7.14. GC-MS analysis of CO produced from photochemical reduction reactions (a) with unlabelled CO_2 and (b) with $^{13}CO_2$ catalyzed by CdS/CNT/CoPc in TEOA-acetonitrile (1:4). 184

Figure A7.15. (a)-(b), TEM images of CdS/CNT after heat treatment at 150 °C for 1 hour. c, UV-visible absorption spectroscopy of CdS/CNT/CoPc control, whose CoPc was assembled on

CdS/CNT after the CdS/CNT was heated at 150 °C for 1 hour under Ar and cooled down to room temperature. 184

Figure A7.16. Photograph of *in situ* Raman spectroscopy setup. 185

Figure A7.17. Photograph of *in situ* UV-visible spectroscopy setup. 185

Figure A7.18. NMR spectra of MEA solution before and after CO_2 capturing. Red is from high-purity CO_2, and blue is from air. Dimethyl malonic acid was used as an internal standard to determine carbamate concentration. 186

Figure A7.19. Correlation between carbamate concentration and H_2 production rate for photochemical reduction performed with MEA solutions. 186

Figure A7.20. (a)-(b), GS-MS analysis of ^{13}CO produced from photochemical reduction of MEA-captured $^{13}CO_2$ catalyzed by CdS/CNT/CoPc. The m/z 28 signal is caused by N_2 as evidenced by its different retention time from CO (m/z 29). 186

Figure A7.21. Illuminating 0.2 M aqueous MEA (a) without and (b) with CdS/CNT/CoPc (same conditions as photochemical reaction of captured CO_2). (c) Measuring water bath temperature. (d) Increasing water bath temperature as illumination proceeds. (e) Heat absorbed by water bath corresponding to its temperature increase. 187

Figure 8.1. (a) SMA fabrication and CF_x coating. (b) SEM image of SMA-CF_x. (c) SEM image of SMA-CF_x coated with CNT/CoPc-NH_2 catalyst. (d-e) Top-view and side-view SEM images of a single SMA-CF_x pillar coated with CNT/CoPc-NH_2. 204

Figure 8.2. (a) *In situ* Raman spectra of CNT/CoPc-NH_2 on SMA-CF_x from 0.625 V to -0.375 V under 632 nm illumination. (b) LSV curve of SMA-CF_x-CNT/CoPc-NH_2 during *in situ* Raman measurement under illumination or in dark conditions. (c) One-electron reduction of CoPc-NH_2

tracked by changes in resonance Raman intensity. Potential-dependent Raman vibrational frequencies of (d) CoPc-NH_2 1543 cm^{-1} peak and (e) CNT D band. (f) Proposed band diagram at SMA-CF_x-CNT/CoPc-NH_2-solution interfaces. The electrode was tested after pre-conditioning the electrode at -0.5 V for 10 min under 150 mW cm^{-2} Xe lamp irradiation. The red, blue, and green shaded potential region in (b), (c), and (d) indicate the potential range of oxidized, one-electron-reduced, and mixed of oxidized and one-electron-reduced CoPc-NH_2, species, respectively, determined from Raman intensity change in (c). 205

Figure 8.3. PEC CO_2 reduction performance of SMA-CF_x-CNT/CoPc-NH_2 in 0.1 M aqueous $KHCO_3$ under illumination. (a) PEC cell structure. (b) Total photocurrent and product distribution at -0.7 V as a function of time. Methanol concentration was measured after the 30 min reaction and is assumed to be constant within the time window. (c) Stability test at constant photocurrent of 15 mA cm^{-2}. (d) Performance comparison with GO/CoPc-functionalized planar Si (under illumination), and CNT/CoPc-NH_2 deposited on carbon fiber paper (CFP, electrolysis without illumination). (e) *In situ* Raman measurements at -0.9 V at 60 s (top) and 1 hr (bottom), showing generated CO and methanol. 209

Figure 8.4. (a) Comparison of methanol selectivity and partial current density between SMA-CF_x-CNT/CoPc-NH_2 (noted as SMA-CF_x), SMA-CNT/CoPc-NH_2 (noted as SMA), and planar Si-TiO_2-GO/CoPc (noted as Planar). (b) XPS spectra of SMA-CF_x-CNT/CoPc-NH_2 before (upper panel) and after (lower panel) 4 h of PEC CO_2 reduction under 15 mA cm^{-2}. (c) SEM image of the side wall of a single Si pillar (left), and STEM-EDS mapping of the boxed area. (d) Contact angle measurements on SMA-CF_x and SMA. 212

Figure A8.1. Three-dimensional image of SMA obtained by optical profiler. 215

Figure A8.2. Picture of SMA-CF_x photoelectrode with uniformly coated (a) and self-clustered (b) CNT/CoPc-NH_2 layer. The self-clustered assembly of CNT/CoPc-NH_2 on SMA-CF_x enabled light transmission. 215

Figure A8.3. *In situ* Raman spectra of CoPc-NH_2 755 cm^{-1} peak on a pre-conditioned SMA-CF_x electrode after background subtraction. 216

Figure A8.4. (a) *In situ* Raman spectra of CNT/CoPc-NH_2 on n^+-SMA-CF_x from 0.475 V to -0.925 V. (b) LSV diagram of n^+-SMA-CF_x-CNT/CoPc-NH_2 during *in situ* Raman measurement. (c) One-electron reduction of CoPc-NH_2 tracked by changes in resonance Raman intensity at 755 cm^{-1} and 1543 cm^{-1}. (d) Potential-dependent Raman frequency of CoPc-NH_2 1543 cm^{-1} peak. 217

Figure A8.5. Peak analyses of CNT/CoPc-NH_2 from 1233 cm^{-1} to 1800 cm^{-1} on SMA-CF_x (a) before, (b) after pre-condition, and (c) on n^+-SMA-CF_x electrode. Five Lorentz multipeak fittings were used for spectra before CoPc reduction, and three Lorentz multipeak fittings are used for spectra after CoPc reduction. All peak analysis were conducted after background subtraction. 217

Figure A8.6. Raman spectra of SMA-CNT/CoPc-NH_2 electrode with (lower panel) and without CF_x under open circuit potential in 0.1 M $KHCO_3$ (pH 6.8). Peak position of CNT D band and CoPc-NH_2 are extracted by five Lorentz multipeak fittings and summarized in Table A8.1. The fitting results suggest that the trend between $\omega_{D\text{-band}}$ on two electrodes and their OCP do not agree with the trend between 1543 cm^{-1} CoPc-NH_2 peak frequency and their OCP (decreased ω with more negative potential), suggesting absolute $\omega_{D\text{-band}}$ position does not reflect accurate CNT Fermi-level. 218

Figure A8.7. (a) *In situ* Raman spectra of CNT/CoPc-NH_2 on SMA-CF_x without pre-conditioning from 0.675 V to -0.325 V. (b) One-electron reduction of CoPc-NH_2 tracked by change in

resonance Raman intensity. (c) LSV curve of SMA-CF_x-CNT/CoPc-NH_2 during *in situ* Raman measurement. (d-e) Potential-dependent Raman vibrational frequencies of (d) CoPc-NH_2 1543 cm^{-1} peak and (e) CNT D band. 218

Figure A8.8. Calibration of methanol peaks by measuring the SMA-CF_x-CNT/CoPc-NH_2 in 0.1 M $KHCO_3$ solution containing 10% (v/v%) methanol with no applied bias. The methanol peaks are indicated by the stars. 219

Figure A8.9. Photo of a CFP-CNT/CoPc-NH_2 electrode (a), and the electrocatalytic CO_2 reduction performance under dark (b). 219

Figure A8.10. Electrocatalytic performance of n-degenerately doped n^+-SMA-CF_x-CNT/CoPc-NH_2 under -1.05 V applied voltage and dark. 220

Figure A8.11. Activation current curve of the SMA-CF_x-CNT/CoPc-NH_2 under -0.5 V applied potential (and all other same condition as PEC) before constant potential electrolysis. 220

Figure A8.12. PEC performance of SMA-CNT/CoPc-NH_2 without CF_x coating. The top-left corner indicates the pillars height and pitch (H-P). Electrodes were cleaned with HF before drop casting catalyst to remove the insulating native oxide. 221

Figure A8.13. SEM image of the FIB-cut Si pillar sidewall cross-section. 222

Figure A8.14. Photo of a 3-inch wafer fabricated with SMA pattern. 222

Figure A8.15. Contact angle analysis of the SMA without CF_x coating (left) and with CF_x coating (right). 223

Figure A8.16. SMA-CF_x-CNT/CoPc-NH_2 with 1 nm TiO_2 passivation layer under the same testing condition. 223

Figure A8.17. NMR spectrum of electrolyte after PEC. 1 mM DMSO was added to the solution as an internal standard. 224

Figure A8.18. Simulation of the local CO concentration on SMA structure (left) and planar Si (right). 225

Figure A8.19. EDS spectrum of the Si-CF_x interface (green) and bulk Si (blue). The other elements (Pt, Ga) are from the FIB-deposited protective layer. 225

1 Introduction

Semiconductor electrodes serve an essential role in the field of energy conversion, including electrocatalysis, photoelectrochemical cells, and solar cells[1-3] etc. Ever since Gerischer proposed the first semiconductor/electrolyte interface model[4] in 1961, exploring the nature of semiconductors has raised a broad interest. Pioneering studies of the behavior of semiconductor/electrolyte junction under dark and illumination condition have been carried out by Bard,[5-10], Nate,[11-13] Wrighton,[11, 14-15] Memming,[16-18] and Chazalviel[19-20] et al and their co-workers in 1970s-1980s. For instance, Bard[7, 9] and Wrighton[14-15] et al have carried out cyclic voltammetry (CV) measurements of semiconductors in contact with different redox species under dark and illumination condition, revealing the rectifying junction nature and interface energetics of semiconductor/electrolyte junction. Based on these pioneering studies, we first introduce the mathematical description of semiconductor/electrolyte junction properties and their potential-current behavior in dark and under illumination.

1.1. Description of semiconductor/electrolyte junction under equilibrium

Take an n-type semiconductor for example, Figure 1.1a shows the band alignment before its Fermi-level (electrochemical potential) equilibrate with the solution redox species $E(A/A^-)$. The conduction (E_c), valance band (E_v) as well as its Fermi-level (E_f) energy remains flat across the semiconductor/electrolyte junction. The Fermi-level at this condition is called flatband Fermi-level (E_{fb}). The Fermi-level of semiconductor is higher than $E(A/A^-)$ due to the electron donor type (n-type) of doping. Its Fermi-level can be written as:

$$E_f = E_c + kTln(\frac{n}{N_c}) \quad 1.1$$

Where n is the electron concentration at position x. At the flatband conditions before quilibrium, n equal to the semiconductor dopant level N_d. k is Boltzmann constant; T is temperature; N_c is the density of energy states within few kT above E_c.

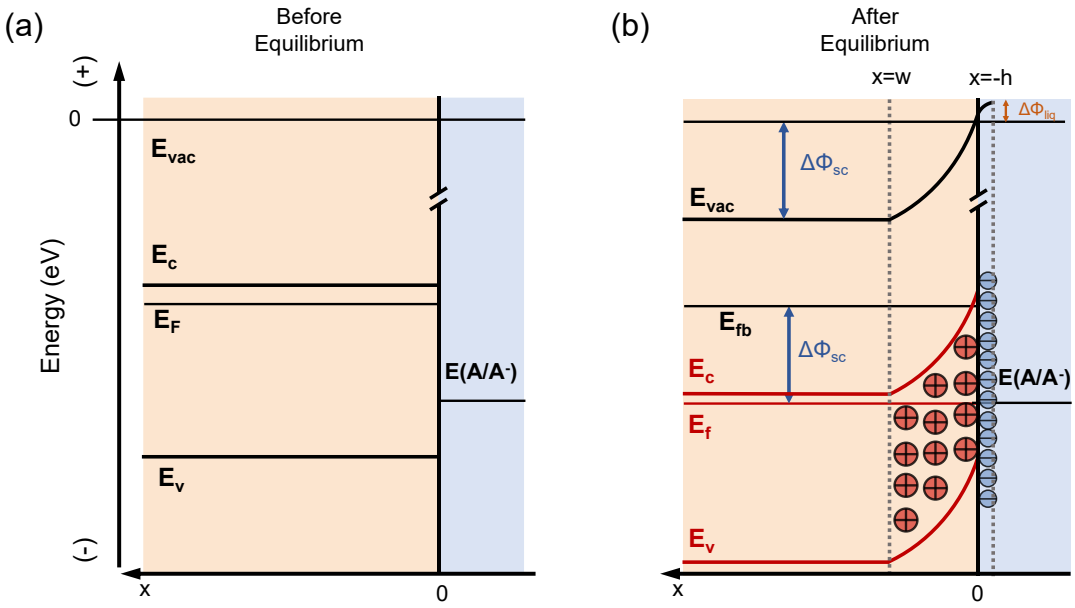

Figure 1.1 Energy diagram between a n-type semiconductor/electrolyte junction (a) before and (b) after equilibrium with redox couple (A/A^-) in solution. Here distant x describes the position of semiconductor/electrolyte junction, x=0 is the interface, x>0 describes the semiconductor phase, and x<0 describes the liquid phase.

Upon Fermi-level equilibrium, electrons from semiconductor flow to the solution until E_f=E(A/A^-). Conduction and valance energy will bend upward from the bulk semiconductor (x=∞) to the interface (x=0), forming a barrier height V_{bi} of

$$V_{bi} = \frac{E_{fb} - E(A/A^-)}{e} \qquad 1.2$$

where e is the charge of electron. In semiconductor side, a region where only positively charged ionized dopant is form from x=0 to x=w, which is called semiconductor depletion layer or space charge region (SCR). In the solution side, a layer of negative charge is formed very close to the

interface to compensate for the positive charge on semiconductor side, which is call double layer or Helmholtz layer. The Fermi-level relative to the local vacuum energy remains unchanged, but the local vacuum energy changes across the junction. The electrostatic potential difference between bulk semiconductor to bulk solution ($E_{vac}(x=\infty)/q$-$E_{vac}(x=-\infty)/q$) is used to refer to the potential drop across the semiconductor/liquid junction, consist of the potential drop at semiconductor side ($\Delta\Phi_{sc}$) and liquid side ($\Delta\Phi_{liq}$) as shown in Figure 1.1b, with their relation follows:

$$C_{sc}\Delta\phi_{sc} = C_H\Delta\phi_{liq} \quad 1.3$$

Where C_{sc} and C_H are the capacitance of semiconductor and solution double layer, respectively. Because C_H are usually orders of magnitude larger than C_{sc}, semiconductor potential drop dominates the potential drop across the semiconductor/electrolyte junction with $\Delta\phi_{liq} \ll \Delta\phi_{sc} \approx \Delta\phi_{total}$.

We can further obtain a quantitative description of electric field and potential drop across the semiconductor/electrolyte junction as a function of distance x.[21-23] Herein, we again follow the approximation that potential drop at the semiconductor side dominates the potential drop across the junction so that $\phi(x=0)=0$. Assuming only the uniformly distributed ionized dopant contributes to the charge at the semiconductor SCR under this equilibrium condition (abrupt approximation) with its density (ρ) equal to dopant density N_d. At bulk semiconductor when x>w, $\rho(x)$=0. The electric field at the semiconductor side can be written as a function of distant to the interface:

$$\boldsymbol{E(x)} = \frac{1}{\varepsilon\varepsilon_0}\int_0^x \rho(x)\,dx = -\frac{N_d}{\varepsilon\varepsilon_0}(w-x), 0 \le x \le w \quad 1.4$$

Where ε and ε_0 are the dielectric constant of vacuum and relative dielectric constant of semiconductor, respectively. Largest electric strength occurs at the semiconductor/electrolyte

interface with an amplitude of $\frac{N_d w}{\varepsilon\varepsilon_0}$. Potential at semiconductor can be derived by integrating the electric field as a function of distance following Equation 1.5:

$$V(x) = -\int_0^x \boldsymbol{E}(\boldsymbol{x})\, dx = \frac{N_d}{2\varepsilon\varepsilon_0}(w^2 - (w-x)^2), 0 \le x \le w \quad 1.5$$

The potential at the bulk semiconductor $V(x = w) = \frac{N_d w^2}{2\varepsilon\varepsilon_0}$. The depletion width can be further written as Equation 1.6.

$$w = \sqrt{\frac{2\varepsilon\varepsilon_0 V_{bi}}{N_d}} \quad 1.6$$

The electron concentration at a given position can be written out following Boltzmann distribution shown in Equation 1.1:

$$n(x) = n_b \exp[-\frac{eV(x)}{kT}] \quad 1.7$$

Where bulk carrier concentration n_b equals dopant concentration with $n_b = N_d$. The surface electron concentration n_s relates to the built-in potential at the semiconductor with

$$n_s = n_b \exp(-\frac{eV_{bi}}{kT}) = n_b \exp(-\frac{E_{fb} - E(A/A^-)}{kT}) \quad 1.8$$

We can also describe the capacitance-potential behavior of the semiconductor under abrupt approximation. Total charge in semiconductor can be expressed by:

$$Q_{sc} = AewN_d \quad 1.9$$

Where A is the electrode area. The capacitance can be written combining Equations 1.6 and 1.9:

$$C_{sc} = \frac{dQ_{sc}}{d\Delta\phi_{sc}} = A\sqrt{\frac{e\varepsilon\varepsilon_0 N_d}{2\Delta\phi_{sc}}} = A\sqrt{\frac{e\varepsilon\varepsilon_0 N_d}{2V_{bi}}} \quad 1.10$$

In a more rigorous derivation that solves the Poisson-Boltzmann equation by abandoning the abrupt approximation,[24] an additional thermal energy term will arise. By writing the inverse square of semiconductor capacitance as a function of applied potential, one gets the Mott-Schottky

equation form of the capacitance-voltage behavior, which is widely applied to extract the flatband potential of a semiconductor.[24]

$$\frac{1}{C_{sc}} = \frac{2}{e\varepsilon\varepsilon_0 N_d A^2}(V - V_{fb} - \frac{kT}{e}) \quad 1.11$$

1.2. Potential-current behavior of semiconductor/electrolyte junction under dark and illumination conditions

Figure 1.2 described a simplified interfacial charge transfer process between a n-type semiconductor and a solution redox species (A/A^-) in the dark and under illumination. A can be reduced to A^- and regenerated back to A in reaction with electrons on conduction band (dark process) and photogenerated holes in valance band (light process) following the reaction equilibrium:

$$e^- + A \xrightarrow{k_{et}} A^-$$

$$A^- \xrightarrow{k_{et}^{-1}} e^- + A$$

$$h^+ + A^- \xrightarrow{k_{ht}} A$$

$$A \xrightarrow{k_{ht}^{-1}} h^+ + A^-$$

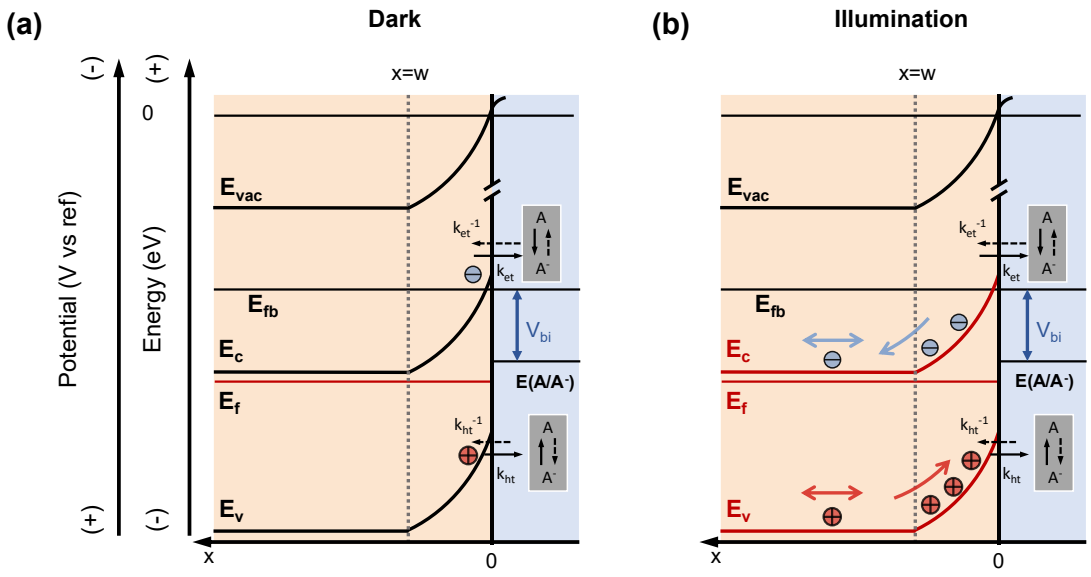

Figure 1.2 n-type semiconductor electrode under (a) electrochemical with no light illumination and (b) photoelectrochemical with monochromatic light excitation conditions. A simple regenerative cell condition is assumed, where [A] is the only oxidative species and [A^-] is the only reductive species, both will interact with semiconductor conductor band electrons and valance band holes.[22]

Under the dark condition, we mainly consider the conduction process where electron is the majority carrier in n-type semiconductor. The electron injection rate from semiconductor to solution is:

$$j_c^+ = k_{et} n_s [A] \qquad 1.12$$

Back electron transfer rate from solution to conduction band edge is:

$$j_c^- = k_{et}^{-1} [A^-] \qquad 1.13$$

In Equations 1.12 and 1.13, k_{et} and k_{et}^{-1} are the rate constant of electron forward and reverse injection, respectively; [A] and [A^-] are the concentration of oxidized and reduced species, respectively. Under equilibrium condition where no net electron current passes through the surface,

we can equate Equation 1.12 and 1.13 and obtain $k_{et}^{-1} = k_{et} n_{so}[A]/[A^-]$, where n_{so} is the surface electron concentration under equilibrium conditions. Therefore, the net electron transfer rate on the surface can be written as:

$$\frac{dn}{dt} = j_c^+ - j_c^- = k_{et}[A](n_s - n_{s0}) \quad 1.14$$

Current across the interface can be expressed as the number of charges flows per unit of time on a certain surface area A:

$$I_c = -eA\left(\frac{dn}{dt}\right) = -eAk_{et}[A](n_s - n_{s0}) \quad 1.15$$

We define the sign of electron current flowing out of the interface to be negative, and hole current flowing out of the interface to be positive. Under the equilibrium condition, surface electron concentration is written follows Equation 1.8 with $n_{s0} = n_b \exp(-\frac{eV_{bi}}{kT})$. When an addition potential V is applied on the potential to shift the Fermi-level away from its equilibrium, surface electron concentration can be written as:

$$n_s = n_b \exp(-\frac{V_{bi}+V}{kT}) \quad 1.16$$

Inserting the n_s and n_{so} into Equation 1.15 to replace n_s, we have:

$$I_c = -eAk_{et}[A]n_{s0}\left[exp\left(-\frac{V}{kT}\right) - 1\right] = -I_{c0}\left[exp\left(-\frac{V}{kT}\right) - 1\right] \quad 1.17$$

I_{c0} is also called the exchanged current density when $j_c^+ = j_c^-$. Based on Equation 1.17, we can tell that when applied potential is more negative than equilibrium potential V(A/A^-), electron will flow to the solution; when applied potential is more positive than V(A/A^-), net current will be oxidative current. We summarized these two scenarios as forward potential and reverse potential, respectively.

Likewise, we can write the hole valance band current in the dark as:

$$I_v = -I_{v0}\left[exp\left(\frac{V}{kT}\right) - 1\right] \quad 1.18$$

Where I_{v0} is the valance band exchange current density. Considering hole is the minority charge carrier under the dark condition, where $p_{s0} \ll n_{s0}$ in semiconductor depletion region, we can neglect the contribution of I_v dark process during the derivation of photocurrent across the junction.

As shown in Figure 1.2b, upon CW illumination of the semiconductor/electrolyte junction, photogenerated charge carrier will be generated in bulk and SCR part of semiconductor. Photogenerated electrons will be swiped to the bulk and will not contribute to the increase of surface electron concentration n_s. Photogenerated holes will diffuse and drift to the surface forming photocurrent I_{ph}. Assuming a fast surface reaction kinetics where photogenerated charges reaches the interface will transfer to the solution, total current across the semiconductor/electrolyte junction can be written as:

$$I = I_{ph} - I_{c0}\left[exp\left(-\frac{V}{kT}\right) - 1\right] \quad 1.19$$

Photogenerated minority current can be approach by summing up the drift current j_{sc} and diffusion current j_{diff}. Drift current consists of the photogenerated holes in the SCR (0<x<w), while diffusion current refers to the hole current generated in the bulk that diffuse to the SCR boundary x=w. Drift current can be calculated considering the charge generation in SCR:

$$j_{sc} = eP_0[1 - \exp(-\alpha w)] \quad 1.20$$

Where P_0 is the monochromatic photon flux incident on the semiconductor surface at x=0, α is the absorption coefficient of the monochromatic light within semiconductor media. Diffusion current can be calculated by solving the diffusion equation for photogenerated holes:

$$D\frac{\mathrm{d}^2p(x)}{\mathrm{d}z^2} - \frac{p(x)-p_0}{\tau} + P_0\alpha\exp(-\alpha x) = 0 \quad 1.21$$

Where D is the diffusion coefficient of holes; τ is the lifetime of the minority carriers; p(x) and p_0 are the hole concentration at distant x and equilibrium hole density, respectively. In Equation 1.21, the first term accounts for the hole diffusion, the second term accounts for the recombination in

the bulk semiconductor, and third term accounts for the hole generation at distance x. One can solve the diffusion current at the depletion layer edge by applying the boundary conditions $p=p_0$ at $x = \infty$, and $p=p_d$ at $x = w$:

$$j_{\text{diff}} = -j_0[\frac{p_{\text{d}}}{p_0} - 1] + \frac{eP_0\alpha L_{\text{p}}}{1+\alpha L_{\text{p}}}\exp(-\alpha x) \quad 1.22$$

With

$$j_0 = \frac{eDn_{\text{i}}^2}{N_{\text{D}}L_{\text{p}}} \quad 1.23$$

Where L_p is the hole diffusion length with $L_p = (D\tau)^{1/2}$. By further assuming that $p_d=0$ at semiconductor reverse bias conditions, summing up Equation 1.20 and 1.22, photogenerated minority current can be express as:

$$I_{ph} = A(j_{sc} + j_{\text{diff}}) = A[j_0 + eP_0\left[1 - \frac{\exp(-\alpha w)}{1+\alpha L_{\text{p}}}\right]] \quad 1.24$$

This is the Gärtner current describing the ideal photogenerated current across the semiconductor-metal Schottky junction.[25] In our simple model, current-potential behavior under monochromatic illumination across semiconductor/electrolyte junction can be written assuming no recombination occurs in SCR and at the surface:

$$I = A[j_0 + eP_0\left[1 - \frac{\exp(-\alpha w)}{1+\alpha L_{\text{p}}}\right]] - I_{c0}\left[exp\left(-\frac{V}{kT}\right) - 1\right] \quad 1.25$$

1.3. Progress of understanding semiconductor/electrolyte junctions

Fundamental kinetic study of semiconductor electrodes, which mainly involves charge carrier transfer and recombination process at bulk and semiconductor/electrolyte junction started at the 1970s through electrochemical methods, can help us better understand the nature of semiconductor electrodes, shedding light on further design and fabrication of devices with better energy conversion efficiency. Williams et al[26] studied irreversible process in n-TiO_2-OH^- interface

model and conclude that in order to achieve high quantum efficiency (80%-100%), the time constant for interfacial charge transfer needs to be shorter than 0.5 ps based on calculations of experimental data. Later on, Kuhne et al[27] evaluated Tafel plots of illuminated bare p-InP and different catalyst-coated p-InP photoelectrodes under different illumination power for hydrogen evolution reaction (HER): logarithm of photocurrent densities is plotted as a function of flatband potential shift, analyzed by impedance-potential measurement. The authors believed that the shift of flatband potential measured under the photoelectrochemical condition is the same as the kinetic overvoltage for HER at the catalyst surface. This measurement introduce determination of cathodic transfer coefficient α_c, Schottky barrier ideality factor n and the exchange current density j_0 of InP photoelectrodes. The following report by Kuhne et al[28] analyzed the impedance data in recombination region of p-InP and Pt-coated p-InP photocurrent-voltage curve, providing not only information of α_c, n, and j_0 but also a charge transfer kinetics model. Impedance measurement techniques have also been adopted by Lewis and co-workers[29-30] to study rate constant for majority charge carriers transfer across semiconductor/electrolyte junction. n-Si/CH_3OH-viologen$^{2+/+}$ interface was studied in Mott-Schottky plot and J-V curved, exhibiting a first-order reaction kinetic dependent of electron concentration at semiconductor surface n_s and first-order kinetic dependent on acceptor concentration in solution [A]. The charge transfer rate constant k_{et} was calculated to be $\sim 6\times 10^{17}$ cm^4 s^{-1} at n-Si/CH_3OH-viologen$^{2+/+}$ interface[29] using the charge-transfer equation described with Equation 1.12.[23] Later, charge-transfer rate constants were also studied at n-ZnO in contact with different redox species in aqueous solution[30]. The driving force dependence of k_{et} shows agreement with Marcus-Hush model for interfacial electron transfer.

Another type of experiment to evaluate charge transfer kinetics involves direct measurement of charge carriers through time-resolved spectroscopy technique. Gottesfeld et al[31]

measure the photoluminescence decay of CdS single crystal electrode in contact with the electrolyte. The analysis yielded a charge carrier lifetime in bulk electrode to be 2.5 ps and surface recombination velocity larger than 10^6 cm s^{-1} in contact of charge mediators, for instance, S^{2-}. An observation of longer time scale of charge carriers (μs-ms) for water oxidation within n-hematite photoanode have been reported Durrant group[32] via transient absorption spectroscopy, a laser pump-probe technique, to study charge carrier dynamics. A bias dependence of charge carriers is also observed as shown in Figure 1.3: photogenerated holes exhibiting a microsecond decay timescale at open circuit potential (-0.1 V vs Ag/Cl), similar to the decay timescale of isolated films. However, signal shows a much longer-lived lifetime of 3 ± 1 s under +0.4 V vs Ag/AgCl, indicating long-lived holes due to the depletion of electrons in space charge region under positive bias. Moreover, charge carrier lifetime decreases to 400 ± 100 ms after adding hole scavenger methanol to the system, indicating the consumption of long-lived holes responsible for water oxidation.

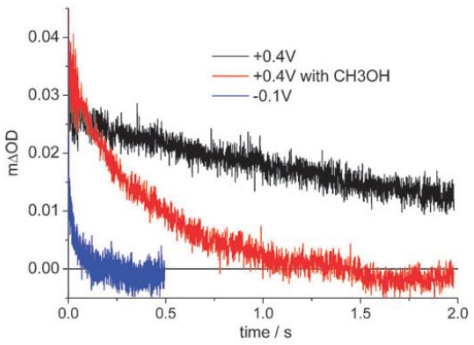

Figure 1.3. Transient absorption kinetic of hematite photoanodes measured under applied bias of -0.1 V *vs* Ag/AgCl in 0.1 M NaOH (aq) (blue), +0.4 V *vs* Ag/AgCl with methanol in 0.1 M NaOH (aq) (red), +0.4 V *vs* Ag/AgCl in 0.1 M NaOH (aq) as a function of time. Kinetics are obtained upon pump excitation at 355 nm and probe at 580 nm. Reproduced with permission from Stephanie R. Pendlebury, Monica Barroso, Alexander J. Cowan, Kevin Sivula, Junwang Tang, Michael

Gratzel, David Klug, and James R. Durrant, *Chemical Communication*, 2011, 47, 716-718. Copyright Royal Society of Chemistry 2011.[32]

Further kinetic research on hematite photoelectrode was update by Durrant and co-workers[33] using photoinduced absorption spectroscopy (PIA) to develop water oxidation reaction rate law analysis on various metal oxide surface.[33-36] By establishing a kinetic model (Figure 1.4a), the kinetic relationship between surface hole density, determined by surface hole absorption, and steady-state photocurrent are proposed:

$$\frac{dp_s}{dt} = J_{holes} - k_{WO} \cdot {p_s}^{\beta} \qquad 1.26$$

where p_s is surface hole densities, J_{holes} is the flux of holes towards the surface, k_{WO} is the water oxidation rate constant, and β is the rate order regarding surface accumulated holes. Based on this model, the reaction order is analyzed as a function of surface hole density as shown in Figure 1.4b. This analysis shows a transition of water oxidation reaction from one to three when surface hole density changes from 1 to 2 [holes] nm^{-2} by increasing the illumination power.

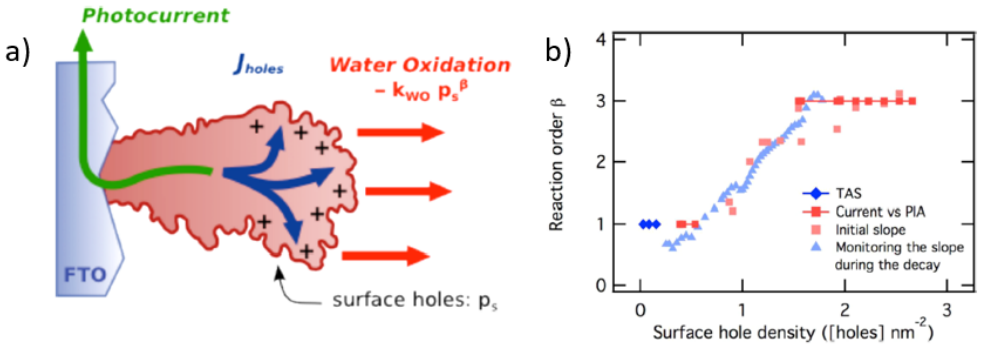

Figure 1.4. (a) Proposed water oxidation kinetic model at hemitite surface (b) change of water oxidation reaction order, dertemined by different experimental techniques, as a function of surface hole density. Reproduced from Florian Le Formal, Ernest Pastor, S. David Tilley, Camilo A. Mesa, Stephanie R. Pendlebury, Michael Gratzel, and James R. Durrant, *Journal of the American Chemical Society*, 2015, 137, 6629-6637.[33]

As for the further interfacial time-resolved kinetic study, Cuk[37] and co-workers developed transient IR technique to detect the vibrational stretch of interfacial titanium oxyl radicals Ti-O·, an important intermediate on the $SrTiO_3$ surface during photocatalytic water oxidation process. They also determined the trapping of the photogenerated holes will be trapped at the surface generating one-electron intermediates Ti-O· and Ti-O·-Ti, with formation time of Ti-O· to be 1.3 ± 0.2 ps.[38] Later study investigated the decay pathways for these two parallel transition states at microsecond timescale. They also showed that reaction conditions can be adjusted to allow selection between the two pathways.[39]

Furthermore, Yang and Beard et al[40] studied interfacial carrier dynamics at bare p-$GaInP_2$, $GaInP_2/TiO_2$ p-n junction and $GaInP_2$/Pt Schottky junction interface applying transient reflectance spectroscopy (TRS) technique. The change of reflectance $\frac{\Delta R}{R}$ at $GaInP_2$ bandgap position (1.8 eV) can be assigned to the change of transient photoinduced electric field (ΔF), which can reflect the change of carrier density. The TRS results reveal the charge separation driven by the internal electric field in the p-$GaInP_2/TiO_2$ p-n junction and p-$GaInP_2$/Pt Schottky junction. Compared with p-$GaInP_2$/Pt electrode, p-$GaInP_2/TiO_2$ exhibits a better separation efficiency due to its p-n junction nature. Their further study investigate the built-in field evolution on n-GaAs photoanode using TRS and inspect the effect of Fermi-level pinning due to the mid-gap surface states.[41] TRS is also applied to study the carrier dynamics on GaP/TiO_2 photocathode by Lian and Xu et al.[42-43] GaP/TiO_2 is first study as a function of TiO_2 protection layer thickness.[43] A direct relationship is established between the TRS signal and the separated charge carriers concentration under a weak field limit. Increasing the TiO_2 layer from 0 to 35 nm will increase the built-in field in the GaP depletion region which will enhance both the interfacial electron transfer rate and efficiency from GaP to TiO_2 on the picosecond timescale. The following study performs *in situ* investigation of

GaP/5 nm TiO_2 photocathode to measure the charge separation efficiency under HER conditions using TRS. By comparing bias-dependent TRS with the over incident light-to-current conversion efficiency (IPCE) under this *in situ* condition, it is confirmed that TRS directly measures the separated electrons responsible for HER reaction at an early timescale and can be a probe of charge carrier separation efficiency of the photoelectrochemical water reduction process.

1.4. Challenges in studying the semiconductor/electrolyte junctions for oxygen evolution reaction, hydrogen evolution reaction and CO_2 reduction reactions.

Although macroscopic features including current and quantum efficiency of semiconductor/electrolyte junction properties have been extensively studied through J-V curves analysis and impedance spectroscopy measurement, more microscopic properties, for example, electric field across the semiconductor/electrolyte junction, surface reaction intermediates and surface catalyst functions, need further investigation through *in situ* spectroscopic investigations. Moreover, as more novel hybrid photocatalyst being developed with modification of co-catalyst on the semiconductors for more efficient photo(electro)chemical oxygen evolution reaction (OER), hydrogen evolution reaction (HER) and CO_2 reduction,[44-68] charge carrier dynamics on these hybrid photo(electro)catalyst need to be further understood by time-resolve techniques. On the one hand, studying charge carrier dynamics offers more mechanistic insight of individual steps that affect the photon utilization, such as charge separation, transport, and transfer steps. On the other hand, charge-carrier dynamics investigation offers a clearer picture of how semiconductor photosensitizer and the modified co-catalyst interact.

In this thesis, we tend to address the gap of knowledge on two aspects. On the first aspect, we apply several *in situ* spectroscopic techniques to investigate the photoelectrode-(catalyst)/electrolyte junction. In Chapter 3, we use *in situ* Second Harmonic Generation to

characterize the potential distribution of rutile TiO_2(100)/electrolyte junction. Bias-dependent behavior is studied as a function of single crystal azimuthal angle and light polarization. In Chapter 4, we further use Second Harmonic Generation to investigate the built-in potential change and surface hole accumulation under *operando* OER condition. The rate-determining step of OER on TiO_2 is investigated through isotope effect experiments. In Chapter 8, we utilize *in situ* Raman spectroscopy to study the complicated Silicon based semiconductor micropillar array (SMA)/CNT/CoPc-NH_2-solution junction for efficient CO_2 to methanol reduction reaction. We found that the Fermi-level alignment of the junction is greatly related to the one-electron reduction of CoPc-NH_2 molecular catalyst mobilized on photoelectrode surface.

On the other hand, we use transient absorption and transient reflectance spectroscopy to study the charge carrier dynamics of semiconductor photo(electro)catalyst. In Chapter 5, we study the charge carrier dynamics on a TiO_2 photoanode modified with a polyoxometalate water oxidation catalyst that is capable for stable and efficient OER under acidic condition. Through transient absorption spectroscopy, we observed the ultrafast hole transfer from photosensitizer to catalyst. In Chapter 7, we investigate an efficient CO_2 reduction photocatalyst with CdS as photosensitizer and CNT/CoPc as CO_2 catalyst. Transient absorption spectroscopy in visible and near-IR range unambiguously investigated the charge carrier dynamics that involves the photogenerated electrons transfer from CdS to CNT, and later electron accumulation on CNT. In Chapter 6, we use transient reflectance spectroscopy to study the carrier dynamics on a GaP/TiO_2 photocathode for HER. The TRS study reveals how the electrolyte concentration affects the charge recombination of GaP/TiO_2 at long timescale ranging from nanosecond to microsecond, which will influence the photocatalysis quantum efficiency.

1.5. Reference

1. Chen, Z.; Cummins, D.; Reinecke, B. N.; Clark, E.; Sunkara, M. K.; Jaramillo, T. F., Core–shell MoO_3–MoS_2 Nanowires for Hydrogen Evolution: A Functional Design for Electrocatalytic Materials. *Nano Lett.* **2011,** *11* (10), 4168-4175.
2. Grätzel, M., Photoelectrochemical cells. *Nature* **2001,** *414* (6861), 338.
3. O'regan, B.; Grätzel, M., A low-cost, high-efficiency solar cell based on dye-sensitized colloidal TiO_2 films. *Nature* **1991,** *353* (6346), 737.
4. Gerischer, H., *Adv. Electrochem. Electrochem. Eng.* **1961,** *1* (139).
5. Dunn, W. W.; Aikawa, Y.; Bard, A. J., Characterization of particulate titanium dioxide photocatalysts by photoelectrophoretic and electrochemical measurements. *J. Am. Chem. Soc.* **1981,** *103* (12), 3456-3459.
6. Fan, F. R. F.; Bard, A. J., Semiconductor electrodes. 24. Behavior of photoelectrochemical cells based on p-type gallium arsenide in aqueous solutions. *J. Am. Chem. Soc.* **1980,** *102* (11), 3677-3683.
7. Frank, S. N.; Bard, A. J., Semiconductor electrodes. II. Electrochemistry at n-type titanium dioxide electrodes in acetonitrile solutions. *J. Am. Chem. Soc.* **1975,** *97* (26), 7427-7433.
8. Kohl, P. A.; Bard, A. J., Semiconductor electrodes. 13. Characterization and behavior of n-type zinc oxide, cadmium sulfide, and gallium phosphide electrodes in acetonitrile solutions. *J. Am. Chem. Soc.* **1977,** *99* (23), 7531-7539.
9. Laser, D.; Bard, A. J., Semiconductor electrodes. IV. Electrochemical behavior of n- and p-type silicon electrodes in acetonitrile solutions. *J. Phys. Chem.* **1976,** *80* (5), 459-466.
10. Bard, A. J.; Bocarsly, A. B.; Fan, F. R. F.; Walton, E. G.; Wrighton, M. S., The concept of Fermi level pinning at semiconductor/liquid junctions. Consequences for energy conversion efficiency and selection of useful solution redox couples in solar devices. *J. Am. Chem. Soc.* **1980,** *102* (11), 3671-3677.
11. Dominey, R. N.; Lewis, N. S.; Wrighton, M. S., Fermi level pinning of p-type semiconducting indium phosphide contacting liquid electrolyte solutions: rationale for efficient photoelectrochemical energy conversion. *J. Am. Chem. Soc.* **1981,** *103* (5), 1261-1263.
12. Santangelo, P. G.; Miskelly, G. M.; Lewis, N. S., Cyclic voltammetry at semiconductor photoelectrodes. 1. Ideal surface-attached redox couples with ideal semiconductor behavior. *J. Phys. Chem.* **1988,** *92* (22), 6359-6367.
13. Santangelo, P. G.; Miskelly, G. M.; Lewis, N. S., Voltammetry of semiconductor electrodes. 2. Cyclic voltammetry of freely diffusing redox species and rotating semiconductor disk voltammetry. *J. Phys. Chem.* **1989,** *93* (16), 6128-6136.
14. Aruchamy, A.; Wrighton, M. S., A comparison of the interface energetics for n-type cadmium sulfide/- and cadmium telluride/nonaqueous electrolyte junctions. *J. Phys. Chem.* **1980,** *84* (22), 2848-2854.

15. Schneemeyer, L. F.; Wrighton, M. S., Flat-band potential of n-type semiconducting molybdenum disulfide by cyclic voltammetry of two-electron reductants: interface energetics and the sustained photooxidation of chloride. *J. Am. Chem. Soc.* **1979,** *101* (22), 6496-6500.
16. Meissner, D.; Memming, R.; Kastening, B., Photoelectrochemistry of cadmium sulfide. 1. Reanalysis of photocorrosion and flat-band potential. *J. Phys. Chem.* **1988,** *92* (12), 3476-3483.
17. Meissner, D.; Lauermann, I.; Memming, R.; Kastening, B., Photoelectrochemistry of cadmium sulfide. 2. Influence of surface-state charging. *J. Phys. Chem.* **1988,** *92* (12), 3484-3488.
18. Kelly, J. J.; Memming, R., The Influence of Surface Recombination and Trapping on the Cathodic Photocurrent at p-Type III-V Electrodes. *J. Electrochem. Soc.* **1982,** *129* (4), 730-738.
19. Chazalviel, J. N., Electrochemical transfer via surface states: a new formulation for the semiconductor/electrolyte interface. *J. Electrochem. Soc.* **1982,** *129* (5), 963-969.
20. Chazalviel, J. N.; Truong, T. B., Experimental study of the n-silicon/acetonitrile interface: Fermi level pinning and surface states investigation. *J. Am. Chem. Soc.* **1981,** *103* (25), 7447-7451.
21. Tan, M. X.; Laibinis, P. E.; Nguyen, S. T.; Kesselman, J. M.; Stanton, C. E.; Lewis, N. S., Principles and Applications of Semiconductor Photoelectrochemistry. In *Progress in Inorganic Chemistry*, 1994; pp 21-144.
22. Kumar, A.; Santangelo, P. G.; Lewis, N. S., Electrolysis of water at strontium titanate ($SrTiO_3$) photoelectrodes: distinguishing between the statistical and stochastic formalisms for electron-transfer processes in fuel-forming photoelectrochemical systems. *J. Phys. Chem.* **1992,** *96* (2), 834-842.
23. Lewis, N. S., An Analysis of Charge Transfer Rate Constants for Semiconductor/Liquid Interfaces. *Annu. Rev. Phys. Chem.* **1991,** *42* (1), 543-580.
24. Memming, R., Solid–Liquid Interface. In *Semiconductor Electrochemistry*, WILEY-VCH Verlag GmbH: 2015; pp 89-125.
25. Gärtner, W. W., Depletion-Layer Photoeffects in Semiconductors. *Physical Review* **1959,** *116* (1), 84-87.
26. Williams, F.; Nozik, A. J., Irreversibilities in the mechanism of photoelectrolysis. *Nature* **1978,** *271*, 137.
27. Kühne, H. M.; Schefold, J., Tafel Plots from Illuminated Photoelectrodes A New Insight Into Charge Transfer Mechanism. *J. Electrochem. Soc.* **1990,** *137* (2), 568-575.
28. Schefold, J.; Kühne, H. M., Charge transfer and recombination kinetics at photoelectrodes: A quantitative evaluation of impedance measurements. *J. Electroanal. Chem. Interfacial Electrochem.* **1991,** *300* (1), 211-233.
29. Farjardo, A. M.; Lewis, N. S., Rate Constants for Charge Transfer Across Semiconductor-Liquid Interfaces. *Science* **1996,** *274* (5289), 969-972.
30. Hamann, T. W.; Gstrein, F.; Brunschwig, B. S.; Lewis, N. S., Measurement of the driving force dependence of interfacial charge-transfer rate constants in response to pH changes at n-ZnO/H_2O interfaces. *Chem. Phys.* **2006,** *326* (1), 15-23.

31. Evenor, M.; Gottesfeld, S.; Harzion, Z.; Huppert, D.; Feldberg, S. W., Time-resolved photoluminescence in the picosecond time domain from cadmium sulfide crystals immersed in electrolytes. *J. Phys. Chem.* **1984,** *88* (25), 6213-6218.
32. Pendlebury, S. R.; Barroso, M.; Cowan, A. J.; Sivula, K.; Tang, J.; Grätzel, M.; Klug, D.; Durrant, J., Dynamics of photogenerated holes in nanocrystalline α-Fe_2O_3 electrodes for water oxidation probed by transient absorption spectroscopy. *Chem. Commun.* **2011,** *47* (2), 716-718.
33. Le Formal, F.; Pastor, E.; Tilley, S. D.; Mesa, C. A.; Pendlebury, S. R.; Grätzel, M.; Durrant, J. R., Rate Law Analysis of Water Oxidation on a Hematite Surface. *J. Am. Chem. Soc.* **2015,** *137* (20), 6629-6637.
34. Mesa, C. A.; Francàs, L.; Yang, K. R.; Garrido-Barros, P.; Pastor, E.; Ma, Y.; Kafizas, A.; Rosser, T. E.; Mayer, M. T.; Reisner, E.; Grätzel, M.; Batista, V. S.; Durrant, J. R., Multihole water oxidation catalysis on haematite photoanodes revealed by operando spectroelectrochemistry and DFT. *Nat. Chem.* **2019**.
35. Kafizas, A.; Ma, Y.; Pastor, E.; Pendlebury, S. R.; Mesa, C.; Francàs, L.; Le Formal, F.; Noor, N.; Ling, M.; Sotelo-Vazquez, C.; Carmalt, C. J.; Parkin, I. P.; Durrant, J. R., Water Oxidation Kinetics of Accumulated Holes on the Surface of a TiO_2 Photoanode: A Rate Law Analysis. *ACS Catal.* **2017,** *7* (7), 4896-4903.
36. Ma, Y.; Mesa, C. A.; Pastor, E.; Kafizas, A.; Francàs, L.; Le Formal, F.; Pendlebury, S. R.; Durrant, J. R., Rate Law Analysis of Water Oxidation and Hole Scavenging on a $BiVO_4$ Photoanode. *ACS Energy Lett.* **2016,** *1* (3), 618-623.
37. Herlihy, D. M.; Waegele, M. M.; Chen, X.; Pemmaraju, C.; Prendergast, D.; Cuk, T. J. N. c., Detecting the oxyl radical of photocatalytic water oxidation at an n-$SrTiO_3$/aqueous interface through its subsurface vibration. *Nat. Chem.* **2016,** *8* (6), 549.
38. Chen, X.; Choing, S. N.; Aschaffenburg, D. J.; Pemmaraju, C. D.; Prendergast, D.; Cuk, T., The Formation Time of Ti–O• and Ti–O•–Ti Radicals at the n-SrTiO3/Aqueous Interface during Photocatalytic Water Oxidation. *J. Am. Chem. Soc.* **2017,** *139* (5), 1830-1841.
39. Chen, X.; Aschaffenburg, D. J.; Cuk, T., Selecting between two transition states by which water oxidation intermediates decay on an oxide surface. *Nature Catalysis* **2019,** *2* (9), 820-827.
40. Yang, Y.; Gu, J.; Young, J. L.; Miller, E. M.; Turner, J. A.; Neale, N. R.; Beard, M. C., Semiconductor interfacial carrier dynamics via photoinduced electric fields. *Science* **2015,** *350* (6264), 1061-1065.
41. Chen, X.; Pekarek, R. T.; Gu, J.; Zakutayev, A.; Hurst, K. E.; Neale, N. R.; Yang, Y.; Beard, M. C., Transient Evolution of the Built-in Field at Junctions of GaAs. *ACS Appl. Mater. Interfaces* **2020,** *12* (36), 40339-40346.
42. Xu, Z.; Hou, B.; Zhao, F.; Suo, S.; Liu, Y.; Shi, H.; Cai, Z.; Hill, C. L.; Musaev, D. G.; Mecklenburg, M.; Cronin, S. B.; Lian, T., Direct *in situ* Measurement of Quantum Efficiencies of Charge Separation and Proton Reduction at TiO_2-Protected GaP Photocathodes. *J. Am. Chem. Soc.* **2023,** *145* (5), 2860-2869.

43. Xu, Z.; Hou, B.; Zhao, F.; Cai, Z.; Shi, H.; Liu, Y.; Hill, C. L.; Musaev, D. G.; Mecklenburg, M.; Cronin, S. B.; Lian, T., Nanoscale TiO_2 Protection Layer Enhances the Built-In Field and Charge Separation Performance of GaP Photoelectrodes. *Nano Lett.* **2021,** *21* (19), 8017-8024.
44. Irani, R.; Plate, P.; Höhn, C.; Bogdanoff, P.; Wollgarten, M.; Höflich, K.; van de Krol, R.; Abdi, F. F., The role of ultra-thin MnO_x co-catalysts on the photoelectrochemical properties of BiVO4 photoanodes. *Journal of Materials Chemistry A* **2020,** *8* (11), 5508-5516.
45. Lin, F.; Boettcher, S. W., Adaptive semiconductor/electrocatalyst junctions in water-splitting photoanodes. *Nature Materials* **2014,** *13* (1), 81-86.
46. Liu, T.; Li, W.; Wang, D. Z.; Luo, T.; Fei, M.; Shin, D.; Waegele, M. M.; Wang, D., Low Catalyst Loading Enhances Charge Accumulation for Photoelectrochemical Water Splitting. *Angewandte Chemie International Edition* **2023**.
47. Guo, Q.; Zhao, Q.; Crespo-Otero, R.; Di Tommaso, D.; Tang, J.; Dimitrov, S. D.; Titirici, M.-M.; Li, X.; Jorge Sobrido, A. B., Single-Atom Iridium on Hematite Photoanodes for Solar Water Splitting: Catalyst or Spectator? *J. Am. Chem. Soc.* **2023,** *145* (3), 1686-1695.
48. Tilley, S. D.; Cornuz, M.; Sivula, K.; Grätzel, M., Light-Induced Water Splitting with Hematite: Improved Nanostructure and Iridium Oxide Catalysis. *Angew. Chem. Int. Ed.* **2010,** *49* (36), 6405-6408.
49. Liu, G.; Eichhorn, J.; Jiang, C.-M.; Scott, M. C.; Hess, L. H.; Gregoire, J. M.; Haber, J. A.; Sharp, I. D.; Toma, F. M., Interface engineering for light-driven water oxidation: unravelling the passivating and catalytic mechanism in $BiVO_4$ overlayers. *Sustainable Energy & Fuels* **2019,** *3* (1), 127-135.
50. Jang, J.-W.; Du, C.; Ye, Y.; Lin, Y.; Yao, X.; Thorne, J.; Liu, E.; McMahon, G.; Zhu, J.; Javey, A.; Guo, J.; Wang, D., Enabling unassisted solar water splitting by iron oxide and silicon. *Nat. Commun.* **2015,** *6* (1), 7447.
51. Thorne, J. E.; Jang, J.-W.; Liu, E. Y.; Wang, D., Understanding the origin of photoelectrode performance enhancement by probing surface kinetics. *Chemical Science* **2016,** *7* (5), 3347-3354.
52. Ye, K.-H.; Wang, Z.; Gu, J.; Xiao, S.; Yuan, Y.; Zhu, Y.; Zhang, Y.; Mai, W.; Yang, S., Carbon quantum dots as a visible light sensitizer to significantly increase the solar water splitting performance of bismuth vanadate photoanodes. *Energy & Environmental Science* **2017,** *10* (3), 772-779.
53. Kim, T. W.; Choi, K.-S., Nanoporous $BiVO_4$ Photoanodes with Dual-Layer Oxygen Evolution Catalysts for Solar Water Splitting. *Science* **2014,** *343* (6174), 990-994.
54. Nellist, M. R.; Laskowski, F. A. L.; Qiu, J.; Hajibabaei, H.; Sivula, K.; Hamann, T. W.; Boettcher, S. W., Potential-sensing electrochemical atomic force microscopy for in operando analysis of water-splitting catalysts and interfaces. *Nature Energy* **2018,** *3* (1), 46-52.
55. Ma, Y.; Kafizas, A.; Pendlebury, S. R.; Le Formal, F.; Durrant, J. R., Photoinduced Absorption Spectroscopy of CoPi on $BiVO_4$: The Function of CoPi during Water Oxidation. *Adv. Funct. Mater.* **2016,** *26* (27), 4951-4960.

56. Ma, Y.; Le Formal, F.; Kafizas, A.; Pendlebury, S. R.; Durrant, J. R., Efficient suppression of back electron/hole recombination in cobalt phosphate surface-modified undoped bismuth vanadate photoanodes. *J. Mater. Chem. A* **2015,** *3* (41), 20649-20657.
57. Abdi, F. F.; Firet, N.; van de Krol, R., Efficient $BiVO_4$ Thin Film Photoanodes Modified with Cobalt Phosphate Catalyst and W-doping. *ChemCatChem* **2013,** *5* (2), 490-496.
58. Abdi, F. F.; van de Krol, R., Nature and Light Dependence of Bulk Recombination in Co-Pi-Catalyzed $BiVO_4$ Photoanodes. *J. Phys. Chem. C* **2012,** *116* (17), 9398-9404.
59. Zhong, D. K.; Choi, S.; Gamelin, D. R., Near-Complete Suppression of Surface Recombination in Solar Photoelectrolysis by "Co-Pi" Catalyst-Modified W:$BiVO_4$. *J. Am. Chem. Soc.* **2011,** *133* (45), 18370-18377.
60. Klahr, B.; Gimenez, S.; Fabregat-Santiago, F.; Bisquert, J.; Hamann, T. W., Photoelectrochemical and Impedance Spectroscopic Investigation of Water Oxidation with "Co–Pi"-Coated Hematite Electrodes. *J. Am. Chem. Soc.* **2012,** *134* (40), 16693-16700.
61. Barroso, M.; Cowan, A. J.; Pendlebury, S. R.; Grätzel, M.; Klug, D. R.; Durrant, J. R., The Role of Cobalt Phosphate in Enhancing the Photocatalytic Activity of α-Fe_2O_3 toward Water Oxidation. *Journal of the American Chemical Society* **2011,** *133* (38), 14868-14871.
62. Zheng, M.; Cao, X.; Ding, Y.; Tian, T.; Lin, J., Boosting photocatalytic water oxidation achieved by $BiVO_4$ coupled with iron-containing polyoxometalate: Analysis the true catalyst. *Journal of Catalysis* **2018,** *363*, 109-116.
63. Lauinger, S. M.; Piercy, B. D.; Li, W.; Yin, Q.; Collins-Wildman, D. L.; Glass, E. N.; Losego, M. D.; Wang, D.; Geletii, Y. V.; Hill, C. L., Stabilization of Polyoxometalate Water Oxidation Catalysts on Hematite by Atomic Layer Deposition. *ACS Applied Materials & Interfaces* **2017,** *9* (40), 35048-35056.
64. Lauinger, S. M.; Sumliner, J. M.; Yin, Q.; Xu, Z.; Liang, G.; Glass, E. N.; Lian, T.; Hill, C. L., High Stability of Immobilized Polyoxometalates on TiO_2 Nanoparticles and Nanoporous Films for Robust, Light-Induced Water Oxidation. *Chemistry of Materials* **2015,** *27* (17), 5886-5891.
65. Shang, B.; Rooney, C. L.; Gallagher, D. J.; Wang, B. T.; Krayev, A.; Shema, H.; Leitner, O.; Harmon, N. J.; Xiao, L.; Sheehan, C.; Bottum, S. R.; Gross, E.; Cahoon, J. F.; Mallouk, T. E.; Wang, H., Aqueous Photoelectrochemical CO_2 Reduction to CO and Methanol over a Silicon Photocathode Functionalized with a Cobalt Phthalocyanine Molecular Catalyst. *Angewandte Chemie* **2023,** *135* (4).
66. Shang, B.; Zhao, F.; Choi, C.; Jia, X.; Pauly, M.; Wu, Y.; Tao, Z.; Zhong, Y.; Harmon, N.; Maggard, P. A.; Lian, T.; Hazari, N.; Wang, H., Monolayer Molecular Functionalization Enabled by Acid–Base Interaction for High-Performance Photochemical CO_2 Reduction. *ACS Energy Lett.* **2022,** *7* (7), 2265-2272.
67. Zeng, G.; Qiu, J.; Li, Z.; Pavaskar, P.; Cronin, S. B., CO2 Reduction to Methanol on TiO_2-Passivated GaP Photocatalysts. *ACS Catal.* **2014,** *4* (10), 3512-3516.
68. Qiu, J.; Zeng, G.; Pavaskar, P.; Li, Z.; Cronin, S. B., Plasmon-enhanced water splitting on TiO2-passivated GaP photocatalysts. *Phys. Chem. Chem. Phys.* **2014,** *16* (7), 3115-3121.

2 Experimental Methods

2.1. Transient absorption and reflectance spectroscopy

2.1.1. Transient absorption Spectroscopy

Transient absorption (TA) spectroscopy techniques serve as a characterization method in Chapter 5 and Chapter 7. Specifically, visible and mid-IR are used as probe beams in TA used in Chapter 5; visible and near-IR are used as probe beams in TA used in Chapter 7. In this section, we introduce the TA in femtosecond to sub-nanoseconds time scale, using visible, near-IR and mid-IR as probe (femtosecond TA), and TA in nanoseconds to microsecond time scale (Nanosecond TA).

Femtosecond visible and near-IR TA measurements were performed at room temperature in a Helios spectrometer (Ultrafast Systems LLC) with pump and probe beams derived from an amplified Ti:sapphire laser system (Coherent Astrella, 800 nm, 5.5 mJ $pulse^{-1}$, 35 fs, and 1 kHz repetition rate). An 80:20 beam splitter split the 800 nm output pulse of the amplifier into two parts. 80% of the power was used to pump an Optical Parametric Amplifier (visible-OPA, Opera, Coherent) for visible-to-near-IR pump beam generation. Two tunable near-IR pulses, i.e. signal and idler, from 1.1 to 2.7 μm are first generated. The signal and idler beams were separated with a dichroic mirror to generate tunable visible pump beams via sum-frequency generation with the 800 nm fundamental pulse. For example, the 550 nm beam came from the sum-frequency generation between the 1760 nm idler and the 800 nm fundamental pulse. The 400 nm pump beam was generated by frequency-doubling of the 800 nm fundamental pulse. A continuously variable neutral-density filter wheel was used to adjust the power of the pump beam. The pump beam was focused on the sample with a beam waist of about 620 μm. A white light continuum from 380 to 850 nm (1.5 to 3.3 eV) or from 850 to 1300 nm (0.95 to 1.5 eV) was generated by attenuating and

focusing ~10 μJ of the 800 nm pulse into a CaF_2 or sapphire window, respectively. This probe beam was focused with an Aluminum parabolic reflector on the sample with a beam waist of about 150 μm. After passing through the sample, the probe beam was focused into a fiber-coupled multichannel spectrometer with complementary metal-oxide-semiconductor (CMOS) sensors and detected at a frequency of 1 kHz. The delay between the pump and probe pulses was controlled by a motorized probe delay stage. The pump beam was chopped by a synchronized chopper at 500 Hz. The change in absorbance of the sample with and without pump was calculated as ΔA. The instrument response function (IRF) of this system was measured by measuring solvent or substrate responses of the test system under the same experimental conditions.

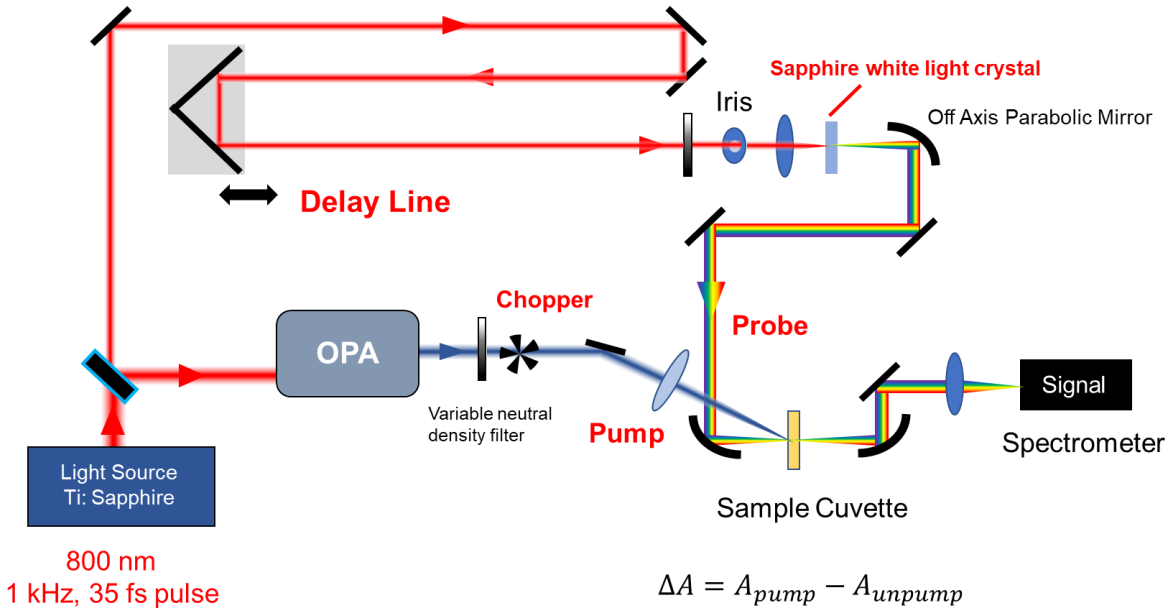

Figure 2.1. TA spectroscopy operation process using visible or near-IR as probe.

In femtosecond mid-IR TA measurement, output from the same visible-OPA is used as pump beam; it was focused on the IR sample stage with a beam waist of 410 μm. 40 % of 800 nm fundamental out (2 mJ) is used to pump an OPA (IR-Opera, Coherent) for mid-IR probe generation. Two tunable near-IR signal and idler pulses from 1.1 to 2.5 μm were generated. The signal and

idler pulses were further combined in a 1-mm-thick $AgGaS_2$ crystal to generate a tunable mid-IR pulse from 3 to 10 μm by difference frequency generation (DFG). The mid-IR beam was focused on the sample stage at a beam waist of around 290 μm to overlap with pump beam. After passing the sample, mid-IR probe was dispersed into a spectrograph and detected with a 32-element infrared HgCdTe (MCT) array detector at a frequency of 1k Hz. The pump beam was chopped by a synchronized chopper to 500 Hz. The delay between pump and probe pulses are controlled by a motorized pump delay stage. The typical IRF of mid-IR TA experiments was determined to be around 170 fs using a silicon wafer.

Nanosecond TA measurements were performed with an EOS spectrometer (Ultrafast Systems LLC). The pump pulse was derived from the Ti:sapphire laser system and visible-OPA described previously. A continuously variable neutral-density filter was used to adjust the power of the pump beam. The pump beam was focused to a size in a diameter of 1100 μm on the sample surface. A white light continuum (380-1700 nm, 0.5 ns pulse width, 2 kHz repetition rate) was generated by focusing a Nd:YAG laser into a photonic crystal fiber. A digital delay generator (CNT-90, Pendulum Instruments) was used to control the delay time between the pump and probe pulses. The probe was focused onto the 1 mm pathlength sample cuvette with a beam waist of about 200 μm. After passing through the sample, the probe beam was reflected and focused into a fiber-coupled multichannel spectrometer with CMOS sensors at a detection frequency of 1 kHz. The IRF of this nanosecond detection system was measured to be ~ 400 ps.

2.1.2. Transient reflectance spectroscopy

Transient reflectance (TR) spectroscopy technique is the main characterization method used in Chapter 6. The pump and probe pulses sources used in the femtosecond and nanosecond TR spectroscopy are derived in the same way as described in section 2.1.1. Different from the

transmission probe configuration, TR spectroscopy detect the probe reflection change from the sample surface between pumped and unpumped condition (ΔR/R) as a function of pump probe time delay as shown in Figure 2.2. The angle of incidence (AOI) for probe pulses is set at 45 degrees and 25 degrees for pump pulses. The pump excitation depth and probe depths are determined by the imaginary (k) and real (n) part of sample's refractive index as shown in Equation 2.1 and 2.1. For samples with large refractive index, TR spectroscopy can provide unique surface sensitivity that TA spectroscopy lacks.

$$d_{pump} = \frac{1}{\alpha} = \frac{\lambda}{4\pi k} \quad 2.1$$

$$d_{probe} = \frac{1}{\alpha} = \frac{\lambda}{4\pi n} \quad 2.2$$

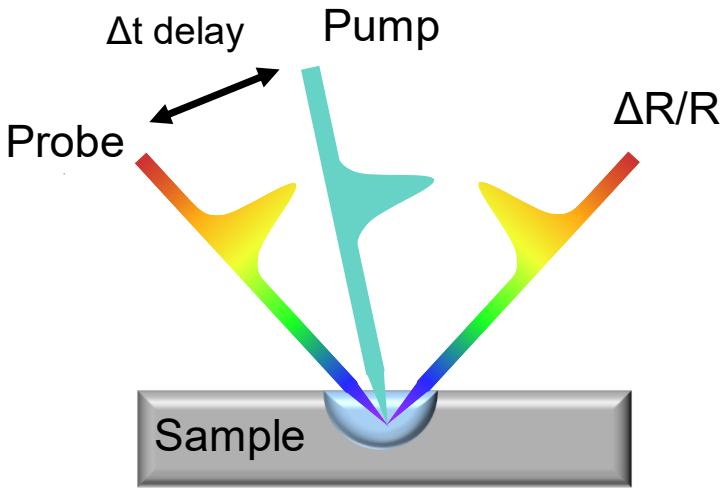

Figure 2.2. Schematic of transient reflectance spectroscopy.

2.2. Second Harmonic Generation spectroscopy

The second harmonic generation (SHG) is based on the regenerative amplified Ti: sapphire laser system (Coherent Astrella, 800 nm, 5 mJ/pulse, 35 fs pulse width, and 1 kHz repetition rate) mentioned in section 2.1. In the SHG process used in chapter 3 and 4 as shown in Figure 2.3, 1 kHz, 35 femtosecond 800 nm pulsed light is used as the fundamental probe, derived from Astrella

laser system. The fundamental probe power is tuned to be around 3 mW with a variable neutral density filter (Thorlabs, NDC-50C-4M-A) and further focused down to a beam size with a waist of 100 μm at the sample surface using a f = 100 mm lens (Thorlabs, LBF254-100-A). Fundamental light reaches the sample surface on an incident angle of 45 degrees. 800 nm polarization is controlled by a half-wave plate (Thorlabs, AQWP05M-600). Second Harmonic Generation is collected and collimated using a f = 50 mm lens (Thorlabs, LBF254-050-A). After passing two 400 nm bandpass filters (Thorlabs, FBH400-10) and linear polarizer (Thorlabs, LPVISE100-A), the signal is measured by a Bialkali Amplified Photomultiplier Tube (PMT) detector (Thorlabs, PMM01). Tube voltage is powered by a 1.3 V DC power supply (GW INSTEK, GPD-230S). Upon signal collection, it is further processed by a boxcar average (Stanford Research SR200 Series) for noise filtering. The gated signal is averaged 1000 times by the boxcar average and sent to a data acquisition board, read out by a homebuilt LabVIEW software. The collected voltage signal is transformed into SHG counts using the transimpedance gain and responsivity parameter provided by the manufacturer. In Figure 2.3, we present the SHG setup with the sample placed in a typical three-electrode electrochemical setup. As mentioned in Chapter 3 and 4 in detail, the sample will be adapted to meet different experimental purposes, for example, azimuthal-angle-resolved solid-air SHG, azimuthal-angle-resolved solid-liquid bias-dependent SHG, and *in situ* EFISH under light illumination.

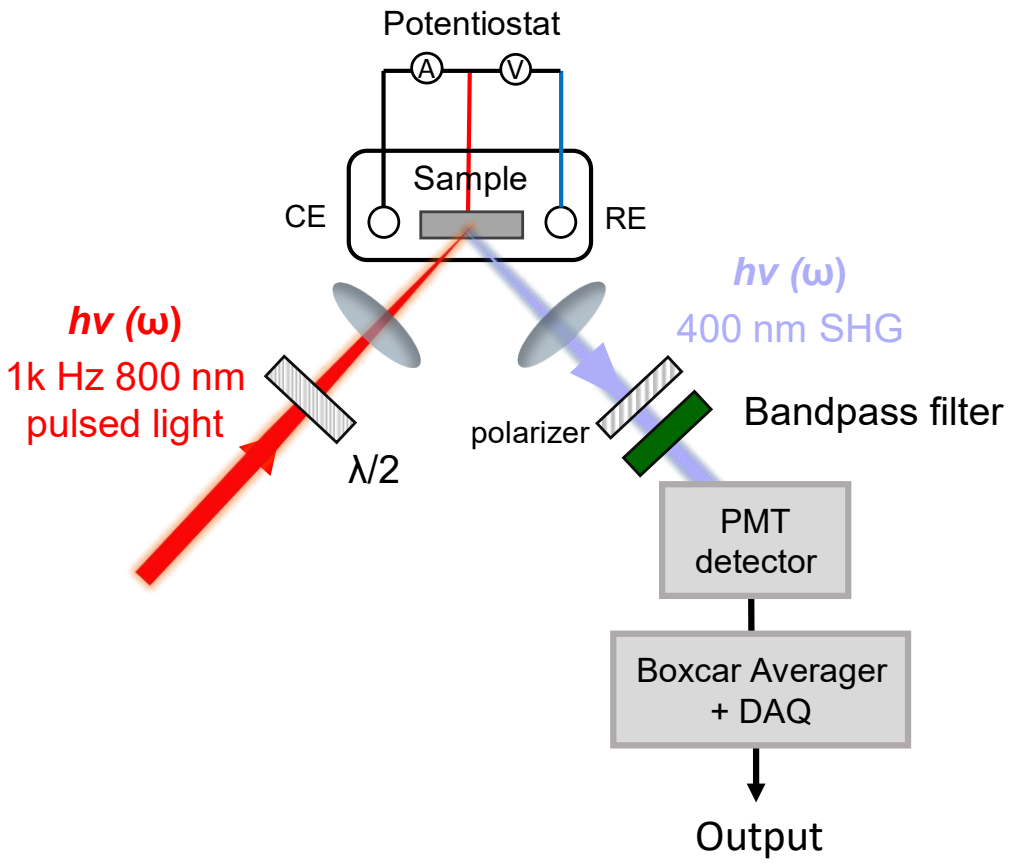

Figure 2.3. Second Harmonic generation spectroscopy with sample in a typical three-electrode electrochemical setup.

2.3. *In situ* Raman spectroscopy

The *in situ* Raman spectroscopy is used in chapter 8 with a setup shown in Figure 2.4. This home-built Raman system includes a polarized 632.8 nm He-Ne laser source (Thorlabs, HNL210LB), silica broadband dielectric mirrors (Thorlabs, BB1-E02) and a 633 nm long pass beam splitter (Semrock, LP02-633RE-25) for beam guiding, a 50 × objective (Newport, MLWD-50X, 0.55 NA, 13 mm working distance) for focusing and Raman collection, a 633 nm single-notch filter (Semrock, NF03-633E-25) for filtering, and an electron-multiplied charge-coupled device (Newton EMCCD, Andor) for signal collection. The sample (electrode) is mounted in a

three-electrode electrochemical cell, which sits on a translational stage to adjust the sample to meet the focal point of the objective lens.

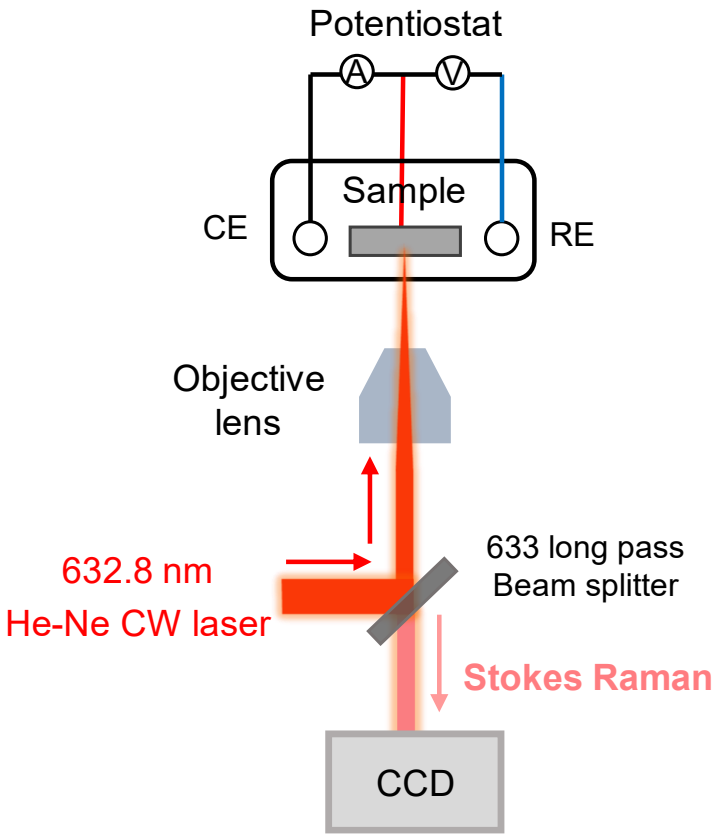

Figure 2.4. *In situ* Raman spectroscopy with sample in a typical three-electrode electrochemical setup.

3 *In situ* Investigation of Electric Field Distribution on TiO_2(100)-electrolyte Junction by Azimuthal-Angle-Resolved Second Harmonic Generation

3.1. Introduction

Understanding the electric distribution and charge transfer at the solid-liquid interface is vital in energy conversion, including charge storage process in battery and supercapacitor, [1-9] charge transfer process on metal and semiconductor electrode for hydrogen evolution, oxygen evolution (HER and OER), [10-19] and CO_2 reduction process. [20-24] This requires a surface-specific, contactless method to investigate the interfacial structural and electric field information. The nonlinear optical second harmonic generation (SHG) technique, a non-linear optical phenomenon in which a medium interacts with two incident photons of the same frequency to produce a photon with double frequency, is developed as a unique tool to investigate various aspect such as ionic adsorption at electrode interface, surface molecular orientation, and interfacial electric field at electrode/electrolyte junction. [25-35] More notably, SHG serves as an *in situ*, non-invasive, and time-resolved technique without the need for surface modification or damage. In various applications, investigating the third-order nonlinear susceptibility contribution ($\chi^{(3)}$) induced by the electric field is crucial for understanding key properties of the electrode-liquid interface in (photo)electrochemical catalysis, such as the potential of zero charge and flatband potential. [25-27, 32] Nonetheless, directly extracting these values from bias-dependent SHG behavior on a surface with a non-negligible second-order susceptibility ($\chi^{(2)}$) is challenging. Predicting the potential minimum of the electrode-electrolyte junction using the bias-dependent SHG minimum potential is not feasible without knowledge of the amplitude ratio and relative phase and difference between $\chi^{(2)}$ and $\chi^{(3)}$. [27, 28] Hence, it is important to establish the relationship between $\chi^{(2)}$ and $\chi^{(3)}$,

particularly on an anisotropic surface, by conducting an azimuthal-angle-resolved bias-dependent SHG study.

TiO_2 plays a crucial role in energy conversion process, serving as an effective electron transporting layer in dye-sensitized and perovskite solar cells; [36-41] a vital protection layer for III-V semiconductor photoelectrode; [16, 19, 20, 42] and a photoelectrode itself. [43-45] It can serve as a benchmark semiconductor electrode material for our SHG study. This report investigates the bias-dependent SHG behavior at Niobium (Nb)-doped Rutile TiO_2 (100)-electrolyte junction as a function of crystal azimuthal angle, defined as the angle between incident plane and TiO_2 [001] axis, and the combination of light polarization. Rotational anisotropic experiments reveal a two-fold surface symmetry (C_{2v}) on TiO_2 surface under pp, ps, and sp polarizations. Bias-dependent SHG experiments are conducted at various representative azimuthal angles and different light polarizations at TiO_2-electrolyte junction. A quadratic bias-dependent SHG intensity response is observed at both positive and negative side of TiO_2 flatband potential. Relative phase difference and amplitude ratio between the bias-independent and bias-dependent non-linear susceptibility contribution have been analyzed in both TiO_2 depletion and accumulation region as a function of azimuthal angle and polarization. Notably, regardless of the anisotropic surface feature, sp $\Phi = 0^o$ exhibits the best agreement between the SHG signal minimum potential (V_{min}) and its flatband potential (V_{fb}). This consistency between V_{fb} and V_{min} is observed across 7 pH units in a pH-dependent study, showcasing the effectiveness of azimuthal-angle-resolved bias-dependent SHG measurement on an anisotropic surface.

3.2. Materials and Methods

3.2.1 Materials

Nb-doped rutile (100) TiO_2 (wt 0.5%) with a dopant concentration of ~1.4×10^{20} cm^{-3} (1 cm by 1 cm, 0.5 mm thickness, MTI Corporation) is used in our study. The electrode is prepared according to a previously reported procedure to expose the (100) surface[46]. The electrode is further photoelectrochemically etched to remove surface states in 0.1 M H_2SO_4 a 2 V vs Ag/AgCl applied bias under a 150 W Xe lamp for 1 h before the bias-dependent SHG and electrochemical measurement, following previously reported procedures. [47, 48]

18 MΩ cm Milli-Q water is used as solvent in our electrochemistry experiment. 0.1 M pH 7 buffer is obtained by adding 1.549 g sodium phosphate dibasic heptahydrate (Macron Chemicals) and 0.583 g sodium phosphate monobasic monohydrate (Macron Chemicals) in 100 mL supporting electrolyte 1 M $NaClO_4$ (Acros Organics, 99+% for analysis) solution. 10 mL of Citric-phosphate buffer solutions of different pH are made by mixing x mL of 0.1 M citric acid (Sigma-Aldrich, 99.5+%) and y mL 0.2 M of Na_2HPO_4 (Macron Chemicals) solution containing 1 M $NaClO_4$ supporting electrolyte following Table S1. Final pHs are measured using a pH meter (Accumet AB 15). Two batches of pH solutions are used in Figure 3.7, where pH-dependent CV, Mott-Schottky and SHG on sp $\Phi = 0^o$ share the same batch of pH solutions, SHG on pp $\Phi = 90^o$ uses another batch of pH buffer solutions. All solutions used in this study are deoxygenated by purging Ar for 10 mins.

Table 1. Recipe for making 10 mL citric-phosphate buffer solution.

x mL 0.1 M citric acid	y mL 0.2 M Na_2HPO_4	pH
10	0	2
7.96	2.04	3

6.14	3.86	4
4.86	5.14	5
3.58	6.42	6
1.28	8.72	7
0.48	9.52	8
0	10	9.24

3.2.2 Experimental Method

A 1 kHz, 35 femtosecond 800 nm pulsed light is used as the fundamental probe of our SHG experiment. Fundamental probe is derived from a regenerative amplified Ti: sapphire laser system (Coherent Astrella, 800 nm, 5 mJ/pulse, 35 fs pulse width, and 1 kHz repetition rate). The fundamental probe power is tuned to be 3 mW by a variable neutral density filter (Thorlabs, NDC-50C-4M-A) and further focused down to a beam size with a waist of 100 μm at the sample surface using a f = 100 mm lens (Thorlabs, LBF254-100-A). Fundamental light reaches the sample surface on an incident angle of 45 degrees. 800 nm polarization is controlled by a half-wave plate (Thorlabs, AQWP05M-600). Second Harmonic Generation is collected and collimated using a f = 50 mm lens (Thorlabs, LBF254-050-A). After passing two 400 nm bandpass filters (Thorlabs, FBH400-10) and linear polarizer (Thorlabs, LPVISE100-A), the signal is measured by a Bialkali Amplified Photomultiplier Tube (PMT) detector (Thorlabs, PMM01). Tube voltage is powered by a 1.3 V DC power supply (GW INSTEK, GPD-230S). Upon signal collection, it is further processed by a boxcar average (Stanford Research SR200 Series) for noise filtering. The gated signal is averaged 1000 times by the boxcar average and sent to a data acquisition board, read out by a homebuilt LabVIEW software. The collected voltage signal is transformed into SHG counts using the transimpedance gain and responsivity parameter provided by the manufacturer.

Angle-resolved, *in situ* SHG and electrochemical measurements are conducted in a three-electrode electrochemical cell (modified from Gaoss Union, C031) as shown in Figure 3.3. A Pt is used as a counter electrode and Ag/AgCl is used as a reference electrode. TiO_2 single crystal is ohmic-contact to a gold rod electrode on the unpolished side with Gallium-Indium eutectic (Sigma-Aldrich, 495425-5G), the whole act as a working electrode in our *in situ* electrochemical experiment. Electrochemical measurements are performed using an SP-240 potentiostat (BioLogic). Impedance measurements are measured under 550 Hz Ac frequency with a 0.007 V superimposed ac amplitude with negative scan direction.

Monochromic 360 nm continuous-wave (CW) light is provided by a 365 nm LED (Thorlabs, M365 L3) with a 360 nm bandpass filter (Thorlabs, FB360-10, FWHM=10 ± 2 nm). The current pass through the LED is controlled by a DC driver (Thorlabs, DC2200).

TiO2 azimuthal angle is determined using a Rigaku XtaLAB Synergy-S equipped with single crystal Bruker APEX II CCD diffractometer in Emory X-ray Crystallography Center.

3.2.3 Bias-dependent SHG equation derivation

The intensity of second harmonic generation (($I(2\omega)$) is given by Equation 3.1,

$$I(2\omega) \propto \int_{-\infty}^{\infty} \left(\boldsymbol{\chi}_{\boldsymbol{eff}}^{(\mathbf{2})} + \boldsymbol{\chi}_{\mathbf{sc}}^{(\mathbf{3})} : \boldsymbol{E}_{dc-sc}(x) + \boldsymbol{\chi}_{\mathbf{liq}}^{(\mathbf{3})} : \boldsymbol{E}_{dc-liq}(x) \right) I(\omega)^2 dx \qquad 3.1$$

where $\boldsymbol{E}_{dc-sc}(x)$ and $\boldsymbol{E}_{dc-liq}(x)$ stands for the electric field at the semiconductor space charge region and liquid double layer as a function of distance, respectively; $\chi_{eff}^{(2)}$ is the second-order contribution from semiconductor surface and interfacial electrolyte and $\chi^{(3)}$ stands for third-order susceptibility; $I(\omega)$ is the intensity of fundamental light. The signal is integrated from the bulk solution ($x = -\infty$) to bulk semiconductor side ($x = \infty$) to cover the region where electric field exist. On n-TiO_2 side, 400 nm penetration depth is around 50 μm. [49] The typical space charge region width ($x = w$) of our TiO_2 crystal is around 14 nm (with 2 V of built-in potential, calculated

using Equation 3.2 and dopant densities N_d extracted from Figure 2a). Electric field should be integrated from the surface ($x = 0$) to the space charge region boundary ($x = w$).

$$w = \sqrt{\frac{2\epsilon\epsilon_0}{eN_d}\left(V - V_{fb}\right)} \tag{3.2}$$

Moreover, the Debye screening length of TiO_2 is calculated to be 1.2 nm using equation S3, much smaller than the coherence length of 800 nm fundamental light (~9 μm). 800 nm fundamental will not be diphase in TiO_2, therefore, the real term of $\chi^{(3)}$ will dominate the phase matching factor as discussed in previous papers. [50, 51]

$$L_D = \sqrt{\frac{\epsilon\epsilon_0 k_B T}{e^2 N_d}} \tag{3.3}$$

The total contribution of the DC electric field in the semiconductor side can be written as following Equation 3.4 and equals the electrostatic potential drop across the depletion region ($\Delta\Phi_{sc}$).

$$\int_0^w \boldsymbol{E}_{dc}(x)dx = \Phi_w - \Phi_0 = \Delta\Phi_{sc} \tag{3.4}$$

Likewise, the electric field in the double layer can also be integrated into the double-layer potential drop $\Delta\Phi_{liq}$. Therefore, the relation between second harmonic generation intensity ($I(2\omega)$) and potential drop can be written as Equation 3.5:

$$I(2\omega) = \left|P_{(2\omega)}\right|^2 \propto \left|\boldsymbol{\chi}^{(2)}_{\boldsymbol{eff}} + \boldsymbol{\chi}^{(3)}_{\mathbf{sc}}\Delta\Phi_{sc} + \boldsymbol{\chi}^{(3)}_{\mathbf{liq}}\Delta\Phi_{liq}\right|^2 I(\omega)^2 \tag{3.5}$$

Bias-dependent SHGF response can be treated in two parts, where the phase difference of each term is illustrated in Figure 3.1. At the semiconductor accumulation region ($V_{app} < V_{fb}$), applied potential differences occur on the liquid side and $\chi^{(3)}$ response from the semiconductor side vanishes. [27] We use β to describe the relative phase difference between $\chi^{(2)}_{eff}$ and $\chi^{(3)}_{\mathrm{liq}}\Delta\Phi_{liq}$ term. A quadratic relationship can be written as such:

$$I(2\omega) \propto \left|\chi_{eff}^{(2)} + e^{i\beta}\chi_{\mathrm{liq}}^{(3)}\Delta\Phi_{liq}\right|^2 I(\omega)^2$$

$$= \left(\left|\chi_{eff}^{(2)}\right|^2 + \left|\chi_{\mathrm{liq}}^{(3)}(\mathrm{V}_{app} - \mathrm{V}_{fb})\right|^2 + 2cos\beta\ \chi_{eff}^{(2)}\ \chi_{\mathrm{liq}}^{(3)}(\mathrm{V}_{app} - \mathrm{V}_{fb})\right)\ I(\omega)^2 \qquad 3.6$$

At the semiconductor depletion region ($\mathrm{V}_{app} > \mathrm{V}_{fb}$), the applied potential difference resides on the semiconductor side ($d\mathrm{V}_{app} = d\Delta\Phi_{sc}$), only $\chi_{\mathrm{sc}}^{(3)}$ the term is bias-dependent, with the potential drop on the liquid side ($\Delta\Phi_{liq}$) remains unchanged. [52, 53] We use χ_{bid} term to include the contribution of two bias independent term $\chi_{eff}^{(2)}$ and $\chi_{\mathrm{liq}}^{(3)}\Delta\Phi_{liq}$ and γ to be the phase difference between χ_{bid} and $\chi_{\mathrm{sc}}^{(3)}\Delta\Phi_{sc}$ term. Quadratic relationship can be written as such:

$$I(2\omega) \propto \left|\chi_{bid} + e^{i\gamma}\chi_{\mathrm{sc}}^{(3)}\Delta\Phi_{\mathrm{sc}}\right|^2 I(\omega)^2$$

$$= \left(|\chi_{bid}|^2 + \left|\chi_{\mathrm{sc}}^{(3)}(\mathrm{V}_{app} - V_{fb})\right|^2 + 2\cos\gamma\ \chi_{bid}\ \chi_{\mathrm{sc}}^{(3)}(V_{app} - V_{fb})\right)\ I(\omega)^2 \qquad 3.7$$

(a) $\mathrm{V}_{app} < \mathrm{V}_{fb}$, accumulation region

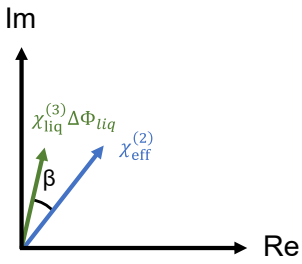

(b) $\mathrm{V}_{app} > \mathrm{V}_{fb}$, depletion region

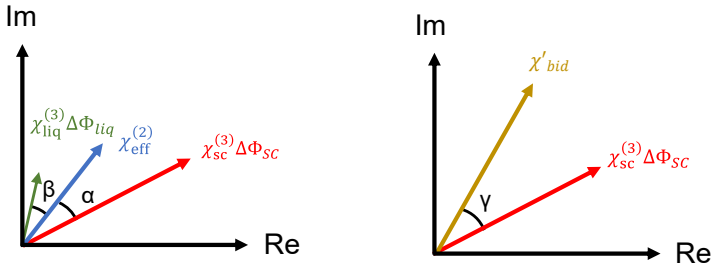

Figure 3.1. An Argand diagram of Equation 3.6 and 3.7, demonstrates the contribution of each term to the total SHG susceptibility in (a) the semiconductor accumulation region and (b) the semiconductor depletion region.

3.3. Results and discussion

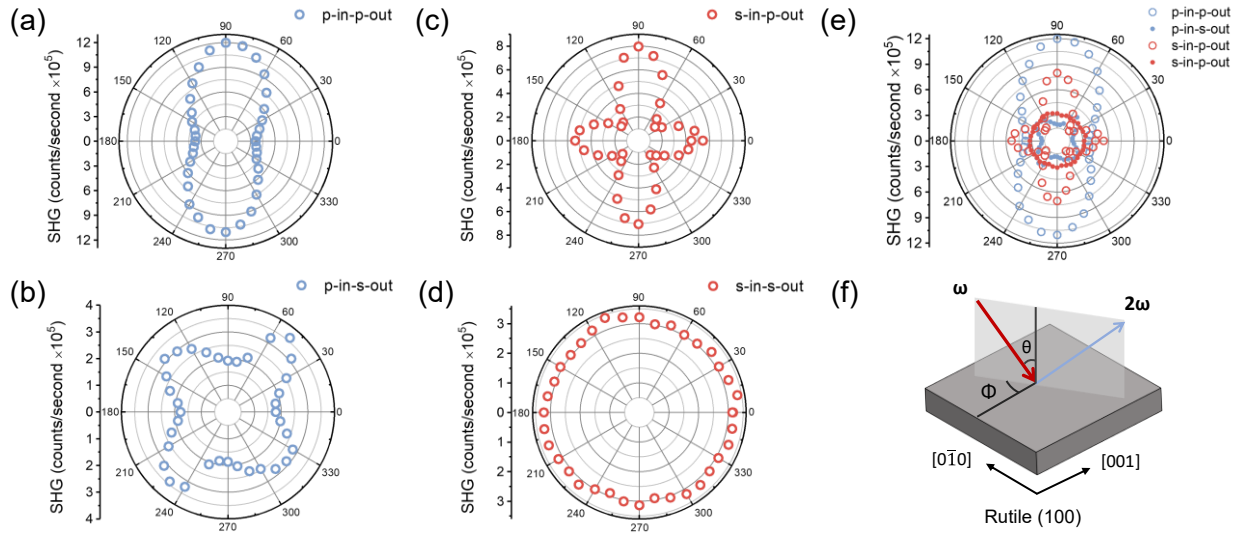

Figure 3.2. Azimuthal angle dependence of SHG signal of rutile TiO_2 (100) with (a) p in p out, (b) p in s out, (c) s in p out and (d) s in s out fundamental and SHG polarization combination. (e) SHG signal summarizing (a)-(d) polarization combination. (f) Illustration of experimental condition, where azimuthal angle Φ is defined as the angle between incident plane and [001] crystal axis.

The rotational anisotropy Second Harmonic Generation is first carried out on Nb-doped rutile TiO_2 (100) surface as illustrated in Figure 3.2, with a fundamental incident angle θ of 45°. The azimuthal angle (Φ) is defined as the angle between TiO_2 [001] axis and incident plan as depicted in Figure 3.2f. This experiment characterizes the solid-air SHG as a function of Φ. A two-fold symmetry (C_{2v}) in pp, ps, and sp polarization combinations as shown in Figure 3.2a-c, consistent with a previous study on the TiO_2 (100) surface. [54] In pp and ps polarization, signal

minima occur at 0° and 180°, but the signal maxima differ. In pp polarization, the signal maxima are 90° and 180°, while in ps polarization, they are at 50° and 230°, with a secondary peak at 140° and 320°. Conversely, in sp polarization, the behavior contrasts with that of ps polarization, with signal maxima at 0° and 180°, and signal minima at 50°, 140°, 230° and 320°. Notably, ss polarization reveals nearly isotropic surface symmetry and lower SHG intensity compared to other three polarization combinations we investigated, possibly due to the small in-plane dipole moment at Rutile TiO_2 (100). This azimuthal dependent characterization of solid-air interface mainly results from the collective response of electrons at TiO_2 (100) surface in the presence of laser electromagnetic field, providing insights into the distribution of electron densities on the surface. [54] Subsequently, we aim to investigate how the surface electron distribution affects the relationship between bias-independent ($\chi^{(2)}_{\text{eff}}$ contribution) and bias-dependent SHG terms ($\chi^{(3)}$ contribution) when the crystal is in contact with electrolyte and under applied potential, where a DC electric field exist across the junction.

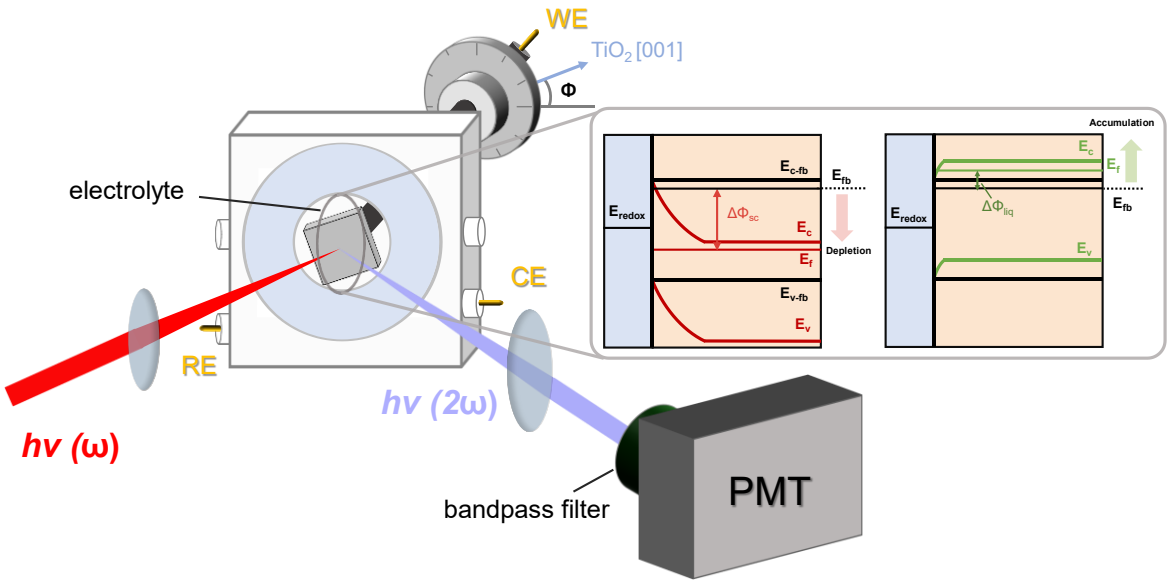

Figure 3.3. Schematic of *in situ* azimuthal-angle-resolved SHG setup. Inset illustrates the band alignment of semiconductor-electrolyte junction under semiconductor flatband (black), depletion (red), and accumulation (green) region conditions.

As shown in Figure 3.3 inset, when applied potential is more positive ($V_{app} > V_{fb}$) or more negative ($V_{app} < V_{fb}$) than flatband potential, n-type TiO_2 (100) is in the depletion or the accumulation region, respectively. In the semiconductor depletion region, a spatially varying electrostatic potential profile is formed mainly in the semiconductor space charge region (SCR). In semiconductor accumulation region, the spatially varying electrostatic potential profile is formed mainly in solution double layer. [27, 55] The formation of the electric field at the semiconductor/electrolyte junction will interact with the fundamental laser pulses and contribute to the Second Harmonic Generation process. This provides a direct probe of the interfacial electric field in the semiconductor/electrolyte junction. [27, 29-33, 56, 57] With the involvement of an electric field, the relationship between second harmonic generation (SHG) intensity ($I(2\omega)$) and potential profile can be written as Equation 3.8a and b:

$$I(2\omega) \propto \left|\chi_{\text{eff}}^{(2)} + e^{i\beta}\chi_{\text{liq}}^{(3)}\Delta\Phi_{liq} + e^{i\alpha}\chi_{\text{sc}}^{(3)}\Delta\Phi_{sc}\right|^2 I(\omega)^2 \quad 3.8$$

$$= \left|\chi_{eff}^{(2)} + e^{i\beta}\chi_{\text{liq}}^{(3)}(V_{app} - V_{fb})\right|^2 I(\omega)^2 \qquad (V_{app} < V_{fb}) \quad 3.8a$$

$$= \left|\chi_{bid} + e^{i\gamma}\chi_{\text{sc}}^{(3)}(V_{app} - V_{fb})\right|^2 I(\omega)^2 \qquad (V_{app} > V_{fb}) \quad 3.8b$$

The detailed derivations of Equation 3.8a and 3.8b are provided in Section 3.2.3. In Equation 3.8a and 3.8b, $\chi_{eff}^{(2)}$ is the second order susceptibility which contains the contribution from solid surface and interfacial electrolyte layers; $\chi_{\text{sc}}^{(3)}$ and $\chi_{\text{liq}}^{(3)}$ are third-order response arising from the DC electric field, at the semiconductor SCR and electrolyte double layer, respectively; V_{app} and V_{fb} are the applied bias at the semiconductor back contact and flatband potential of the

semiconductor verse reference electrode (Ag/AgCl in this study), respectively; $\Delta\Phi_{sc}$ and $\Delta\Phi_{liq}$ are the electrostatic potential drop at semiconductor depletion region and solution double layer, respectively, with $\Delta\Phi_{sc} = V_{app} - V_{fb}$ in the semiconductor depletion region and $\Delta\Phi_{liq} = V_{app} - V_{fb}$ in the accumulation region; α and β are the relative phase difference between $\chi^{(2)}_{eff}$ and $\chi^{(3)}_{sc}$, $\chi^{(3)}_{liq}$, respectively; γ is the phase difference between $\chi^{(3)}_{sc}$ and χ_{bid}, the effective susceptibility of first two bias-independent term in Equation 3.8 when $V_{app} > V_{fb}$. From Equation 3.8a and 3.8b, a piecewise quadratic relationship between SHG intensity and applied potential is established at both sides of the flatband potential.

The accuracy of predicting the semiconductor's V_{fb} based on the bias-dependent SHG minimum, as indicated by Equation 3.6a and 3.6b, depends on the relative phase difference (β and γ) between the bias-dependent and bias-independent terms and their relative amplitude χ_{bid}/χ_{bd}. $V_{min} = V_{fb}$ occurs only when the relative phase difference (β and γ) is 90°, eliminating the cross term, or when $\chi_{bd} \gg \chi_{bid}$, that allows ignoring of the bias-independent contribution. [27] These conditions are typical unmet, particularly on an anisotropic surface where $\chi^{(2)}_{eff}$ is not negligible. In this study, we employ an *in situ* azimuthal-angle-resolved SHG technique to investigate the connection between azimuthal angle, laser polarization, and SHG intensity.

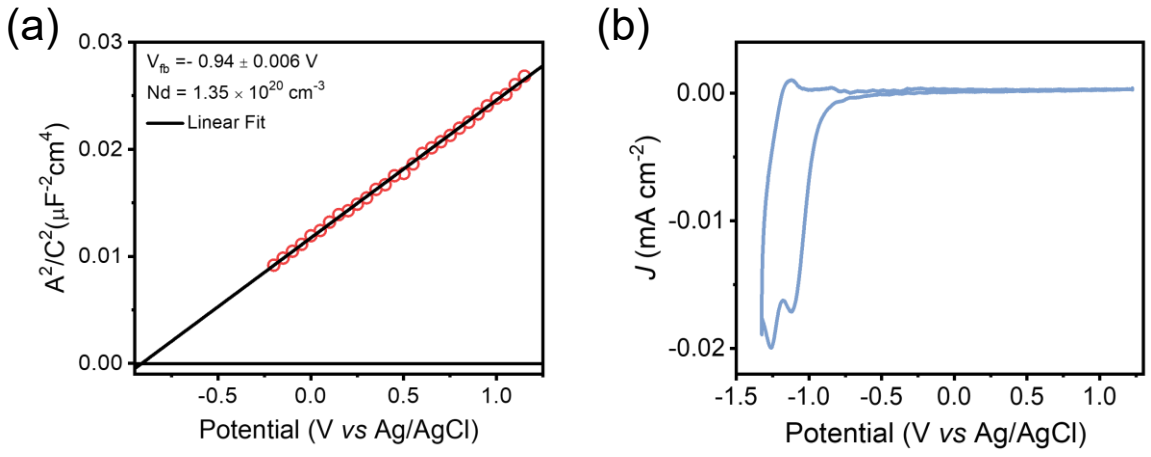

Figure 3.4. (a) Mott-Schottky experiment of rutile TiO_2 (100) electrode using 550 Hz AC frequency and 7 mV amplitude of AC bias perturbation under negative scan direction. (b) Representative cyclic voltammetry during SHG process with a scan rate of 3.5 mV/s in 0.1 M pH 7 phosphate buffer solution containing 1 M Na_4ClO_4 supporting electrolyte.

In this homodyne detection scheme, it's crucial to accurately determine the value of V_{fb} to extract information regarding relative phase and non-linear susceptibility. We perform a Mott-Schottky measurement on TiO_2 electrode to determine the V_{fb}, where the capacitance-voltage response is independent on the TiO_2 (100) crystal angle. This experiment is conducted in a 0.1 M pH 7 phosphate buffer solution (1 M Na_4ClO_4 as the supporting electrolyte) within the same electrochemical cell for the subsequent bias-dependent SHG experiment. As depicted in Figure 3.4a, the flatband potential of the electrode can be determined using the following relation: [27, 53, 58-60]

$$\frac{A^2}{C_s^2} = \frac{2}{q\varepsilon\varepsilon_0 N_d}\left(V - V_{fb} - \frac{kT}{q}\right) \quad 3.9$$

Here, N_d, C_s, and A denote the dopant density of semiconductor, interfacial capacitance, and electrode area, respectively; q represents the elementary charge; ε_0 and ε are the dielectric constant of free space and relative dielectric constant of the semiconductor, respectively; k is the Boltzmann's constant; T is the temperature. Under the assumption that majority of the electrostatic potential difference across the junction occurs in the semiconductor SCR ($\Delta\Phi_{sc} \gg \Delta\Phi_{liq}$) in the presence of a high ionic strength electrolyte, [53, 59, 61] the flatband potential of the semiconductor is calculated to be -0.94$\pm$ 0.006 V vs Ag/AgCl. The obtained dopant density is around 1.35×10^{20} cm^{-3}, which is closely corresponds to the value specified by the manufacturer (0.5% Nb dopant equates to ca. 1.4×10^{20} cm^{-3} dopant concentration). The flatband potential value will serve as a fixed fitting parameter in Equation 3.6a and 3.6b in the subsequent analysis.

Azimuthal-angle-resolved bias-dependent SHG measurements are further carried out using the same TiO_2 used for Mott-Schottky measurement. In the setup shown in Figure 3.3, the back side of rutile TiO_2 (100) makes ohmic contact with a gold rod electrode in a perpendicular manner, serving as the working electrode of a three-electrode system. The crystal azimuthal angle can be adjusted by rotating the rod electrode, and a continuous rotation mount is fixed on the working electrode to record changes in the TiO_2 azimuthal angle. For pp and ss polarization, we selected two typical Φ values, 0° and 90°. For ps and sp polarization, we chose four typical Φ of 0°, 50°, 90°, and 140°, due to their more intricate surface symmetry, as illustrated in Figure 3.2b and c.

In situ bias-dependent SHG measurements are performed under cyclic voltammetry (CV) conditions, employing a slow scan rate of 3.5 mV/s spanning from -1.325 to 1.225 V. As illustrated in the representative CV at sp Φ = 0° under SHG conditions (Figure 3.4b), negligible current is observed when $V_{app} > V_{fb}$, this indicates that the electrode is in a depletion region, and fundamental pulses do not excite the semiconductor through multi-photon absorption process. On the negative side of flatband potential, some redox features are observed, which we will discuss in the following section. In Figure 3.5, we employ Equation 3.8a and 3.8b to fit the bias-dependent SHG data, utilizing V_{fb} obtained from Mott-Schottky shown in Figure 3.4 as a boundary condition. Data collected from both negative and positive scan directions are analyzed as no hysteresis between different scan directions is observed. The bias-dependent SHG results reveal several notable features. First, at azimuthal angles where dry film SHG signal are minimal, such as, pp Φ = 0°, and ps Φ = 0°, 90°, $\chi_{sc}^{(3)}$ term is also smaller compared to angles with a amore significant dry film SHG contribution, like pp Φ = 90°, and ps Φ = 50°, 140°. Furthermore, p-polarized SHG output dominants regardless of s and p fundamental input. This phenomenon may stem from the electric

field direction in TiO_2 SCR better aligns with the p polarization. The fitting results from both the depletion and accumulation regions are summarized in Table 2 and Table A1.

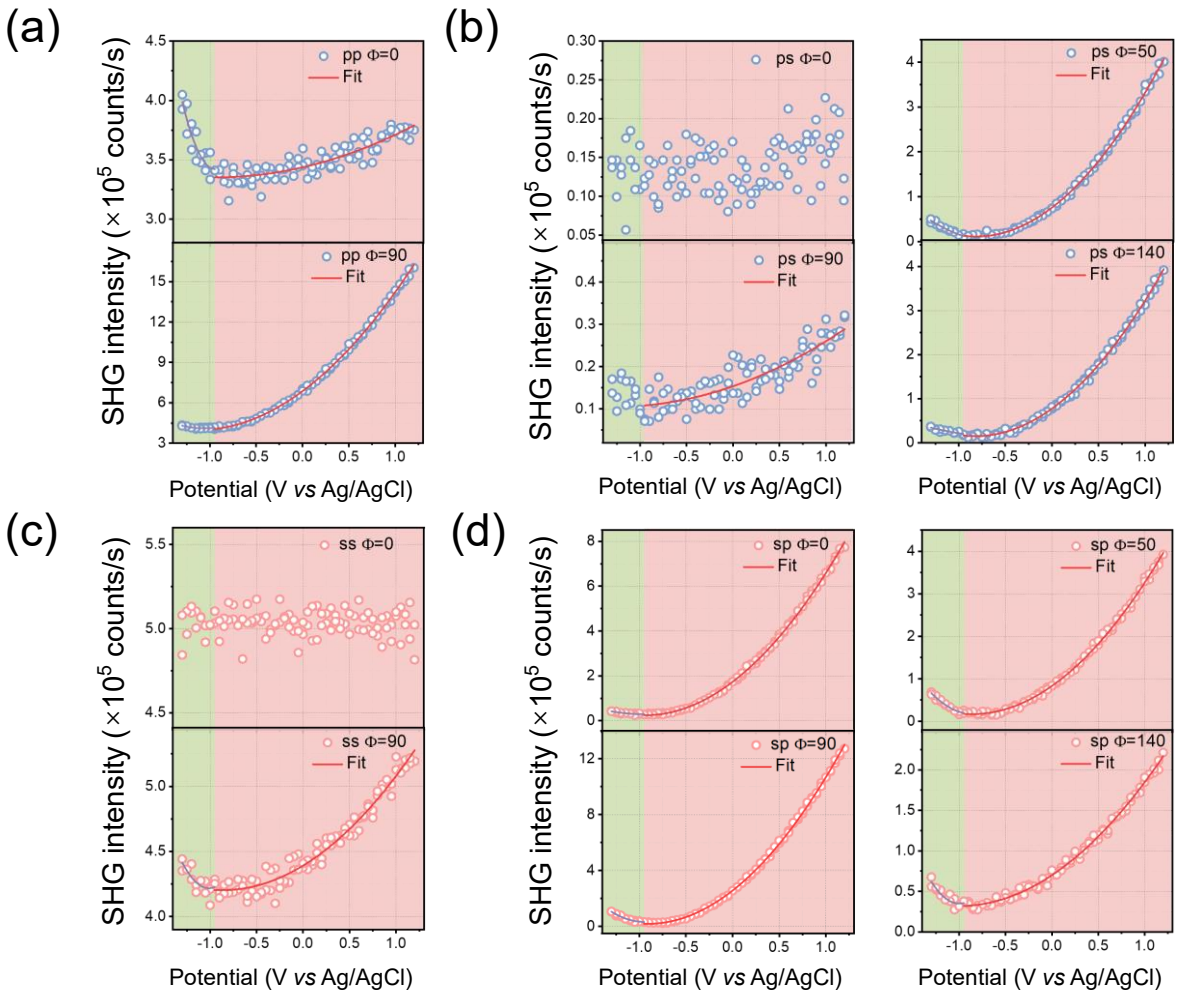

Figure 3.5. Azimuthal angle dependent SHG response as a function of applied potential in pH 7 buffer solution with (a) p in p out; (b) p in s out; (c) s in s out and (d) s in p out polarization combination. The green and red part indicate the semiconductor accumulation and depletion region, respectively, using the V_{fb} extracted from impedance measurement.

For a clearer understanding of the impact of azimuthal angle and light polarization on SHG intensity, we plot the relative phase difference between TiO_2 χ_{bid} and χ_{sc} γ, along with the non-linear susceptibility ratio χ_{bid}/χ_{sc}, as functions of Φ and light polarization in Figure 3.6. Under

several conditions, it was observed that combinations such as pp Φ = 0°, sp Φ = 0°, and ss Φ = 90° exhibit a γ value of approximately 90°. Nevertheless, in the case of pp Φ = 0° and ss Φ = 90°, the bias-independent term contribution is excessively large, with a χ_{bid}/χ_{bd} of 5.95 ± 0.68 and 4.08± 0.16, respectively. Consequently, this results in a lower R^2 value for the fitting and a wider data error range, even if the obtained SHG signal minimum potential closely approaches the semiconductor flatband potential. In the case of other combinations, such as ps Φ = 50°, 140°, and sp Φ = 50°, 90°, although χ_{bid}/χ_{bd} values smaller than 0.4 can be achieved, they are not sufficiently small to be disregarded. With a deviation of relative phase from 90°, V_{fb} and V_{min} still do not match. It is worth noting that with ss polarization, despite the dry film SHG exhibiting a nearly isotropic dry film SHG response, there remains a distinction in bias-dependent SHG behavior between Φ = 0° and Φ = 90°. Specifically, Φ = 0° shows no bias-dependency, while Φ = 90° exhibits a bias-dependent behavior with a relatively small $\chi_{sc}^{(3)}$ compared to χ_{bid}. This phenomenon may be attributed to the interaction between TiO_2 and solution ions (HPO_4^{2-} and $H_2PO_4^{2-}$), resulting in the formation of a single-atom monolayer that causes a subtle change in surface dipole moment. The slight change does not significantly impact polarizations with a strong intrinsic surface anisotropic dipole moment but has a substantial effect on polarizations that are inherently weak, such as s-in-s-out. In summary, we deduce that the minimum SHG response potential V_{min} under an azimuthal angle of 0° with sp polarization provides the best prediction for the flatband potential V_{fb}.

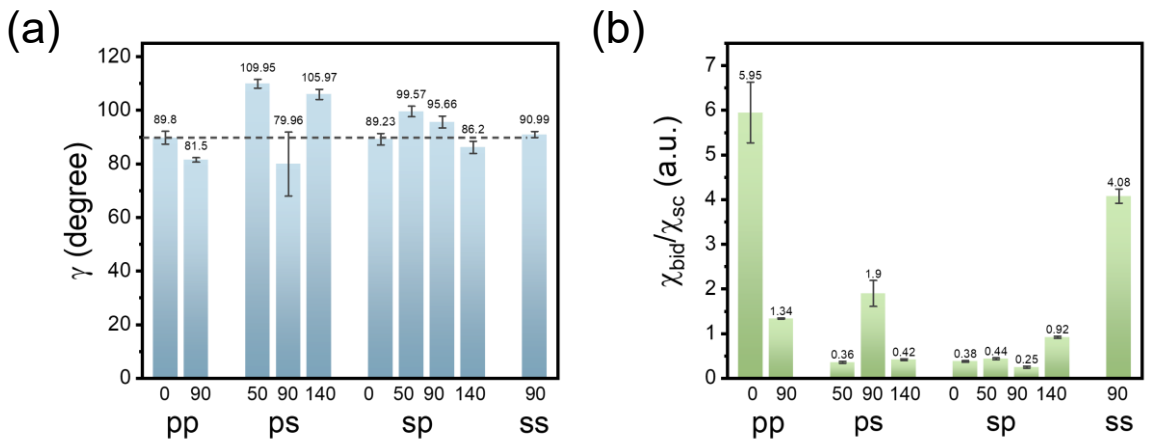

Figure 3.6. Summary of (a) relative phase difference and (b) amplitude ratio between $\chi_{sc}^{(3)}$ and bias-independent non-linear susceptibility. Dash line in (a) indicates γ = 90° values.

Similar results are obtained from the analysis from the TiO_2 accumulation region. Specifically, sp Φ = 0° exhibits the closest match between V_{min} and V_{fb}, albeit with a larger data error range and smaller R^2. This limitation arises primarily from the constrained potential range (350 mV potential window) designed to prevent H_2 generation from TiO_2 surface, which could otherwise impact SHG collection efficiency. Interestingly, we observed that $\chi_{liq}^{(3)}$ is comparable to or even larger than $\chi_{sc}^{(3)}$ across most of the tested angles and light polarizations (Table A1). The dependence of the solution third-order nonlinear susceptibility $\chi_{liq}^{(3)}$ on the crystal angle can be attributed to variations in surface molecule, including adsorbates and surface water dipole moments as the orientation of an anisotropic surface changes. [25] It is important to acknowledge that our bias-dependent analysis at TiO_2 accumulation region is subject to inaccuracies, primarily due to the restricted potential range we employed. To achieve a more precise analysis of $\chi_{liq}^{(3)}$ as a function of substrate crystal angle, it is advisable to perform such investigation under non-aqueous conditions with a wider potential window. This would allow for a comprehensive study of surface

ion adsorption and double-layer electric field distribution. However, this is beyond the scope of our current study and will be the focus of our future research.

Table 2. Fitting parameters of bias-dependent SHG response using Equation 3.6b at different substrate azimuthal angles and light polarizations.

Polarization	Φ	V_{min} (V vs Ag/AgCl)	γ (degree)	$\chi_{bid}/\chi_{sc}^{(3)}$	R^2
pp	0	-0.95 ± 0.25	89.83 ± 2.39	5.95 ± 0.68	0.7806
	90	-1.13 ± 0.02	81.50 ± 0.84	1.34 ± 0.01	0.9990
ps	0		N/A		
	50	-0.81 ± 0.01	109.94 ± 1.63	0.36 ± 0.02	0.9985
	90	-1.27 ± 0.43	79.96 ± 11.93	1.90 ± 0.29	0.7684
	140	-0.82 ± 0.02	105.97 ± 1.88	0.42 ± 0.02	0.9980
sp	0	-0.94 ± 0.01	89.23 ± 2.14	0.38 ± 0.02	0.9991
	50	-0.86 ± 0.02	99.57 ± 1.95	0.44 ± 0.02	0.9983
	90	-0.91 ± 0.01	95.66 ± 2.22	0.25 ± 0.02	0.9993
	140	-1.00 ± 0.04	86.20 ± 2.28	0.92 ± 0.02	0.9948
ss	0		N/A		
	90	-0.87 ± 0.08	90.99 ± 1.14	4.08 ± 0.16	0.9636

To further assess the effectiveness of bias-dependent SHG in reflecting the semiconductor built-in potential, we conduct SHG, CV, and Mott-Schottky experiments in solutions with different pH levels, as illustrated in Figure 3.7 and A3.2. Figure 3.7a displays the CV results, revealing two pairs of "redox" features in superimposed on water reduction current when $V_{app} < V_{fb}$. The exact nature of these "redox behaviors" remains a subject of debate. One possibility is that they arise from the reduction of Ti (IV) to Ti (III), followed by a subsequent reduction to Ti (II). [62, 63] Other

studies have also noted the specific ion adsorption/desorption on metal oxide/hydroxide electrodes can result in additional CV features. [64, 65] In our case, this is also highly likely given that both phosphate and citrate anions in our electrolyte can acts as a specific adsorbate on TiO_2. However, definitively determining the electrochemical nature of "redox" features falls outside the scope of our study. As a tentative designation, we label them as the first and second oxidation and reduction peaks based on their proximity to the TiO_2 flatband potentials. The peak positions of first and second redox peak potentials are extracted from the plot of the current density derivatives plotted as a function of applied potential (Figure A3.1). Intriguingly, these peak potentials also exhibit pH dependence, with slopes of 63.8 ± 2.4 ($E_{1st\ ox}$), 60.5 ± 2.1 (E_{2nd} ox), 60.2 ± 2.0 ($E_{1st\ red}$), and 54.7 ± 1.8 ($E_{2nd\ red}$) mV/pH as shown in Figure 3.7c. These values are close to the Nernstian behavior value of 59 mV/pH. These redox peak potentials are believed to be pH-sensitive, despite various arguments regarding their electrochemical nature. Mott-Schottky analysis of TiO_2 (100) revealed a pH-dependent V_{fb} value from pH 1.8 to 8.5, with a slope of 65.5 ± 1.1 mV/pH as summarized in Figure 3.7d. Furthermore, we conduct bias-dependent SHG experiments on the same electrode under various pH buffer solutions. Two typical azimuthal angles and light polarizations (pp $\Phi = 90^o$ and sp $\Phi = 0^o$) are selected to investigate their pH-dependent behaviors, as depicted in Figure A3.2. A quadratic function is used to fit and extract the minimum bias-dependent response in TiO_2 depletion region, as summarized in Figure 3.7d. In the sp $\Phi = 0^o$ dataset, V_{min} exhibits a pH-dependent change with a slope of 69.5 ± 3.9 mV/pH, consistent with the V_{fb} values extracted from capacitance analysis. This finding aligns with conclusion of the previous angle-resolved measurement, where it is observed that χ_{bid} and $\chi_{sc}^{(3)}$ are orthogonal to each other. It is noteworthy that the slope values obtained from both impedance and SHG measurements deviate from the Nernstian behavior, which predicts a flatband potential dependence on pH of 59 mV/pH. [58-60] This

can be attributed to the "discreteness of surface charge adsorption" effect, [66, 67] where the surface adsorbates impact the Helmholtz layer potential drop, leading to a slope greater than 59 mV/pH. It is reasonable to consider such an effect in our study, especially since both phosphate and citrate anions can specifically adsorb on TiO_2 surfaces. In the pp $\Phi = 90^o$ dataset, although V_{min} also shows a pH-dependent behavior, there is an offset of ca. -300 mV observed between V_{min} and V_{fb}, with a more positive slop of 75.2 ± 2.1 mV/pH. This discrepancy arises from the non-negligible χ_{bid} term and non-orthogonal angle γ measuring 81.50 ± 0.84°. The steeper pH dependent V_{min} slope can be attributed to variation in χ_{bid} and γ, stemming from the alterations in in $\Delta\Phi_{liq}$ at different pH solutions. [55, 66]

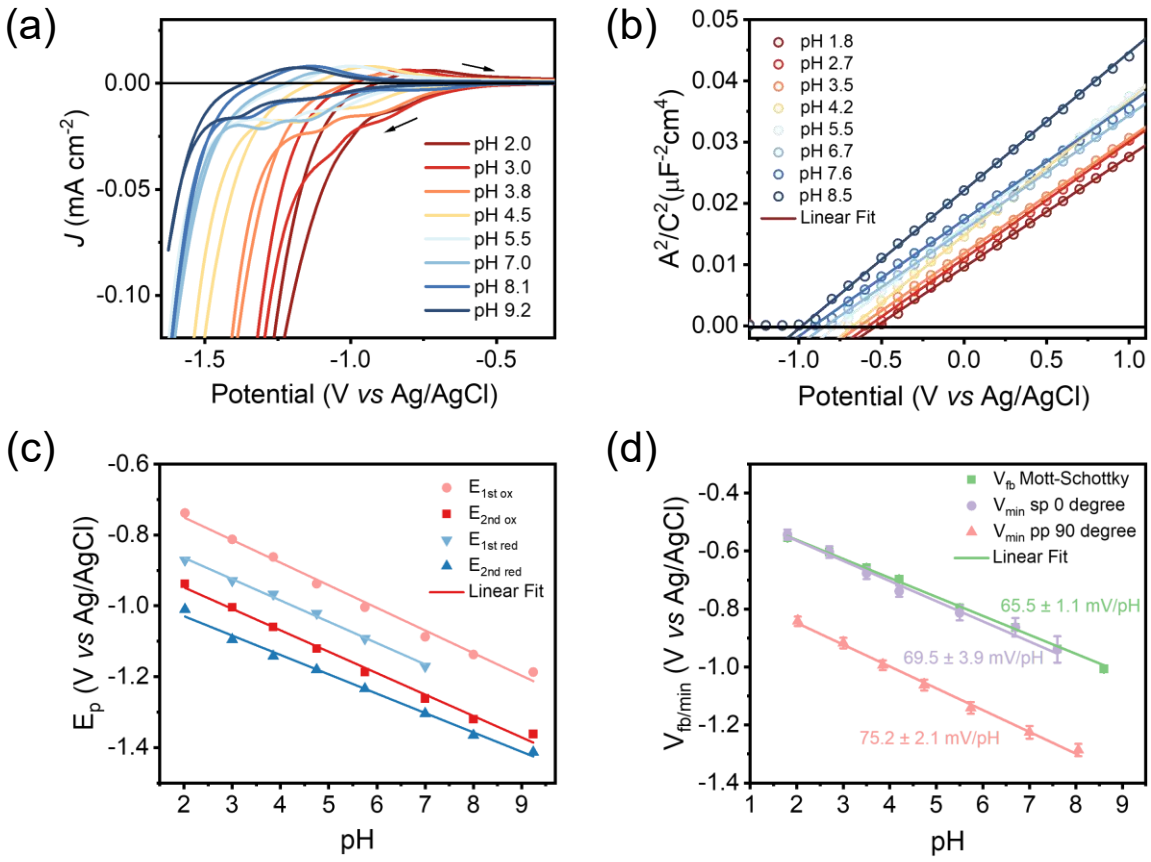

Figure 3.7. pH dependent (a) cyclic voltammetry and (b) Mott-Schottky of rutile TiO_2 (100). (c) Oxidation and reduction peak potential plotted as a function of pH extracted from (a). (d) Summary

of flat-band potential (V_{fb}) extracted from (b) and potential of minimum (V_{min}) extracted from Figure A3.2 plotted as a function of pH. Cyclic voltammetry is measured under scan rate of 3.5mV/s, capacitance is measured under 550 Hz 7mV AC voltage perturbation. Experiments are done in citric-phosphate buffer with pH varying from around 2 to 9.

By deconvoluting the contributions of χ_{bid} and $\chi_{sc}^{(3)}$, this bias-dependent SHG method can serve as a powerful tool for delving into probing the semiconductor's Fermi-level change in addition to investigating its flatband potential. As shown in Figure 3.8a, SHG response of TiO_2 under different light illumination intensity is monitored under different 360 nm light illumination intensities while holding the electrode under open circuit potential (OCP) condition. SHG intensity decreased upon the excitation of TiO_2 electrode. This is because electron density accumulates in TiO_2 SCR upon photo illumination, leading to a decrease of built-in potential. [68-71] Subsequently, the Fermi-level position of TiO_2 can be calculated using the quadratic fitting function Equation 3.8 of its dark response as shown in Figure A3.3. The OCP values extracted from SHG are summarized in Figure 3.8b, showing a good accordance with OCP measured by potentiostat. The error bar of SHG OCP value mainly arises from the CW illumination light scattering into the detector. Apart from the experiments showcased in Figure 3.8, this bias-dependent SHG technique also serves as a powerful *in-situ*, and essentially time-resolved method to probe electrostatic potential changes in semiconductors. Phenomena like light-induced Fermi-level pinning effect on TiO_2 can be investigated using this technique, which will be communicated in a subsequent chapter.

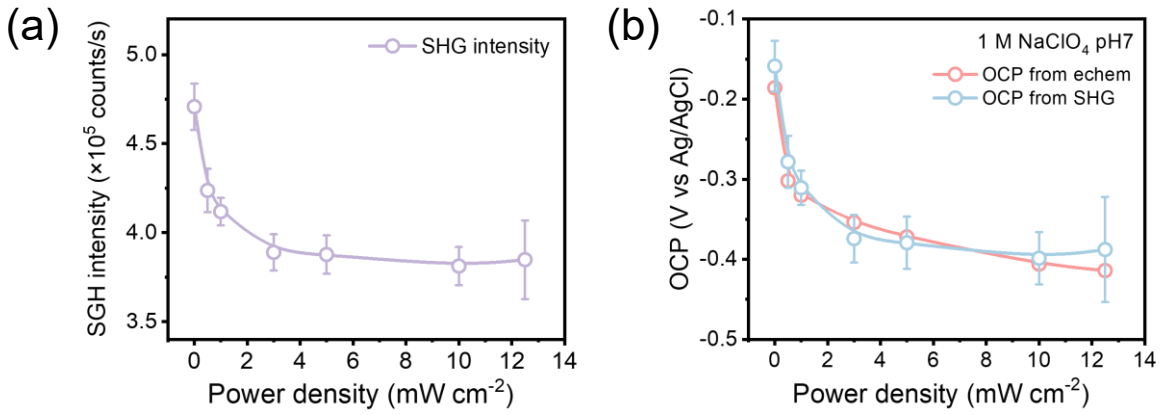

Figure 3.8. (a) SHG intensity of TiO_2 measured under different power densities of 360 nm CW light illumination with electrode held at open circuit condition. (b) Illumination power density dependent OCP values measured by potentiostat (red) and by SHG (blue) calculated from the dark response fitting curve as shown in Figure A3.3. OCP experiments are conducted in a pH 7 1 M $NaClO_4$ solution as electrolyte.

3.4. Conclusion

In summary, this study presents a systematic, *in situ* azimuthal-angle-resolved Second Harmonic Generation investigation at the interface between single crystal rutile TiO_2 (100)-electrolyte junction. This research explores how TiO_2 crystal angle and light polarization impact the bias-dependent SHG response on TiO_2-liquid junction using an angle-resolved electrochemical setup. The potential drop in semiconductor and solution double layer side is observed on both sides of TiO_2 flatband potential. We analyze the relative phase difference and amplitude ratio between bias-independent and bias-dependent susceptibility in both semiconductor depletion and accumulation regions. We discovered that variations in azimuthal angle and light polarization have a significant impact on the ability of SHG signal minimum potential V_{min} to predict the semiconductor flatband potential V_{fb}. The most accurate prediction is achieved with $\Phi = 0^o$ and sp

polarization. The strong correlation between V_{min} and V_{fb} at this angle is further validated through the pH-dependent experiment. This study underscores the importance of considering the surface crystal angle when conducting bias-dependent SHG to measure flatband potential values of semiconductor electrode on a surface with anisotropic symmetry.

Appendix Chapter 3

Supplementary Results

Table A1. Fitting parameters of bias-dependent SHG response using Equation 3.8a at different substrate azimuthal angles and light polarizations, $\boldsymbol{\chi_{sc}^{(3)}/\chi_{liq}^{(3)}}$ is obtained using the $\boldsymbol{\chi_{sc}^{(3)}}$ value from Table 2

Polarization	Φ	V_{min} (V vs Ag/AgCl)	$\boldsymbol{\gamma}$ (degree)	$\boldsymbol{\chi_{eff}^{(2)}/\chi_{liq}^{(3)}}$	$\boldsymbol{\chi_{sc}^{(3)}/\chi_{liq}^{(3)}}$	R^2
pp	0	-0.94 ± 0.09	89.10 ± 6.07	0.86 ± 0.21	0.14 ± 0.03	0.8131
	90	-1.06 ± 0.03	83.18 ± 2.50	1.07 ± 0.19	0.79 ± 0.14	0.6173
ps	0	N/A				
	50	-0.58 ± 0.46	180 ± 105.38	0.35 ± 0.15	1.03 ± 0.44	0.9270
	90	N/A				
	140	-0.28 ± 2.00	136.84 ± 116.42	0.90 ± 1.06	1.96 ± 2.31	0.7963
sp	0	-0.94 ± 0.11	89.3 ± 12.35	0.54 ± 0.17	1.30 ± 0.40	0.7486
	50	-0.86 ± 0.09	106.67 ± 17.74	0.27 ± 0.05	0.60 ± 0.10	0.9547
	90	-0.94 ± 0.04	88.54 ± 8.69	0.24 ± 0.03	0.71 ± 0.07	0.9693
	140	-1.00 ± 0.05	79.73 ± 9.31	0.35 ± 0.06	0.36 ± 0.06	0.8224
ss	0	N/A				
	90	-1.01 ± 0.07	86.70 ± 3.88	1.33 ± 0.38	0.33 ± 0.09	0.5888

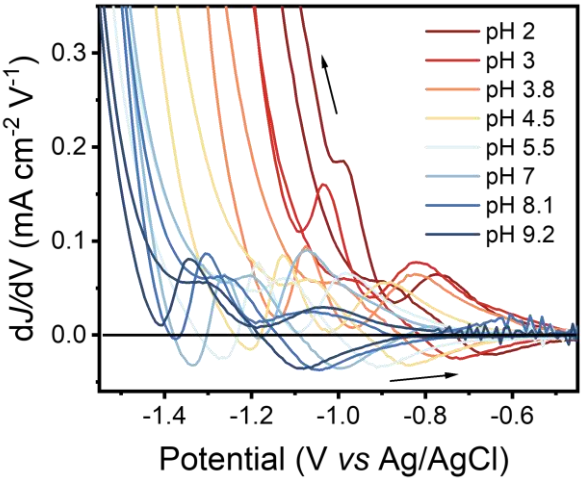

Figure A3.1. Current density derivatives as a function of applied potential at TiO_2-electrolyte junction at different pH. Reduction/oxidation peak positions are determined either from the dJ/dV=0 potential (when there is a peak) or from the d^2J/dV^2=0 potential (shoulder peak).

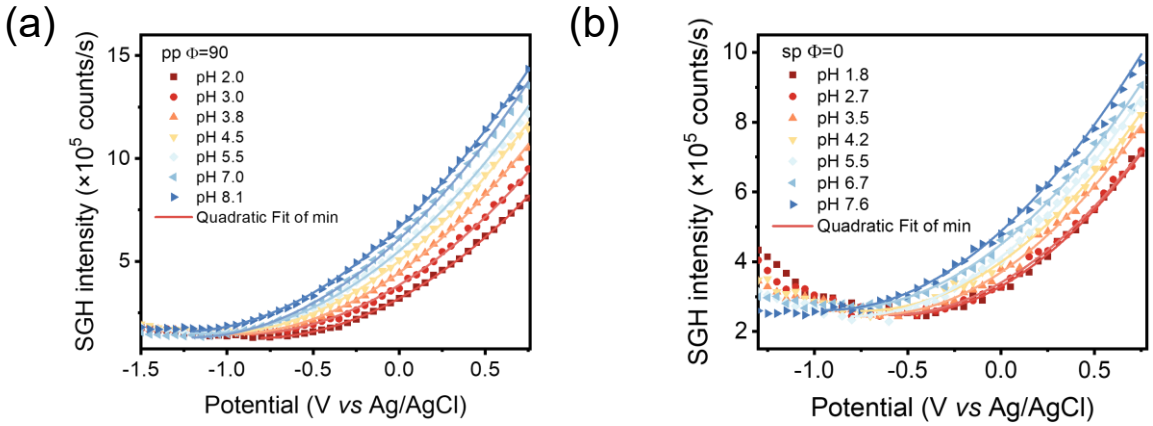

Figure A3.2. Bias-dependent SHG of TiO_2-electrolyte junction in different pH solutions at (a) pp $\Phi = 90^o$ and (b) sp $\Phi = 0^o$ light polarization and TiO_2 azimuthal angle.

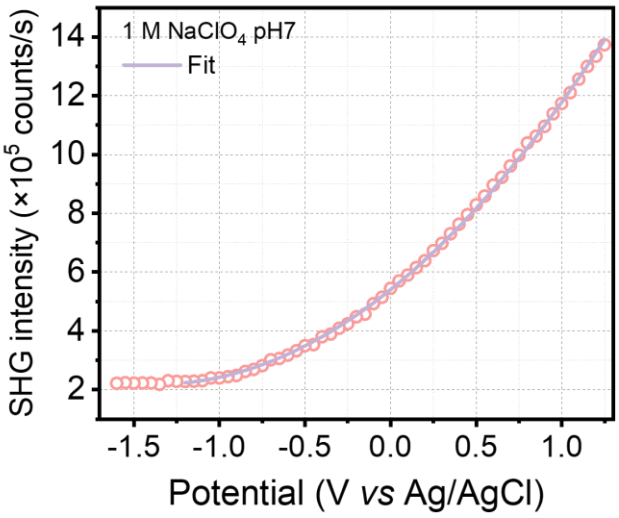

Figure A3.3. Bias-dependent SHG of TiO_2-electrolyte junction in pH 7 1 M $NaClO_4$ solution without 360 nm CW illumination. The quadratic fitting curve is used as a calibration curve to calculate the OCP potential from the SHG intensity change at different illumination power density depicted in Figure 3.8. The SHG is measured at sp $\Phi = 0^o$ light polarization and TiO_2 azimuthal angle.

3.5. Reference

1. Shao, Y.; El-Kady, M. F.; Sun, J.; Li, Y.; Zhang, Q.; Zhu, M.; Wang, H.; Dunn, B.; Kaner, R. B. Design and Mechanisms of Asymmetric Supercapacitors. *Chem. Rev.* **2018**, *118* (18), 9233-9280.

2. González, A.; Goikolea, E.; Barrena, J. A.; Mysyk, R. Review on supercapacitors: Technologies and materials. *Renew. Sust. Energ. Rev.* **2016**, *58*, 1189-1206.

3. Conte, M. Supercapacitors Technical Requirements for New Applications. *Fuel Cells* **2010**, *10* (5), 806-818.

4. Wang, K.; Wang, J.; Zhao, S.; Wang, Z.; Wang, S. The high performance of polyaniline-gel network modified electrode in 3-(2,2,6,6-tetramethyl-piperidiynl-1-oxyl)-1-methylylimidazoliumbromide biredox electrolyte used for supercapacitor. *J. Power Sources* **2019**, *434*, 226745.

5. Prehal, C.; Koczwara, C.; Jäckel, N.; Schreiber, A.; Burian, M.; Amenitsch, H.; Hartmann, M. A.; Presser, V.; Paris, O. Quantification of ion confinement and desolvation in nanoporous carbon supercapacitors with modelling and in situ X-ray scattering. *Nat. Energy* **2017**, *2* (3).

6. Mourad, E.; Coustan, L.; Lannelongue, P.; Zigah, D.; Mehdi, A.; Vioux, A.; Stefan; Favier, F.; Fontaine, O. Biredox ionic liquids with solid-like redox density in the liquid state for high-energy supercapacitors. *Nature Materials* **2017**, *16* (4), 446-453.
7. Presser, V.; Heon, M.; Gogotsi, Y. Carbide-Derived Carbons - From Porous Networks to Nanotubes and Graphene. *Adv. Func. Mater.* **2011**, *21* (5), 810-833.
8. Stoller, M. D.; Park, S.; Zhu, Y.; An, J.; Ruoff, R. S. Graphene-Based Ultracapacitors. *Nano Lett.* **2008**, *8* (10), 3498-3502.
9. Richey, F. W.; Dyatkin, B.; Gogotsi, Y.; Elabd, Y. A. Ion Dynamics in Porous Carbon Electrodes in Supercapacitors Using in Situ Infrared Spectroelectrochemistry. *J. Am. Chem. Soc.* **2013**, *135* (34), 12818-12826.
10. Fujishima, A.; Honda, K. Electrochemical Photolysis of Water at a Semiconductor Electrode. *Nature* **1972**, *238* (5358), 37-38.
11. Weber, M. F.; Dignam, M. J. Efficiency of Splitting Water with Semiconducting Photoelectrodes. *J. Electrochem. Soc.* **1984**, *131* (6), 1258.
12. Bolton, J. R.; Strickler, S. J.; Connolly, J. S. Limiting and realizable efficiencies of solar photolysis of water. *Nature* **1985**, *316* (6028), 495-500.
13. Hu, S.; Xiang, C.; Haussener, S.; Berger, A. D.; Lewis, N. S. An analysis of the optimal band gaps of light absorbers in integrated tandem photoelectrochemical water-splitting systems. *Energy Environ. Sci.* **2013**, *6* (10), 2984-2993.
14. Abdi, F. F.; Han, L.; Smets, A. H. M.; Zeman, M.; Dam, B.; van de Krol, R. Efficient solar water splitting by enhanced charge separation in a bismuth vanadate-silicon tandem photoelectrode. *Nat. Commun.* **2013**, *4*, 2195, Article.
15. Kim, T. W.; Choi, K.-S. Nanoporous $BiVO_4$ Photoanodes with Dual-Layer Oxygen Evolution Catalysts for Solar Water Splitting. *Science* **2014**, *343* (6174), 990-994.
16. Hu, S.; Shaner, M. R.; Beardslee, J. A.; Lichterman, M.; Brunschwig, B. S.; Lewis, N. S. Amorphous TiO_2 coatings stabilize Si, GaAs, and GaP photoanodes for efficient water oxidation. *Science* **2014**, *344* (6187), 1005-1009.
17. Jang, J.-W.; Du, C.; Ye, Y.; Lin, Y.; Yao, X.; Thorne, J.; Liu, E.; McMahon, G.; Zhu, J.; Javey, A.; et al. Enabling unassisted solar water splitting by iron oxide and silicon. *Nat. Commun.* **2015**, *6* (1), 7447.
18. Zandi, O.; Hamann, T. W. Determination of photoelectrochemical water oxidation intermediates on haematite electrode surfaces using operando infrared spectroscopy. *Nat. Chem.* **2016**, *8* (8), 778-783.
19. Xu, Z.; Hou, B.; Zhao, F.; Suo, S.; Liu, Y.; Shi, H.; Cai, Z.; Hill, C. L.; Musaev, D. G.; Mecklenburg, M.; et al. Direct *In Situ* Measurement of Quantum Efficiencies of Charge Separation and Proton Reduction at TiO_2-Protected GaP Photocathodes. *J. Am. Chem. Soc.* **2023**, *145* (5), 2860-2869.
20. Zeng, G.; Qiu, J.; Li, Z.; Pavaskar, P.; Cronin, S. B. CO_2 Reduction to Methanol on TiO_2-Passivated GaP Photocatalysts. *ACS Catal.* **2014**, *4* (10), 3512-3516.

21. Kan, M.; Yan, Z. W.; Wang, X.; Hitt, J. L.; Xiao, L.; McNeill, J. M.; Wang, Y.; Zhao, Y.; Mallouk, T. E. 2-Aminobenzenethiol-Functionalized Silver-Decorated Nanoporous Silicon Photoelectrodes for Selective CO_2 Reduction. *Angew. Chem. Int. Ed.* **2020**, *59* (28), 11462-11469.
22. Shang, B.; Rooney, C. L.; Gallagher, D. J.; Wang, B. T.; Krayev, A.; Shema, H.; Leitner, O.; Harmon, N. J.; Xiao, L.; Sheehan, C.; et al. Aqueous Photoelectrochemical CO_2 Reduction to CO and Methanol over a Silicon Photocathode Functionalized with a Cobalt Phthalocyanine Molecular Catalyst. *Angewandte Chemie* **2023**, *135* (4).
23. Li, Z.; Wang, L.; Wang, T.; Sun, L.; Yang, W. Steering the Dynamics of Reaction Intermediates and Catalyst Surface during Electrochemical Pulsed CO_2 Reduction for Enhanced C_{2+} Selectivity. *J. Am. Chem. Soc.* **2023**, *145* (37), 20655-20664.
24. Suo, S.; Sheehan, C.; Zhao, F.; Xiao, L.; Xu, Z.; Meng, J.; Mallouk, T. E.; Lian, T. Direct Vibrational Stark Shift Probe of Quasi-Fermi Level Alignment in Metal Nanoparticle Catalyst-Based Metal–Insulator–Semiconductor Junction Photoelectrodes. *J. Am. Chem. Soc.* **2023**.
25. Xu, P.; Von Rueden, A. D.; Schimmenti, R.; Mavrikakis, M.; Suntivich, J. Optical method for quantifying the potential of zero charge at the platinum–water electrochemical interface. *Nat. Mater.* **2023**, *22* (4), 503-510.
26. Xu, P.; Huang, A.; Suntivich, J. Phase-Sensitive Second-Harmonic Generation of Electrochemical Interfaces. *J. Phys. Chem. Lett.* **2020**, *11* (19), 8216-8221.
27. Bian, H.-t.; Guo, Y.; Wang, H.-f. Non-parabolic potential dependence of optical second harmonic generation from the Si(111) electrode/electrolyte interface. *Physical Chemistry Chemical Physics* **2018**, *20* (46), 29539-29548
28. Daschbach, J. L.; Fischer, P. R.; Gragson, D. E.; Richmond, G. L. Observation of the Potential-Dependent Second Harmonic Response from the Si(111)/Electrolyte and Si(111)/SiO_2/Electrolyte Interfacial Regions. *J. Phys. Chem.* **1995**, *99* (10), 3240-3250.
29. Lantz, J. M.; Corn, R. M. Time-resolved optical second harmonic generation measurements of picosecond band flattening processes at single crystal TiO_2 electrodes. *J. Phys. Chem.* **1994**, *98* (38), 9387-9390.
30. Lantz, J. M.; Corn, R. M. Electrostatic field measurements and band flattening during electron-transfer processes at single-crystal TiO_2 electrodes by electric field-induced optical second harmonic generation. *J. Phys. Chem.* **1994**, *98* (18), 4899-4905.
31. Corn, R. M.; Higgins, D. A. Optical second harmonic generation as a probe of surface chemistry. *Chem. Rev.* **1994**, *94* (1), 107-125.
32. Lantz, J. M.; Baba, R.; Corn, R. M. Optical second harmonic generation as a probe of electrostatic fields and flatband potential at single-crystal titania electrodes. *J. Phys. Chem.* **1993**, *97* (29), 7392-7395.
33. Guyot-Sionnest, P.; Tadjeddine, A. Study of Ag (111) and Au (111) Electrodes by Optical Second-Harmonic Generation. *J. Chem. Phys.* **1990**, *92* (1), 734-738.
34. Fromondi, I.; Zhu, H.; Feng, Z.; Scherson, D. Dynamics of Oxidation of Well-Defined Adsorbed CO Phases on Pt(111) in Aqueous Acidic Electrolytes: Simultaneous *in Situ* Second

Harmonic Generation and Differential Reflectance Spectroscopy. *J. Phys. Chem. C* **2014**, *118* (48), 27901-27910.
35. Liu, A.; Lin, L.; Lin, Y.; Guo, Y. Nonequilibrium Adsorption and Reorientation Dynamics of Molecules at Electrode/Electrolyte Interfaces Probed via Real-Time Second Harmonic Generation. *J. Phys. Chem. C* **2013**, *117* (3), 1392-1400.
36. Hagfeldt, A.; Boschloo, G.; Sun, L.; Kloo, L.; Pettersson, H. Dye-Sensitized Solar Cells. *Chem. Rev.* **2010**, *110* (11), 6595-6663.
37. Grätzel, M. Dye-sensitized solar cells. *Journal of Photochemistry and Photobiology C: Photochemistry Reviews* **2003**, *4* (2), 145-153.
38. Asbury, J. B.; Hao, E.; Wang, Y.; Ghosh, H. N.; Lian, T. Ultrafast Electron Transfer Dynamics from Molecular Adsorbates to Semiconductor Nanocrystalline Thin Films. *J. Phys. Chem. B* **2001**, *105* (20), 4545-4557.
39. Asbury, J. B.; Wang, Y.-Q.; Hao, E.; Ghosh, H. N.; Lian, T. Evidences of hot excited state electron injection from sensitizer molecules to TiO_2 nanocrystalline thin films. *Research on Chemical Intermediates* **2001**, *27* (4-5), 393-406.
40. Ke, W.; Fang, G.; Wang, J.; Qin, P.; Tao, H.; Lei, H.; Liu, Q.; Dai, X.; Zhao, X. Perovskite Solar Cell with an Efficient TiO_2 Compact Film. *ACS Applied Materials & Interfaces* **2014**, *6* (18), 15959-15965.
41. Lindblad, R.; Bi, D.; Park, B.-W.; Oscarsson, J.; Gorgoi, M.; Siegbahn, H.; Odelius, M.; Johansson, E. M. J.; Rensmo, H. Electronic Structure of $TiO_2/CH_3NH_3PbI_3$ Perovskite Solar Cell Interfaces. *J. Phys. Chem. Lett.* **2014**, *5* (4), 648-653.
42. Xu, Z.; Hou, B.; Zhao, F.; Cai, Z.; Shi, H.; Liu, Y.; Hill, C. L.; Musaev, D. G.; Mecklenburg, M.; Cronin, S. B.; Lian, T. Nanoscale TiO_2 Protection Layer Enhances the Built-In Field and Charge Separation Performance of GaP Photoelectrodes. *Nano Lett.* **2021**, *21* (19), 8017-8024.
43. Kafizas, A.; Ma, Y.; Pastor, E.; Pendlebury, S. R.; Mesa, C.; Francàs, L.; Le Formal, F.; Noor, N.; Ling, M.; Sotelo-Vazquez, C.; et al. Water Oxidation Kinetics of Accumulated Holes on the Surface of a TiO_2 Photoanode: A Rate Law Analysis. *ACS Catalysis* **2017**, *7* (7), 4896-4903.
44. Lauinger, S. M.; Sumliner, J. M.; Yin, Q.; Xu, Z.; Liang, G.; Glass, E. N.; Lian, T.; Hill, C. L. High Stability of Immobilized Polyoxometalates on TiO_2 Nanoparticles and Nanoporous Films for Robust, Light-Induced Water Oxidation. *Chemistry of Materials* **2015**, *27* (17), 5886-5891.
45. Jing, L.; Zhou, J.; Durrant, J. R.; Tang, J.; Liu, D.; Fu, H. Dynamics of photogenerated charges in the phosphate modified TiO2 and the enhanced activity for photoelectrochemical water splitting. *Energy & Environmental Science* **2012**, *5* (4), 6552-6558.
46. Lu, Y.; Jaeckel, B.; Parkinson, B. A. Preparation and Characterization of Terraced Surfaces of Low-Index Faces of Anatase, Rutile, and Brookite. *Langmuir* **2006**, *22* (10), 4472-4475.
47. Tsujiko, A.; Kisumi, T.; Magari, Y.; Murakoshi, K.; Nakato, Y. Selective Formation of Nanoholes with (100)-Face Walls by Photoetching ofn-TiO_2(Rutile) Electrodes, Accompanied by Increases in Water-Oxidation Photocurrent. *The Journal of Physical Chemistry B* **2000**, *104* (20), 4873-4879.

48. Praet, A.; Vanden Kerchove, F.; Gomes, W. P.; Cardon, F. The photoelectrochemical etching of TiO_2 single crystals. *Solar Energy Materials* **1983**, *7* (4), 481-490.
49. Siefke, T.; Kroker, S.; Pfeiffer, K.; Puffky, O.; Dietrich, K.; Franta, D.; Ohlídal, I.; Szeghalmi, A.; Kley, E. B.; Tünnermann, A. Materials Pushing the Application Limits of Wire Grid Polarizers further into the Deep Ultraviolet Spectral Range. *Advanced Optical Materials* **2016**, *4* (11), 1780-1786.
50. Ohno, P. E.; Saslow, S. A.; Wang, H.-F.; Geiger, F. M.; Eisenthal, K. B. Phase-referenced nonlinear spectroscopy of the α-quartz/water interface. *Nat. Commun.* **2016**, *7* (1), 13587.
51. Wen, Y.-C.; Zha, S.; Liu, X.; Yang, S.; Guo, P.; Shi, G.; Fang, H.; Shen, Y. R.; Tian, C. Unveiling Microscopic Structures of Charged Water Interfaces by Surface-Specific Vibrational Spectroscopy. *Physical Review Letters* **2016**, *116* (1).
52. Bard, A. J.; Bocarsly, A. B.; Fan, F. R. F.; Walton, E. G.; Wrighton, M. S. The concept of Fermi level pinning at semiconductor/liquid junctions. Consequences for energy conversion efficiency and selection of useful solution redox couples in solar devices. *Journal of the American Chemical Society* **1980**, *102* (11), 3671-3677.
53. De Gryse, R. On the Interpretation of Mott-Schottky Plots Determined at Semiconductor/Electrolyte Systems. *Journal of The Electrochemical Society* **1975**, *122* (5), 711.
54. Chabeda, D.; Bhattacharyya, D.; Kelly, H. R.; Gebre, S. T.; Tangen, I.; Kubiak, C. P.; Batista, V. S.; Lian, T. Unlocking the Facet-Dependent Ligand Exchange on Rutile TiO_2 of a Rhenium Bipyridyl Catalyst for CO_2 Reduction. *J. Phys. Chem. C* **2023**, *127* (17), 8126-8135.
55. Memming, R. Solid–Liquid Interface. In *Semiconductor Electrochemistry*, WILEY-VCH Verlag GmbH, 2015; pp 89-125.
56. Corn, R. M.; Romagnoli, M.; Levenson, M. D.; Philpott, M. R. The potential dependence of surface plasmon-enhanced second-harmonic generation at thin film silver electrodes. *Chemical physics letters* **1984**, *106* (1-2), 30-35.
57. Richmond, G. Characterization of the silver-aqueous electrolyte interface by optical second harmonic generation. *Langmuir* **1986**, *2* (2), 132-139.
58. Kennedy, J. H.; Frese, K. W. Flatband Potentials and Donor Densities of Polycrystalline α - Fe_2O_3 Determined from Mott - Schottky Plots. *Journal of The Electrochemical Society* **1978**, *125* (5), 723-726.
59. Tomkiewicz, M. The Potential Distribution at the TiO_2 Aqueous Electrolyte Interface. *Journal of The Electrochemical Society* **1979**, *126* (9), 1505-1510.
60. Cooper, G.; Turner, J. A.; Nozik, A. J. Mott - Schottky Plots and Flatband Potentials for Single Crystal Rutile Electrodes. *Journal of The Electrochemical Society* **1982**, *129* (9), 1973-1977.
61. Peter, L. Kinetics and mechanisms of light-driven reactions at semiconductor electrodes: Principles and techniques. *Photoelectrochemical Water Splitting: Materials, Processes and Architectures* **2013**, *9*.
62. Bhola, R.; Bhola, S. M.; Mishra, B.; Olson, D. L. Electrochemical Behavior of Titanium and Its Alloys as Dental Implants in Normal Saline. *Research Letters in Physical Chemistry* **2009**, *2009*, 1-4.

63. Oliveira, N. T. C.; Guastaldi, A. C. Electrochemical behavior of Ti–Mo alloys applied as biomaterial. *Corrosion Science* **2008**, *50* (4), 938-945.
64. Moss, R. E.; Pérez-Roa, R. E.; Anderson, M. A. Effects of pH on Phosphate Adsorption to Hematite as Studied with Cyclic Voltammetry and Electrochemical Impedance Spectroscopy. *J. Electrochem. Soc.* **2013**, *160* (2), 105-112.
65. Moss, R. E.; Jackowski, J. J.; De Souza Castilho, M.; Anderson, M. A. Development and Evaluation of a Nanoporous Iron (Hydr)oxide Electrode for Phosphate Sensing. *Electroanalysis* **2011**, *23* (7), 1718-1725.
66. Gerischer, H. Neglected problems in the pH dependence of the flatband potential of semiconducting oxides and semiconductors covered with oxide layers. *Electrochimica Acta* **1989**, *34* (8), 1005-1009.
67. Grahame, D. C. Discreteness-of-charge-effects in the inner region of the electrical double layer. *Zeitschrift für Elektrochemie, Berichte der Bunsengesellschaft für physikalische Chemie* **1958**, *62* (3), 264-274.
68. Kumar, A.; Santangelo, P. G.; Lewis, N. S. Electrolysis of water at strontium titanate ($SrTiO_3$) photoelectrodes: distinguishing between the statistical and stochastic formalisms for electron-transfer processes in fuel-forming photoelectrochemical systems. *J. Phys. Chem.* **1992**, *96* (2), 834-842.
69. Walter, M. G.; Warren, E. L.; McKone, J. R.; Boettcher, S. W.; Mi, Q.; Santori, E. A.; Lewis, N. S. Solar Water Splitting Cells. *Chem. Rev.* **2010**, *110* (11), 6446-6473.
70. Ye, K.-H.; Li, H.; Huang, D.; Xiao, S.; Qiu, W.; Li, M.; Hu, Y.; Mai, W.; Ji, H.; Yang, S. Enhancing photoelectrochemical water splitting by combining work function tuning and heterojunction engineering. *Nat. Commun.* **2019**, *10* (1).
71. Wu, H.; Zhang, L.; Du, A.; Irani, R.; Van De Krol, R.; Abdi, F. F.; Ng, Y. H. Low-bias photoelectrochemical water splitting via mediating trap states and small polaron hopping. *Nat. Commun.* **2022**, *13* (1).

4 Direct *Operando* Observation of Surface Charge Build-up on TiO_2 Photoanode Under Water Oxidation Conditions by EFISH

4.1. Introduction

Photoelectrochemical water splitting is an important way to achieve artificial photosynthesis, in which solar energy is converted into chemical energy stored in H_2 fuels. The overall water splitting reaction is composed of oxygen evolution reaction (OER) on the anode and H_2 evolution reaction (HER) on the cathode; the OER is typically the kinetic bottleneck due to the four-electron-transfer process and sluggish water oxidation rate at most commonly used metal oxide electrodes. [1-3] Various strategies have been adopted to increase the water oxidation efficiency at photoanode materials, which is usually characterized by incident photon to current conversion efficiency (IPCE). IPCE is determined by the product of quantum efficiencies of a series of steps, i.e. $IPCE = \phi_{abs} \times \phi_{CS} \times \phi_{cat}$, where the incident photons absorption efficiency (ϕ_{abs}) is the fraction of incident photons absorbed by the photoelectrode; the charge separation quantum efficiency (ϕ_{CS}) is the fraction of the photo-generated minority carriers that reach the surface; and the surface catalysis efficiency (ϕ_{cat}) is the fraction of surface minority carrier that proceeds with OER reaction, as shown in the following equation. [4-7] The photons absorption efficiency ϕ_{abs} can be improved by coupling light sensitizer to photoelectrodes. [4, 8] ϕ_{CS} can be increased by several strategies: doping engineering can increase the minority charge mobility and carrier lifetime; [9-11] nanostructure engineering can effectively shorten the carrier diffusion length and reaction surface area; [5, 12] heterojunction construction can increase the built-in field for charge separation. [7, 13-15] Finally, ϕ_{cat} can be increased by deposition of surface catalysts. [5, 16-19]

One of the most important parameters of semiconductor/liquid junctions is the band-bending (or built-in potential) in the semiconductor spacer layer region that drives charge

separation and suppress charge recombination. However, due to the sluggish rate for many solar fuel forming reactions, including water oxidation, the photogenerated minority carriers accumulate at the semiconductor surface and alter the potential distribution across the semiconductor/liquid junction, which is called 'band flattening' or 'light-induced Fermi level pinning'. [7, 20-22] The surface minority carrier accumulation lead to the reduction of built-in potential in semiconductor ΔV_{bi} and the increase of potential drop in Helmholtz layer ΔV_H. The surface trapped minority carriers have been characterized in various photoelectrodes by electrochemical measurement including electrochemical impedance spectroscopy (EIS), [23-27] IMPS, [6] electroreflectance, [28] and photocurrent analysis. [29-31] However, the origin of light-induced Fermi level pinning, the chemical nature of the surface trapped hole, and how it will impact the photoelectrochemical charge separation behavior are still not well understood. For example, Memming et al suggest that surface states not only act as a recombination center, but also provide charge transfer pathways to redox couples in the electrolyte. [29-31] Bockris et al measures the capacitance of surface states and argue that the measured surface states originate from the ion adsorption from the solution and act as faradaic mediators. [32] Peter et al, Leng et al, and Kuhne et al believe that the increased potential drop at the Helmholtz layer ΔV_H due to the minority carrier accumulation at the surface increases the charge transfer rate constant k_{ct}. [26, 27, 33, 34] More recently, there have been many reports of improved water oxidation performance of photoanodes by adding catalyst layers, but the mechanism of the improvement remains unclear. [2, 35-50] Some have argued that the application of metal oxide coating or surface catalyst such as CoPi to the surface suppress the surface recombination by increasing the band bending or passivating the defect cites, which increases both charge separation ϕ_{CS} and catalysis efficiency ϕ_{cat}, investigated by photoinduced absorption spectroscopy, impedance spectroscopy, and intensity-modulated photocurrent spectroscopy

(IMPS). [2, 35-40] Others believes application of co-catalyst essentially accelerates the catalysis efficiency ϕ_{cat} acting as a hole collector and an active OER catalyst, demonstrated by potential sensing techniques, and other photoelectrochemical characterization. [41-47]

Therefore, it is of significance to investigate the light-induced Fermi level pinning at semiconductor/electrolyte catalytic junction and understand the electrochemical behavior of surface states, particularly in an *in situ/operando* manner. Several techniques have been developed for investigating the potential/electric field at (photo)catalytic interface. For instance, Kelvin probe force microscopy is widely utilized to map the surface voltage in nanoscale photocatalytic structure. [51-54] Nonetheless, it necessitates close contact between the probe and material, rendering it infeasible to operate under *in situ/operando* catalytic conditions. A more recent development involves a dual-working electrode for *in situ* probing of surface potential of semiconductor electrode or surface co-catalyst. [55-59] However, this method typically mandates an ion-permeable ohmic contact between the working electrode and the probe electrodes, which may alters the surface properties. Vibrational optical methods like sum-frequency generation[60, 61] or Raman spectroscopy[62, 63] are developed to measure the electric field at electrode/photoelectrode surface by detecting changes in surface molecules' vibrational frequency under varying applied potentials. Nevertheless, these methods still necessitate surface molecular modification, which might potentially alter the junction, especially the properties related to surface trap states. [64-66] Hence, the necessity for a surface noninvasive, *in situ/operando* electric field sensitive method emerges to investigate the trap state related light-induced Fermi-level pinning effect.

The non-linear optical second harmonic generation (SHG) technique offers a distinctive advantage in characterizing electric field at solid-air interfaces[67-69] and electrode/electrolyte junctions[21, 70-74] without necessitating surface modification. Moreover, SHG can be employed

under (photo)electrocatalytic *in situ/operando* conditions and is essentially a time-resolve technique. [21, 67-69, 75] In this work, we report using the electric field induced second harmonic generation (EFISH) as a probe to specifically measure the *operando* built-in potential drop in a rutile (100) TiO_2 photoanode under different illumination conditions. Light-induced Fermi-level pinning at the semiconductor/electrolyte junction is observed due to photogenerated hole accumulation. The relationship between built-in potential screening and minority carrier accumulation is established. Kinetic isotope measurements indicate PCET to be the OER rate-determining step on TiO_2. The chemical nature of the surface accumulated holes and the effect of electrolyte on light-induced Fermi level pinning is further discussed. We believe that EFISH probe of Fermi-level pinning can be a general technique applicable to other PEC photoelectrodes.

4.2. Materials and Methods

Rutile TiO_2 (100) single crystal electrode, surface cleaning method and EFISH methodology in the chapter are same as what's mentioned in Chapter 3, section 3.2.1 and 3.2.2.

Aqueous solutions are used in the experiments in this work, where 18MΩ cm Milli-Q water is used as H_2O solvent, deuterium oxide (Aldrich Chemistry) is used as D_2O solvent. H_2O is used as the solvent by default unless otherwise mentioned. 1 M $NaClO_4$ (Acros Organics, 99+% for analysis) is used as supporting electrolyte. 0.1 M pH 7 phosphate buffer is obtained by adding 1.549 g sodium phosphate dibasic heptahydrate (Macron Chemicals) and 0.583 g sodium phosphate monobasic monohydrate (Macron Chemicals) in 100 mL 1 M $NaClO_4$ solution. pH 12.7 solution is obtained by titrating 1 M $NaClO_4$ with 1 M NaOH (Macron Fine chemicals) solution until pH reaches 12.7. Sodium chloride (Macron Chemicals), sodium sulfite anhydrous (Fisher Scientific), hydrogen peroxide solution (Sigma-Aldrich, 30 wt. % in H_2O), formic acid (Fisher

Scientific, 88%), and sodium sulfite (Sigma-Aldrich, ACS reagent) are used as solute for different control experiments.

The illumination source used in this chapter is monochromic 360 nm continuous-wave (CW) light, provided by a 365 nm LED (Thorlabs, M365 L3) with a 360 nm bandpass filter (Thorlabs, FB360-10, FWHM=10 $\pm$ 2 nm). The LED is controlled by a DC driver (Thorlabs, DC2200). The 360 nm CW light illuminates the sample at a normal angle of incident with a beam area of 0.055 cm^2, overlapping with the 800 nm fundamental probe.

In-situ EFISH and electrochemical measurements are conducted in a three-electrode system as shown in Figure 4.1, using a graphite electrode as a counter electrode and Ag/AgCl as a reference electrode. Detail experimental setup is described in Section 2.3. Electrochemical measurements are performed using a CHI 660e electrochemical workstation (CH Instruments). Impedance measurements are measured under the negative scan direction with a 550 Hz AC frequency with a 0.005 V amplitude.

4.3. Results and Discussions

4.3.1 *Operando* EFISH of TiO_2 under illumination

Bias-dependent Second Harmonic Generation (SHG) is conducted using a setup shown in Figure 4.1, where the TiO_2 single crystal is placed is a specific azimuthal angle depicted in the figure inset. The relationship between second harmonic generation (SHG) intensity ($I(2\omega)$) and applied potential V_{app} has been demonstrated in a previous chapter 3 and is given by Equations 3.8a and 3.8b,

$$I(2\omega) \propto \left|\chi^{(2)}_{\text{eff}} + e^{i\beta}\chi^{(3)}_{\text{liq}}\Delta\Phi_{liq} + e^{i\alpha}\chi^{(3)}_{\text{sc}}\Delta\Phi_{sc}\right|^2 I(\omega)^2 \quad 3.8$$

$$= \left|\chi^{(2)}_{eff} + e^{i\beta}\chi^{(3)}_{\text{liq}}(\mathrm{V}_{app} - \mathrm{V}_{fb})\right|^2 I(\omega)^2 \qquad (\mathrm{V}_{app} < \mathrm{V}_{fb}) \quad 3.8a$$

$$= \left|\chi_{bid} + e^{i\gamma}\chi_{\mathrm{sc}}^{(3)}(\mathrm{V}_{app} - \mathrm{V}_{fb})\right|^2 I(\omega)^2 \qquad (\mathrm{V}_{app} > \mathrm{V}_{fb}) \quad 3.8\mathrm{b}$$

In Equation 3.8, $\chi_{eff}^{(2)}$ is the second-order susceptibility which includes the contribution from solid surface and interfacial electrolytes; ($\chi_{\mathrm{sc}}^{(3)}$and $\Delta\Phi_{sc}$) and($\chi_{\mathrm{liq}}^{(3)}$ and $\Delta\Phi_{liq}$) are the third-order susceptibility and potential drop at the semiconductor space charge region (SCR) and electrolyte double layer (EDL), respectively, that give rise to the EFISH contributions; $\mathrm{V_{app}}$ and $\mathrm{V_{fb}}$ are the applied potential at the semiconductor back contact and flatband potential of the semiconductor verse reference electrode (Ag/AgCl in this study), respectively; α and β are the phase differences between $\chi_{eff}^{(2)}$ and $\chi_{\mathrm{sc}}^{(3)}$, $\chi_{\mathrm{liq}}^{(3)}$, respectively; From Equation 3.8, a piecewise quadratic relationship between SHG intensity and applied potential is established at both sides of the flatband potential. At the negative side of $\mathrm{V_{fb}}$, the accumulation region, Equation 3.8 is simplified to Equation 3.8a, in which $\chi_{\mathrm{liq}}^{(3)}$ term is bias dependent and $\chi_{\mathrm{sc}}^{(3)}$ term vanishes. [74] At the positive side of $\mathrm{V_{fb}}$ ($\mathrm{V_{app}} > \mathrm{V_{fb}}$), the depleition region, Equation 3.8 is simplified to Equation 3.8b, in which only the $\chi_{\mathrm{sc}}^{(3)}$ term is bias dependent, $\Delta\Phi_{liq}$ is independent on the potential, [76, 77] and γ is the phase difference between $\chi_{sc}^{(3)}$ and bias-independent term χ_{bid}. It has been demonstrated by our previous Chapter 3 that the shape of bias-dependent SHG is strongly affected by the azimuthal angle of an anisotropic surface and the light polarization. In the case of rutile TiO_2 (100), it was determined that at s-in-p-out polarization with TiO_2 [001] axis placed in parallel to the light incidental plane, the relative phase between SHG bias-independent term (χ_{bid}) and bias-dependent term ($\chi_{\mathrm{sc}}^{(3)}$) γ is 90º. This means the bias-dependent SHG signal has a minimum potential ($\mathrm{V_{min}}$) that equals $\mathrm{V_{fb}}$. In this study, we adopt this TiO_2 crystal azimuthal angle and s-in-p-out polarization to investigate the light-induced Fermi-level pinning effect. Because the electric field term becomes

dominant in the bias-dependent SHG behavior, we call this measurement Electric Field Induced Second Harmonic Generation (EFISH) in the following section.

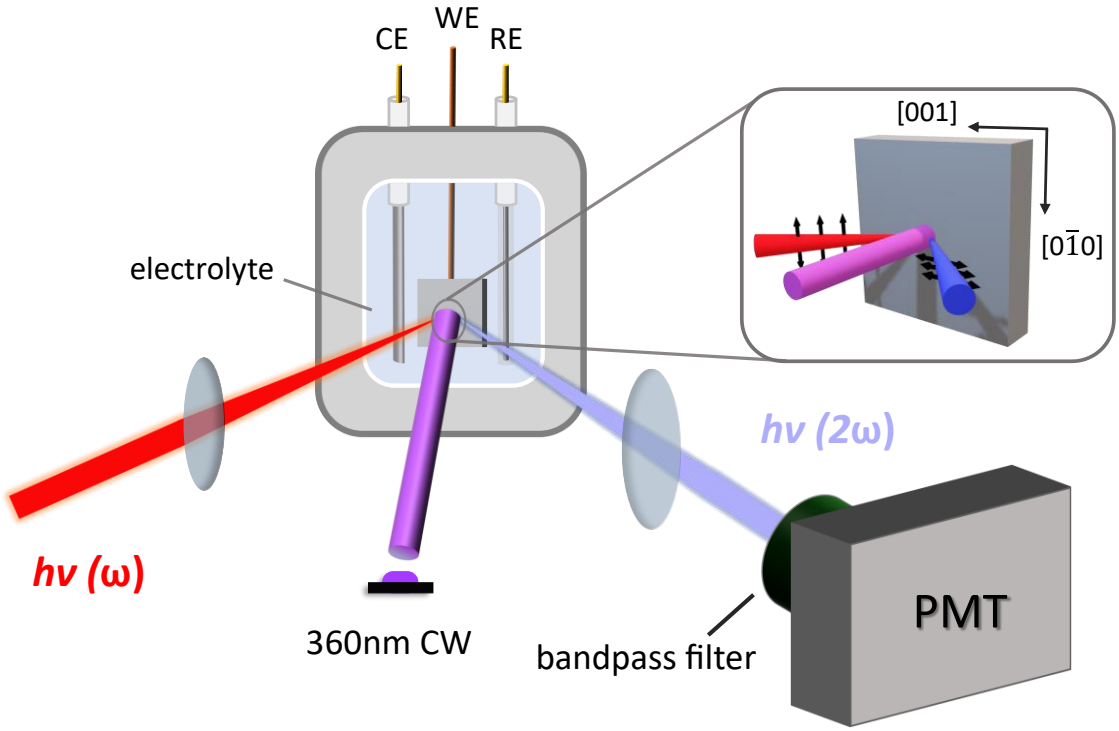

Figure 4.1. Schematic of steady-state EFISH setup. The zoom-in panel indicates the second harmonic generation uses an s-in-p-out polarization and the adopted crystal azimuthal angle. 1 kHz 35 fs 800 nm pulses are used as the fundamental light.

As depicted in Figure 4.1, EFISH is conducted on TiO_2/electrolyte junction to study the light-induced Fermi-level pinning effect, where 800 nm fundamental light incident on the sample at 45° angle of incident acting as a probe of TiO_2 built-in potential, 360 nm CW light illuminates the sample at 0° angle of incident. EFISH experiments are carried out in 1 M $NaClO_4$ solution under different light illumination during the negative scan of Cyclic Voltammetry (CV) measurement as shown in Figure 4.2a. The electrolyte solution was stirred during the measurement to avoid surface pH variation. EFISH measurement can be treated as a measurement of steady state at a given potential due to the slow scan rate (3.53 mV/s). The EFISH intensities in the dark show

a quadratic response as a function of applied potential with a minimal value (i.e., V_{fb}) at -0.933 $\pm$ 0.019 V vs Ag/AgCl fitted with Equation 1b. Upon 360 nm illumination, EFISH intensities decrease from the dark response starting at ca. -0.3 V vs Ag/AgCl to more positive potentials. According to Equation 1b, this indicates a reduced potential drop in the SCR region. To better visualize the extent of the built-in potential change under different illumination conditions and applied potential, the actual built-in potential and built-in potential change under illumination are calculated using the dark EFISH response as a calibration curve as indicated in Figure 4.2a. The change of built-in potential (ΔV_{bi}) is plotted as a function of applied potential in Figure 4.2b. Because the potential difference between the bulk electrode and the bulk solution is fixed by the potentiostat, the decrease of built-in potential in the semiconductor equals to increase in the potential drop in the double layer. This phenomenon is referred to as light-induced Fermi-level pinning or band edge unpinning caused by accumulation of photogenerated minority carriers on the surface. [20, 22] From the ΔV_{bi}-potential response, there are three features worth pointing out. Firstly, under a certain illumination intensity, ΔV_{bi} increase with applied potential and reach a plateau value after a certain positive potential, agreeing well with the trend of photocurrent as shown in Figure 4.2c. Secondly, with higher illumination intensity, a larger ΔV_{bi} is observed under a certain positive potential. Unlike photocurrent, where the photocurrent densities increase linearly with the illumination power densities, the increase of ΔV_{bi} with power density follows a different relationship. These features indicate that charge distribution across the semiconductor/electrolyte interface are altered during illumination. Although we only present the ΔV_{bi}-V plot under the negative scan direction, the data obtained from negative and positive scans agrees well with each other (Figure A4.1). All EFISH and impedance data presented in this paper are conducted under the negative scan direction unless otherwise stated.

Transient photocurrent (TPC) measurements were also conducted under chopped chrono-amperometry conditions to evaluate the charge separation on TiO_2 photoanode under a typical illumination power density (10 mW/cm^2) as shown in Figure 4.2d. The photocurrent obtained from CV is plotted in black. Transient photocurrent density J_0 (pink open circles), defined in the inset of Figure 4.2d, represents the surface hole flux that semiconductor bulk and SCR can generate, which is the photocurrent prior to surface hole accumulation and resulting recombination; and the steady state current density J_{inf} (red open circles), reflects the net current density at the junction by summing up the hole current density and electron current density arising from the surface recombination. [2, 7] According to the transient photocurrent measurement, the electrode surface starts to capture holes generated from the bulk and SCR of TiO_2 at -0.5 V vs Ag/AgCl. From -0.5 to 0.3 V, $J_{inf} < J_0$ is observed due to the surface recombination between surface-trapped holes with electrons from the conduction band. [78-80] When the applied potential is larger than 0.3 V, $J_{inf} = J_0$ and J_{inf} reach a plateau as surface recombination is minimized because of larger band bending and smaller surface conduction band electron densities. J_0 shows an onset potential and saturation potential that are more negative compared to J_{inf}, reflecting the additional built-in potential required to suppress the surface recombination. The bias-dependent ΔV_{bi} response from the EFISH measurement agrees well with the potential dependence of J_0 (Figure 4.2d), which suggests that ΔV_{bi} increases with the initial charge separation flux of the semiconductor, consistent with the assignment that it is caused by the surface minority charge (hole) accumulation.

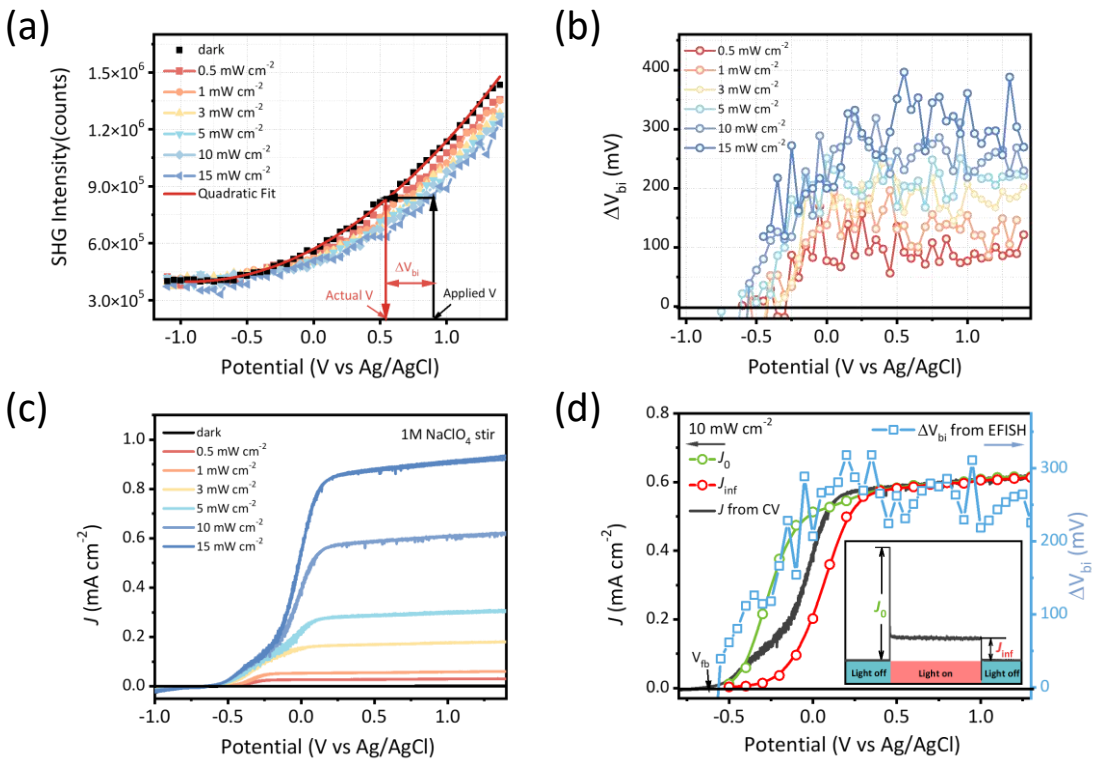

Figure 4.2. (a) EFISH intensity as a function of applied potential on rutile TiO_2 (100) under UV illumination with different power densities. Also shown is an example of determining ΔV_{bi} under 15 mW/cm^2 illumination using the applied potential V_{app} and calculated actual V_{bi} calibrated by quadratic fitting (Equation 3.8b) of dark EFISH response. (b) The change of semiconductor built-in potential ΔV_{bi} as a function of applied potential. (c) Current densities as a function of applied potential under different UV power densities measured by CV with a scan rate of 3.53 mV/s. (d) Comparison of initial photocurrent densities J_0 (pink open circles) and steady state photocurrent density J_{inf} (red open circles) measured by chopped chronoamperometry measurement, current density (J) measured by CV, and ΔV_{bi} under 10 mW/cm^2 illumination. Inset: a representative transient current curve and J_0 and J_{inf} values obtained from chopped chronoamperometry measurement at -0.1 V vs Ag/AgCl. All the above experiments are done in 1 M $NaClO_4$ electrolyte under stirring conditions.

4.3.2 Impedance spectroscopy investigation of light-induced Fermi-level pinning

More evidence of surface charge accumulation can be found in impedance measurements shown in Figure 4.3. The Mott-Schottky measurement on TiO_2 was first conducted under the stirring environment without CW illumination to extract the V_{fb}, as shown in Figure 4.3a. The same high-concentration electrolyte, 1 M $NaClO_4$, is used as the EFISH measurement to ensure the same V_{fb} position and negligible applied potential drops in the solution double layer. [20, 77] The flatband potential V_{fb} of TiO_2 can be extracted following Equation 3.9, [74, 77, 81-83]

$$\frac{A^2}{C_s^2} = \frac{2}{q\varepsilon\varepsilon_0 N_d A^2}\left(V - V_{fb} - \frac{kT}{q}\right) \qquad 3.9$$

where N_d is the doping density of the semiconductor, respectively, C_s and A are the interfacial capacitance and electrode area, respectively, q is the elementary charge, ε_0 and ε are the dielectric constant and the relative dielectric constant of the semiconductor, respectively, k is Boltzmann's constant, and T is the temperature. The flatband potential of the semiconductor under dark condition is determined to be -0.926 $\pm$ 0.001 V vs Ag/AgCl, which agrees with the V_{fb} extracted from EFISH.

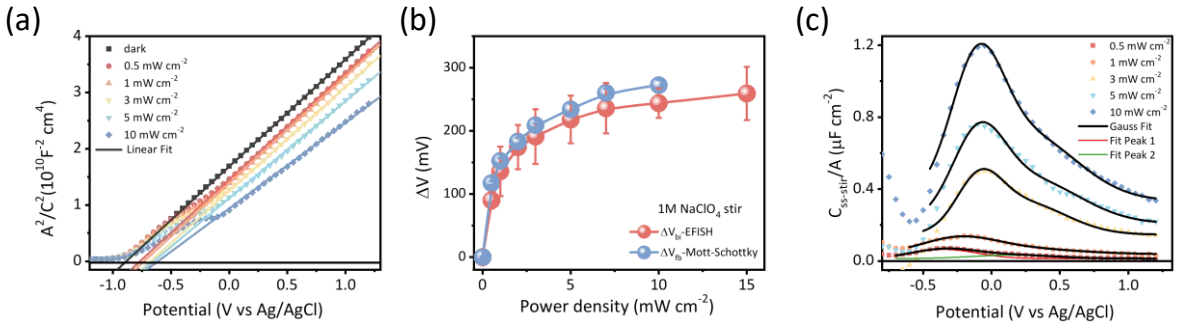

Figure 4.3. (a) Mott-Schottky plot of TiO_2 electrode. (b) Effect of screened potential measured by Mott-Schottky (blue trace) and by EFISH (red trace, extracted at 1 V vs Ag/Ag Cl) as a function of illumination power density. (c) Surface state capacitance as a function of applied potential under different illumination power densities, fitted from (V_{fb} + 0.2) V to 1.2 V vs Ag/AgCl. A fitting

example at 0.5 mW cm^{-2} is plotted. All fitting details summarized in Table A4.1. All the above experiments are done in 1 M $NaClO_4$ electrolyte under stirring conditions.

Upon illumination, TiO_2 Mott-Schottky curve shows a shift towards positive potential while maintaining similar slopes of the linear part. According to Equation 3.9, the flatband potential of TiO_2 shifts anodically with increasing power density, while the donor density within the SCR (N_d) remains almost unchanged. This light-induced Fermi level pinning has been observed on other semiconductor photoelectrodes. [22-25, 29-31] It is reported that the shift of flatband potential and band edge is attributed to the trapping of minority carriers in surface states that leads to a potential redistribution across the semiconductor/electrolyte junction. Interestingly, the trend of flatband potential shift ΔV_{fb} change with illumination power density corresponds well with the trend of ΔV_{bi} (extracted at 1V vs Ag/AgCl) change with power density as shown in the blue and red traces in Figure 4.3b. This means that both EFISH and Mott-Schottky measure the same light-induced Fermi-level pinning phenomenon, reflected by the decrease of built-in potential ΔV_{bi} and anodic shift of flatband potential ΔV_{fb}, respectively.

Light induced flatband potential shift ΔV_{fb} can be attributed to hole accumulation at the interface of the semiconductor/electrolyte junction following previous reports. [21, 22] The energetics and the density of surface states can be obtained in the plot of junction capacitance C as a function of applied potential. As shown in the inset of Figure 4.3c, for a semiconductor/liquid junction under the dark condition and (at potentials with the semiconductor) in the depletion region. the total capacitance is contributed by mainly SCR capacitance (C_{sc}) (see Appendix A4.2 and Figure A4.2 for details). Under illumination, surface minority charge carrier accumulation leads to photogenerated surface states capacitance (C_{ss}) in parallel with the SCR capacitance. The overall

capacitance response of semiconductor/electrolyte junction can be described by Equation 4.1. [22, 32, 76, 84-86]

$$C = C_{sc} + C_{ss} \quad 4.1$$

Therefore, by subtracting the capacitance in the dark from that under excitation, the capacitance response of photo-induced surface states (C_{ss}) can be calculated as shown in Figure 4.3b. The C_{ss}-Potential response can be further fitted by Gaussian distribution of surface states as shown in Equation 4.2: [82, 87, 88]

$$C_{ss} = \frac{qN_{ss}}{\sqrt{2\pi}\sigma} exp\left[-\frac{(V-V_{ss})^2}{2\sigma^2}\right] \quad 4.2$$

where N_{ss} is the surface state density, σ and V_{ss} are the standard deviation and peak of the surface state distribution. From the fitting results shown in Table A4.1, two trap states can be found. The first trap state V_{ss1} is at -0.347 V vs Ag/AgCl at 0.5 mW/cm^2 and shifts to more positive potential until ca. -0.1 V vs Ag/AgCl as the power density increases. The observed ~ 0.25 V shift of the trap state energy corresponds well with the shift of semiconductor band edge position under light illumination measured by EFISH and Mott-Schottky as shown in Figure 4.3c. The second trap state response potential V_{ss2} also shows a shift from ca. 0.10 V vs Ag/AgCl towards ca. 0.26 V vs Ag/AgCl. Moreover, the potentials of these trap states agree well with the potential region where surface recombination occurs, i.e., from -0.5 to +0.2 V according to TPC in Figure 4.2d, suggesting that these surface states are responsible for surface recombination.

The number of surface accumulated charges (ΔQ_{ss}) can be further estimated using Equation 4.3: [20, 22]

$$\Delta Q_{ss} = qp_s = C_H(\Delta V_{bi}) \quad 4.3$$

Using a C_H value of 50 μF/cm^2, [82] a surface charge density of 12 μC/cm^2 is obtained under 10 mW/cm^2 UV illumination, giving rise to the surface charge density p_s of 7.6×10^{13} cm^{-2}. The

order of magnitude of surface hole density (ca. 10^{13}-10^{14} cm^{-2}) also agrees with previous transient photocurrent analysis on n-TiO_2, corresponding to about 1.5% of surface atoms being positively charged with a hole. [28, 89, 90] What worth mention is that the shift of ΔV_{fb} can be also be caused by change of local pH under conditions of insufficiently fast mass transport. As is discussed in Appendix A4.3, control experiments show that under rigorous stirring conditions (i.e. fast mass transport) described above, the effect of local pH can be neglected.

4.3.3 Isotope effect on EFISH and Photocurrent

The previous section has confirmed that built-in potential loss ΔV_{bi} obtained from EFISH reflects the extent of hole accumulation at the surface states. It is also important to understand the chemical nature of these surface states, which provides information on the rate-determining step during the OER. Herein, both EFISH and photocurrent were measured in both H2O and D2O, as shown in Figure 4.4. Firstly, ΔV_{bi} measured by EFISH are analyzed as a function of illumination power density and applied potential. As shown in Figure 4.4a, plateaued ΔV_{bi} measured in H_2O and D_2O are compared as a function of power density. Under the same applied potential (1 V vs Ag/AgCl), ΔV_{bi} in D_2O increases faster with increasing power density than in H_2O and reaches a higher saturation level. Moreover, at 10 mW/cm^2 power density, not only ΔV_{bi} has a larger value in D_2O, but it also shows an earlier onset potential as shown in Figure 4.4b. These EFISH experiment results mean that surface holes are more easily accumulated in D_2O solution, where the hole transfer process across TiO_2/electrolyte junction is more kinetically hindered. Photocurrents measured from the cyclic voltammetry show a later onset potential and a smaller plateau current density in D_2O compared to H_2O solution as shown in Figure 4.3c, which further convinces that greater hole accumulation will lead to a larger surface recombination rate and thus a smaller overall current. These results suggest that the reaction intermediate is related to the

proton-coupled electron transfer (PCET) rate-determining step. The kinetic isotope effect is calculated based on the water oxidation rate, i.e., steady state photocurrent ratio between H_2O and D_2O shown in Equation 4.4.

$$KIE(rate) = \frac{J(H_2O)}{J(D_2O)} \quad 4.4$$

A KIE of around 1.08 was observed in pH 7 1 M $NaClO_4$ solution, verifying that the proton-coupled electron transfer (PCET) is the rate-limiting step during OER. Assuming the rate-determining step to be a pseudo-first-order reaction, a KIE of 2 based on the rate constant ratio as calculated with Equation 4.5, where the surface hole concentration ratio is known by comparing ΔV_{bi} as shown in Equation 4.3. The observation PCET rate-determining step agrees with the previous experimental finding. [91]

$$\frac{k_{et}(H_2O)}{k_{et}(D_2O)} = \frac{J(H_2O)}{J(D_2O)} \div \frac{p_s(H_2O)}{p_s(D_2O)} \quad 4.5$$

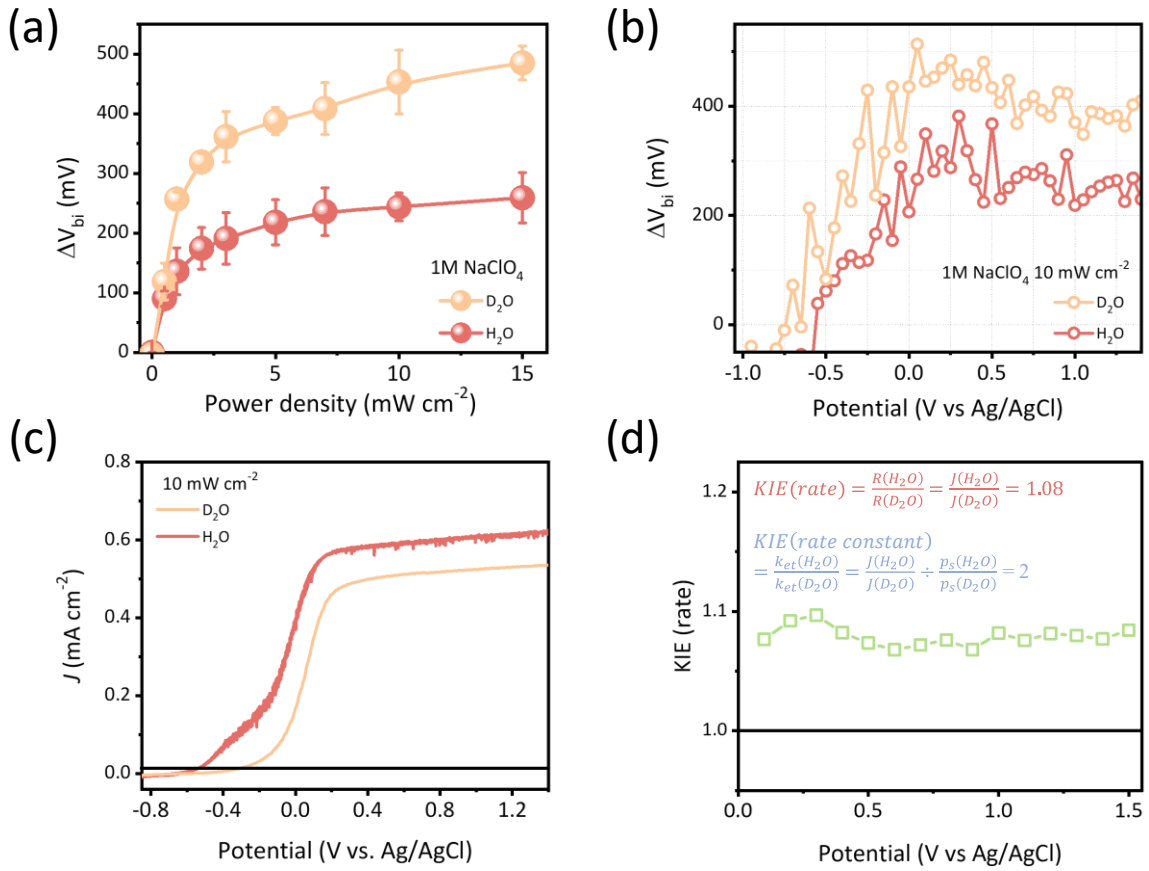

Figure 4.4. (a) ΔV_{bi} (collected at 1V vs Ag/AgCl) as a with illumination power density in H_2O and D_2O. (b) ΔV_{bi}-V plot and (c) *J*-V plot in H_2O and D_2O under 10 mW/cm^2 illumination power density. (d) KIE value calculated from Equation 4.4, measured by light on-off amperometric measurement. All above experiments used 1 M $NaClO_4$ as the electrolyte, H_2O or D_2O as the solvent, and under stirring conditions.

4.3.4 Effect of electrolyte on ΔV_{bi}

The above experiments demonstrate that without surface-charged absorbate, the surface accumulated holes can be detected through the change of surface electric field. It has been previously reported that surface modification, for example, CoPi, [35, 36, 41, 47] $(NiFe)O_x$ [5, 17], and Cl^- [92] modification can provide surface sites to stabilize surface holes. It is suggested that by tuning the inner Helmholtz layer microenvironment, photoelectrode performance can be altered. Inspired by

these studies, we also applied EFISH and impedance measurements in different electrolytes to examine the microenvironment effects. As shown in Figures 4.5 and A4.5, *operando* EFISH, J-V curve, and Mott-Schottky measurements are carried out in pH 7 (1 M $NaClO_4$ buffered with 0.1 M phosphate buffer), and pH 12.7 (1 M $NaClO_4$ buffered with NaOH) electrolytes, respectively. Surprisingly, EFISH behaviors under different illumination power densities are almost identical (Figure 4.5). Mott-Schottky measurements under such conditions agree with the EFISH measurement, showing no difference between dark and illumination conditions (Figures A4.5a, c). These experiments indicate negligible charge accumulation at the semiconductor surface and therefore no change in semiconductor band edge energy. These observations suggest that electrolytes containing sufficient negatively charged surface absorbate such as HPO_4^{2-}, $H_2PO_4^-$, and OH^-, can compensate for the surface accumulated holes and therefore maintain the semiconductor built-in potential. This effect is more obvious in the presence of phosphate buffer, in which the transient photocurrent density J_0 shows little difference from the steady state photocurrent density J_{inf} between photocurrent onset and plateau potential region in TPC measurement (Figure A4.6a). This also indicates that the phosphate group (–Ti–O–P–O^-) that binds to the surface slows down the surface electron-hole recombination, agreeing with previous transient absorption measurements. [93] More evidence of charge compensating effect is observed when replacing the anion from 1M ClO_4^- to Cl^-, which is also known as a surface absorbate on TiO_2. [92, 94-96] As shown in Figure A4.7a, smaller ΔV_{bi} is observed in Cl^- solution compared to ClO_4^- under different power densities at the same applied potential (1 V vs Ag/AgCl). These control experiments further verify that ΔV_{bi} and light-induced Fermi-level pinning originate from the surface hole accumulation. Introduction of surface absorbate can compensate the charges from the surface holes and maintain the semiconductor built-in potential V_{bi}.

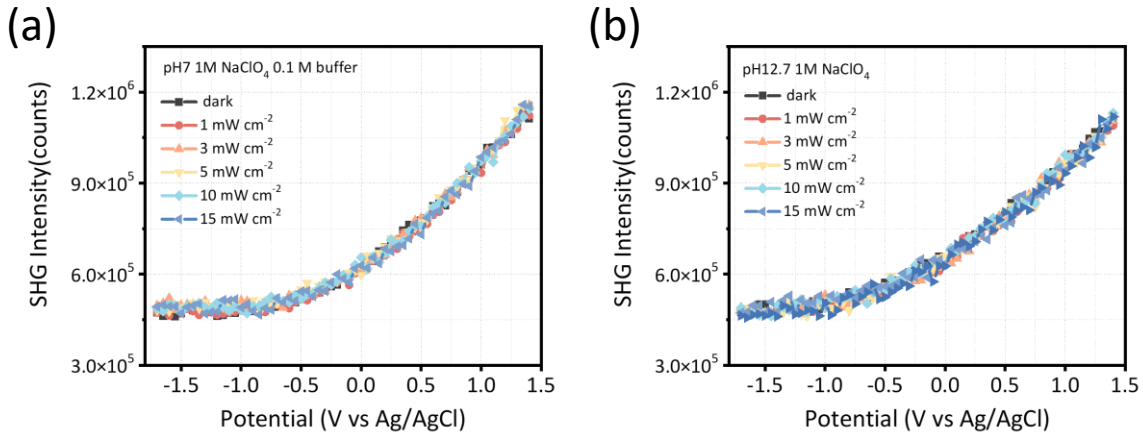

Figure 4.5. Bias-dependence EFISH measured in (a) pH 7 with 0.1 M phosphate buffer, and (b) pH 12.7 buffered; All experiments are conducted under no stirring conditions as surface pH is stabilized by buffer solution.

4.3.5 Nature of surface charge and rate-determining step

From previous experiments, we summarize the light-induced Fermi-level pinning effect in 1M $NaClO_4$ solution using the band diagram as illustrated in Figure 4.6. Band bending and energy of vacuum level are drawn at 1 V vs Ag/AgCl in the dark (black) and under light illumination (red). The electrostatic potential drop across the junction $\Delta\Phi_{tot}$ is manifested by the vacuum energy difference between the bulk semiconductor and bulk solution, divided by the unit charge. In the dark condition, most potential drops in the semiconductor side due to the small capacitance of SCR compared to the electrolyte double layer, with $\Delta\Phi_{tot} \approx \Delta\Phi_{sc,d}$, $\Delta\Phi_{liq,d} \approx 0$. Under light illumination, photogenerated holes ($Q_{ss\text{-}h^+}$) accumulate at the surface states, giving rise to a new capacitive component in parallel to the semiconductor SCR capacitor and increasing the capacitance of the solid. Consequently, the negative charge concentration in the solution double layer increases to achieve total charge neutrality. The potential drop in the double layer increases as the potential drop in SCR decreases following Equation 4.6.

$$\Delta V_{bi} = \Delta\Phi_{sc,d} - \Delta\Phi_{sc,l} = \Delta\Phi_{liq,l} - \Delta\Phi_{liq,d} = \Delta V_H \quad 4.6$$

In Equation 4.6, ΔV_H is the potential change in the electrolyte double layer, which is related to the surface accumulated holes *via* Equation 4.3. As a result of potential redistribution, the semiconductor band edge positively shifted. Without efficient solution mass transport and pH buffer, protons ($Q_{ss\text{-}proton}$) will also accumulate at the surface when the solution is under slow mass transport. These surface protons in the inner Helmholtz layer (including adsorbed and protons in double layer) will further contribute to the positive charge accumulation at TiO_2/electrolyte junction, resulting in larger ΔV_{bi} and band edge movement (Figure A4.4).

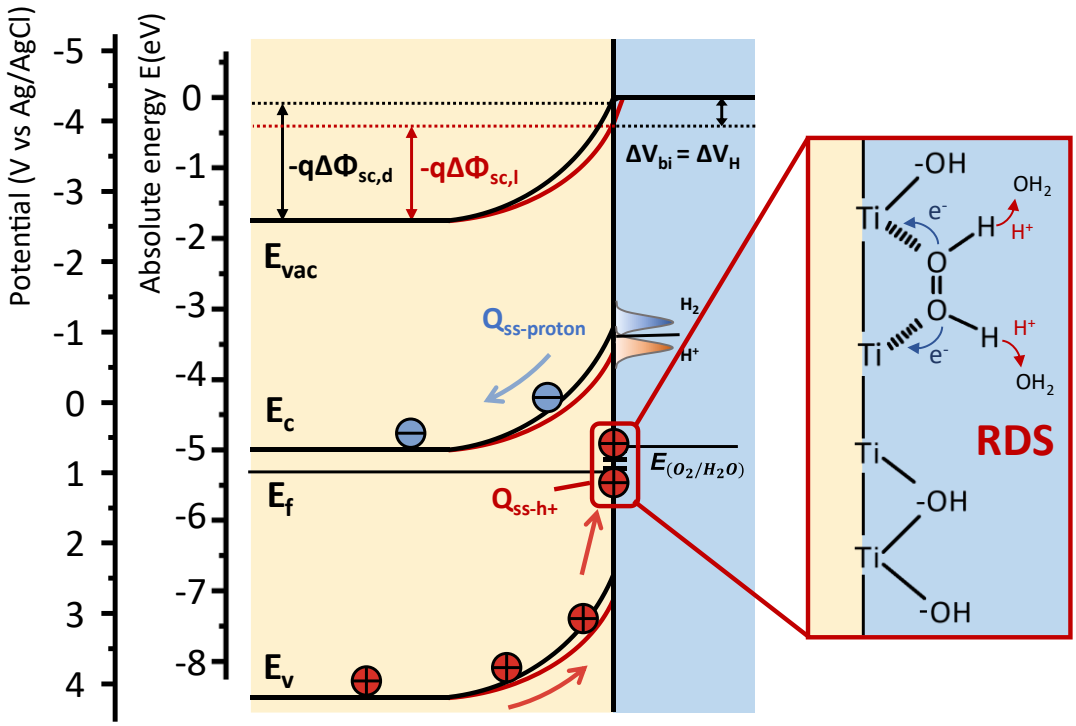

Figure 4.6. Energy diagram of rutile TiO_2 (100) immersed in pH 7 1 M $NaClO_4$ aqueous solution with applied potential at 1 V vs Ag/AgCl in the dark (black) and under illumination (red) with electron energy presented in the absolute energy scale vs vacuum level, and potential in the electrochemical scale, with respect to Ag/AgCl. E_c, E_f, E_c stands for the energy of the conduction

band, Fermi-level, and valance band level of TiO_2, E_{vac} stands for the energy of local vacuum level, ΔV_H and ΔV_{bi} stands for the change of potential drop in solution and in semiconductor, respectively. The insert panel illustrates the proposed PCET rate-determining species during OER.

As demonstrated by previous kinetic isotope experiments, PCET is found to be the rate-determining step of water oxidation in pH 7 unbuffered solution. To further assign the chemical nature of the most possible build-up intermediate species, water oxidation mechanisms need to be discussed. Among various models, mainly two types of mechanisms are widely used for water oxidation on TiO_2. As proposed by Salvador et al and others, [28, 88, 89, 97-99] water oxidation on TiO_2 occurs through the redox photooxidation (RP) mechanism. The photogenerated holes are trapped at the two-fold coordinated bridging oxygen atom, leading to the breaking of Ti-O bond and the generation of one-fold coordinated hydroxyl radical Ti-OH·. Two adjacent Ti-OH· forms bridging hydrogen peroxide. Further oxidation of surface hydrogen peroxide by two holes leads to the evolution of an oxygen molecule and the release of two protons. Finally, water molecules absorbed on hydroxyl vacancies, regenerating the bridging hydroxyl ions. Different from the RP mechanism, Nakato et al and others [100-102] proposed that the nucleophilic attack (NA) mechanism takes place on TiO_2. Water molecules act as a Lewis base, attacking the initial surface-trapped hole and forming hydroxyl radicals. A further hole traps on the surface and also forms a surface oxygen peroxide attached to two adjacent Ti-terminated sites. Following oxidation involves a sequential nucleophilic attack of surface-bound hydrogen peroxide by water, releasing oxygen and protons, and regenerating the Ti-O bridging sites. Interestingly, despite different mechanisms, generation of surface-bound hydrogen peroxide species is proposed, confirmed by observation of O-O stretching mode via *in situ* MIRIR spectroscopy. [100] For both pathways, the PCET elementary step is proposed for further oxidation of surface -Ti-O-O-Ti- species, which agrees with our observation

of PCET rate determining species for water oxidation on (100) TiO_2. Control experiments conducted in 5% H_2O_2 (1.47 M) in 1 M $NaClO_4$ aqueous solution (Figure A4.7b) showed that more surface charges are built up in H_2O_2 solution, verifying that accumulated surface hound chemisorbed HO_2^- species will also contribute to ΔV_{bi}.[103] Supported by our experimental evidence and previous mechanistic study, we thus postulate the chemical nature of the surface accumulated holes to be the surface-bound hydron peroxide species in pH 7 unbuffered solution as shown in the inset of Figure 4.6. Assignment of detailed OER mechanism, however, is beyond the scope of current study. In pH 12.7 basic solution, although no surface hole built-up is found due to the presence of the negatively charged binding group, it is believed that the rate-determining step also involves PCET process as a KIE of ~ 1.05 is observed as shown in Figure A4.6b. However, in pH 7 solution containing phosphate buffer, the mechanism of rate determining step is changed as a KIE of 1 is observed. This agrees with previous mechanistic study on phosphate modified photoelectrodes,[41, 93] where it is argued that photogenerated holes can be captured and stabilized by surface binding phosphate group.

With H_2O_2 proposed as a primary reaction intermediate, it is natural to consider the reaction that happened through localized mid-gap states rather than from the valance band. Compared to bulk oxygen coordination in TiO_2, oxygen at the TiO_2 surface, no matter bridging or terminal, shows 2-fold coordination rather than 3-fold. This results in a decreased Ti-O bond energy and gives rise to higher energy compared to the oxygen 2p orbitals that consist of the TiO_2 valance band.[97] With reaction intermediates forming at certain surface reaction sites, the potential of surface holes should be more negative than the valance band position in Ag/AgCl scale. EFISH control experiments are also carried out using formic acid as a hole collector to verify this mechanism as shown in Figure A4.7c. Power dependence ΔV_{bi} are collected in 0.1 M formic acid

with 1 M $NaClO_4$ as a supporting electrolyte, showing smaller ΔV_{bi}, i.e., less hole accumulation, compared to no formic acid condition. As studied previously by Salvador et al, photooxidation of formic acid by TiO_2 is mainly a result of direct hole transfer from the valance band rather than surface states. [104, 105] Consequently, oxidation of formic acid should exhibit fewer surface hole build-ups as they are not localized at the surface. Our observation is in agreement with the above conclusion and supports the previous argument that water oxidation on TiO_2 follows indirect hole transfer via localized mid-gap surface states. [89, 106-109]

However, concerns may be raised due to the insufficient surface state energy (ca. 0.5 V for V_{ss1} and 0.9 V vs RHE for V_{ss2} at 10 mW/cm^2 for example) extracted from impedance measurement compared to formal water oxidation potential (1.23 V vs RHE). This is because the observed trap states position obtained from impedance measurement is determined not only by the trap states hole/electron capture/emission rate with semiconductor conduction band/valance band, but also by hole/electron transfer rate from surface states to solution. [110] Surface state potential revealed by the quasi-Fermi level of electrons ($E_{F, n}$), i.e., applied potential, can deviate from its real formal potential due to the complicated charge transfer dynamics at semiconductor/electrolyte junction. A more accurate energy level of surface intermedia species can be provided by electroluminescence studies, with an energy level of 1.47 eV below the conduction band edge on TiO_2. [88, 108, 109] This provides evidence of enough driving force for intermediate oxidation.

4.3.6 Impact of ΔV_{bi} to Incident Photon to Current Efficiency

Finally, we discuss how surface hole accumulation and band edge unpinning may affect the water oxidation efficiency, which is usually evaluated by the incident photon to current efficiency (IPCE) of the electrode under 360 nm monochromic illumination. Figure A4.8 compares the saturation photocurrent, measured at 1.6 V vs RHE in different electrolytes as a function of the

illumination power, where photocurrent linearly increases with power density. IPCE can be extracted from the slope of the plot as shown in Equation A4.3. IPCE measured in different solutions is calculated to be around 19% -21%, where in pH 7 unbuffered, pH 7 phosphate buffer, and pH 12.7 NaOH buffer solution, IPCE is calculated to be 20.9%, 19.8%, 20.0%, respectively. The slightly higher IPCE in pH 7 unbuffered solution compared to the buffered solution can be attributed to a larger potential drop in Helmholtz layer ΔV_H, giving rise to a larger driving force for OER reaction. Surprisingly, in a hole scavenger solution Na_2SO_3, which provides a unity hole collection efficiency, the maximum IPCE is calculated to be 20.7%, similar to the IPCE with no hole scavenger. This means that surface recombination is minimized in the photocurrent plateau region, where sufficient band bending is applied. This also means that the main IPCE loss comes from the bulk recombination due to the long penetration depth of 360 nm photon. The results also suggest that compared to the increased ΔV_H, photon flux (light intensity) plays a major role in determining IPCE. This is mainly because TiO_2 surfaces have enough reaction sites to store surface intermediates albeit suffering from sluggish water oxidation kinetics, making photon flux rather than catalytic site turnover frequency the main determining factor for photocurrent. [111] Similar to previous studies on hematite photoanode[27], we also conclude that the recombination in the field-free region is the main efficient loss pathway in photoanode. However, contrary to the conclusion that Fermi-level pinning will strongly positively shift the onset potential, our study found no onset potential loss with and without Fermi-level pinning (Figure A4.4a). In fact, we observed similar photocurrent onset and flatband potential differences under different light intensity as shown in Table A4.2, indicating the free energy can be maintained even if the band edge is unpinned. We attribute this difference conclusion mainly to the excess hole energetics at TiO_2 valence band edge

(2.9 V vs RHE) and at surface states, allowing it to achieve photocurrent saturation at ca. 0.8 V vs RHE.

4.4. Conclusion

In summary, we conducted EFISH and impedance analysis on a benchmark material, (100) n-TiO_2 electrode to investigate the light-induced Fermi-level pinning effect during the water oxidation process in 1 M $NaClO_4$ electrolyte. *Operando* EFISH experiment measures the screening of built-in potential in TiO_2 depletion region ΔV_{bi} under UV illumination as a function of applied potential and UV light illumination power density. The trend of ΔV_{bi} as a function of illumination power density agrees well with the flat-band potential shift measured by the Mott-Schottky measurement. We demonstrate that under efficient mass transport conditions, the contribution of ΔV_{bi} is attributed to hole accumulation at TiO_2 surface states. Kinetic isotope experiments provide information on the chemical nature of surface accumulated holes, where The PCET step is found to be the rate-determining elementary step with an apparent KIE of 1.08 in pH7 electrolyte, calculated from photocurrent ratio. Built-in potential in TiO_2 can be well maintained in other well-buffered electrolytes, which is due to the neutralization effect of the surface-bound negative charge. We found that photocurrent onset is not affected by the light-induced Fermi-level pinning effect. IPCE under 360 nm monochromatic illumination can be slightly enhanced by the increased potential drop in the double layer, but the main loss occurs from bulk recombination due to the small hole diffusion length and long penetration depth. From this benchmark study, we demonstrated that EFISH can be a universal, *in situ/operando* technique to investigate the surface charge accumulation effect in different photoelectrodes and shed light on the chemical nature of rate-determining species.

Appendix Chapter 4

Appendix A4.1. EFISH and ΔV_{bi} acquired under negative and positive scan directions.

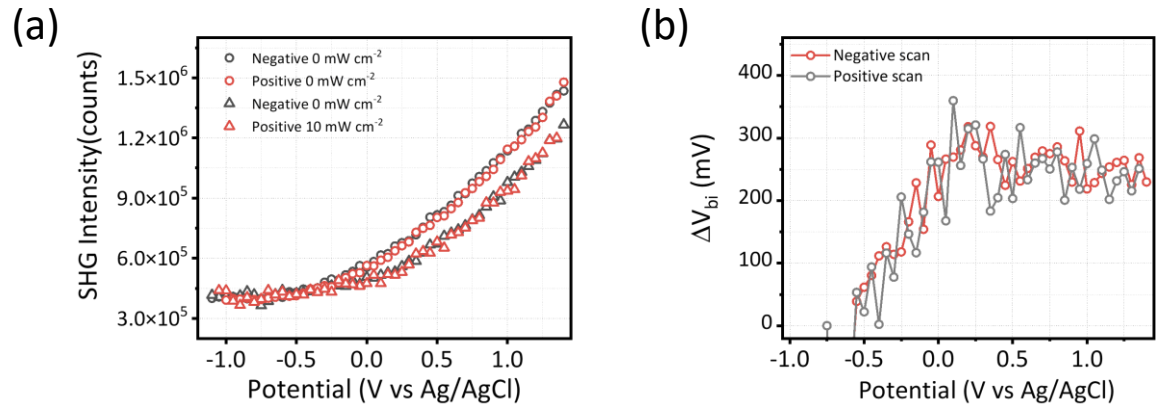

Figure A4.1. (a) TiO_2 EFISH intensity as a function of applied potential under 0 (open circle) and 10 (open triangle) mW/cm^2 360 nm illumination at negative (grey) and positive (red) potential scan direction. (b) ΔV_{bi} as a function of applied potential under 10 mW/cm^2 illumination under negative (grey) and positive (red) potential scan direction.

Appendix A4.2. Equivalent circuit of semiconductor/electrolyte junction and Gauss fitting of surface state capacitance.

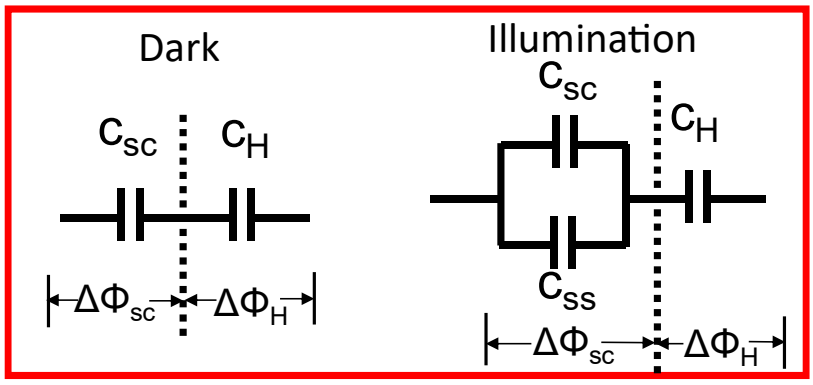

Figure A4.2. Simplified equivalent circuit of semiconductor/electrolyte with and without illumination, only showing the capacitance component.

Under dark condition and at semiconductor depletion region, the capacitance of semiconductor (C_{sc}) and electrolyte double layer (C_H) are in series, the total capacitance can be written as Equation A4.1:

$$C_{tot} = \frac{C_{sc}C_H}{C_{sc}+C_H} = C_{sc}/(1+\frac{C_{sc}}{C_H}) \quad \text{A4.1}$$

As $C_H \gg C_{sc}$ under the electrolyte concentration used in our study, semiconductor capacitance dominates the overall capacitance response, i.e., $C_{tot} \approx C_{sc}$.

Table A4.1. Gauss fitting result of surface state capacitance C_{ss} response from Figure 4.3c.

Power density (mW/cm^2)	**0.5**	**1**	**3**	**5**	**10**
V_{ss1} (V vs AgAgCl)	-0.353 ± 0.020	-0.235 ± 0.019	-0.092 ± 0.008	-0.096 ± 0.010	-0.107 ± 0.005
σ_1 (V)	0.211 ± 0.009	0.247 ± 0.029	0.163 ± 0.026	0.209 ± 0.050	0.189 ± 0.022
N_{ss1} (10^{11}cm^{-2})	1.60 ± 0.23	2.90 ± 1.15	6.65 ± 3.70	13.60 ± 12.60	19.00 ± 7.80
V_{ss2} (V vs AgAgCl)	0.099 ± 0.008	0.012 ± 0.110	0.239 ± 0.158	0.293 ± 0.423	0.258 ± 0.164
σ_1 (V)	0.275 ± 0.055	0.509 ± 0.076	0.303 ± 0.090	0.396 ± 0.264	0.365 ± 0.098
N_{ss2} (10^{11}cm^{-2})	0.83 ± 0.30	3.55 ± 0.94	8.26 ± 0.46	14.10 ± 18.30	20.7 ± 10.6

Appendix A4.3. Effect of local pH change on ΔV_{bi}

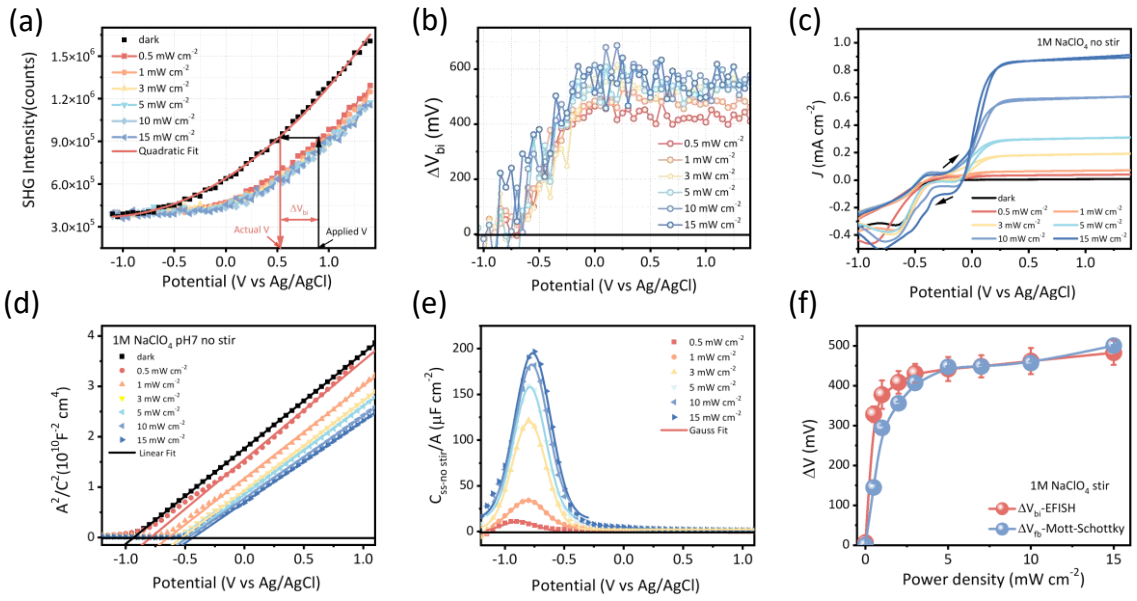

Figure A4.3. EFISH and impedance measurement of TiO_2/electrolyte junction under no solution stirring condition. (a) EFISH intensity, (b) ΔV_{bi}, (c) current densities, (d) Mott-Schottky plot, and (e) surface state capacitance C_{ss} as a function of applied potential under different illumination power densities. (f) Effect of screened potential measured by Mott-Schottky (blue) and by EFISH (red, extracted at 1 V vs Ag/AgCl) as a function of illumination power density. 1 M $NaClO_4$ is used as electrolyte.

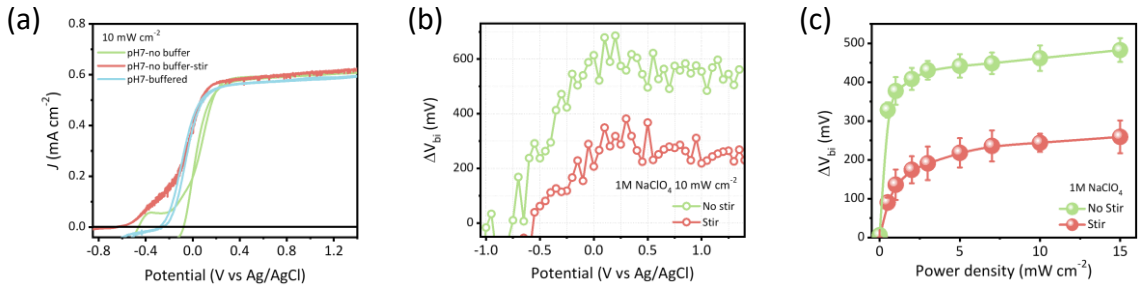

Figure A4.4. (a) J-V plot measured in pH 7 1 M $NaClO_4$ solution with (red) and without (green) stirring conditions, and in 0.1 M pH 7 sodium phosphate buffer without stirring (blue) under 10 mW/cm^2 illumination. (b) ΔV_{bi} plot as a function of applied potential with (red) and without (green)

stirring under 10 mW/cm^2 illumination. (c) ΔV_{bi} (collected at 1V vs Ag/AgCl) plotted as a function of illumination intensity with (red) and without (green) stirring.

In the analysis of results presented in Figures 4.2 and 4.3, we have assumed negligible contribution of the accumulation of positively charged surface adsorbate, i.e., surface proton, to the observed potential screening ΔV_{bi} under the measurement conditions with rigorous stirring (i.e., fast mass transport). The effect of surface protonation can be examined by conducting EFISH and electrochemical measurements under conditions of no stirring (slow mass transport). As shown in Figure A4.3 and A4.4, ΔV_{bi} – V plot measured under no stirring conditions shows a similar trend but with an earlier onset potential at ca. -0.75 V and larger saturation value under the same illumination power density. This indicate that additional species contribute to ΔV_{bi} under these conditions compared to rigorous stirring. Considering the possible ionic species in our electrolyte (Na^+, ClO_4^-, H^+ and OH^-), only protons can be the positively charged surface absorbates species that contribute to ΔV_{bi}.[22, 82, 112] Experimental evidence of surface proton accumulation under no stirring conditions can also be found in CV and impedance measurement. In cyclic voltammetry shown in Figure A4.3c, a pair of photo-induced 'redox peaks' can be resolved before the photocurrent onset region under illumination. Without illumination, only reductive features can be observed. A larger reduction current can be observed under light illumination. Correspondingly, a large $C_{ss\text{-}no\ stir}$ response appears in the potential range where CV reductive peak appears, at ca. -0.75 V vs Ag/AgCl (Figure A4.3e). These features can be explained by the following: the surface protons generated during OER conditions (anodic scan) are reduced by electrons at the energy level close to the conduction band during the CV negative scan. A further comparison of CV between stirring and non-stirring conditions under 10 mW/cm^2 (Figure A4.4a) shows that onset potential is more anodic without stirring compared to that under stirring condition and in pH 7

buffer solution. Based on the Nernst equation, the delayed onset means that surface pH under no buffer and non-stirring condition is more acidic than the pH in bulk solution due to the limited proton mass transport, consistent with previous reports using ring-disk electrodes. [28, 98] When the solution is stirred, photocurrent shows a similar onset compared to the buffer solution. Moreover, both the large C_{ss} response centered at ca. -0.75 V and CV 'redox feature' disappeared when stirring. This provides convincing evidence that the accelerated mass transport between bulk solution and electrode surface can minimize surface proton and dissolved oxygen accumulation. ΔV_{bi} measured under stirring conditions can be regarded as a result of only surface hole accumulation during the sluggish water oxidation process.

Appendix A4.4. Effect of electrolyte on ΔV_{bi} and photocurrent and KIE values

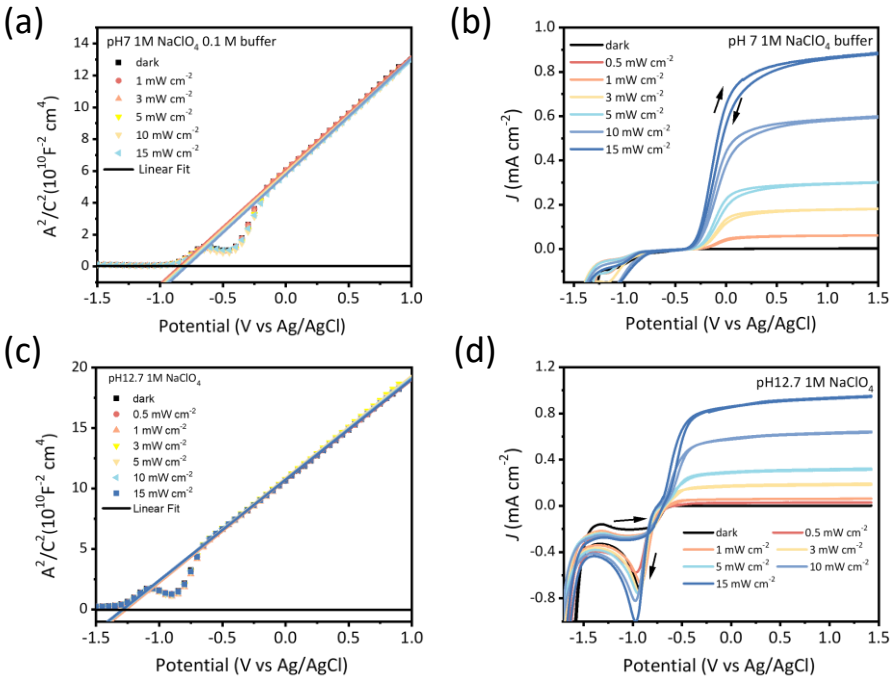

Figure A4.5. Mott-Schottky plot in (b) pH 7 with 0.1 M phosphate buffer, and (e) pH 12.7 buffered; J-V curve in (c) pH 7 with 0.1 M phosphate buffer, and (f) pH 12.7 under different illumination

power densities. All experiments are conducted under no stirring conditions as surface pH is stabilized by buffer solution.

Conversions between Ag/AgCl reference electrode (filled with 1M KCl) and reversible hydrogen electrode (RHE) are made following Equation A4.1:

$$E_{RHE} = 0.222 + E_{Ag/AgCl} + 0.059 * pH \quad \text{A4.2}$$

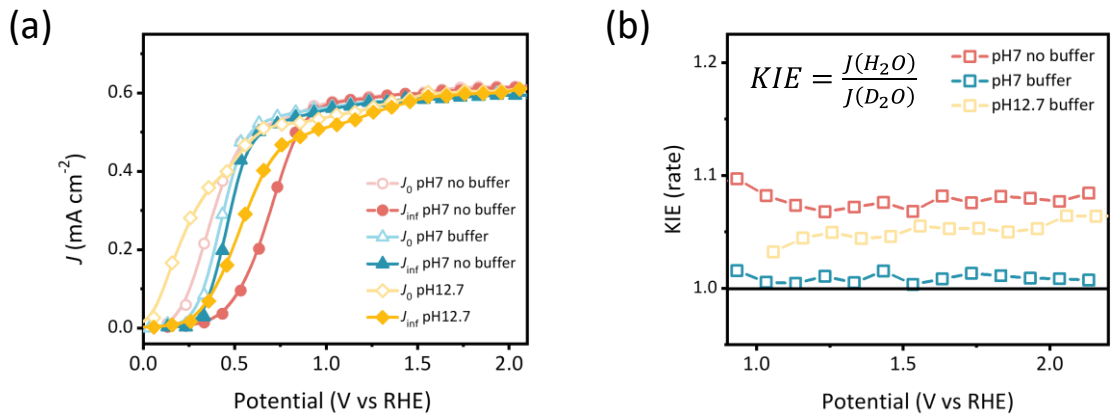

Figure A4.6. (a) Steady (solid symbol) and transient (open symbol) photocurrent density as a function of applied potential measured in pH 7 unbuffered (red), pH 7 buffered (blue), and pH 12.7 buffered (yellow) solution extracted from light on-off amperometric measurement. (b) KIE values in pH 7 unbuffered (red), pH 7 buffered (blue), and pH 12.7 buffered (yellow) solution as a function of applied potential. All experiments are performed under stirring conditions.

Appendix A4.5. Effect of other solution adsorbate on ΔV_{bi}

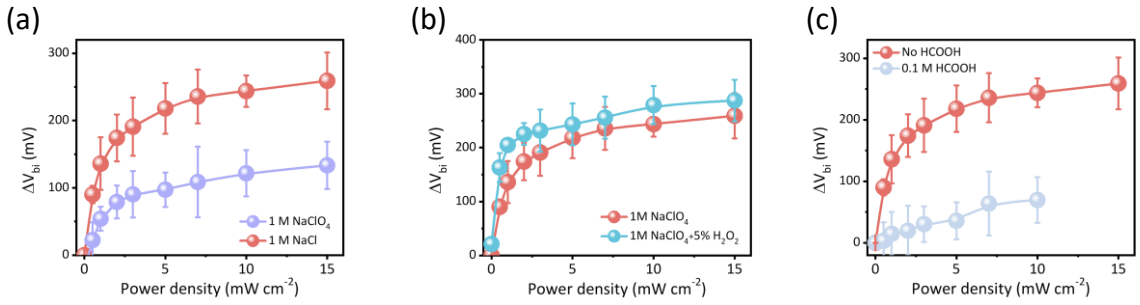

Figure A4.7. Power dependent ΔV_{bi} comparison collected between (a) 1 M $NaClO_4$ (red) and 1 M NaCl (purple), (b) 1 M $NaClO_4$ and 1M $NaClO_4$ containing 5% H_2O_2 (blue) electrolyte, and (c) 1 M $NaClO_4$ and 1 M $NaClO_4$ containing 0.1 M HCOOH (light blue). ΔV_{bi} is measured at 1V vs Ag/AgCl applied potential under stirring conditions.

Appendix A4.6. Separation between flatband (V_{fb}) and photocurrent onset (V_{onset}) potential and calculation of IPCE

Table A4.2. Summary of flatband potential and photocurrent onset as a function of light illumination in 1M $NaClO_4$ electrolyte, stirring condition, where flatband potential is extracted from Figure 4.3b, onset potential is defined by the potential cross point between the tangent of photocurrent at current inflection region and the extrapolation of the exchange current baseline. [80]

Power density (mW/cm^2)	V_{fb} (V vs Ag/AgCl)	V_{onset} (V vs Ag/AgCl)	$V_{onset-fb}$ (V)
0	-0.93	-	-
0.5	-0.80	-0.47	0.33
1	-0.78	-0.45	0.33
3	-0.71	-0.47	0.24
5	-0.68	-0.37	0.31
10	-0.64	-0.27	0.37

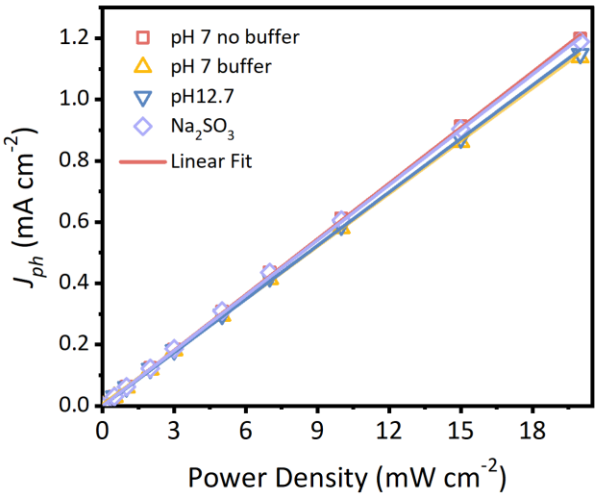

Figure A4.8. Photocurrent comparison in different electrolytes under 1.6 V vs RHE. IPCE can be calculated from the slope of the fitting following Equation A4.2.

IPCE can be calculated using the following equation[78],

$$\text{IPCE} = \frac{J_{ph} \times 1239.8}{P_{mono} \times \lambda} \times 100\% \qquad \text{A4.3}$$

where J_{ph} (mA cm^{-2}) is the photocurrent density; P_{mono} (mW cm^{-2}) is the power density of monochromatic incident light; λ (nm) is the wavelength of monochromatic light; and 1239.8 (V nm) is a coefficient from the multiplication of speed of light, reciprocal of unit charge and Planck's constant. The IPCE calculated for pH 7 (unbuffered), pH 7 (0.1 M phosphate buffer), pH 12.7, and 0.33 M Na_2SO_3 are 20.9%, 19.8%, 20.0%, and 20.7%, respectively.

4.5. References

1. Cowan, A. J.; Durrant, J. R. Long-lived charge separated states in nanostructured semiconductor photoelectrodes for the production of solar fuels. *Chem. Soc. Rev.* **2013**, *42* (6), 2281-2293

2. Peter, L. M.; Wijayantha, K. G. U.; Tahir, A. A. Kinetics of light-driven oxygen evolution at α-Fe_2O_3 electrodes. *Faraday Discuss.* **2012**, *155*, 309-322.

3. Abrantes, L. M.; Peter, L. M. Transient photocurrents at passive iron electrodes. *Journal of Electroanalytical Chemistry and Interfacial Electrochemistry* **1983**, *150* (1-2), 593-601.

4. Ye, K.-H.; Wang, Z.; Gu, J.; Xiao, S.; Yuan, Y.; Zhu, Y.; Zhang, Y.; Mai, W.; Yang, S. Carbon quantum dots as a visible light sensitizer to significantly increase the solar water splitting performance of bismuth vanadate photoanodes. *Energy & Environmental Science* **2017**, *10* (3), 772-779.

5. Kim, T. W.; Choi, K.-S. Nanoporous $BiVO_4$ Photoanodes with Dual-Layer Oxygen Evolution Catalysts for Solar Water Splitting. *Science* **2014**, *343* (6174), 990-994.

6. Klotz, D.; Grave, D. A.; Rothschild, A. Accurate determination of the charge transfer efficiency of photoanodes for solar water splitting. *Physical Chemistry Chemical Physics* **2017**, *19* (31), 20383-20392.

7. Xu, Z.; Hou, B.; Zhao, F.; Suo, S.; Liu, Y.; Shi, H.; Cai, Z.; Hill, C. L.; Musaev, D. G.; Mecklenburg, M.; et al. Direct *In Situ* Measurement of Quantum Efficiencies of Charge Separation and Proton Reduction at TiO_2-Protected GaP Photocathodes. *J. Am. Chem. Soc.* **2023**, *145* (5), 2860-2869.

8. Xie, S.; Su, H.; Wei, W.; Li, M.; Tong, Y.; Mao, Z. Remarkable photoelectrochemical performance of carbon dots sensitized TiO_2 under visible light irradiation. *J. Mater. Chem. A* **2014**, *2* (39), 16365-16368.

9. Shen, S.; Kronawitter, C. X.; Wheeler, D. A.; Guo, P.; Lindley, S. A.; Jiang, J.; Zhang, J. Z.; Guo, L.; Mao, S. S. Physical and photoelectrochemical characterization of Ti-doped hematite photoanodes prepared by solution growth. *Journal of Materials Chemistry A* **2013**, *1* (46), 14498.

10. Shen, S.; Guo, P.; Wheeler, D. A.; Jiang, J.; Lindley, S. A.; Kronawitter, C. X.; Zhang, J. Z.; Guo, L.; Mao, S. S. Physical and photoelectrochemical properties of Zr-doped hematite nanorod arrays. *Nanoscale* **2013**, *5* (20), 9867.

11. Ling, Y.; Wang, G.; Wheeler, D. A.; Zhang, J. Z.; Li, Y. Sn-Doped Hematite Nanostructures for Photoelectrochemical Water Splitting. *Nano Letters* **2011**, *11* (5), 2119-2125.

12. Kay, A.; Cesar, I.; Grätzel, M. New Benchmark for Water Photooxidation by Nanostructured α-Fe_2O_3 Films. *Journal of the American Chemical Society* **2006**, *128* (49), 15714-15721.

13. Selim, S.; Francàs, L.; García-Tecedor, M.; Corby, S.; Blackman, C.; Gimenez, S.; Durrant, J. R.; Kafizas, A. WO_3/$BiVO_4$: impact of charge separation at the timescale of water oxidation. *Chemical Science* **2019**, *10* (9), 2643-2652, 10.1039/C8SC04679D.

14. Hermans, Y.; Murcia-López, S.; Klein, A.; van de Krol, R.; Andreu, T.; Morante, J. R.; Toupance, T.; Jaegermann, W. Analysis of the interfacial characteristics of $BiVO_4$/metal oxide

heterostructures and its implication on their junction properties. *Physical Chemistry Chemical Physics* **2019**, *21* (9), 5086-5096, 10.1039/C8CP07483F.

15. Xu, Z.; Hou, B.; Zhao, F.; Cai, Z.; Shi, H.; Liu, Y.; Hill, C. L.; Musaev, D. G.; Mecklenburg, M.; Cronin, S. B.; Lian, T. Nanoscale TiO_2 Protection Layer Enhances the Built-In Field and Charge Separation Performance of GaP Photoelectrodes. *Nano Lett.* **2021**, *21* (19), 8017-8024.

16. Moss, B.; Hegner, F. S.; Corby, S.; Selim, S.; Francàs, L.; López, N.; Giménez, S.; Galán-Mascarós, J.-R.; Durrant, J. R. Unraveling Charge Transfer in CoFe Prussian Blue Modified BiVO4 Photoanodes. *ACS Energy Letters* **2019**, *4* (1), 337-342.

17. Liu, G.; Eichhorn, J.; Jiang, C.-M.; Scott, M. C.; Hess, L. H.; Gregoire, J. M.; Haber, J. A.; Sharp, I. D.; Toma, F. M. Interface engineering for light-driven water oxidation: unravelling the passivating and catalytic mechanism in $BiVO_4$ overlayers. *Sustainable Energy & Fuels* **2019**, *3* (1), 127-135.

18. Zhang, S.; Shangguan, P.; Tong, S.; Zhang, Z.; Leng, W. Enhanced Photoelectrochemical Oxidation of Water over Ti-Doped α-Fe_2O_3 Electrodes by Surface Electrodeposition InOOH. *The Journal of Physical Chemistry C* **2019**, *123* (40), 24352-24361.

19. de Respinis, M.; Joya, K. S.; De Groot, H. J. M.; D'Souza, F.; Smith, W. A.; van de Krol, R.; Dam, B. Solar Water Splitting Combining a $BiVO_4$ Light Absorber with a Ru-Based Molecular Cocatalyst. *J. Phys. Chem. C* **2015**, *119* (13), 7275-7281.

20. Peter, L. Kinetics and mechanisms of light-driven reactions at semiconductor electrodes: Principles and techniques. *Photoelectrochemical Water Splitting: Materials, Processes and Architectures* **2013**, *9*.

21. Lantz, J. M.; Corn, R. M. Electrostatic field measurements and band flattening during electron-transfer processes at single-crystal TiO_2 electrodes by electric field-induced optical second harmonic generation. *The Journal of Physical Chemistry* **1994**, *98* (18), 4899-4905.

22. Memming, R. Solid–Liquid Interface. In *Semiconductor Electrochemistry*, 2015; pp 89-125.

23. van den Meerakker, J. E. A. M.; Kelly, J. J.; Notten, P. H. L. The Minority Carrier Recombination Resistance: A Useful Concept in Semiconductor Electrochemistry. *Journal of The Electrochemical Society* **1985**, *132* (3), 638-642.

24. Van Den Meerakker, J. E. A. M. The reduction of iodine at GaAs: the role of potential-redistribution at the semi-conductor/electrolyte interface. *Electrochimica Acta* **1985**, *30* (4), 435-440.

25. Lincot, D.; Vedel, J. Recombination and charge transfer at the illuminated n-CdTe/electrolyte interface: Simplified kinetic model. *Journal of Electroanalytical Chemistry and Interfacial Electrochemistry* **1987**, *220* (2), 179-200.

26. Leng, W. H.; Zhang, Z.; Zhang, J. Q.; Cao, C. N. Investigation of the Kinetics of a TiO_2 Photoelectrocatalytic Reaction Involving Charge Transfer and Recombination through Surface States by Electrochemical Impedance Spectroscopy. *The Journal of Physical Chemistry B* **2005**, *109* (31), 15008-15023.

27. Upul Wijayantha, K. G.; Saremi-Yarahmadi, S.; Peter, L. M. Kinetics of oxygen evolution at α-Fe_2O_3 photoanodes: a study by photoelectrochemical impedance spectroscopy. *Physical Chemistry Chemical Physics* **2011**, *13* (12), 5264.
28. Tafalla, D.; Pujadas, M.; Salvador, P. Direct measurements of flat-band potential shifts under illumination of the semiconductor-electrolyte interface by electrolyte electroreflectance. *Surface Science* **1989**, *215* (1), 190-200.
29. Kelly, J. J.; Memming, R. The Influence of Surface Recombination and Trapping on the Cathodic Photocurrent at p-Type III-V Electrodes. *Journal of The Electrochemical Society* **1982**, *129* (4), 730-738.
30. Meissner, D.; Memming, R.; Kastening, B. Photoelectrochemistry of cadmium sulfide. 1. Reanalysis of photocorrosion and flat-band potential. *The Journal of Physical Chemistry* **1988**, *92* (12), 3476-3483.
31. Meissner, D.; Lauermann, I.; Memming, R.; Kastening, B. Photoelectrochemistry of cadmium sulfide. 2. Influence of surface-state charging. *The Journal of Physical Chemistry* **1988**, *92* (12), 3484-3488.
32. Chandrasekaran, K.; Bockris, J. O. M. Determination of concentration of surface states at the illuminated semiconductor—electrolyte interface. *Electrochimica Acta* **1987**, *32* (9), 1393-1402.
33. Zhang, S.; Leng, W. Questioning the rate law in the analysis of water oxidation catalysis on haematite photoanodes. *Nature Chemistry* **2020**, *12* (12), 1097-1098.
34. Kühne, H. M.; Schefold, J. Tafel Plots from Illuminated Photoelectrodes: A New Insight Into Charge Transfer Mechanism. *J. Electrochem. Soc.* **1990**, *137* (2), 568-575.
35. Ma, Y.; Kafizas, A.; Pendlebury, S. R.; Le Formal, F.; Durrant, J. R. Photoinduced Absorption Spectroscopy of CoPi on $BiVO_4$: The Function of CoPi during Water Oxidation. *Adv. Funct. Mater.* **2016**, *26* (27), 4951-4960.
36. Ma, Y.; Le Formal, F.; Kafizas, A.; Pendlebury, S. R.; Durrant, J. R. Efficient suppression of back electron/hole recombination in cobalt phosphate surface-modified undoped bismuth vanadate photoanodes. *J. Mater. Chem. A* **2015**, *3* (41), 20649-20657,
37. Cummings, C. Y.; Marken, F.; Peter, L. M.; Tahir, A. A.; Wijayantha, K. G. U. Kinetics and mechanism of light-driven oxygen evolution at thin film α-Fe_2O_3 electrodes. *Chemical Communications* **2012**, *48* (14), 2027.
38. Barroso, M.; Cowan, A. J.; Pendlebury, S. R.; Grätzel, M.; Klug, D. R.; Durrant, J. R. The Role of Cobalt Phosphate in Enhancing the Photocatalytic Activity of α-Fe_2O_3 toward Water Oxidation. *J. Am. Chem. Soc.* **2011**, *133* (38), 14868-14871.
39. Klahr, B.; Gimenez, S.; Fabregat-Santiago, F.; Bisquert, J.; Hamann, T. W. Photoelectrochemical and Impedance Spectroscopic Investigation of Water Oxidation with "Co–Pi"-Coated Hematite Electrodes. *J. Am. Chem. Soc.* **2012**, *134* (40), 16693-16700.
40. Abdi, F. F.; van de Krol, R. Nature and Light Dependence of Bulk Recombination in Co-Pi-Catalyzed $BiVO_4$ Photoanodes. *J. Phys. Chem. C* **2012**, *116* (17), 9398-9404.

41. Zhong, D. K.; Choi, S.; Gamelin, D. R. Near-Complete Suppression of Surface Recombination in Solar Photoelectrolysis by “Co-Pi” Catalyst-Modified W:$BiVO_4$. *J. Am. Chem. Soc.* **2011**, *133* (45), 18370-18377.
42. Zhong, D. K.; Cornuz, M.; Sivula, K.; Grätzel, M.; Gamelin, D. R. Photo-assisted electrodeposition of cobalt–phosphate (Co–Pi) catalyst on hematite photoanodes for solar water oxidation. *Energy & Environmental Science* **2011**, *4* (5), 1759.
43. Zhong, D. K.; Gamelin, D. R. Photoelectrochemical Water Oxidation by Cobalt Catalyst (“Co−Pi”)/α-Fe_2O_3 Composite Photoanodes: Oxygen Evolution and Resolution of a Kinetic Bottleneck. *J. Am. Chem. Soc.* **2010**, *132* (12), 4202-4207.
44. Nellist, M. R.; Laskowski, F. A. L.; Qiu, J.; Hajibabaei, H.; Sivula, K.; Hamann, T. W.; Boettcher, S. W. Potential-sensing electrochemical atomic force microscopy for in operando analysis of water-splitting catalysts and interfaces. *Nat. Energy* **2018**, *3* (1), 46-52.
45. Nellist, M. R.; Qiu, J.; Laskowski, F. A. L.; Toma, F. M.; Boettcher, S. W. Potential-Sensing Electrochemical AFM Shows CoPi as a Hole Collector and Oxygen Evolution Catalyst on $BiVO_4$ Water-Splitting Photoanodes. *ACS Energy Lett.* **2018**, *3* (9), 2286-2291.
46. Jiang, T.; Li, Y.; Yan, S.; Zou, Z. Silicon photoanodes partially covered by Ni@Fe core-shell particles with in situ formed gradient-enhanced junction electric field for photoelectrochemical water oxidation. *Appl. Phys. Lett.* **2019**, *115* (21), 213904.
47. Abdi, F. F.; Firet, N.; van de Krol, R. Efficient $BiVO_4$ Thin Film Photoanodes Modified with Cobalt Phosphate Catalyst and W-doping. *ChemCatChem* **2013**, *5* (2), 490-496.
48. Liu, T.; Li, W.; Wang, D. Z.; Luo, T.; Fei, M.; Shin, D.; Waegele, M. M.; Wang, D. Low Catalyst Loading Enhances Charge Accumulation for Photoelectrochemical Water Splitting. *Angew. Chem. Int. Ed.* **2023**.
49. Lauinger, S. M.; Piercy, B. D.; Li, W.; Yin, Q.; Collins-Wildman, D. L.; Glass, E. N.; Losego, M. D.; Wang, D.; Geletii, Y. V.; Hill, C. L. Stabilization of Polyoxometalate Water Oxidation Catalysts on Hematite by Atomic Layer Deposition. *ACS Applied Materials & Interfaces* **2017**, *9* (40), 35048-35056.
50. Thorne, J. E.; Jang, J.-W.; Liu, E. Y.; Wang, D. Understanding the origin of photoelectrode performance enhancement by probing surface kinetics. *Chemical Science* **2016**, *7* (5), 3347-3354.
51. Liu, Y.; Zhang, M.; Wang, Z.; He, J.; Zhang, J.; Ye, S.; Wang, X.; Li, D.; Yin, H.; Zhu, Q.; et al. Bipolar charge collecting structure enables overall water splitting on ferroelectric photocatalysts. *Nat. Commun.* **2022**, *13* (1).
52. Chen, R.; Ren, Z.; Liang, Y.; Zhang, G.; Dittrich, T.; Liu, R.; Liu, Y.; Zhao, Y.; Pang, S.; An, H.; et al. Spatiotemporal imaging of charge transfer in photocatalyst particles. *Nature* **2022**, *610* (7931), 296-301.
53. Chen, R.; Pang, S.; An, H.; Zhu, J.; Ye, S.; Gao, Y.; Fan, F.; Li, C. Charge separation via asymmetric illumination in photocatalytic Cu_2O particles. *Nat. Energy* **2018**, *3* (8), 655-663.
54. Chen, R.; Fan, F.; Dittrich, T.; Li, C. Imaging photogenerated charge carriers on surfaces and interfaces of photocatalysts with surface photovoltage microscopy. *Chem. Soc. Rev.* **2018**, *47* (22), 8238-8262,

55. Lin, F.; Boettcher, S. W. Adaptive semiconductor/electrocatalyst junctions in water-splitting photoanodes. *Nat. Mater.* **2014**, *13* (1), 81-86.
56. Nellist, M. R.; Laskowski, F. A. L.; Lin, F.; Mills, T. J.; Boettcher, S. W. Semiconductor–Electrocatalyst Interfaces: Theory, Experiment, and Applications in Photoelectrochemical Water Splitting. *Acc. Chem. Res.* **2016**, *49* (4), 733-740.
57. Qiu, J.; Hajibabaei, H.; Nellist, M. R.; Laskowski, F. A. L.; Hamann, T. W.; Boettcher, S. W. Direct in Situ Measurement of Charge Transfer Processes During Photoelectrochemical Water Oxidation on Catalyzed Hematite. *ACS Central Science* **2017**, *3* (9), 1015-1025.
58. Forrest, A.; Qiu, J.; Nellist, M. R.; Oener, S. Z.; Gordon, A. M.; Boettcher, S. W. Transient photocurrents on catalyst-modified n-Si photoelectrodes: insight from dual-working electrode photoelectrochemistry. *Sustainable Energy & Fuels* **2018**, *2* (9), 1995-2005.
59. Chen, R.; Zhang, D.; Wang, Z.; Li, D.; Zhang, L.; Wang, X.; Fan, F.; Li, C. Linking the Photoinduced Surface Potential Difference to Interfacial Charge Transfer in Photoelectrocatalytic Water Oxidation. *J. Am. Chem. Soc.* **2023**.
60. Clark, M. L.; Ge, A.; Videla, P. E.; Rudshteyn, B.; Miller, C. J.; Song, J.; Batista, V. S.; Lian, T.; Kubiak, C. P. CO_2 Reduction Catalysts on Gold Electrode Surfaces Influenced by Large Electric Fields. *J. Am. Chem. Soc.* **2018**, *140* (50), 17643-17655.
61. Bhattacharyya, D.; Videla, P. E.; Palasz, J. M.; Tangen, I.; Meng, J.; Kubiak, C. P.; Batista, V. S.; Lian, T. Sub-Nanometer Mapping of the Interfacial Electric Field Profile Using a Vibrational Stark Shift Ruler. *J. Am. Chem. Soc.* **2022**, *144* (31), 14330-14338.
62. Lake, W. R.; Meng, J.; Dawlaty, J. M.; Lian, T.; Hammes-Schiffer, S. Electro-inductive Effect Dominates Vibrational Frequency Shifts of Conjugated Probes on Gold Electrodes. *J. Am. Chem. Soc.* **2023**, *145* (41), 22548-22554.
63. Suo, S.; Sheehan, C.; Zhao, F.; Xiao, L.; Xu, Z.; Meng, J.; Mallouk, T. E.; Lian, T. Direct Vibrational Stark Shift Probe of Quasi-Fermi Level Alignment in Metal Nanoparticle Catalyst-Based Metal–Insulator–Semiconductor Junction Photoelectrodes. *J. Am. Chem. Soc.* **2023**.
64. Hara, K.; Dan-Oh, Y.; Kasada, C.; Ohga, Y.; Shinpo, A.; Suga, S.; Sayama, K.; Arakawa, H. Effect of Additives on the Photovoltaic Performance of Coumarin-Dye-Sensitized Nanocrystalline TiO_2 Solar Cells. *Langmuir* **2004**, *20* (10), 4205-4210.
65. Wang, P.; Zakeeruddin, S. M.; Humphry-Baker, R.; Moser, J. E.; Grätzel, M. Molecular-Scale Interface Engineering of TiO_2 Nanocrystals: Improve the Efficiency and Stability of Dye-Sensitized Solar Cells. *Adv. Mater.* **2003**, *15* (24), 2101-2104.
66. McGuigan, S.; Tereniak, S. J.; Donley, C. L.; Smith, A.; Jeon, S.; Zhao, F.; Sampaio, R. N.; Pauly, M.; Keller, L.; Collins, L.; et al. Discovery of a Hybrid System for Photocatalytic CO_2 Reduction via Attachment of a Molecular Cobalt-Quaterpyridine Complex to a Crystalline Carbon Nitride. *ACS Applied Energy Materials* **2023**, *6* (20), 10542-10553.
67. Wang, W.; Lüpke, G.; Ventra, M. D.; Pantelides, S. T.; Gilligan, J. M.; Tolk, N. H.; Kizilyalli, I. C.; Roy, P. K.; Margaritondo, G.; Lucovsky, G. Coupled Electron-Hole Dynamics at the Si/SiO2. *Physical Review Letters* **1998**, *81* (19), 4224-4227.

68. Bloch, J.; Mihaychuk, J. G.; Van Driel, H. M. Electron Photoinjection from Silicon to Ultrathin SiO_2 Films via Ambient Oxygen. *Physical Review Letters* **1996**, *77* (5), 920-923.

69. Mihaychuk, J. G.; Bloch, J.; Liu, Y.; van Driel, H. M. Time-dependent second-harmonic generation from the Si–SiO_2 interface induced by charge transfer. *Opt. Lett.* **1995**, *20* (20), 2063-2065.

70. Lantz, J. M.; Baba, R.; Corn, R. M. Optical second harmonic generation as a probe of electrostatic fields and flatband potential at single-crystal titania electrodes. *J. Phys. Chem.* **1993**, *97* (29), 7392-7395.

71. Guyot‐Sionnest, P.; Tadjeddine, A. Study of Ag (111) and Au (111) Electrodes by Optical Second‐Harmonic Generation. *J. Chem. Phys.* **1990**, *92* (1), 734-738.

72. Xu, P.; Von Rueden, A. D.; Schimmenti, R.; Mavrikakis, M.; Suntivich, J. Optical method for quantifying the potential of zero charge at the platinum–water electrochemical interface. *Nat. Mater.* **2023**, *22* (4), 503-510.

73. Xu, P.; Huang, A.; Suntivich, J. Phase-Sensitive Second-Harmonic Generation of Electrochemical Interfaces. *J. Phys. Chem. Lett.* **2020**, *11* (19), 8216-8221.

74. Bian, H.-t.; Guo, Y.; Wang, H.-f. Non-parabolic potential dependence of optical second harmonic generation from the Si(111) electrode/electrolyte interface. *Phys. Chem. Chem. Phys.* **2018**, *20* (46), 29539-29548

75. Lantz, J. M.; Corn, R. M. Time-resolved optical second harmonic generation measurements of picosecond band flattening processes at single crystal TiO2 electrodes. *J. Phys. Chem.* **1994**, *98* (38), 9387-9390.

76. Bard, A. J.; Bocarsly, A. B.; Fan, F. R. F.; Walton, E. G.; Wrighton, M. S. The concept of Fermi level pinning at semiconductor/liquid junctions. Consequences for energy conversion efficiency and selection of useful solution redox couples in solar devices. *J. Am. Chem. Soc.* **1980**, *102* (11), 3671-3677.

77. De Gryse, R. On the Interpretation of Mott-Schottky Plots Determined at Semiconductor/Electrolyte Systems. *Journal of The Electrochemical Society* **1975**, *122* (5), 711.

78. Ma, Y.; Pendlebury, S. R.; Reynal, A.; Le Formal, F.; Durrant, J. R. Dynamics of photogenerated holes in undoped $BiVO_4$ photoanodes for solar water oxidation. *Chemical Science* **2014**, *5* (8), 2964-2973.

79. Le Formal, F.; Pendlebury, S. R.; Cornuz, M.; Tilley, S. D.; Grätzel, M.; Durrant, J. R. Back Electron–Hole Recombination in Hematite Photoanodes for Water Splitting. *J. Am. Chem. Soc.* **2014**, *136* (6), 2564-2574.

80. Le Formal, F.; Sivula, K.; Grätzel, M. The Transient Photocurrent and Photovoltage Behavior of a Hematite Photoanode under Working Conditions and the Influence of Surface Treatments. *J. Phys. Chem. C* **2012**, *116* (51), 26707-26720.

81. Kennedy, J. H.; Frese, K. W. Flatband Potentials and Donor Densities of Polycrystalline α - Fe_2O_3 Determined from Mott‐Schottky Plots. *Journal of The Electrochemical Society* **1978**, *125* (5), 723-726.

82. Tomkiewicz, M. The Potential Distribution at the TiO_2 Aqueous Electrolyte Interface. *Journal of The Electrochemical Society* **1979**, *126* (9), 1505-1510.
83. Cooper, G.; Turner, J. A.; Nozik, A. J. Mott-Schottky Plots and Flatband Potentials for Single Crystal Rutile Electrodes. *Journal of The Electrochemical Society* **1982**, *129* (9), 1973-1977.
84. Pu, P.; Cachet, H.; Sutter, E. M. M. Electrochemical impedance spectroscopy to study photo - induced effects on self-organized TiO_2 nanotube arrays. *Electrochimica Acta* **2010**, *55* (20), 5938-5946.
85. Kobayashi, H.; Mizuno, F.; Nakato, Y. Improvement in Hydrogen Photoevolution Efficiency for Platinum-Deposited Indium Phosphide Electrodes by the Removal of Surface States. *Japanese Journal of Applied Physics* **1994**, *33* (Part 1, No. 10), 6065-6070.
86. Dare-Edwards, M. P.; Hamnett, A.; Trevellick, P. R. Alternating-current techniques in semiconductor electrochemistry. *Journal of the Chemical Society, Faraday Transactions 1: Physical Chemistry in Condensed Phases* **1983**, *79* (9), 2111.
87. Tomkiewicz, M. The Nature of Surface States on Chemically Modified TiO2 Electrodes. *Journal of The Electrochemical Society* **1980**, *127* (7), 1518-1525.
88. Kong, D.-S.; Wei, Y.-J.; Li, X.-X.; Zhang, Y.; Feng, Y.-Y.; Li, W.-J. pH Dependent Behavior and Effects of Photoinduced Surface States during Water Photooxidation at TiO_2/Solution Interface: Studied by Capacitance Measurements. *J. Electrochem. Soc.* **2014**, *161* (3), H144-H153.
89. Salvador, P. Kinetic approach to the photocurrent transients in water photoelectrolysis at n-titanium dioxide electrodes. 1. Analysis of the ratio of the instantaneous to steady-state photocurrent. *The Journal of Physical Chemistry* **1985**, *89* (18), 3863-3869.
90. Lu, Y.; Jaeckel, B.; Parkinson, B. A. Preparation and Characterization of Terraced Surfaces of Low-Index Faces of Anatase, Rutile, and Brookite. *Langmuir* **2006**, *22* (10), 4472-4475.
91. Zhang, Y.; Zhang, H.; Ji, H.; Ma, W.; Chen, C.; Zhao, J. Pivotal Role and Regulation of Proton Transfer in Water Oxidation on Hematite Photoanodes. *J. Am. Chem. Soc.* **2016**, *138* (8), 2705-2711.
92. Zhang, X.; Cui, H.; Humayun, M.; Qu, Y.; Fan, N.; Sun, X.; Jing, L. Exceptional performance of photoelectrochemical water oxidation of single-crystal rutile TiO_2 nanorods dependent on the hole trapping of modified chloride. *Scientific Reports* **2016**, *6* (1), 21430.
93. Jing, L.; Zhou, J.; Durrant, J. R.; Tang, J.; Liu, D.; Fu, H. Dynamics of photogenerated charges in the phosphate modified TiO_2 and the enhanced activity for photoelectrochemical water splitting. *Energy Environ. Sci.* **2012**, *5* (4), 6552-6558.
94. Piscopo, A.; Robert, D.; Weber, J. V. Influence of pH and chloride anion on the photocatalytic degradation of organic compounds: Part I. Effect on the benzamide and para-hydroxybenzoic acid in TiO_2 aqueous solution. *Applied Catalysis B: Environmental* **2001**, *35* (2), 117-124.
95. Wang, K.-H.; Hsieh, Y.-H.; Wu, C.-H.; Chang, C.-Y. The pH and anion effects on the heterogeneous photocatalytic degradation of o-methylbenzoic acid in TiO_2 aqueous suspension. *Chemosphere* **2000**, *40* (4), 389-394.

96. Chen, H. Y.; Zahraa, O.; Bouchy, M. Inhibition of the adsorption and photocatalytic degradation of an organic contaminant in an aqueous suspension of TiO_2 by inorganic ions. *Journal of Photochemistry and Photobiology A: Chemistry* **1997**, *108* (1), 37-44.
97. Salvador, P. Mechanisms of water photooxidation at n-TiO_2 rutile single crystal oriented electrodes under UV illumination in competition with photocorrosion. *Progress in Surface Science* **2011**, *86* (1-2), 41-58.
98. Tafalla, D.; Salvador, P. Analysis of the photocurrent transient behaviour associated with flatband potential shifts during water splitting at n-TiO_2 electrodes. *Journal of Electroanalytical Chemistry and Interfacial Electrochemistry* **1989**, *270* (1), 285-295.
99. Salvador, P. Subbandgap photoresponse of n-TiO_2 electrodes: Transient photocurrent-time behaviour. *Surface Science* **1987**, *192* (1), 36-46.
100. Nakamura, R.; Nakato, Y. Primary Intermediates of Oxygen Photoevolution Reaction on TiO2 (Rutile) Particles, Revealed by in Situ FTIR Absorption and Photoluminescence Measurements. *Journal of the American Chemical Society* **2004**, *126* (4), 1290-1298.
101. Valdés, Á.; Qu, Z. W.; Kroes, G. J.; Rossmeisl, J.; Nørskov, J. K. Oxidation and Photo-Oxidation of Water on TiO2 Surface. *J. Phys. Chem. C* **2008**, *112* (26), 9872-9879.
102. Kafizas, A.; Ma, Y.; Pastor, E.; Pendlebury, S. R.; Mesa, C.; Francàs, L.; Le Formal, F.; Noor, N.; Ling, M.; Sotelo-Vazquez, C.; et al. Water Oxidation Kinetics of Accumulated Holes on the Surface of a TiO2 Photoanode: A Rate Law Analysis. *ACS Catal.* **2017**, *7* (7), 4896-4903.
103. Ferrer, I. J.; Muraki, H.; Salvador, P. Detection of surface states associated with adsorbed hydrogen peroxide on titanium dioxide by impedance and electrolyte electroreflectance measurements. *J. Phys. Chem.* **1986**, *90* (13), 2805-2807.
104. Mora-Seró, I.; Villarreal, T. L.; Bisquert, J.; Pitarch, Á.; Gómez, R.; Salvador, P. Photoelectrochemical Behavior of Nanostructured TiO_2 Thin-Film Electrodes in Contact with Aqueous Electrolytes Containing Dissolved Pollutants: A Model for Distinguishing between Direct and Indirect Interfacial Hole Transfer from Photocurrent. *J. Phys. Chem. B* **2005**, *109* (8), 3371-3380.
105. Villarreal, T. L.; Gómez, R.; Neumann-Spallart, M.; Alonso-Vante, N.; Salvador, P. Semiconductor Photooxidation of Pollutants Dissolved in Water: A Kinetic Model for Distinguishing between Direct and Indirect Interfacial Hole Transfer. I. Photoelectrochemical Experiments with Polycrystalline Anatase Electrodes under Current Doubling an. *J. Phys. Chem. B* **2004**, *108* (39), 15172-15181.
106. Salvador, P.; Gutierrez, C. The nature of surface states involved in the photo- and electroluminescence spectra of n-titanium dioxide electrodes. *J. Phys. Chem.* **1984**, *88* (16), 3696-3698.
107. Salvador, P.; Decker, F. The generation of hydrogen peroxide during water photoelectrolysis at n-titanium dioxide. *J. Phys. Chem.* **1984**, *88* (25), 6116-6120.
108. Nakato, Y.; Tsumura, A.; Tsubomura, H. Photo- and electroluminescence spectra from an n-titanium dioxide semiconductor electrode as related to the intermediates of the photooxidation reaction of water. *J. Phys. Chem.* **1983**, *87* (13), 2402-2405.

109. Wilson, R. H. Observation and Analysis of Surface States on TiO_2 Electrodes in Aqueous Electrolytes. *J. Electrochem. Soc.* **1980**, *127* (1), 228-234.
110. Iqbal, A.; Hossain, M. S.; Bevan, K. H. The role of relative rate constants in determining surface state phenomena at semiconductor–liquid interfaces. *Phys. Chem. Chem. Phys.* **2016**, *18* (42), 29466-29477
111. Wadsworth, B. L.; Beiler, A. M.; Khusnutdinova, D.; Reyes Cruz, E. A.; Moore, G. F. Interplay between Light Flux, Quantum Efficiency, and Turnover Frequency in Molecular-Modified Photoelectrosynthetic Assemblies. *J. Am. Chem. Soc.* **2019**, *141* (40), 15932-15941.
112. Morrison, S. R. *Electrochemistry at semiconductor and oxidized metal electrodes*. **1980**.

5 The Charge Transfer Mechanism on a Cobalt-Polyoxometalate-TiO_2 Photoanode for Water Oxidation in Acid

5.1. Introduction

Solar energy is the most attractive renewable replacement for fossil fuels because it is plentiful, inexhaustible, and widely distributed. However, due to the diffuse and intermittent nature of solar irradiation, energy harvested from the sun must be efficiently converted into chemical fuels that are storable, transportable, and usable upon demand. This requirement has motivated the development of sustainable artificial photosynthetic processes, with the aim of mimicking natural photosynthesis to generate fuels from water and carbon dioxide utilizing solar energy. Therefore, a significant effort has been directed towards increasing the performance of solar fuel-generating devices in recent years.[1-5] The oxygen evolution reaction (OER) is thus of great importance because it is the critical (photo)anode reaction for (photo)electrochemical production of solar fuels including H_2 from water and hydrocarbons from CO_2.[6-8] The multielectron transfer OER process involves multiple reaction intermediates, and a high overpotential is needed to overcome the sluggish kinetics. Among the different water splitting devices, the acidic proton exchange membrane (PEM) water electrolyzer offers benefits such as high current density and high-purity hydrogen output, but uses precious iridium and ruthenium oxides for the OER,[9] prompting the quest for more affordable catalysts. Yan et at. prepared iridium single-atoms (Ir-SAs) on ultrathin $NiCo_2O_4$ porous nanosheets, boosting OER activity and stability in acid.[10] Similarly, Wang et al. produced a nickel-stabilized RuO_2 catalyst in a PEM electrolysis cell with improved stability for OER in acidic media.[11] Efforts to replace iridium and ruthenium oxides include using MnO_x catalyst by Nocera and co-workers, which uses a “self-healing” process

for acid-compatible OER.[12] The catalyst regrows MnO_x films during catalysis, improving activity after potential cycling.[13]

Cobalt-based heterogeneous electrocatalysts have proven more active than manganese, intensifying the focus on cobalt oxide. Schaak et al.'s Co_3O_4/FTO electrode maintained significant performance in 0.5 M H_2SO_4,[14] while Nocera's team created a $CoFePbO_x$ mixed metal oxide that exhibited enhanced stability in acidic media.[15] Galan-Mascaros et al. synthesized a carbon-coated Co_3O_4@C catalyst, providing stable oxygen formation in 1 M H_2SO_4 solution for more than 40 h.[16] Liu et al. reported a nanofibrous La and Mn co-doped cobalt spinel catalyst which exhibited a low overpotential and sustained OER activity over an extended period (>360 h) in acidic electrolyte. A PEM electrolyzer using this catalyst exhibited impressive current densities and low degradation.[17] Meanwhile, Co-doped MoS_2[18] and a $MoS_2/Co_9S_8/Ni_3S_2$/Ni composite[19] were explored, though they underperformed RuO_2.[18]

A range of cobalt polyoxometalates (Co-POMs) are effective water oxidation catalysts (WOCs), and [20-31] and unlike metal oxides, they have a discrete structure that aid precise experimental and computational correlations. The first reported Co-POM, $[Co_4(H_2O)_2(PW_9O_{34})_2]^{10-}$ (Co_4POM), successfully served as a WOC using $Ru(bpy)_3^{3+}$ as the oxidant[20] and later using $Ru(bpy)_3^{2+}$ as a photosensitizer and $S_2O_8^{2-}$ as the sacrificial agent.[30] Unlike ruthenium POM WOCs that are effective and stable both in solution and when supported on a variety of electrodes, the Co-POMs generally decompose to Co^{2+} or CoO_x when immobilized under water oxidation conditions, although this decomposition is generally much slower than water oxidation and can be reversed under some conditions (Co-POMs can form from Co^{2+} and POM ligands).[22, 29] A lower onset potential for OER was achieved with a molybdenum-containing Co_4POM.[31] The barium salt of the Co-POM, $[Co_9(H_2O)_6(OH)_3(HPO_4)_2(PW_9O_{34})_3]^{16-}$ (**Co_9POM**)[25]

in a carbon paste anode was reported to be a more effective WOC than the consensus operationally optimal WOC, IrO_2.[23]

*Photo*electrochemical OER performance of semiconductor photoelectrodes can be significantly improved by many of the aforementioned WOCs, including photoelectrodes modified by MnO_x,[32] IrO_x,[33-36] $(NiFe)O_x$,[37-39] Fe(Ni)OOH,[40-41] Co-Pi,[42-49] and POMs.[50-52] These co-catalysts function to suppress electron-hole recombination by increasing the band bending[43-44, 49], and to collect photogenerated holes acting as OER active sites. [42, 48] The synergic effect of WOCs on heterogeneous photoelectrodes, however, remains under debate in general and requires additional mechanistic understanding. For POM WOCs, various studies reported their successful immobilization on semiconductors in different POM-semiconductor hybrid photocatalytic OER systems, including ALD coating[51] and electrostatic interaction.[50, 52-54] However, the interaction between POMs and semiconductor photo(electro)catalysts as well as how POMs function at the heterogeneous interface to enhance OER performance, are not well understood.

This study directly addresses the dynamics and specific mechanistic role of a molecular WOC, the polyoxometalate, $Na_8K_8[Co_9(H_2O)_6(OH)_3(HPO_4)_2(PW_9O_{34})_3]\cdot 49H_2O$ (**Co_9POM**), immobilized on photoanode surface (TiO_2) using several photoelectrochemical techniques, transient absorption spectroscopy in two different spectral regions and other experiments. The resulting TiO_2-APS-**Co_9POM** photoanode which is robust in acid and exhibits enhanced current densities compared to bare TiO_2 and other control TiO_2 modifications, serves as an effective platform to probe these mechanistically key points.

5.2. Material and Methods

5.2.1 Sample synthesis

Materials and solvents were purchased as ACS analytical or reagent grade and used as received. $Na_8K_8[Co_9(H_2O)_6(OH)_3(HPO_4)_2(PW_9O_{34})_3]\cdot 49H_2O$ (**Co_9POM**) was obtained following a method described in the literature.[55]

The preparation of TiO_2 and TiO_2 coated with **Co_9POM** photoelectrodes is based on our previous report with modifications.[56] The fluorine-doped tin oxide substrates, FTO (Pilkington TEC15, ~ 15 Ω/sq resistance), were cleaned by sonicating sequentially in deionized water, acetone, and ethanol for 20 min each time, followed by blowing dry with nitrogen gas. Before coating, the top area of substrate was covered by one layer of adhesive tape (40 μm thickness) to provide a noncoated area for electrical conductance for the final electrode. The bottom area (smaller than the top area) was also covered by one layer of adhesive tape for the following Doctor blade coating process. The 20 nm-sized TiO_2 paste (Dyesol, 90-T) was then applied in the center of the substrate and distributed with a glass rod sliding over the tape-covered substrates on the side. The substrates were sintered at 500 °C for 1 hour, yielding a ~10-20 μm thick nanostructured TiO_2 film. For TiO_2-APS sample, TiO_2 electrodes with noncoated area covered by Teflon tape were suspended in an anhydrous toluene mixture of 6% 3-aminopropyltrimethoxysilane (APS) for 6 hours at 70 °C. After the attachment of APS ligand, the resulting films were washed with toluene, acetone, and ethanol. The film is further soaked in DI water overnight to remove the excess APS ligand. For TiO_2-**Co_9POM** sample, the TiO_2-APS sample is soaked 1 mM aqueous solution of the **Co_9POM** overnight after taken out from toluene and washed with acetone and ethanol. The electrodes were rinsed with 5 mL of water three times and dried in air. Functionalization of $H_3PW_{12}O_{40}$ on TiO_2 shares the same procedure with making TiO_2-**Co_9POM**, the only difference is soaking TiO_2-APS

in 1mM $H_3PW_{12}O_{40}$ rather than 1mM of **Co_9POM** overnight. For all photoanode samples, the top area of the electrodes was connected with a conductive copper tape and sealed with Epoxy adhesive (Henkel Loctite Hysol 1C Epoxi).

Cobalt-phosphate water oxidation catalyst (Co-Pi)[57] modified TiO_2 photoelectrode is prepared according to the literature.[58-59] A three-electrode cell was used with TiO_2 working electrode, Ag/AgCl (1 M KCl) reference electrode, and Pt mesh counter electrode. 0.9 V vs. Ag/AgCl was applied in a solution of 0.5 mM cobalt nitrate in 0.1 M potassium phosphate buffer at pH 7. The amount of Co–Pi deposited was controlled by the deposition time, where we deposited Co-Pi for 300 s under 8 $\mu A/cm^2$ current density.

5.2.2 Generation Characterization Methods

The purity of the **Co_9POM** was confirmed by the Fourier transform infrared (FT-IR) (Figure A5.1a) and the water content was determined by thermogravimetric analysis (TGA) (Figure A5.1b). Infrared spectra (2% sample in KBr pellet) were recorded on a Nicolet TM 6700 Fourier transform infrared (FT-IR) spectrometer. X-ray photoelectron spectroscopy (XPS) was conducted on a thermos K-ALPHA XPS instrument. The TGA data were collected on a Mettler Toledo TGA instrument. Diffuse reflectance spectroscopy was measured on a Cary 5000 UV-Vis/NIR instrument. Gas chromatography (GC) analysis of the gas phase was analyzed using an Agilent 7890 gas chromatograph with a 5 Å molecular sieve column, a thermal conductivity detector, and argon as carrier gas. The FOXY Forspor probe experiments are carried out using a NeoFox Phase Measurement system (Ocean Insight, Orlando, USA) equipped with FOSPOR-R oxygen sensor (1000-micron fiber). The Raman spectroscopy is measured in a home-built Raman setup as described in previous literature.[60] ICP is collected by Thermo Fisher iCAP ICP-MS (Inductively Coupled Plasma - Mass Spectrometer) instrument.

5.2.3 Photoelectrochemical Characterizations

Cyclic voltammograms (CVs), linear sweep voltammograms (LSVs) and bulk electrolysis data were obtained using a BAS CV-50W electrochemical analyzer and conducted at room temperature (25 ± 2 °C) in a custom 50 mL quartz cell (C012-2, Gaoss Union) equipped with airtight adapters and purged with argon gas prior to use. Mott-Schottky and AC impedance measurements are performed with a CHI 660e electrochemical station in the same quartz cell.

In Mott-Schottky experiment, 500 Hz of 5 mV of AC voltage are used in superposition with the DC potential. In AC impedance measurement, potential is held at 1.23 V_{RHE} while scanning 5 mV AC voltage frequency from 100 kHz to 1 Hz.

CVs and LSVs were recorded in a standard three-electrode configuration with a glassy carbon working electrode (S = 0.07 cm^2) or **Co_9POM** coated FTO working electrode (S = 1.0 cm^2), a platinum wire counter electrode and a 3 M KCl Ag/AgCl (+0.210 V vs. RHE) reference electrode in a 0.1 M pH = 2 sulfate buffer solution as determined by an Orion pH meter (model 230A). In this work, all potentials measured against Ag/AgCl were then converted to the reversible hydrogen electrode (RHE) scale using: E (potential, versus RHE) = E (versus Ag/AgCl) + 0.210 V + 0.0591×pH. The scan rate used in voltametric experiments was 100 mV/s, positive scan direction is used in LSVs in this study. A 100 mW/cm^2 365 nm LED light was focused on the photoelectrode.

Bulk electrolysis was conducted in a 0.1 M pH = 2 sulfate buffer solution with the potential held at 0.73 V_{RHE} under 20 mW/cm^2 365 nm LED UV illumination. TiO_2-**Co_9POM** photoanode was used as a working electrode in bulk electrolysis in a H-cell (C012-1, Gaoss Union) with a Nafion 115 proton exchange membrane platinum wire counter electrode from working and reference chamber. The headspace during bulk electrolysis was then analyzed by GC as described in the method section. Number of electrons transferred during bulk electrolysis was calculated by

Faraday's law of electrolysis Q = nFN, where Q is the number of coulombs, F = 96485 C/mol is Faraday's constant, N is the moles of substrate electrolyzed and n is the stoichiometric number of electrons consumed (4 in the case of oxygen evolution reaction). In the GC measurements, when the data collection were complete, 1.7 C of charge passed through the system. Headspace gas (200 μL) is injected into the GC for analysis and repeated 4 times to reduce the error.

Incident photon-to-current efficiency (IPCE) of TiO_2 and TiO_2-**Co_9POM** are measured under chopped light illumination under 1.23 V_{RHE} applied potential and calculated using the following Equation A4.2:

$$\text{IPCE} = \frac{J_{ph} \times 1239.8}{P_{mono} \times \lambda} \times 100\% \qquad \text{A4.2}$$

where J_{ph} (mA/cm^2) is the photocurrent; P_{mono} (mW/cm^2) is the power density of monochromatic incident light; λ (nm) is the wavelength of monochromatic light; and 1239.8 (V nm) is a coefficient from the multiplication of speed of light, reciprocal of unit charge and Planck's constant.

5.3. Results and Discussion

5.3.1 Characterization of TiO_2 and TiO_2-Co_9POM photoelectrodes

Co_9POM and TiO_2 photoelectrodes with electrostatically immobilized **Co_9POM** (TiO_2-APS-Co_9POM or "TiO_2-**Co_9POM**" in this article for brevity) are synthesized and purified as described in the experimental section. After treating nanoporous TiO_2 films with the cationic silylating agent (APS), the anionic **Co_9POM** is absorbed onto the TiO_2 photoelectrode via strong electrostatic interaction. Repeated washings of the TiO_2-**Co_9POM** with organic solvents as well as water show no displacement of the POM into solution consistant with the very strong electrostatic binding of **Co_9POM** (16- charge) and the positively-charged terminal ammonium groups of the APS units as well as the robust covalent bonding of the silyl terminus of APS with the TiO_2 surface oxygens. Several techniques indicate that intact **Co_9POM** is successfully

immobilized on the TiO_2 surface. First, Raman spectroscopy indicates the attachment of **Co_9POM** on TiO_2 as shown in Figure 5.1b. The TiO_2 displays four characteristic peaks (black diamonds) of the of anatase phase at 151, 390, 505 and 626 cm^{-1} corresponding to E_g, B_{1g}, A_{1g}, and E_g modes, respectively.[61-62] Second, the Fourier transform infrared (FT-IR) spectrum (Figure A5.1a) of **Co_9POM** has stretching peaks which are characteristic of Keggin-structure-derived polytungstates at 803 cm^{-1} ν(W-O_c-W, c = octahedral edge-sharing), 886 cm^{-1} ν(W-O_b-W, b = octahedral corner-sharing), 935 cm^{-1} ν(W-O_d, d = terminal), and 1029 cm^{-1} ν(P-O_a, a = tetrahedral). These peaks are consistent with previously reported **Co_9POM**.[63] The well-documented vibrational peaks of **Co_9POM** are also observed on Raman of TiO_2-**Co_9POM** (red stars, Figure 5.1b).[63] On TiO_2-**Co_9POM**, the characteristic peaks of both TiO_2 and **Co_9POM** are both clearly present, confirming successful surface immobilization of **Co_9POM** on TiO_2. Third, the diffuse reflectance spectra (Figure 5.1a) of TiO_2, TiO_2-APS, and TiO_2-APS-**Co_9POM** all show a band-edge absorption around 390 nm (3.2 eV). TiO_2 and TiO_2-APS have a similar and small absorption in the visible region, but TiO_2-APS-**Co_9POM** has a higher absorption due to the bound **Co_9POM**.

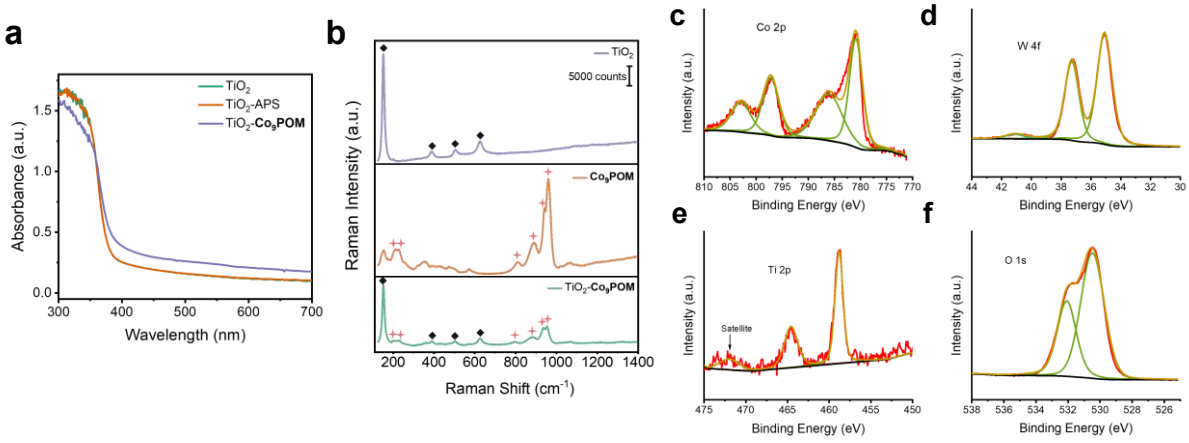

Figure 5.1. (a) Diffuse-reflectance of TiO_2, TiO_2-APS, and TiO_2-**Co_9POM** samples on sapphire substrates. (b) *ex-situ* Raman spectroscopy of TiO_2, solid **Co_9POM**, and TiO_2-**Co_9POM** on FTO

substrates, where diamonds and stars represent the characteristic Raman peaks of anatase TiO_2 and **Co_9POM**, respectively. (c-f) Co 2p, W 4f, Ti 2p, and O 1s are the X-ray photoelectron spectra of the as-prepared TiO_2-**Co_9POM** sample.

To further assess the incorporation of **Co_9POM** onto the TiO_2 photoelectrode, X-ray photoelectron spectroscopy (XPS) was conducted on the TiO_2 -**Co_9POM** film. Figure A5.2 and XPS spectra of TiO_2-**Co_9POM** clearly show the presence of TiO_2 (Ti 2p peak and O 1s peak), APS (C 1s peak, N 1s peak, and Si 2p peak), and **Co_9POM** (Co 2p peak, W 4f peak, and O 1s peak) (Figures 5.1c-f). The XPS spectrum of Ti 2p (Figure 5.1e) has significantly split spin-orbit components (Δ_{oxide} = 5.7 eV) with the Ti $2p_{3/2}$ peak and the Ti $2p_{1/2}$ peak locate at 458.5 eV and 464.2 eV, respectively. A broad satellite peak at 472 eV is consistent with the literature.[64] The signal-to-noise ratios of these Ti peaks are understandably low because the TiO_2 surface is covered by APS and **Co_9POM**. The XPS spectrum of W 4f (Figure 5.1d) shows the binding energies of 35.28 eV ($4f_{7/2}$) and 37.48 eV ($4f_{5/2}$), which are typical for W(VI) centers. The loss feature for W(VI) at 41 eV is also observed. Figure 5.1c displays the XPS spectrum of Co 2p with the binding energies of 780.7 eV ($2p_{3/2}$) and 797.1 eV ($2p_{1/2}$). Associated with these peaks are two observable satellite peaks at 786.4 eV and 803.0 eV. These features correspond to the Co(II) oxidation state and will be used for comparison in the following characterizations. The O 1s XPS spectrum in Figure 5.1f can be fitted with two peaks located at 530.5 eV and 532.2 eV, which are assigned to oxygen atoms in the chemical environment of W-O (POM) and Si-O (APS), respectively. ICP experiments quantify a Co loading of 7.7 μg per cm^2 of sample geometric area, corresponding to *ca.* 0.9 wt % of Co on TiO_2.

5.3.2 Photoelectrochemical Oxygen Evolution Reaction Performance of TiO_2-Co_9POM

Figure 5.2 shows the effect of **Co_9POM** and APS modification on TiO_2 photoelectrode as evaluated by a series of PEC characterizations in a pH 2 sulfate buffer acidic solution (details in the Experimental Section). Figure 5.2a shows that under the dark conditions, TiO_2, TiO_2-APS and TiO_2-**Co_9POM** electrodes exhibit negligible current when scanned to positive potentials, though there is an oxidation peak at around 0.0 V vs. RHE (all potential in this study are reference to reversible hydrogen electrode, unless otherwise mentioned) that can be attributed to the Ti(III)/Ti(IV) redox couple.[65] When the UV light is turned on, the photocurrent increases substantially and reaches a plateau at around 0.25 V for TiO_2, TiO_2-APS and TiO_2-**Co_9POM**. Photocurrents on TiO_2 and TiO_2-APS are nearly the same. In contrast, the saturated photocurrent of TiO_2-**Co_9POM** is nearly three times that of TiO_2 and TiO_2-APS. To explain the photocurrent enhancement mechanism, a series of photoelectrochemical studies were conducted. Figure 5.2b shows the open circuit measurement upon dark and light illumination. The open circuit potential (OCP) of TiO_2 and TiO_2-**Co_9POM** are similar under dark conditions at ~290 mV. Under UV illumination, however, the OCP of TiO_2-**Co_9POM** reaches a more negative value (-0.038 V) than that of TiO_2 (0.121 V). Moreover, OCP of TiO_2-**Co_9POM** shows a slower recovery to its dark equilibrium potential when the light is off compared to pure TiO_2. These phenomena can be attributed to the synergic effect of band edge modification and the charge transfer effect. The first effect can be confirmed by the *ca.* 100 mV more negative flat-band potential (U_{fb}) of TiO_2-**Co_9POM** (-0.16 V) compared to TiO_2 (-0.08 V) and TiO_2-APS (-0.06 V) extracted from Mott-Schottky analysis (Figure 5.2c). This is because highly charged **Co_9POM** modifies and decreases the band edge position and the flatband potential, giving rise to a larger interfacial electric field. This enables a faster electron-hole separation and a larger electron concentration build-up as

indicated by the OCP_{light}, under illumination. On the other hand, **Co_9POM** can extract and store photogenerated holes acting as an efficient WOC, which can also result in a higher electron concentration under light illumination. When illumination is off, the OCP on TiO_2-**Co_9POM** relaxes more slowly to the initial dark level OCP_{dark} compared to pure TiO_2. This observation is different from the previous OCP study on phosphorus-modified $BiVO_4$, where modified $BiVO_4$ exhibits a larger OCP photovoltage and a faster OCP_{ligh} relaxation when illumination is off.[66] This can be understood by the more energetically positive electron trap state position on TiO_2 compared to $BiVO_4$, which leads to more rapid electron concentration equilibrium on TiO_2. Upon surface modification with **Co_9POM**, however, POM states with energies close to the TiO_2 conduction band edge are introduced to the system. These states are likely related to the reduction/oxidation of tungsten (Figure A5.5a). These coupled states will act as shallow electron trap states and lead to slower attainment of OCP equilibrium when illumination is ceased.

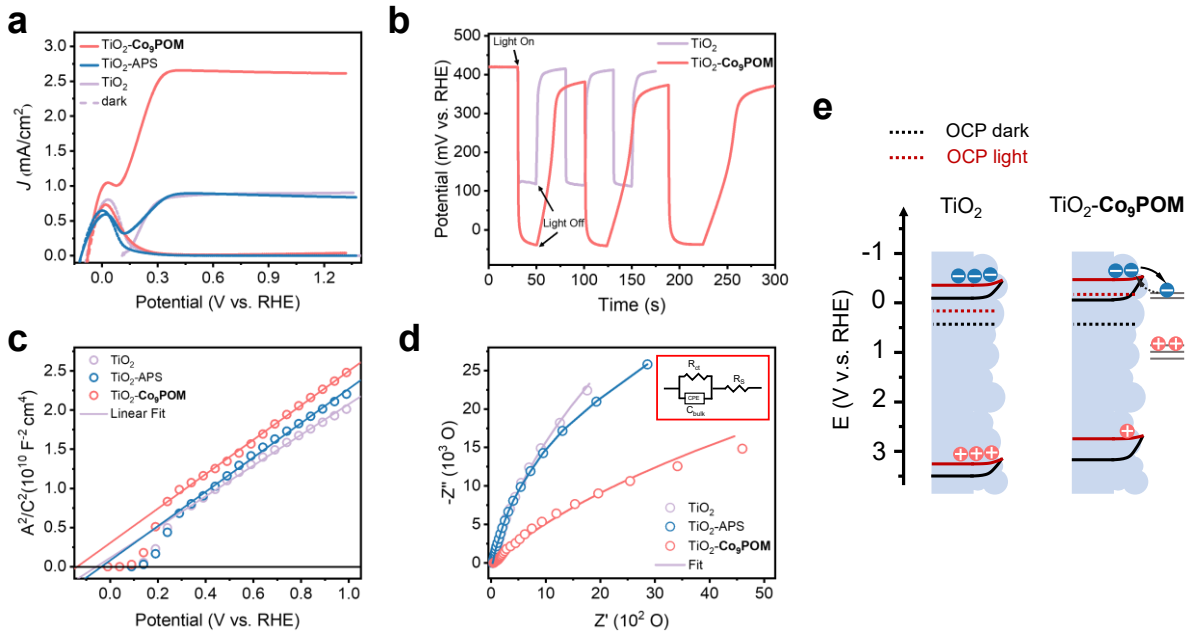

Figure 5.2. (a) J-V curve of TiO_2, TiO_2-APS, and TiO_2-**Co_9POM** in the dark (dash curve) and under 100 mW/cm^2 365 nm UV illumination (solid curve). (b) Open circuit potential (OCP) of

TiO_2 and TiO_2-**Co_9POM** under dark and 100 mW/cm2 365 nm UV illumination. (c) Mott-Schottky analysis of TiO_2, TiO_2-APS, and TiO_2-**Co_9POM** photoanode under dark conditions. (d) Nyquist plot for electrochemical impedance spectroscopy conducted on TiO_2 and TiO_2-**Co_9POM** at 1.23 V under 12.8 mW/cm^2 UV illumination. Inset shows the equivalent circuit to fit the plot. (e) Band structure schematic of TiO_2 and TiO_2-**Co_9POM** under illumination and dark OCP process. All experiments are performed under pH 2 sulfate buffer solution.

AC impedance measurements performed on TiO_2, TiO_2-APS, and TiO_2-**Co_9POM** further reveal the function of APS and the WOC, **Co_9POM**, under light illumination. As shown in Figure 5.2d and Table A5.1, TiO_2-**Co_9POM** exhibits a smaller trapping resistance and a larger capacitance compared to TiO_2 and TiO_2-APS. The decreased resistance can be attributed to accelerated hole transfer from TiO_2 to **Co_9POM** and from **Co_9POM** to water. Meanwhile, **Co_9POM** can store more photogenerated holes as a WOC, which explains the increased photoanode capacitance compared to TiO_2. The impedance of TiO_2 and TiO_2-APS samples, however, are very similar. These experiments along with the LSV performance and Mott-Schottky experiments, indicate that the APS ligands behave more as a spectator than as a passivation layer on TiO_2.

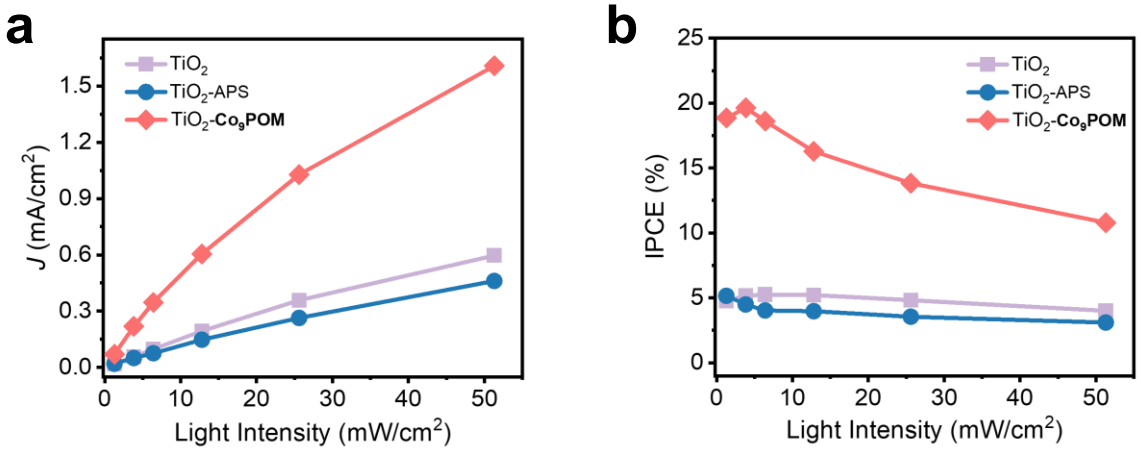

Figure 5.3. Excitation fluence-dependent (a) photocurrent and (b) incident photo-to-current efficiency (IPCE) of TiO_2, TiO_2-APS, and TiO_2-**Co_9POM** measured at 1.23 V_{RHE} under 365 nm UV illumination.

Figure 5.3a gives the excitation fluence-dependent photocurrent densities of TiO_2, TiO_2-APS, and TiO_2-**Co_9POM** photoanodes. The corresponding incident photon-to-current efficiencies (IPCE) are calculated in Figure 5.3b. TiO_2 and TiO_2-APS show a steady IPCE of around 5% independent of illumination intensity. The loss of efficiency is mainly attributed to bulk and surface recombination due to the sluggish oxygen evolution reaction. Notably, on TiO_2-**Co_9POM**, IPCE remains unchanged at around 18% before 6.4 mW/cm^2 and decreases at a higher intensity. This indicates that the catalyst turnover rate lags behind the surface photogenerated hole collection rate at higher illumination intensity, shifting the efficiency limiting step from photon generation and separation rate to catalyst operation rate. This also indicates the **Co_9POM** acts as the reaction active sites on this modified photoanode.

The formation of oxygen in our system was confirmed by following the response of oxygen sensor in a chronoamperometry experiment at 0.73 V applied potential and 20 mW/cm^2 365 nm UV illumination as shown in Figures 5.4a and A5.6. With the light on, the O_2 concentration near the electrode increases from 4.0 to 5.5 μM; with light off, the [O_2] slowly decreases due to diffusion of the O_2. When the light is on again, [O_2] increases again from 5.0 to 6.4 μM. These concentrations are much lower than the O_2 solubility in fresh water under 1 atm O_2, 25°C (1.2 mM).[67] Therefore, no gas bubbles are expected on the electrode during the short periods of light illumination. The stability of the electrode and accumulated products was also evaluated under the same chronoamperometry conditions. Figure 5.4b shows the photocurrent remains stable for 5 hours passing *ca.* 3.0 C of charge on the electrode. The initial fast decay is related to the capacitance, a

non-Faradaic process, which was addressed in previous studies.[63] GC measurement of the accumulated oxygen product shows an OER Faradaic efficiency of 96.5 ± 5.5 % after corrections for air leakage into the system. X-ray photoelectron spectroscopy of Co, W and oxygen, as well as Raman spectroscopy of TiO_2-**Co_9POM** photoanodes after chronoamperometric studies were conducted to assess the stability of the surface-anchored POM. XPS show that both the Co and W peaks are well maintained (Figures A5.2b-d). Significantly, these peaks are quite distinct from the XPS peaks of Co_3O_4 (Figure A5.3). Characteristic Raman peaks of **Co_9POM** on TiO_2-**Co_9POM** are still observed after chronoamperometric studies (Figure A5.4). These collective data indicate the structural integrity of **Co_9POM** after long-time use and establish that **Co_9POM**-modified TiO_2 acts as an efficient and fairly robust OER photoanode.

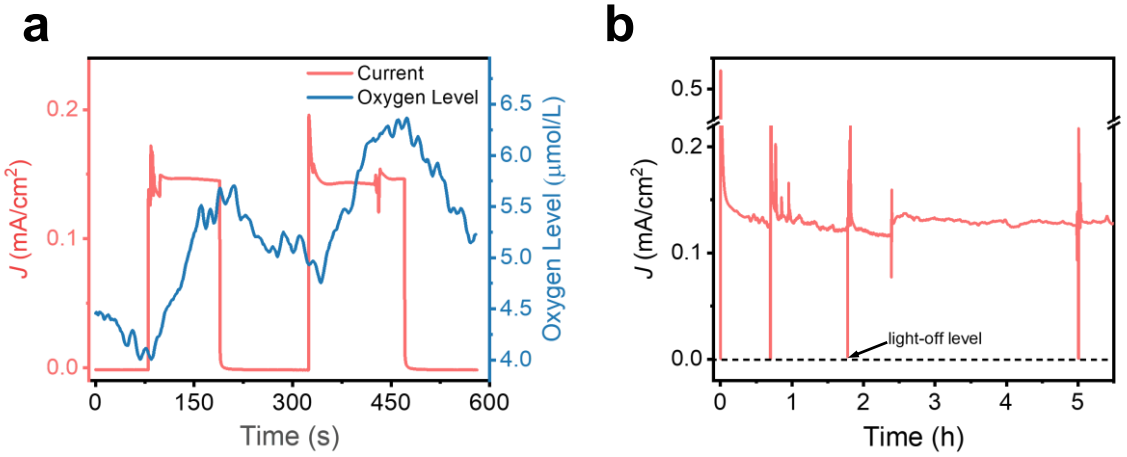

Figure 5.4. (a) FOXY Forspor oxygen probe during chronoamperometry and (b) chronoamperometric stability test of TiO_2-**Co_9POM** photoanode collected at 0.73 V under 20 mW/cm^2 365 nm UV illumination in pH 2 sulfate buffer.

Control experiments using TiO_2 photoelectrodes modified by non-transition-metal substituted POMs and Co-Pi confirm the indispensable role of **Co_9POM** for the water oxidation reaction under acidic conditions. Figures A5.5b and c, show that both $H_3PW_{12}O_{40}$- and Co-Pi-

coated TiO_2 photoelectrodes exhibit inferior activity than a pure TiO_2 photoelectrode. For $H_3PW_{12}O_{40}$-modified TiO_2, the lack of metal catalytic center and the blocking of TiO_2 surface reaction sites leads to decreased photocurrent. These results also confirm that a Co center and not the polytungstate ligands are requisite for catalytic water oxidation. Significantly, although Co-Pi has been extensively reported as a superior water oxidation co-catalyst in neutral and alkaline solutions,[42-45, 47-49] it does not act as an active catalyst in acidic conditions. Moreover, the decreased photocurrent may be due to the absorption of Co-Pi at 365 nm, leading to an inferior light harvesting efficiency by TiO_2 and worse photocurrent.

5.3.3 Transient Absorption Spectroscopy Probing Charge Transfer Dynamics in TiO_2-Co_9POM

The above PEC studies show that **Co_9POM** modification of TiO_2 strongly enhances photocurrent which can be attributed to **Co_9POM** acting as an active OER catalyst. However, it's hard to rule out the possibility that **Co_9POM** modification passivates the surface states and suppresses recombination from the above experiments. Therefore, more direct evidence of the charge transfer dynamics is needed. Herein, we apply transient absorption (TA) spectroscopies to study the photophysics of TiO_2, TiO_2-APS and TiO_2-**Co_9POM** photoanodes in both visible (TA-vis) and mid-IR regions (TA-IR), with the data shown in Figure 5.5, Figures A5.7 and A5.8. Before detailed analysis of the TA spectra and kinetics of TiO_2-**Co_9POM**, a series of control experiments were done on TiO_2 to assign the spectra features observed in the visible range after excitation. As shown in Figure 5.5a and Figure A5.7a, similar broad positive signals were observed upon excitation of both TiO_2 and TiO_2-**Co_9POM** film on FTO substrate. The broad signal in the visible range is assigned to be a convolution contribution of both electron and hole signals, where the trapped hole and electrons have maximum absorption peaks at 520 and 770 nm, respectively.[68-71]

We extract the TiO_2 kinetics from 460-520 nm and compare their decay behavior in DI H_2O, in an electron scavenger solution (0.1 M $Na_2S_2O_8$ aqueous solution), and in a hole scavenger solution (30% methanol aqueous solution) in Figure A5.7d. The decay kinetics decay are much faster in 30% methanol solution and slightly slower in electron scavenger solution. This indicates that the kinetics from 460-520 nm mainly originate from photogenerated holes in nanoporous TiO_2. Kinetics at this range can be further used to represent the kinetic decay of photogenerated holes.

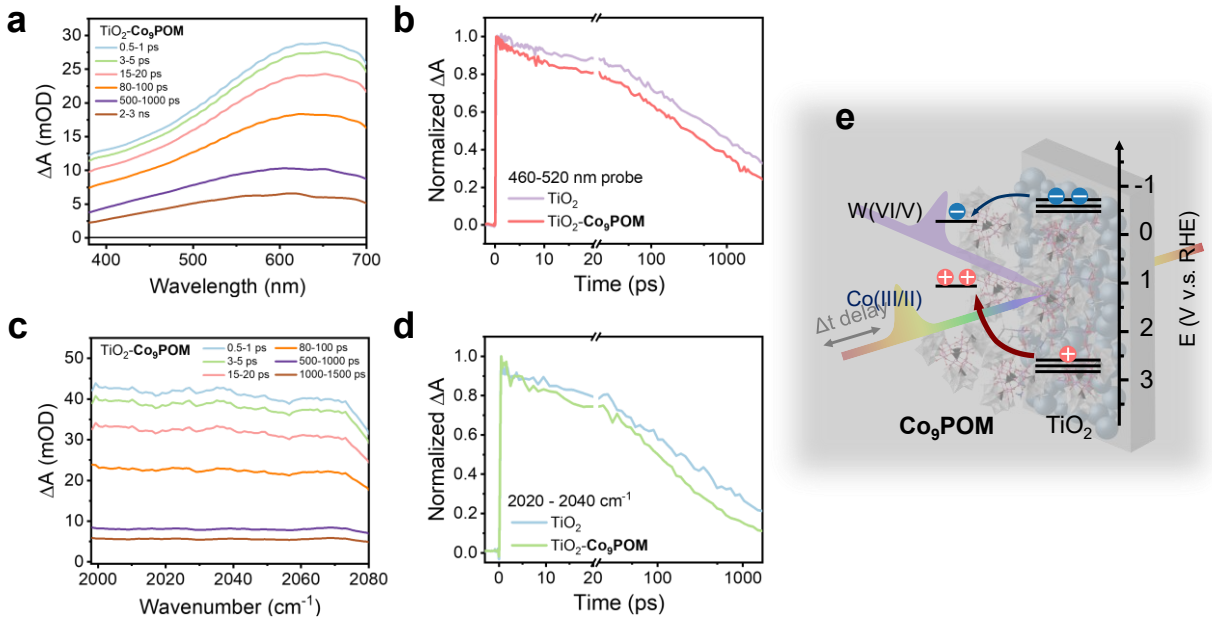

Figure 5.5. Transient absorption spectra of TiO_2-**Co9POM** films under 350 nm pump and (a) visible (c) mid-IR probe. Normalized transient absorption decay kinetics on TiO_2 and TiO_2-**Co9POM** probed at (b) 460-520 nm in the visible and (d) 2020-2040 cm^{-1} in the mid-IR following 350 nm excitation. (e) Schematic illustration of charge transfer mechanism between TiO_2 and **Co9POM**. Samples for TA-vis experiments are deposited on FTO substrates, samples for TA-IR experiments are deposited on a sapphire window to avoid extensive absorption by tin oxide. An excitation power density of 462 $\mu J/cm^2$ is used in all TA experiments.

Excitation fluence-dependent hole kinetic decays are compared in Figures A5.7b-c. Interestingly, the maximum signal amplitude scales linearly with power density, but signal decay half-time and signal residual decay scale with increased excitation power. This means that the number of photogenerated holes scales linearly with excitation power but recombination becomes faster with more generated carriers. This can be explained by the trap-assisted electron-hole recombination. Fluence-dependent hole kinetics is fit well by a power law decay $A = (t - t_0)^{-\beta}$, with β lying within 0.25 ± 0.002 for all decays. Dispersive bimolecular recombination is often observed in metal oxides and organic semiconductor materials.[72-75] Figures 5.5b and A5.7e further compare the hole decay kinetics of TiO_2, TiO_2-APS, and TiO_2-**Co$_9$POM** photoelectrodes. Hole decay kinetics in TiO_2 and TiO_2-APS are very similar, while signal decay accelerates in TiO_2-**Co$_9$POM**. This further clarifies the previous proposals: **Co$_9$POM** acts as a water oxidation catalyst that extracts photogenerated holes on the picosecond timescale rather than suppressing surface recombination. APS acts as a spectator and does not affect the hole kinetics.

In addition, TR-IR spectroscopies were conducted on TiO_2, TiO_2-APS, and TiO_2-**Co$_9$POM** samples to probe the photogenerated electron kinetics in the TiO_2 conduction band as shown in Figures 5.5c, d and Figure A5.8. All samples showed a broad positive signal from 2000 to 2080 cm^{-1} upon excitation. The signal can be assigned to the TiO_2 conduction band free electron absorption.[76-78] The TA-IR spectra rule out **Co$_9$POM** or APS excited states or oxidized states as important due to the lack of IR transitions in this region (Figure A5.1a and reference 79[79]). As shown in Figure A5.8d, the electron signal in TiO_2 shows similar decay features with or without APS treatment, meaning that APS is not reduced by TiO_2 conduction band electrons and remains stable during all our reported experiments. Notably, the electron signal decays faster when **Co$_9$POM** is attached to TiO_2-APS which is entirely consistent with TiO_2 conduction band electrons

capable of reducing tungsten in **Co_9POM**, a thermodynamically favorable process (~ -0.2 V, Figure A5.5a, compared to TiO_2 conduction band edge, -0.4 V).[80] These findings are also in agreement with the slow OCP recovery from light to dark states of TiO_2-**Co_9POM**, where tungsten states close to the TiO_2 conduction band are introduced in the coupled system. Despite this unfavorable electron transfer process observed in dry film TA-IR measurement conditions, we believe this effect is greatly mitigated under OER conditions as sufficient positive applied potential can decrease the electron population in nanoporous TiO_2. From the above TA-vis and TA-IR experiments, we establish that TiO_2-**Co_9POM** is a highly coupled system that can achieve both electron and hole transfer as summarized in Figure 5.5e, with the APS ligand likely serving as both electron and hole transfer highway.

5.4. Conclusions

We report a POM immobilization method by first anchoring the cationic APS ligand on a metal oxide light absorber followed by treatment of the metal oxide-APS with a solution of a POM WOC, **Co_9POM**. The resulting **Co_9POM**-functionalized TiO_2 photoelectrode, TiO_2-APS-**Co_9POM** or "TiO_2-**Co_9POM**" in this study, exhibits a three-fold photocurrent enhancement compared to bare TiO_2 in aqueous acidic conditions. The structural integrity of the catalyst, **Co_9POM**, is maintained for up to 5 hours of operation. To the best of our knowledge, this is the first application of an efficient POM-based catalytic photoanode that achieves efficient water photoxidation in acid. Extensive mechanistic studies conclude that the enhancement of photocurrent is mainly due to **Co_9POM** acting as a fast hole collector and active catalytic center rather than as a passivator of surface states. TA spectroscopy further verifies the fast photogenerated hole transfer from TiO_2 to **Co_9POM** at the ps timescale. The highly charged

Co_9POM-modified surface also modulates the TiO_2 band edge, enabling a suitable surface electric field to separate the surface photogenerated charge carrier.

Appendix Chapter 5

Supplementary General Characterization

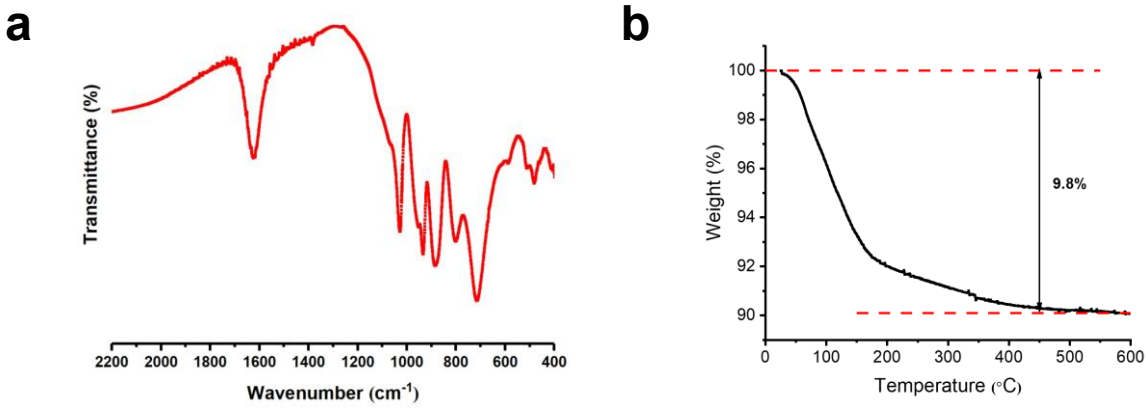

Figure A5.1. (a) FT-IR spectroscopy and (b) TGA of **Co_9POM**.

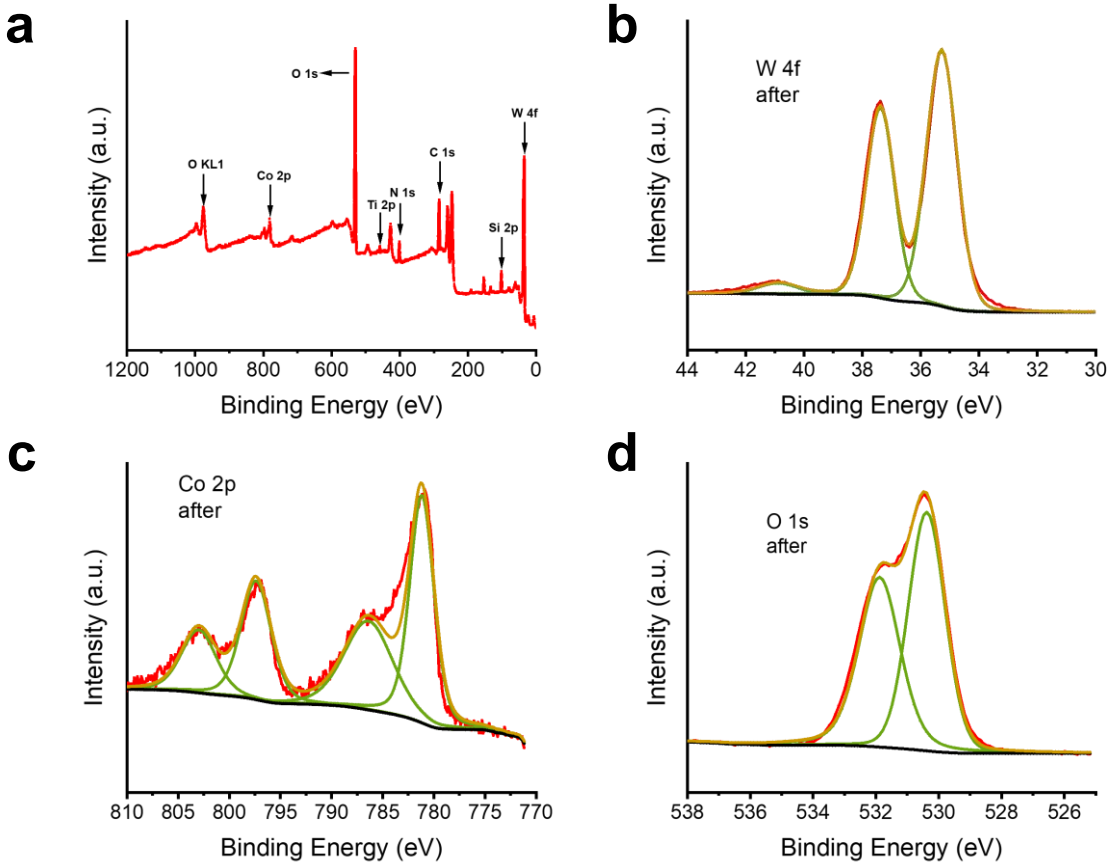

Figure A5.2. (a) Full XPS of TiO_2-**Co_9POM** before bulk electrolysis. XPS of (b) W 4f, (c) Co 2p, and (d) O 1s of TiO_2-**Co_9POM** after bulk electrolysis.

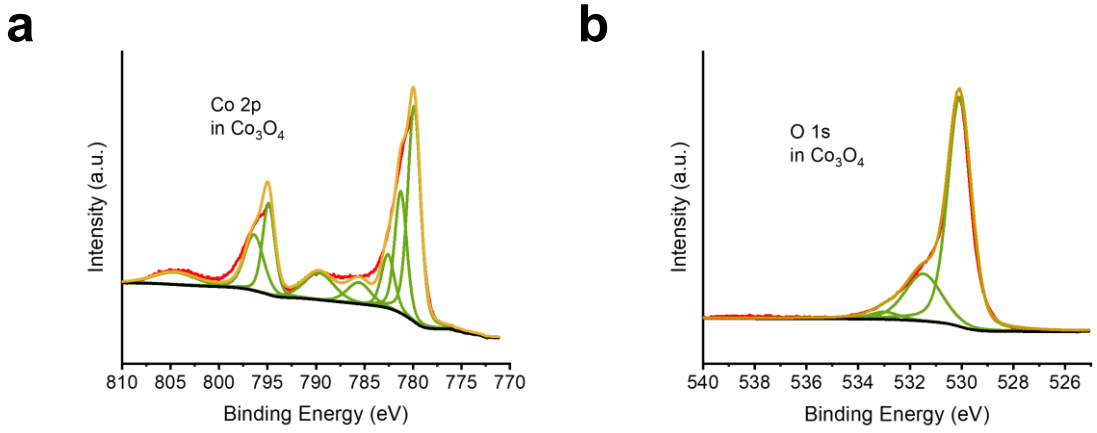

Figure A5.3. XPS of (a) Co 2p and (b) O 1s in Co_3O_4 solids.

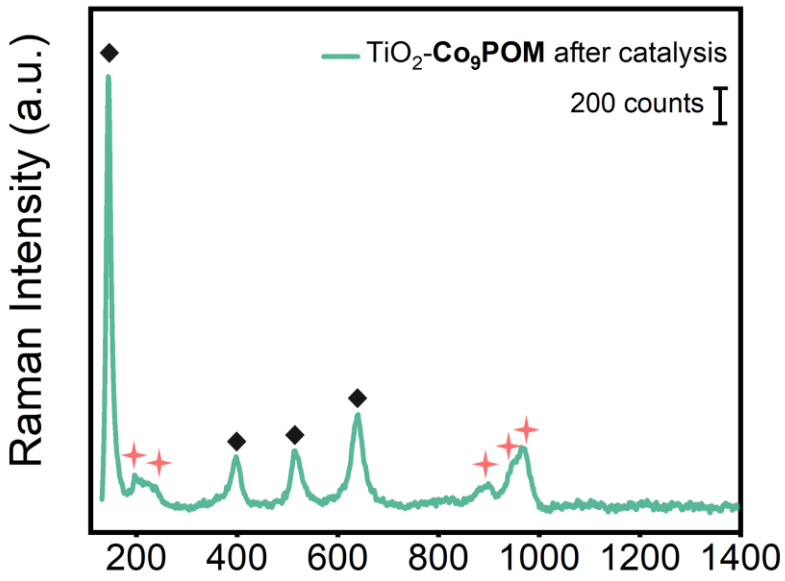

Figure A5.4. Raman spectroscopy of TiO_2-**Co$_9$POM** on FTO substrates after passing around 3.0 C of charge on the electrode for OER reaction as described in Figure 5.4b. Black diamonds and red stars represent the feature Raman peaks for anatase TiO_2 and **Co$_9$POM**, respectively.

Supplementary PEC Characterization and AC Impedance Fitting Parameters

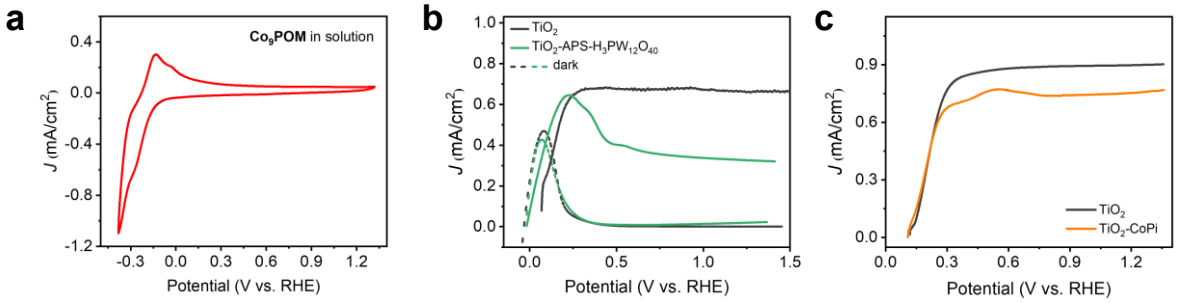

Figure A5.5. (a) Cyclic voltammetry of **Co$_9$POM** in pH 2 buffer solution (b) J-V curve of $H_3PW_{12}O_{40}$ modified TiO_2 and (c) J-V photocurrent of Co-Pi modified TiO_2 under 100 mW cm^{-2} 365 nm LED light illumination.

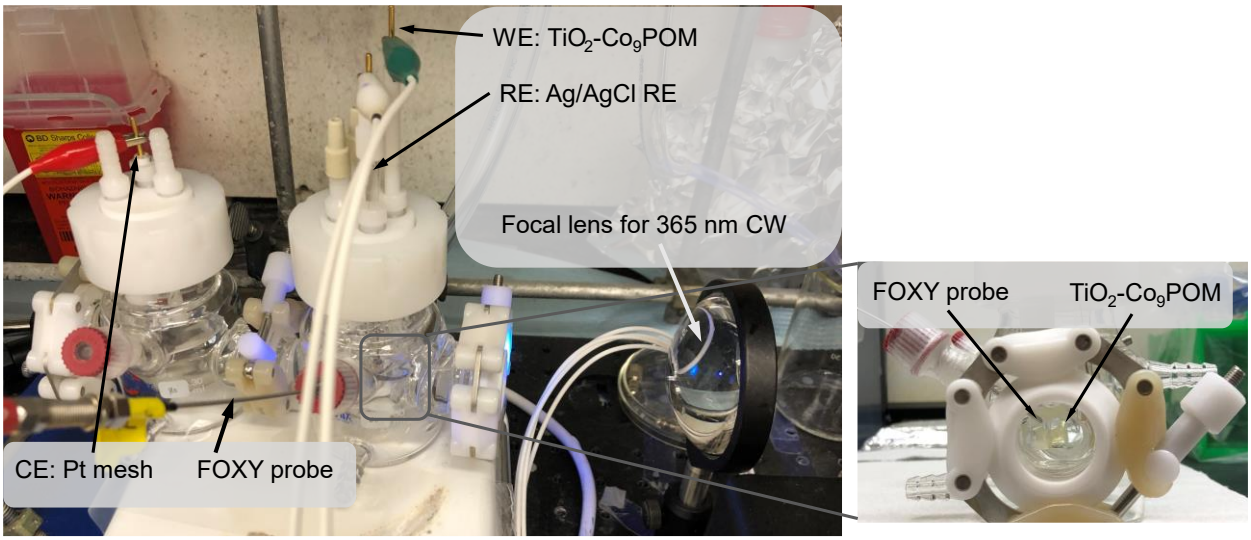

Figure A5.6. FOXY Forspor oxygen probe setup during OER condition. Right panel shows the zoom-in of probe and electrode relative position.

Table A5.1. AC impedance fitting parameter of TiO_2, TiO_2-APS and TiO_2-**Co_9POM** photoanode.

	TiO_2	TiO_2-APS	TiO_2-**Co_9POM**
U_{fb} (V_{RHE})	-0.083±0.017	-0.062±0.020	-0.164±0.009
R_s (Ohm/cm^2)	25.41±0.17	27.88±0.12	46.32±0.28
R_{ct} (kOhm/cm^2)	567.8±292	410.3±80.6	153.3±28.2
CPE-Q (μF/cm^2)	7.70±0.10	6.67±0.05	126.2±0.16
CPE-α	0.978±0.002	0.979±0.001	0.904±0.002

Supplementary Transient Absorption Spectroscopy

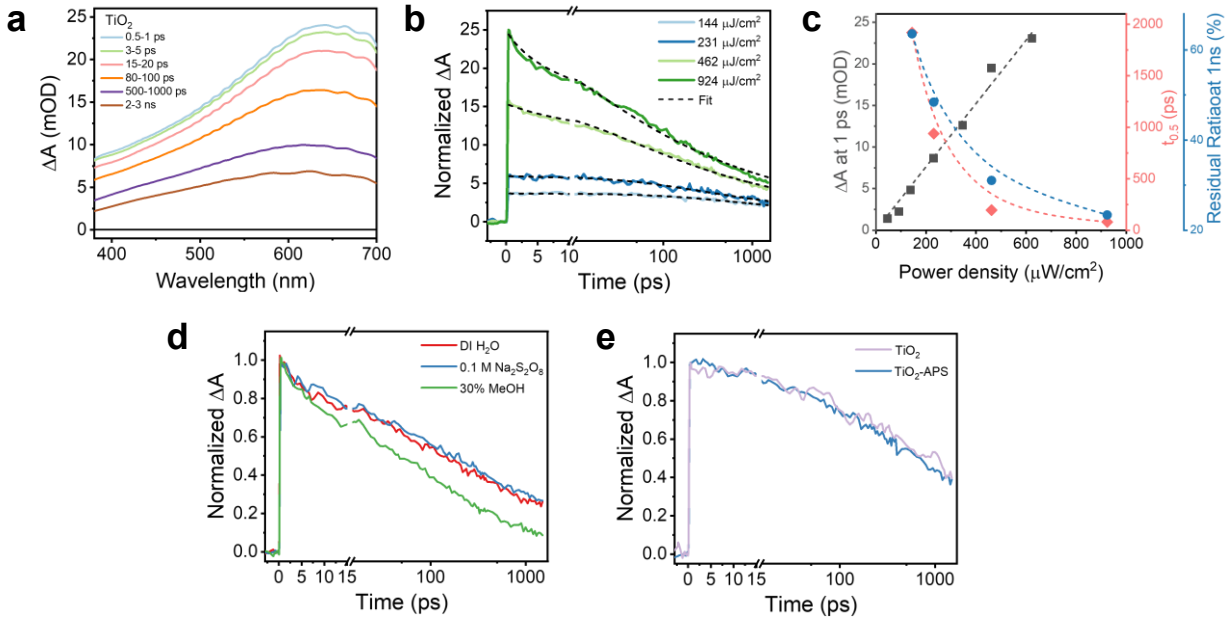

Figure A5.7. Transient absorption spectroscopy of TiO_2 on FTO pumped by 350 nm pulses and probed by visible white light: (a) TA-vis spectra; excitation fluence dependent of (b) kinetic decay and (c) maximum signal amplitude, half lifetime and signal residual as a function of power density; (d) kinetic decay in DI water, 0.1 M $Na_2S_2O_8$, and 30% methanol; (e) normalized hole decay kinetics on of TiO_2 and TiO_2-APS. All signal kinetics decays are extracted by averaging 460-520 nm, excitation power density of 462 μJ/cm^2 are used in (a), and 231 μJ/cm^2 are used in (d) and (e).

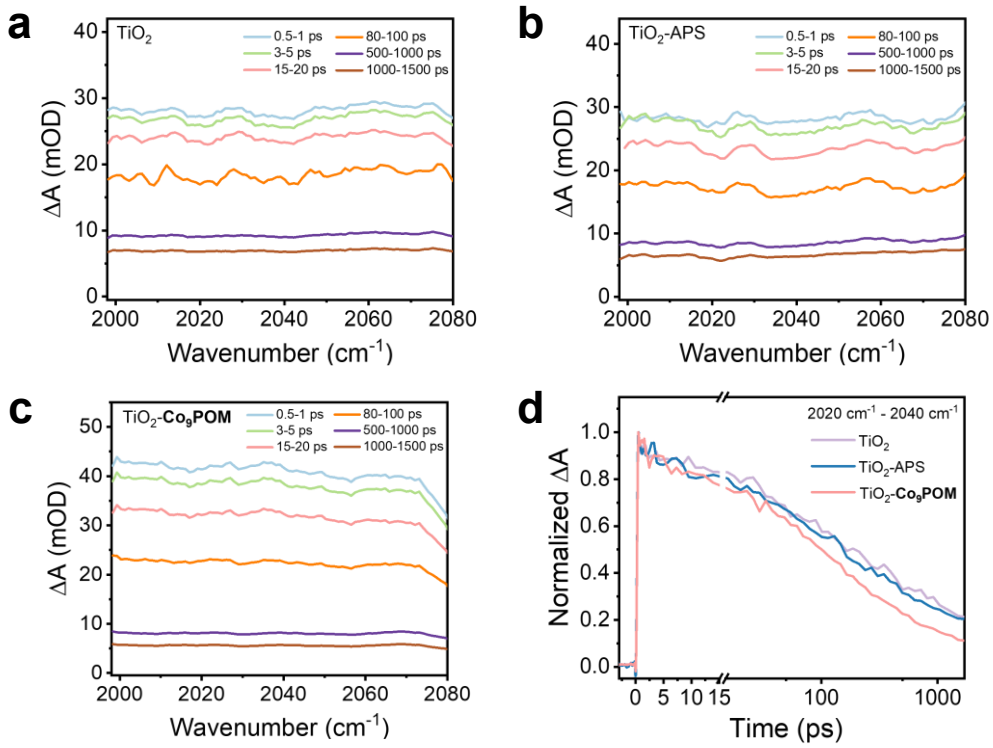

Figure A5.8. TA-IR spectra on (a) TiO_2, (b) TiO_2-APS, and (c) TiO_2-**Co_9POM** samples. (d) Kinetics comparison of three samples from 2020-2040 cm^{-1}. TA-IR experiments are conducted under 462 $\mu J/cm^2$ 350-nm pump, with all samples deposited on sapphire windows.

5.5. References

1. Lewis, N. S.; Nocera, D. G., Powering the planet: Chemical challenges in solar energy utilization. *Proc. Natl Acad. Sci. USA* **2006,** *103*, 15729-15735.
2. Hisatomi, T.; Kubota, J.; Domen, K., Recent advances in semiconductors for photocatalytic and photoelectrochemical water splitting. *Chem. Soc. Rev.* **2014,** *43* (22), 7520-7535.
3. Takata, T.; Jiang, J.; Sakata, Y.; Nakabayashi, M.; Shibata, N.; Nandal, V.; Seki, K.; Hisatomi, T.; Domen, K., Photocatalytic water splitting with a quantum efficiency of almost unity. *Nature* **2020,** *581* (7809), 411-414.
4. Zhou, P.; Navid, I. A.; Ma, Y.; Xiao, Y.; Wang, P.; Ye, Z.; Zhou, B.; Sun, K.; Mi, Z., Solar-to-hydrogen efficiency of more than 9% in photocatalytic water splitting. *Nature* **2023,** *613* (7942), 66-70.
5. Stamenkovic, V. R.; Strmcnik, D.; Lopes, P. P.; Markovic, N. M., Energy and fuels from electrochemical interfaces. *Nat. Mater.* **2016,** *16* (1), 57-69.
6. Han, L.; Dong, S.; Wang, E., Transition-Metal (Co, Ni, and Fe)-Based Electrocatalysts for the Water Oxidation Reaction. *Adv. Mater.* **2016,** *28* (42), 9266-9291.
7. Suen, N. T.; Hung, S. F.; Quan, Q.; Zhang, N.; Xu, Y. J.; Chen, H. M., Electrocatalysis for the oxygen evolution reaction: recent development and future perspectives. *Chem. Soc. Rev.* **2017,** *46* (2), 337-365.
8. Song, J.; Wei, C.; Huang, Z. F.; Liu, C.; Zeng, L.; Wang, X.; Xu, Z. J., A review on fundamentals for designing oxygen evolution electrocatalysts. *Chem. Soc. Rev.* **2020,** *49* (7), 2196-2214.
9. Yu, Z. Y.; Duan, Y.; Feng, X. Y.; Yu, X.; Gao, M. R.; Yu, S. H., Clean and Affordable Hydrogen Fuel from Alkaline Water Splitting: Past, Recent Progress, and Future Prospects. *Adv. Mater.* **2021,** *33* (31), e2007100.
10. Yin, J.; Jin, J.; Lu, M.; Huang, B.; Zhang, H.; Peng, Y.; Xi, P.; Yan, C. H., Iridium Single Atoms Coupling with Oxygen Vacancies Boosts Oxygen Evolution Reaction in Acid Media. *J. Am. Chem. Soc.* **2020,** *142* (43), 18378-18386.
11. Wu, Z. Y.; Chen, F. Y.; Li, B.; Yu, S. W.; Finfrock, Y. Z.; Meira, D. M.; Yan, Q. Q.; Zhu, P.; Chen, M. X.; Song, T. W.; Yin, Z.; Liang, H. W.; Zhang, S.; Wang, G.; Wang, H., Non-iridium-based electrocatalyst for durable acidic oxygen evolution reaction in proton exchange membrane water electrolysis. *Nat. Mater.* **2023,** *22* (1), 100-108.
12. Huynh, M.; Bediako, D. K.; Nocera, D. G., A functionally stable manganese oxide oxygen evolution catalyst in acid. *J. Am. Chem. Soc.* **2014,** *136* (16), 6002-10.
13. Huynh, M.; Shi, C.; Billinge, S. J.; Nocera, D. G., Nature of Activated Manganese Oxide for Oxygen Evolution. *J. Am. Chem. Soc.* **2015,** *137* (47), 14887-904.
14. Mondschein, J. S.; Callejas, J. F.; Read, C. G.; Chen, J. Y. C.; Holder, C. F.; Badding, C. K.; Schaak, R. E., Crystalline Cobalt Oxide Films for Sustained Electrocatalytic Oxygen Evolution under Strongly Acidic Conditions. *Chemistry of Materials* **2017,** *29* (3), 950-957.

15. Huynh, M.; Ozel, T.; Liu, C.; Lau, E. C.; Nocera, D. G., Design of template-stabilized active and earth-abundant oxygen evolution catalysts in acid. *Chem. Sci.* **2017,** *8* (7), 4779-4794.
16. Yu, J.; Garces-Pineda, F. A.; Gonzalez-Cobos, J.; Pena-Diaz, M.; Rogero, C.; Gimenez, S.; Spadaro, M. C.; Arbiol, J.; Barja, S.; Galan-Mascaros, J. R., Sustainable oxygen evolution electrocatalysis in aqueous 1 M H_2SO_4 with earth abundant nanostructured Co_3O_4. *Nat. Commun.* **2022,** *13* (1), 4341.
17. Chong, L.; Gao, G.; Wen, J.; Li, H.; Xu, H.; Green, Z.; Sugar, J. D.; Kropf, A. J.; Xu, W.; Lin, X. M.; Xu, H.; Wang, L. W.; Liu, D. J., La- and Mn-doped cobalt spinel oxygen evolution catalyst for proton exchange membrane electrolysis. *Science* **2023,** *380*, 609-616.
18. Xiong, Q.; Zhang, X.; Wang, H.; Liu, G.; Wang, G.; Zhang, H.; Zhao, H., One-step synthesis of cobalt-doped MoS_2 nanosheets as bifunctional electrocatalysts for overall water splitting under both acidic and alkaline conditions. *Chem. Commun.* **2018,** *54* (31), 3859-3862.
19. Yang, Y.; Yao, H.; Yu, Z.; Islam, S. M.; He, H.; Yuan, M.; Yue, Y.; Xu, K.; Hao, W.; Sun, G.; Li, H.; Ma, S.; Zapol, P.; Kanatzidis, M. G., Hierarchical Nanoassembly of $MoS_2/Co_9S_8/Ni_3S_2$/Ni as a Highly Efficient Electrocatalyst for Overall Water Splitting in a Wide pH Range. *J. Am. Chem. Soc.* **2019,** *141* (26), 10417-10430.
20. Yin, Q.; Tan, J. M.; Besson, C.; Geletii, Y. V.; Musaev, D. G.; Kuznetsov, A. E.; Luo, Z.; Hardcastle, K. I.; Hill, C. L., A Fast Soluble Carbon-Free Molecular Water Oxidation Catalyst Based on Abundant Metals. *Science* **2010,** *328*, 342-345.
21. Vickers, J. W.; Lv, H.; Sumliner, J. M.; Zhu, G.; Luo, Z.; Musaev, D. G.; Geletii, Y. V.; Hill, C. L., Differentiating homogeneous and heterogeneous water oxidation catalysis: confirmation that $[Co_4(H_2O)_2(\alpha\text{-}PW_9O_{34})_2]^{10-}$ is a molecular water oxidation catalyst. *J. Am. Chem. Soc.* **2013,** *135* (38), 14110-8.
22. Lv, H.; Song, J.; Geletii, Y. V.; Vickers, J. W.; Sumliner, J. M.; Musaev, D. G.; Kogerler, P.; Zhuk, P. F.; Bacsa, J.; Zhu, G.; Hill, C. L., An exceptionally fast homogeneous carbon-free cobalt-based water oxidation catalyst. *J. Am. Chem. Soc.* **2014,** *136* (26), 9268-71.
23. Blasco-Ahicart, M.; Soriano-Lopez, J.; Carbo, J. J.; Poblet, J. M.; Galan-Mascaros, J. R., Polyoxometalate electrocatalysts based on earth-abundant metals for efficient water oxidation in acidic media. *Nat Chem* **2018,** *10* (1), 24-30.
24. Arens, J. T.; Blasco-Ahicart, M.; Azmani, K.; Soriano-López, J.; García-Eguizábal, A.; Poblet, J. M.; Galan-Mascaros, J. R., Water oxidation electrocatalysis in acidic media with Co-containing polyoxometalates. *J. Catal.* **2020,** *389*, 345-351.
25. Goberna-Ferron, S.; Vigara, L.; Soriano-Lopez, J.; Galan-Mascaros, J. R., Identification of a nonanuclear $\{Co^{II9}\}$ polyoxometalate cluster as a homogeneous catalyst for water oxidation. *Inorg. Chem.* **2012,** *51* (21), 11707-15.
26. Mukhopadhyay, S.; Debgupta, J.; Singh, C.; Kar, A.; Das, S. K., A Keggin Polyoxometalate Shows Water Oxidation Activity at Neutral pH: POM@ZIF-8, an Efficient and Robust Electrocatalyst. *Angew. Chem., Int. Ed.* **2018,** *57* (7), 1918-1923.
27. Paille, G.; Gomez-Mingot, M.; Roch-Marchal, C.; Lassalle-Kaiser, B.; Mialane, P.; Fontecave, M.; Mellot-Draznieks, C.; Dolbecq, A., A Fully Noble Metal-Free Photosystem Based

on Cobalt-Polyoxometalates Immobilized in a Porphyrinic Metal-Organic Framework for Water Oxidation. *J. Am. Chem. Soc.* **2018,** *140* (10), 3613-3618.
28. Folkman, S. J.; Soriano-Lopez, J.; Galan-Mascaros, J. R.; Finke, R. G., Electrochemically Driven Water-Oxidation Catalysis Beginning with Six Exemplary Cobalt Polyoxometalates: Is It Molecular, Homogeneous Catalysis or Electrode-Bound, Heterogeneous CoO_x Catalysis? *J. Am. Chem. Soc.* **2018,** *140* (38), 12040-12055.
29. Sullivan, K. P.; Wieliczko, M.; Kim, M.; Yin, Q.; Collins-Wildman, D. L.; Mehta, A. K.; Bacsa, J.; Lu, X.; Geletii, Y. V.; Hill, C. L., Speciation and Dynamics in the $[Co_4V_2W_{18}O_{68}]^{10-}$/Co(II)aq/$CoO_x$ Catalytic Water Oxidation System. *ACS Catal.* **2018,** *8* (12), 11952-11959.
30. Huang, Z.; Luo, Z.; Geletii, Y. V.; Vickers, J. W.; Yin, Q.; Wu, D.; Hou, Y.; Ding, Y.; Song, J.; Musaev, D. G.; Hill, C. L.; Lian, T., Efficient light-driven carbon-free cobalt-based molecular catalyst for water oxidation. *J. Am. Chem. Soc.* **2011,** *133* (7), 2068-71.
31. Martin-Sabi, M.; Soriano-Lopez, J.; Winter, R. S.; Chen, J. J.; Vila-Nadal, L.; Long, D. L.; Galan-Mascaros, J. R.; Cronin, L., Redox tuning the Weakley-type polyoxometalate archetype for the oxygen evolution reaction. *Nat. Catal.* **2018,** *1* (3), 208-213.
32. Irani, R.; Plate, P.; Höhn, C.; Bogdanoff, P.; Wollgarten, M.; Höflich, K.; van de Krol, R.; Abdi, F. F., The role of ultra-thin MnOx co-catalysts on the photoelectrochemical properties of $BiVO_4$ photoanodes. *Journal of Materials Chemistry A* **2020,** *8* (11), 5508-5516.
33. Lin, F.; Boettcher, S. W., Adaptive semiconductor/electrocatalyst junctions in water-splitting photoanodes. *Nature Materials* **2014,** *13* (1), 81-86.
34. Liu, T.; Li, W.; Wang, D. Z.; Luo, T.; Fei, M.; Shin, D.; Waegele, M. M.; Wang, D., Low Catalyst Loading Enhances Charge Accumulation for Photoelectrochemical Water Splitting. *Angewandte Chemie International Edition* **2023**.
35. Guo, Q.; Zhao, Q.; Crespo-Otero, R.; Di Tommaso, D.; Tang, J.; Dimitrov, S. D.; Titirici, M.-M.; Li, X.; Jorge Sobrido, A. B., Single-Atom Iridium on Hematite Photoanodes for Solar Water Splitting: Catalyst or Spectator? *J. Am. Chem. Soc.* **2023,** *145* (3), 1686-1695.
36. Tilley, S. D.; Cornuz, M.; Sivula, K.; Grätzel, M., Light-Induced Water Splitting with Hematite: Improved Nanostructure and Iridium Oxide Catalysis. *Angew. Chem. Int. Ed.* **2010,** *49* (36), 6405-6408.
37. Liu, G.; Eichhorn, J.; Jiang, C.-M.; Scott, M. C.; Hess, L. H.; Gregoire, J. M.; Haber, J. A.; Sharp, I. D.; Toma, F. M., Interface engineering for light-driven water oxidation: unravelling the passivating and catalytic mechanism in $BiVO_4$ overlayers. *Sustainable Energy & Fuels* **2019,** *3* (1), 127-135.
38. Jang, J.-W.; Du, C.; Ye, Y.; Lin, Y.; Yao, X.; Thorne, J.; Liu, E.; McMahon, G.; Zhu, J.; Javey, A.; Guo, J.; Wang, D., Enabling unassisted solar water splitting by iron oxide and silicon. *Nat. Commun.* **2015,** *6* (1), 7447.
39. Thorne, J. E.; Jang, J.-W.; Liu, E. Y.; Wang, D., Understanding the origin of photoelectrode performance enhancement by probing surface kinetics. *Chemical Science* **2016,** *7* (5), 3347-3354.
40. Ye, K.-H.; Wang, Z.; Gu, J.; Xiao, S.; Yuan, Y.; Zhu, Y.; Zhang, Y.; Mai, W.; Yang, S., Carbon quantum dots as a visible light sensitizer to significantly increase the solar water splitting

performance of bismuth vanadate photoanodes. *Energy & Environmental Science* **2017,** *10* (3), 772-779.

41. Kim, T. W.; Choi, K.-S., Nanoporous $BiVO_4$ Photoanodes with Dual-Layer Oxygen Evolution Catalysts for Solar Water Splitting. *Science* **2014,** *343* (6174), 990-994.

42. Nellist, M. R.; Laskowski, F. A. L.; Qiu, J.; Hajibabaei, H.; Sivula, K.; Hamann, T. W.; Boettcher, S. W., Potential-sensing electrochemical atomic force microscopy for in operando analysis of water-splitting catalysts and interfaces. *Nature Energy* **2018,** *3* (1), 46-52.

43. Ma, Y.; Kafizas, A.; Pendlebury, S. R.; Le Formal, F.; Durrant, J. R., Photoinduced Absorption Spectroscopy of CoPi on $BiVO_4$: The Function of CoPi during Water Oxidation. *Adv. Funct. Mater.* **2016,** *26* (27), 4951-4960.

44. Ma, Y.; Le Formal, F.; Kafizas, A.; Pendlebury, S. R.; Durrant, J. R., Efficient suppression of back electron/hole recombination in cobalt phosphate surface-modified undoped bismuth vanadate photoanodes. *J. Mater. Chem. A* **2015,** *3* (41), 20649-20657.

45. Abdi, F. F.; Firet, N.; van de Krol, R., Efficient BiVO4 Thin Film Photoanodes Modified with Cobalt Phosphate Catalyst and W-doping. *ChemCatChem* **2013,** *5* (2), 490-496.

46. Abdi, F. F.; van de Krol, R., Nature and Light Dependence of Bulk Recombination in Co-Pi-Catalyzed $BiVO_4$ Photoanodes. *J. Phys. Chem. C* **2012,** *116* (17), 9398-9404.

47. Zhong, D. K.; Choi, S.; Gamelin, D. R., Near-Complete Suppression of Surface Recombination in Solar Photoelectrolysis by "Co-Pi" Catalyst-Modified W:$BiVO_4$. *J. Am. Chem. Soc.* **2011,** *133* (45), 18370-18377.

48. Klahr, B.; Gimenez, S.; Fabregat-Santiago, F.; Bisquert, J.; Hamann, T. W., Photoelectrochemical and Impedance Spectroscopic Investigation of Water Oxidation with "Co–Pi"-Coated Hematite Electrodes. *J. Am. Chem. Soc.* **2012,** *134* (40), 16693-16700.

49. Barroso, M.; Cowan, A. J.; Pendlebury, S. R.; Grätzel, M.; Klug, D. R.; Durrant, J. R., The Role of Cobalt Phosphate in Enhancing the Photocatalytic Activity of α-Fe_2O_3 toward Water Oxidation. *Journal of the American Chemical Society* **2011,** *133* (38), 14868-14871.

50. Zheng, M.; Cao, X.; Ding, Y.; Tian, T.; Lin, J., Boosting photocatalytic water oxidation achieved by $BiVO_4$ coupled with iron-containing polyoxometalate: Analysis the true catalyst. *Journal of Catalysis* **2018,** *363*, 109-116.

51. Lauinger, S. M.; Piercy, B. D.; Li, W.; Yin, Q.; Collins-Wildman, D. L.; Glass, E. N.; Losego, M. D.; Wang, D.; Geletii, Y. V.; Hill, C. L., Stabilization of Polyoxometalate Water Oxidation Catalysts on Hematite by Atomic Layer Deposition. *ACS Applied Materials & Interfaces* **2017,** *9* (40), 35048-35056.

52. Lauinger, S. M.; Sumliner, J. M.; Yin, Q.; Xu, Z.; Liang, G.; Glass, E. N.; Lian, T.; Hill, C. L., High Stability of Immobilized Polyoxometalates on TiO_2 Nanoparticles and Nanoporous Films for Robust, Light-Induced Water Oxidation. *Chem. Mater.* **2015,** *27* (17), 5886-5891.

53. Wang, Y.; Cao, X.; Hu, Q.; Liang, X.; Tian, T.; Lin, J.; Yue, M.; Ding, Y., FeO_x Derived from an Iron-Containing Polyoxometalate Boosting the Photocatalytic Water Oxidation Activity of Ti^{3+}-Doped TiO_2. *ACS Applied Materials & Interfaces* **2019,** *11* (26), 23135-23143.

54. Hu, Q.; Meng, X.; Dong, Y.; Han, Q.; Wang, Y.; Ding, Y., A stable iron-containing polyoxometalate coupled with semiconductor for efficient photocatalytic water oxidation under acidic condition. *Chemical Communications* **2019,** *55* (78), 11778-11781.
55. Galán-Mascarós, J. R.; Gómez-Garcia, C. J.; Borrás-Almenar, J. J.; Coronado, E., High nuclearity magnetic clusters: Magnetic properties of a nine cobalt cluster encapsulated in a polyoxometalate, $[Co_9(OH)_3(H_2O)_6(HPO_4)_2(PW_9O_{34})_3]^{16-}$. *Adv. Mater.* **1994,** *6* (3), 221-223.
56. Lauinger, S. M.; Sumliner, J. M.; Yin, Q.; Xu, Z.; Liang, G.; Glass, E. N.; Lian, T.; Hill, C. L., High Stability of Immobilized Polyoxometalates on TiO_2 Nanoparticles and Nanoporous Films for Robust, Light-Induced Water Oxidation. *Chem. Mater.* **2015,** *27* (17), 5886-5891.
57. Kanan, M. W.; Nocera, D. G., In Situ Formation of an Oxygen-Evolving Catalyst in Neutral Water Containing Phosphate and Co^{2+}. *Science* **2008,** *321*, 1072-1075.
58. Zhong, D. K.; Choi, S.; Gamelin, D. R., Near-complete suppression of surface recombination in solar photoelectrolysis by "Co-Pi" catalyst-modified W:$BiVO_4$. *J. Am. Chem. Soc.* **2011,** *133* (45), 18370-18377.
59. Zhong, D. K.; Cornuz, M.; Sivula, K.; Grätzel, M.; Gamelin, D. R., Photo-assisted electrodeposition of cobalt–phosphate (Co–Pi) catalyst on hematite photoanodes for solar water oxidation. *Energy Environ. Sci.* **2011,** *4* (5), 1759-1764.
60. Suo, S.; Sheehan, C.; Zhao, F.; Xiao, L.; Xu, Z.; Meng, J.; Mallouk, T. E.; Lian, T., Direct Vibrational Stark Shift Probe of Quasi-Fermi Level Alignment in Metal Nanoparticle Catalyst-Based Metal–Insulator–Semiconductor Junction Photoelectrodes. *J. Am. Chem. Soc.* **2023**.
61. El-Deen, S. S.; Hashem, A. M.; Abdel Ghany, A. E.; Indris, S.; Ehrenberg, H.; Mauger, A.; Julien, C. M., Anatase TiO_2 nanoparticles for lithium-ion batteries. *Ionics* **2018,** *24* (10), 2925-2934.
62. Challagulla, S.; Tarafder, K.; Ganesan, R.; Roy, S., Structure sensitive photocatalytic reduction of nitroarenes over TiO_2. *Scientific Reports* **2017,** *7* (1).
63. Blasco-Ahicart, M.; Soriano-Lopez, J.; Carbo, J. J.; Poblet, J. M.; Galan-Mascaros, J. R., Polyoxometalate electrocatalysts based on earth-abundant metals for efficient water oxidation in acidic media. *Nat. Chem.* **2018,** *10* (1), 24-30.
64. Chen, X.; Burda, C., The Electronic Origin of the Visible-Light Absorption Properties of C-, N- and S-Doped TiO_2 Nanomaterials. *J. Am. Chem. Soc.* **2008,** *130*, 5018-5019.
65. Amorello, D.; Ledda, F.; Romano, V.; Zingales, R., Batch Experiments for the Determination of the Ti(IV,III) Couple Formal Potential in 1 $mol \cdot dm^{-3}$ HCl, 2 $mol \cdot dm^{-3}$ NaCl Medium at 25 °C. *J. Solution Chem.* **2008,** *38* (2), 259-263.
66. Wu, H.; Zhang, L.; Du, A.; Irani, R.; Van De Krol, R.; Abdi, F. F.; Ng, Y. H., Low-bias photoelectrochemical water splitting via mediating trap states and small polaron hopping. *Nat. Commun.* **2022,** *13* (1).
67. Xing, W.; Yin, M.; Lv, Q.; Hu, Y.; Liu, C.; Zhang, J., 1 - Oxygen Solubility, Diffusion Coefficient, and Solution Viscosity. In *Rotating Electrode Methods and Oxygen Reduction Electrocatalysts*, Xing, W.; Yin, G.; Zhang, J., Eds. Elsevier: Amsterdam, 2014; pp 1-31.

68. Yoshihara, T.; Katoh, R.; Furube, A.; Tamaki, Y.; Murai, M.; Hara, K.; Murata, S.; Arakawa, H.; Tachiya, M., Identification of Reactive Species in Photoexcited Nanocrystalline TiO_2 Films by Wide-Wavelength-Range (400−2500 nm) Transient Absorption Spectroscopy. *J. Phys. Chem. B* **2004,** *108* (12), 3817-3823.
69. Cowan, A. J.; Tang, J.; Leng, W.; Durrant, J. R.; Klug, D. R., Water Splitting by Nanocrystalline TiO_2 in a Complete Photoelectrochemical Cell Exhibits Efficiencies Limited by Charge Recombination. *J. Phys. Chem. C* **2010,** *114* (9), 4208-4214.
70. Kafizas, A.; Wang, X.; Pendlebury, S. R.; Barnes, P.; Ling, M.; Sotelo-Vazquez, C.; Quesada-Cabrera, R.; Li, C.; Parkin, I. P.; Durrant, J. R., Where Do Photogenerated Holes Go in Anatase:Rutile TiO_2? A Transient Absorption Spectroscopy Study of Charge Transfer and Lifetime. *J. Phys. Chem. A* **2016,** *120* (5), 715-723.
71. Jing, L.; Zhou, J.; Durrant, J. R.; Tang, J.; Liu, D.; Fu, H., Dynamics of photogenerated charges in the phosphate modified TiO_2 and the enhanced activity for photoelectrochemical water splitting. *Energy & Environmental Science* **2012,** *5* (4), 6552-6558.
72. Yang, W.; Godin, R.; Kasap, H.; Moss, B.; Dong, Y.; Hillman, S. A. J.; Steier, L.; Reisner, E.; Durrant, J. R., Electron Accumulation Induces Efficiency Bottleneck for Hydrogen Production in Carbon Nitride Photocatalysts. *J. Am. Chem. Soc.* **2019,** *141* (28), 11219-11229.
73. Sachs, M.; Pastor, E.; Kafizas, A.; Durrant, J. R., Evaluation of Surface State Mediated Charge Recombination in Anatase and Rutile TiO_2. *The Journal of Physical Chemistry Letters* **2016,** *7* (19), 3742-3746.
74. Godin, R.; Wang, Y.; Zwijnenburg, M. A.; Tang, J.; Durrant, J. R., Time-Resolved Spectroscopic Investigation of Charge Trapping in Carbon Nitrides Photocatalysts for Hydrogen Generation. *J. Am. Chem. Soc.* **2017,** *139* (14), 5216-5224.
75. Nelson, J.; Chandler, R. E., Random walk models of charge transfer and transport in dye sensitized systems. *Coordination Chemistry Reviews* **2004,** *248* (13), 1181-1194.
76. Yamakata, A.; Ishibashi, T.-a.; Onishi, H., Time-resolved infrared absorption spectroscopy of photogenerated electrons in platinized TiO_2 particles. *Chemical Physics Letters* **2001,** *333* (3), 271-277.
77. Yamakata, A.; Ishibashi, T.-A.; Onishi, H., Water- and Oxygen-Induced Decay Kinetics of Photogenerated Electrons in TiO_2 and Pt/TiO_2: A Time-Resolved Infrared Absorption Study. *J. Phys. Chem. B* **2001,** *105* (30), 7258-7262.
78. Song, J.; Long, J.; Liu, Y.; Xu, Z.; Ge, A.; Piercy, B. D.; Cullen, D. A.; Ivanov, I. N.; McBride, J. R.; Losego, M. D.; Lian, T., Highly Efficient Plasmon Induced Hot-Electron Transfer at Ag/TiO_2 Interface. *ACS Photonics* **2021,** *8* (5), 1497-1504.
79. Brito, R.; Rodríguez, V. A.; Figueroa, J.; Cabrera, C. R., Adsorption of 3-mercaptopropyltrimethoxysilane and 3-aminopropyltrimethoxysilane at platinum electrodes. *Journal of Electroanalytical Chemistry* **2002,** *520* (1), 47-52.
80. Ueda, T., Electrochemistry of Polyoxometalates: From Fundamental Aspects to Applications. *ChemElectroChem* **2018,** *5* (6), 823-838.

6 Semiconductor Photocatalysis Quantum Efficiency Limited by Electrolyte Concentration

6.1. Introduction

Photocatalysis on semiconductor photoelectrodes involves a series of complex events, including but not limited to charge carrier generation, bulk recombination, charge carrier drift, diffusion, interfacial separation, interfacial recombination, and finally the chemical reaction.[1-9] Tracking these individual events and their kinetics enables each step's quantum efficiency (QE) to be quantified, major loss pathways to be identified, and key strategies for improving the device performance to be developed.[1] These processes occur in chronological order, therefore, time-resolved spectroscopic tools have been applied to measure the rates of these processes in these photoelectrodes.[10-12] A series of previous studies have investigated the bulk charge separation and recombination within a one nanosecond time window, providing critical information on the quantum efficiencies of early steps.[10-13] However, studying the later events, such as interfacial recombination, which occur between nanosecond and millisecond timescales that bridges the early charge separation events to slow chemical reaction steps, still remain as both a unsolved technical challenge and mechanistic question.[14-24]

One important aspect that affects the interfacial efficiency in semiconductor photoelectrochemical (PEC) system, but often overlooked, is the electrolyte concentration. Similar to electrochemical (EC) systems, a high enough electrolyte concentration is first responsible for lowering solution resistance.[25] However, a fundamental difference in PEC systems is that the carriers are transiently generated by illumination, not from an external circuit as in EC system. The transiently generated carriers, in turn, induce a potential perturbation that is largely unknown. This photo-induced perturbation results in band flattening and quasi-Fermi level splitting in PEC

systems.[26-30] The potentiostat responds to this perturbation with a time constant (RC constant) that is determined by a combination of double layer capacitance, series resistance, and other cell parameters that are related to electrolyte concentration.[25] Now, as we will demonstrate in this work, if the RC constant is on the same time scale of interfacial charge recombination when the electrolyte concentration is low, the incident photon to current conversion efficiency (IPCE) will decrease as the separated charge carriers undergo undesirably interfacial recombination. Therefore, understanding the relationship between interfacial recombination, electrolyte concentration, and the response time of the external circuit is crucial to interpret the experimental results.

In this work, we aim to provide a clear physical picture of the competition between the interfacial recombination and the external circuit response. In order to do so, we first establish that *in-situ* transient reflectance spectroscopy (TRS) can directly probe the charge carrier's interfacial recombination in a HER capable photocathode *p*-GaP/*n*-TiO_2.[1, 31-33] Then, we study the external circuit response to the transiently photogenerated charge carriers by varying electrolyte concentration. We establish that the response of potentiostat controls the competition between the interfacial charge recombination and HER, which ultimately controls the overall IPCE. Finally, we conclude that the electrolyte concentration needs to be high enough to outcompete the interfacial recombination, which needs to be tailored for different semiconductor photoelectrodes.

6.2. Material and Method

6.2.1. Material preparation

The Zn-doped 100-orientation double side polished gallium phosphide single crystal is obtained from University Wafer. The electrode is prepared according to a published procedure.[32-33] The 5 nm thick TiO_2 layer is deposited via atomic layer deposition (ALD) with $TiCl_4$ and H_2O as Ti and O source at 250 °C. A Ga-In alloy was applied to the back of the electrode for ohmic

contact, followed by conductive copper lead for connection to potentiostat, which is all sealed by an epoxy to only expose the front working surface. The previous study showed that the dopant level determined by Mott-Schottky measurement is $6.4*10^{16}$ cm^{-3}.

6.2.2. Photoelectrochemistry

The photoelectrochemistry is carried out by a CHI 660E electrochemical workstation from CH Instrument. The cell is a 3-electrode setup with Pt wire as counter electrode and Ag/AgCl (1 M KCl) as a reference electrode. The electrolyte is pure water dissolved with indicated solute concentrations ranging from 0.03 M to 6 M $NaNO_3$ or Na_2SO_4. The electrolyte is unbuffered; however, the overall pH is unchanged during the measurement because the 3-electrode is within the same cell compartment. The working electrode distance to the counter electrode, and to the reference electrode are both ~5 mm. The chemicals are purchased from Sigma-Aldrich without further purification. All potential in the text are relative to Ag/AgCl. In the bulk electrolysis setup, the iR compensation is applied to avoid excessive potential drop across the solution.

6.2.3. Transient Reflectance Spectroscopy

Transient Reflectance Spectroscopy is introduced in depth in Chapter 2 Section 2.1.2. The data collection is performed on EOS software, data analysis is performed on Surface Xplorer (Ultrafast systems) and Igor Pro (Wavemetrics).

6.3. Results and Discussions

In our previous study,[1] we found two major loss pathways in a *p*-type GaP HER photocathode protected by a 5 nm *n*-type atomic layer deposited (ALD) TiO_2 (denoted as GaP/TiO_2 in the following text)[32-33] upon excitation: (1) recombination within bulk GaP (occurring within 1 ns) and (2) interfacial recombination (occurring ~100 microsecond) between electrons in TiO_2 and holes in GaP. However, while the bulk separation efficiency is directly measured, the interfacial

QE is deduced from the overall IPCE and the bulk charge separation efficiency. In the study presented here, we aim to directly probe the photogenerated charge carrier's interfacial recombination processes and understand these limiting factors. Figure 6.1a illustrates the 3-electrode photoelectrochemical cell with a GaP/TiO_2 as working electrode, which allows for both femtosecond-pulsed laser illumination and continuous-wave LED illumination. The photocurrent is measured by modulating the illumination on and off at a given applied potential, and the dark current is subtracted from the stable total current, as plotted in Figure 6.1b. This method excludes the non-faradaic charging and discharging current, and the IPCE as calculated by the relation $IPCE = \frac{I_p/q}{P/h\nu}$, where I_p is the photocurrent, q is the elementary charge, P is the illumination power, and $h\nu$ is the photon energy. The IPCE is measured at several different electrolyte concentrations under -1.5 V vs Ag/AgCl, and the results are shown in Figure 6.1c. The IPCE increases with higher electrolyte concentration, from ~2% in pure water to a saturation of ~20% in 0.3 M $NaNO_3$. Further increase of the electrolyte concentration does not increase the IPCE. The iR compensation is then added to exclude the effect of potential drop due to the high solution resistance, and the IPCE shows minimal differences compared to the values obtained without iR compensation.

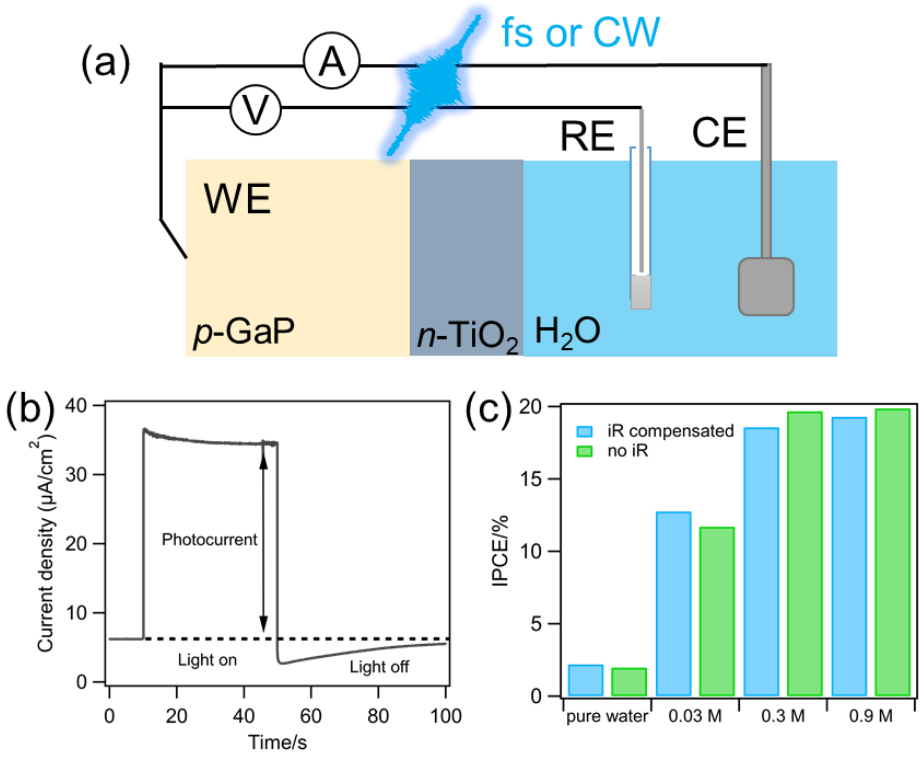

Figure 6.1. Schematic diagram of the *p*-GaP/*n*-TiO_2 water reduction photocathode in a 3-electrode photoelectrochemical cell. (a) The setup allows pulsed (femtosecond 1 kHz ultrafast laser) and continuous wave (CW, LED) illumination. Working electrode: GaP/TiO_2, counter electrode: Pt wire, reference electrode: Ag/AgCl in 1 M KCl. (b) Light on-off measurement of photocurrent for the GaP/TiO_2 in 0.9 M $NaNO_3$ aqueous solution at -1.5 V vs Ag/AgCl under 0.5 mW/cm^2 405 nm LED CW illumination with iR compensation. The dashed line indicates the dark current. (c) Incident photon to current efficiency (IPCE) under 0.5 mW/cm^2 CW 405 nm LED illumination at -1.5 V vs Ag/AgCl in aqueous solution with various $NaNO_3$ concentrations with and without iR compensation by potentiostat.

Figure 6.1c shows that the IPCE increases with higher electrolyte concentration regardless of the iR compensation, indicating that the electrolyte concentration affects one or more of the elementary processes. To gain detailed mechanistic insight, we carried out *in-situ* TRS in the

electrochemical setup illustrated in Figure 6.1a to investigate the effects of electrolytes on the charge separation and recombination processes. Further details of this setup can be found in the Supporting Information section S1.1-1.3. Upon excitation, the GaP/TiO_2 shows two signals, a short-lived free carrier signal that decays in ~100 ps (not shown) and a long-lived separated carrier signal, shown in Figure 6.2a. According to our previous study, the oscillatory signal centered at the direct band gap of GaP (2.78 eV)[34] can be attributed to the Franz-Keldysh Oscillation (FKO) at the weak field limit.[10, 12, 35-38] At this limit, the FKO amplitude is linearly proportional to both the original electric field before optical excitation (E_{DC}) and the photogenerated charge carrier induced electric field change (E_{AC}) through the relation of $\Delta R/R\ (\hbar\omega) \propto E_{DC}E_{AC}$.[35-38] Under the same applied bias, with the same E_{DC}, the FKO amplitude is proportional to E_{AC}, which is proportional to the separated charge carriers across the GaP/TiO_2 *p-n* junction per unit area σ ($E_{AC} \propto \sigma$).[35-38] On the time scale of this study, the photogenerated electrons are fully transferred to the TiO_2 layer, and the FKO signal amplitude change measures the change of photogenerated hole concentration in the GaP. As such, the FKO kinetics provides a direct probe of the decay pathway of the photogenerated holes.

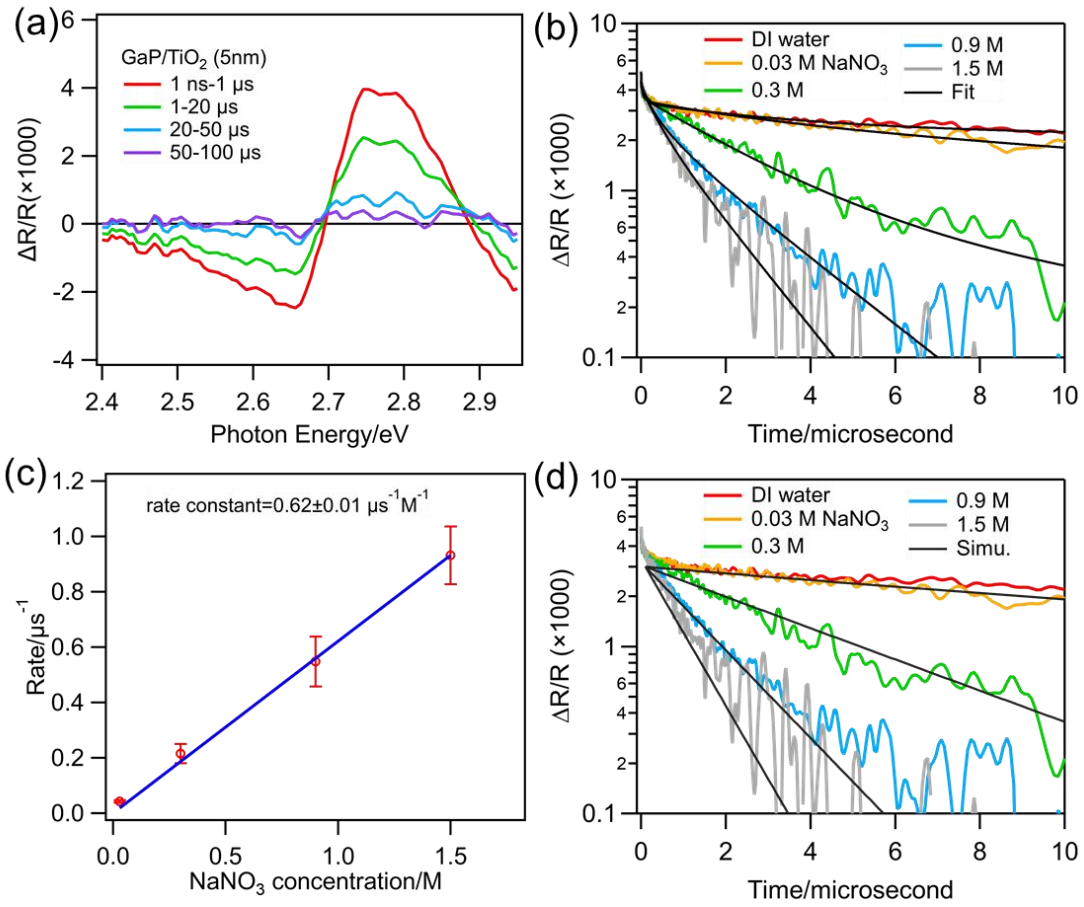

Figure 6.2. (a) Transient reflectance spectra of GaP/TiO_2 at various delay times under 300x pump beam size, 4.4 mW/cm^2 excitation density, -1.5 V vs. Ag/AgCl applied bias, in 0.03 M $NaNO_3$ aqueous solution. (b) FKO kinetics probed at 2.78 eV under -1.5 V applied bias, in various $NaNO_3$ concentrations. The full FKO kinetics 400 μs is shown in Figure A6.3. (c) FKO decay rate plotted as a function of $NaNO_3$ concentration. The linear fit (solid blue line) shows the rate constant of 0.62 $\mu s^{-1}M^{-1}$. (d) Numerical solutions to fit the FKO kinetics from 0.03 to 1.5 M concentration.

In order to study the effect of electrolyte concentration on interfacial recombination process in the GaP/TiO_2 photocathode, a series of TRS experiments was conducted in different electrolyte concentrations as shown in Figure 6.2b. Because of the large carrier mobility in GaP, it is important to identify experimental conditions under which charge carrier lateral diffusion outside the probe

volume is negligible. As shown in Figure A6.1, when the pump beam size is over 300 times larger than the probe, the FKO signal shows negligible dependence on beam size; however, at smaller pump beam size, the FKO signal decays faster at smaller beam size. The decay of the FKO signal at small pump beam sizes can be attributed to a decrease in E_{AC} due to lateral diffusion of carriers (i.e., decreased carriers per unit area $E_{AC} \propto \sigma$). In the following study, the pump beam size is kept at 300 times larger than the probe beam to prevent this undesirable decay in the FKO kinetics (Figure A6.1, S2). Figure A6.1c shows that such lateral diffusion is absent on the dry sample in air, which indicates that the ions in solution are essential for the separated carrier's lateral diffusion.

The electrolyte concentration-dependent TRS is conducted under the same average excitation power of 4.4 mW/cm^2 and bias of -1.5 V. As shown in Figure 6.2b, the FKO signal has the same initial amplitude at ~10 ns, which indicates that the same amount of charge carriers are separated across the *p-n* junction for all of these electrolyte concentrations.[1] With increasing solution electrolyte concentration, the FKO kinetics decay faster: in DI water, the FKO signal is long-lived without significant decay within 100 μs (Figure 6.2b, S3). In contrast, in 1.5 M $NaNO_3$ solution, the FKO signal decays to nearly zero within ~5 μs. The FKO kinetics are fitted to an empirical multi-exponential function (Equation A6.1) to estimate the time constant (Table A6.1). The ion-induced quenching rate (k) can be extracted (Equation A6.2 and Table A6.2), and the quenching rate vs. electrolyte concentration is surprisingly linear, as shown in Figure 6.2c. Assuming a pseudo-first order relation between the cation concentration and the separated carrier lifetime, a rate constant can be obtained via a linear fit to the rate-concentration data in Figure 6.2c. The fitted slope, k_c= 0.62±0.01 μs^{-1}M^{-1}, is the rate constant of FKO signal quenching with respect to the electrolyte concentration.

However, the reason behind FKO signal quenching via solution electrolyte is not straightforward and must be understood with respect to the majority carrier (hole) removal process by the potentiostat. As previously discussed, FKO signal is proportional to the square of electric field difference at GaP/TiO_2 interface with $\Delta R/R\ (\hbar\omega) \propto [(E_{AC} + E_{DC})^2 - {E_{DC}}^2]$.[39] At large applied potential, the GaP/TiO_2 interfacial electric field $E_{x=0}$ is proportional to the square root of interfacial electrostatic potential ϕ_0 according to depletion approximation:[40] $E_{x=0} \propto \sqrt{\phi_{x=0}}$. Therefore, we can re-write the FKO signal to be proportional to the change of surface electrostatic potential: $\Delta R/R\ (\hbar\omega) \propto \phi_{AC,x=0}$. As the applied potential at bulk GaP is kept the same throughout the experiment, the change of surface potential is responsible for the change of electrostatic potential drop at GaP $\phi_{AC,x=0} = \Delta\phi_{AC}$. When there are equal amounts of charge carriers (σ) on both sides of p-n junction, the potential drop ($\Delta\phi$) is proportional to the width of the charge carrier distribution (W): $\Delta\phi \propto \sigma W$. Either the potential drop at GaP ($\Delta\phi_{GaP}$) under dark or its change upon excitation $\Delta\phi_{AC}$ dominates over the potential drop at TiO_2 side due to the much larger depletion width in GaP (~220 nm for -1.5 V) compared to the thin TiO_2 layer (5 nm) (>97% potential drop in GaP). Therefore, we can connect the change of FKO signal with the band flattening potential across the GaP/TiO_2 junction V_{AC}: $\Delta R/R\ (\hbar\omega) \propto \Delta\phi_{AC} \approx V_{AC}$. The main decay pathway of FKO signal is the removal of the holes in GaP to external circuit and the interfacial recombination with separated electrons in TiO_2. Band flattening potential V_{AC}, on the other hand, initiates a potentiostat response to restore the set potential. The potentiostat does so by flowing current from the counter electrode and the corresponding V_{AC} decays by:[25]

$$V_{AC}(t) = V_{AC}(0)e^{-t/RC} \qquad 6.1$$

where the RC constant corresponds to the electrochemical cell's resistance and capacitance, R, is directly related to the electrolyte concentration by:[41]

$$R \approx R_{electrolyte} \propto \frac{1}{\kappa} = \frac{1}{\Lambda_m c} \quad 6.2$$

here κ is the conductance of the solution, Λ_m is the molar conductivity and c is the electrolyte concentration. For a strong electrolyte like $NaNO_3$, Λ_m is approximated to be Λ_m^0, which is the limiting molar conductivity. Thus, the decay rate is directly proportional to the electrolyte concentration c.

The competition between charge carrier dynamics is illustrated in Figure 6.3a. The photogenerated carriers initiate potentiostat removal of holes at a rate of k, which is proportional to the electrolyte concentration c (*process 1* in Figure 6.3a). As the photogenerated holes diminish, the FKO signal decays due to the disappearance of the photo-induced electric field E_{AC}. The removal of holes in GaP has the additional effect of suppressing interfacial recombination. At low electrolyte concentrations, the holes in GaP are long-lived, providing an interfacial recombination channel (k_r, *process 2*) with electrons in TiO_2. At higher electrolyte concentrations, the holes in GaP are removed quickly, effectively shutting down this recombination pathway. As a result, the electrons in TiO_2 survive long enough for the hydrogen reduction reaction with proton/water (k_{ct}, *process 3*).

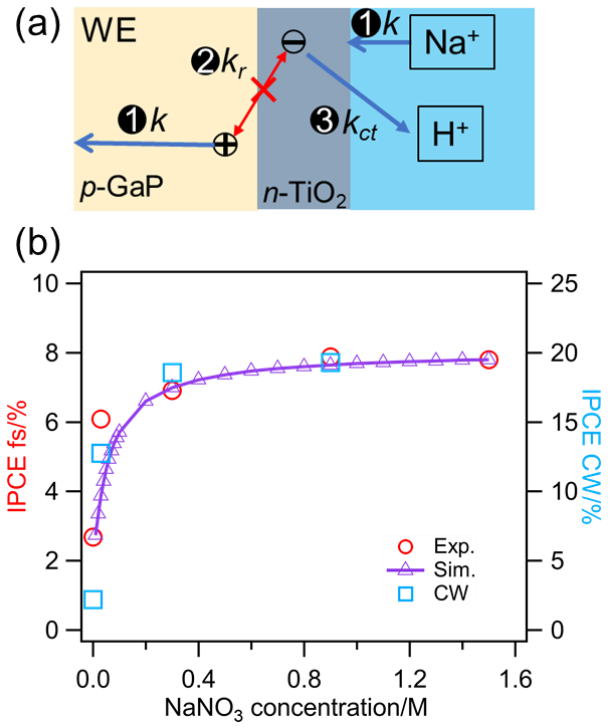

Figure 6.3. (a) Schematic diagram of interfacial recombination suppressed by the potentiostat removing hole in GaP. (b) IPCE at various $NaNO_3$ concentration under -1.5 V applied bias and 4.4 mW/cm^2 pulsed 400 nm excitation (red circle, left axis). The numerical simulation of the IPCE is shown in purple line and triangles. In comparison, the IPCE under -1.5V applied bias and 0.5 mW/cm^2 405 nm LED illumination is also shown (blue box, right axis).

The decay rate of the FKO signal is dictated by the slow rate of k in *process 1*. Thus, the recombination rate constant can be approximated to be $k=k_c c$. Combining Equations. 6.1 and 6.2, the overall decay pathway of $[h^+]$ and $[e^-]$ can be written as:

$$\frac{d[h^+]}{dt} = -k[h^+] - k_r[e^-][h^+] = -k_c c[h^+] - k_r[e^-][h^+] \quad 6.3$$

$$\frac{d[e^-]}{dt} = -k_r[e^-][h^+] \quad 6.4$$

Here, the first term in Equation 6.3 accounts for hole removal by the potentiostat, and the second term accounts for the interfacial recombination loss between electrons (in TiO_2) and holes (in GaP).

However, an analytical solution of Equations 6.3 and 6.4 proves to be difficult. Instead, a numerical solution is used. The numerical solution is obtained by assuming an initial hole and electron concentration $[h^+]=[e^-]=0.003$ (unit is ΔR/R), and then calculating the hole and electron concentration's temporal evolution with 0.01 μs step intervals with Equations 6.3 and 6.4 (Figure A6.4). The numerical solution provides a reasonable fit to the FKO kinetics, as shown in Figure 6.2d. This fitting approach yields k_c=0.62 $\mu s^{-1}M^{-1}$, consistent with the value obtained from the multi-exponential fitting, and k_r is determined to be 10 μs^{-1} (when $[e^-]$=0.003 ΔR/R).

This model is well supported by the *in-situ* IPCE measurements taken in various electrolyte concentrations under the same conditions as the TRS measurements. As shown in Figure A6.4, the electron concentration reaches equilibrium at ~100 μs, and its concentration $[e^-]_{100\mu s}$ corresponds to the total available $[e^-]$ for the chemical reaction (*process 3*), as shown in Figure 6.3a. Therefore, the *in-situ* IPCE can be written as:

$$IPCE = QE_{abs}QE_{CS}^{bulk}QE_{CS}^{int}QE_{RE} = QE_{abs}QE_{bulk} * \frac{[e^-]_{100\mu s}}{[e^-]_0}QE_{RE} \quad 6.5$$

where A accounts for bulk separation QE. $[e^-]_0$ is the initial total electron concentration (0.003 ΔR/R in this case). Here, QE_{bulk} is a constant under a certain applied biases and excitation powers, QE_{abs} is the absorbed photon percentage and is equal to 0.75. The $[e^-]_{100\mu s}$ is simulated for a range of electrolyte concentration, as shown in Figure 6.3b (purple curve). The measured *in-situ* IPCE and the simulated IPCE curve agree well when QE_{bulk} equals 0.104, which means a 10.4% QE for the bulk separation, which is consistent with what we obtained in a previous study (~9%). The QE_{RE} reaches ~100% with an electrolyte concentration of 1 M $NaNO_3$.

Interestingly, the IPCE measured under the same conditions but with CW illumination shows a similar trend, although with overall higher values due to the more efficient bulk separation.[39] As shown in Figure 6.3b, the IPCE under CW illumination increases with higher

$NaNO_3$ concentration, which also matches well with the fitting curve. This observation suggests that the model proposed here in Figure 6.3a is more general than pulsed excitation, and the interfacial recombination that can be suppressed by high cation concentration applies to photoelectrodes with similar structure.

The bias dependence of the FKO kinetics is further investigated at different applied biases under the same excitation power, as shown in Figure 6.4a. These kinetics shows weak bias dependence. This is partially true because at a high electrolyte concentration the FKO kinetics is dominated by first term in Equation 6.3, which is the hole removal by potentiostat. This process, as we will show later, is bias-independent. However, a close inspection of the FKO shows non-negligible differences as shown in Figure A6.5, where at low applied bias (-0.6 V) the FKO kinetics decays slightly faster than at more negative bias (-1.5 V). We believe that the difference is due to the different second term in Equation 6.3, the interfacial recombination. To better demonstrate this term, the FKO kinetics can be fitted by the numerical method described above. The FKO kinetics are first divided by E_{DC} to obtain the correct initial E_{AC}, which is linearly proportional to the hole concentration, followed by a universal scaling between different biases to have the same initial amplitude of 0.003 $\Delta R/R$ for -1.5 V for a simple comparison of the bimolecular recombination rate constant k_r. The treated FKO kinetics and its numerical fitting are shown in Figure 6.4b, where the fitting parameters are shown in Table A6.3.

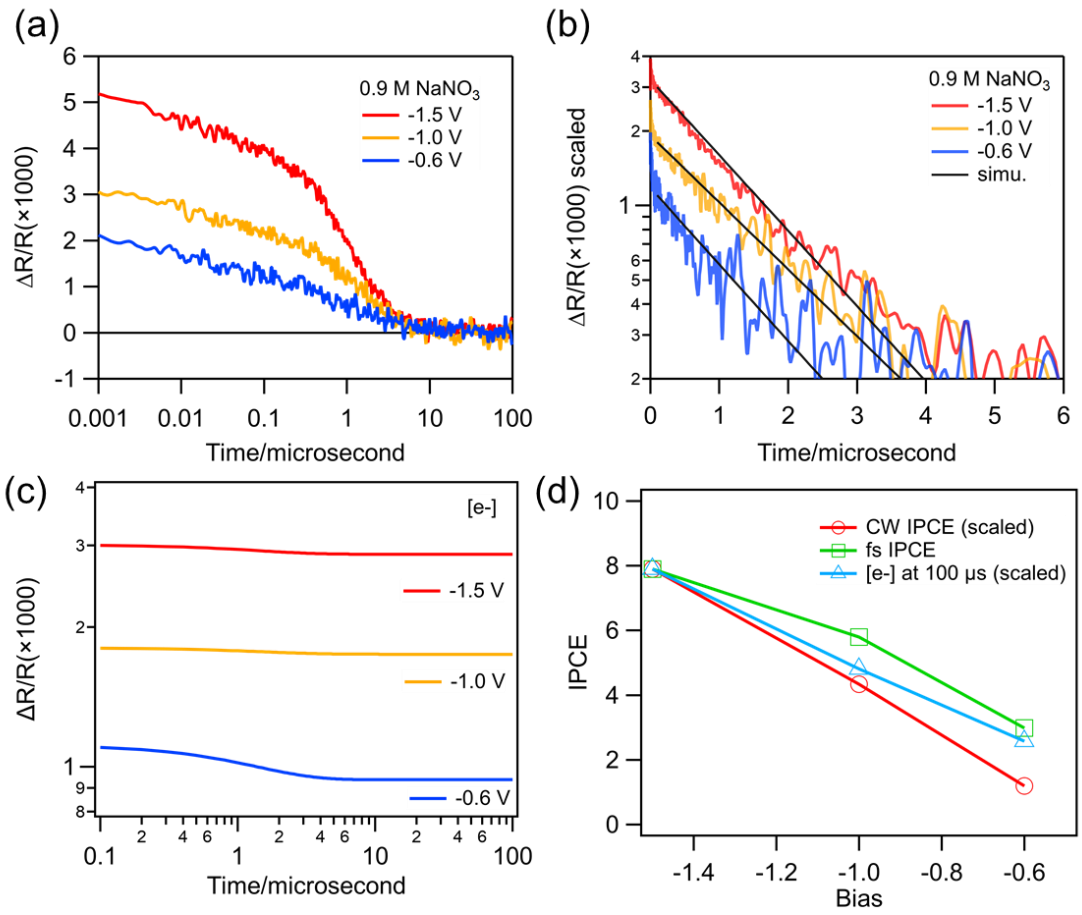

Figure 6.4. FKO kinetics under 300x pump beam size, 400 nm, 4.4 mW/cm^2 excitation, 0.9 M $NaNO_3$ aqueous solution and various applied bias. (a) The raw FKO kinetics. (b) The E_{AC} and its numerical fitting shown in black solid lines. (c) The simulated electron concentration over a 100 μs time window. (d) The IPCE measured *in-situ* under pulsed illumination, steady state CW illumination, and the $[e^-]_{100\mu s}$ from the simulation shown in panel c.

The fitting shows that the bimolecular recombination rate is the same for -1.5 and -1 V, and 10 times larger for -0.6 V, which is consistent with the increased recombination rate constant at low applied bias. The recombination loss is better visualized when $[e^-]_{100\mu s}$ is plotted in Figure 6.4c. Minimum loss of $[e^-]$ for -1.5 and -1 V, and a larger loss for -0.6 V are observed. The electron concentration at 100 μs (i.e., $[e^-]_{100\mu s}$) can again be used to compare the IPCE measured under

pulsed and CW illumination. The good agreement in Figure 6.4d proves our model to be robust. The difference in IPCE (or $[e^-]_{100\mu s}$) is caused by both the initial $[e^-]$ difference from the bulk charge separation (<1 ns) and the interfacial recombination loss demonstrated in this study (~μs).

6.4. Conclusion

Using nanosecond *in-situ* TRS, we have observed sequential events that occur after charge separation across the *p-n* junction. The FKO signal provides a direct probe of the photogenerated carriers interfacial processes. By studying the FKO kinetics, we first learned that the photogenerated carrier diffuses laterally while coupled with solution ions, which causes an artificial decay of the FKO signal. This undesirable decay can be avoided by using a larger pump beam size. The FKO signal also decays faster at higher electrolyte concentrations, due to the potentiostat removing photogenerated holes. The potentiostat response time depends on the electrolyte concentration. The removal of holes, in turn, suppresses the interfacial recombination, which increases the HER efficiency. This model is further verified by the IPCE measured *in-situ* under different excitation source and electrolyte concentrations. The agreement between the interfacial recombination rate determined by different methods proves this model to be robust. We showed a time-resolved picture of processes closely related to photocatalysis on a semiconductor photocathode, detailing the important role of the solution and the potentiostat's response to the overall IPCE. These findings are valuable to the mechanistic understanding of photocatalysis by semiconductors.

Appendix Chapter 6

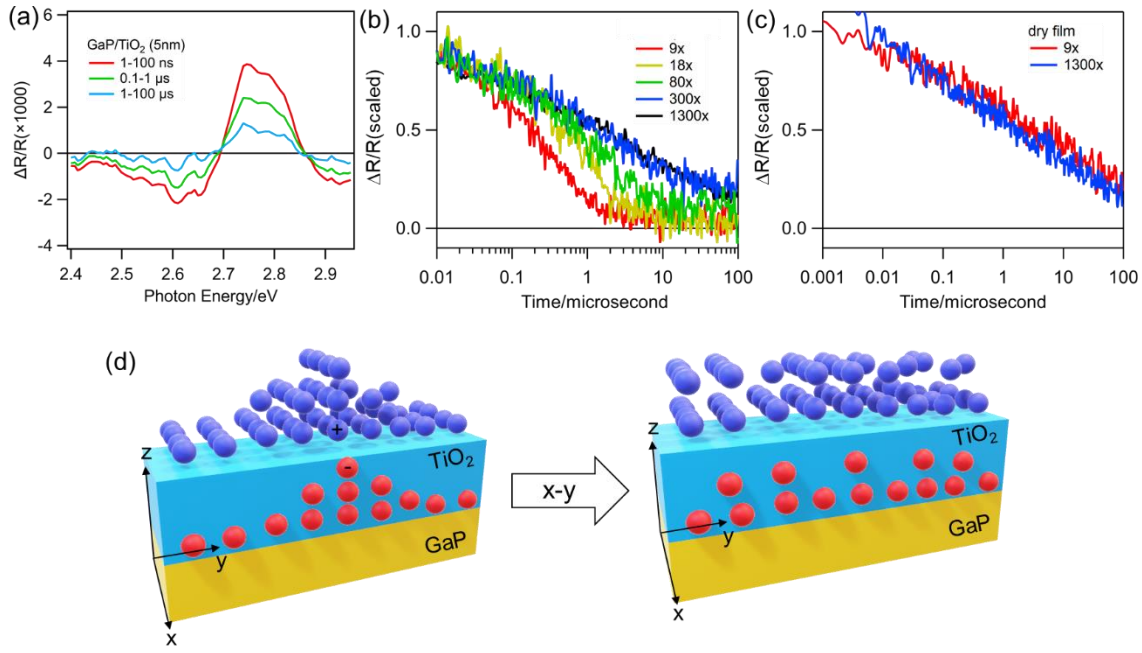

Figure A6.1. (a) Transient reflectance spectra of GaP/TiO_2 at various delay time under -1.5 V vs Ag/AgCl applied bias, in 0.1 M Na_2SO_4 aqueous solution. The sample is excited by 400 nm with an excitation density of 4.4 μJ/cm^2. The relative pump to probe beam size is 300 times. (b) FKO kinetics probed at 2.78 eV with various pump beam sizes. The legend indicates the relative pump to probe size. The excitation power is increased accordingly to maintain the same excitation density of 4.4 μJ/cm^2. Other experimental conditions are kept the same. (c) FKO kinetics comparison of different pump beam sizes of GaP/TiO_2 (5 nm) dry film. The excitation density is the same. (d) Schematics of carrier diffusion at indicated x-y (lateral) direction coupled with cations.

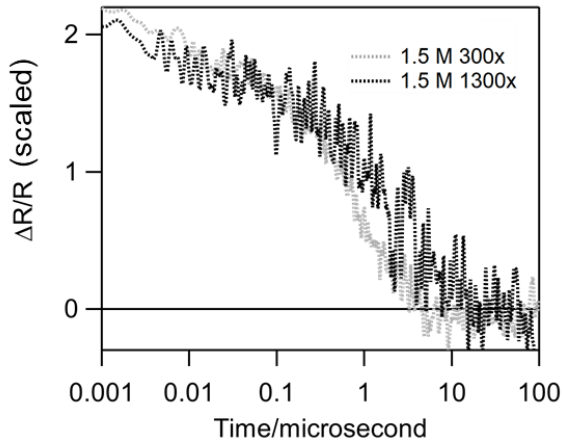

Figure A6.2. FKO kinetics with 300x and 1300x pump beam size with 400 nm 4.4 μJ/cm^2 excitation, -1.5 V vs Ag/AgCl applied bias, and 1.5 M $NaNO_3$ aqueous solution. The similar kinetics show that the x-y diffusion can be neglected even at highest electrolyte concentration.

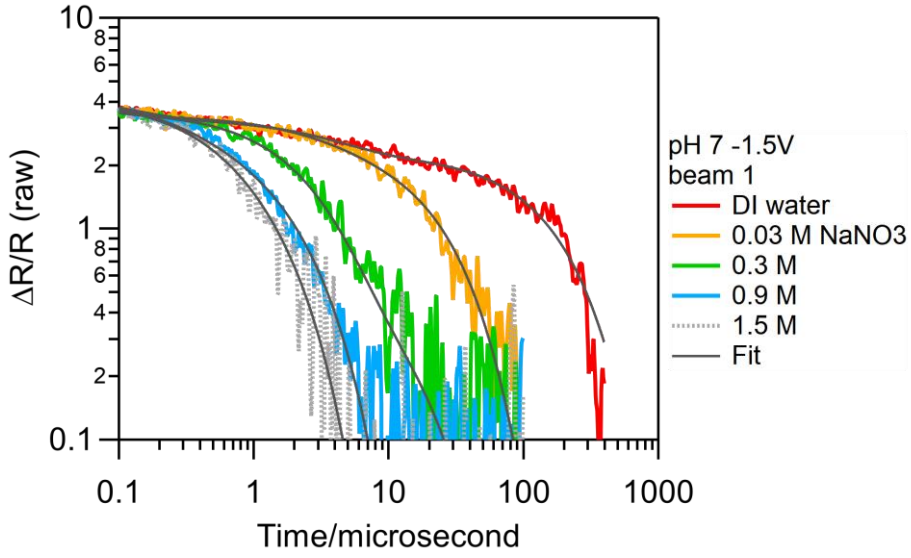

Figure A6.3. Exponential-exponential plot of Figure 6.1b and corresponding multiexponential fit.

The FKO decay kinetics is fitted with a three exponential decay function:

$$\frac{\Delta R}{R} = \sum_i a_i e^{-t/\tau_i} \qquad \text{A6.1}$$

The fitting result to Figure 6.1b is listed below in Table A6.1, a is in the unit of ΔR/R(*1000). τ is in the unit of microsecond.

Table A6.1. Fitting parameter of Figure 6.2b.

	DI water	**0.03 M**	**0.3 M**	**0.9 M**	**1.5 M**
a_0	1.13±0.02	0.98±0.02	0.89±0.03	0.88±0.81	1.00±0.04
a_1	1.07±0.02	0.83±0.05	3.02±0.09	0.88±0.47	1.34±0.07
a_2	2.23±0.02	2.62±0.06	0.60±0.01	2.44±0.76	2.78±0.31
τ_0/μs	0.11±0.00	0.05±0.00	0.03±0.00	0.24±0.11	0.008±0.001
τ_1/μs	3.84±0.25	2.97±0.32	2.52±0.09	0.72±0.85	0.42±0.07
τ_2/μs	192.4±4.3	25.6±0.7	14.3±2.3	2.19±0.31	1.38±0.09

The sum of cation induced quenching rate and the interfacial recombination rate is by averaging the τ_1 and τ_2 with averaged weight of a_1 and a_2. The interfacial recombination rate is approximated to the DI water decay rate, which is 0.008±0.0005 μs^{-1} (132±9 μs). Here, a simple assumption (which is used to provide an estimation of the quenching rate) of the recombination to be independent of electron concentration is used. The quenching rate is then calculated as:

$$k = \tau^{-1} - \tau_{rec}^{-1} = \frac{a_1+a_2}{a_1\tau_1+a_2\tau_2} - \tau_{rec}^{-1} \quad \text{A6.2}$$

The quenching rate in Figure 6.2c is listed in Table A6.2.

Table A6.2. Sodium cation quenching rate.

concentration of $NaNO_3$	**Quenching rate/μs^{-1}**
0.03 M	0.042±0.004
0.3 M	0.216±0.035
0.9 M	0.548±0.090
1.5 M	0.931±0.104

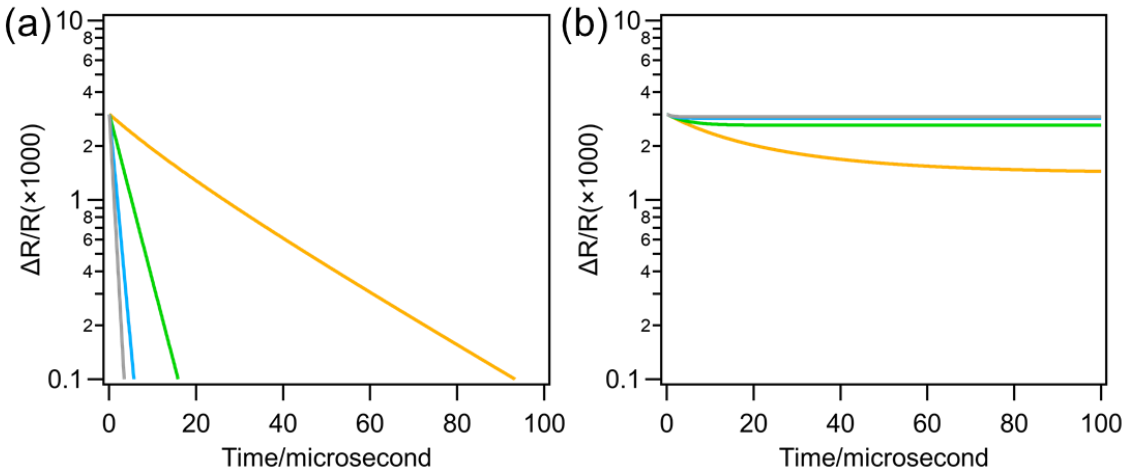

Figure A6.4. Numerical simulation to fit the FKO decay kinetics in Figure 6.2d. (a) hole concentration, (b) electron concentration.

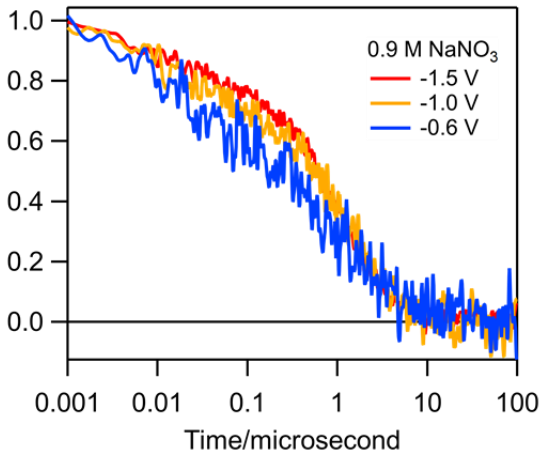

Figure A6.5. Normalized FKO kinetics at 1 ns for Figure 6.4a.

Table A6.3. Simulated FKO kinetics under different bias

Bias	E_{DC} (kV/cm)	k_r	*$[e^-]_0$	$[e^-]_{100\mu s}$	CW IPCE	fs IPCE
-0.6 V	183.185	100	0.0011	0.000937	3.4	1.79
-1.0 V	201.186	10	0.0018	0.001747	12.4	3.48
-1.5 V	221.64	10	0.003	0.00287	22.6	4.744

*$[e^-]_0$=0.003ΔR/R.

6.5. References

1. Xu, Z.; Hou, B.; Zhao, F.; Cai, Z.; Shi, H.; Liu, Y.; Hill, C. L.; Musaev, D. G.; Mecklenburg, M.; Cronin, S. B.; Lian, T., Nanoscale TiO_2 Protection Layer Enhances the Built-In Field and Charge Separation Performance of GaP Photoelectrodes. *Nano Letters* **2021,** *21* (19), 8017-8024.
2. Walter, M. G.; Warren, E. L.; McKone, J. R.; Boettcher, S. W.; Mi, Q.; Santori, E. A.; Lewis, N. S., Solar Water Splitting Cells. *Chem. Rev.* **2010,** *110* (11), 6446-6473.
3. Lewis, N. S.; Nocera, D. G., Powering the planet: Chemical challenges in solar energy utilization. *Proceedings of the National Academy of Sciences* **2006,** *103* (43), 15729-15735.
4. Weber, M. F.; Dignam, M. J., Efficiency of splitting water with semiconducting photoelectrodes. *Journal of The Electrochemical Society* **1984,** *131* (6), 1258-1265.
5. Bolton, J. R.; Strickler, S. J.; Connolly, J. S., Limiting and realizable efficiencies of solar photolysis of water. *Nature* **1985,** *316*, 495.
6. Hu, S.; Xiang, C.; Haussener, S.; Berger, A. D.; Lewis, N. S., An analysis of the optimal band gaps of light absorbers in integrated tandem photoelectrochemical water-splitting systems. *Energy & Environmental Science* **2013,** *6* (10), 2984-2993.
7. Döscher, H.; Geisz, J.; Deutsch, T.; Turner, J., Sunlight absorption in water–efficiency and design implications for photoelectrochemical devices. *Energy & Environmental Science* **2014,** *7* (9), 2951-2956.
8. Seitz, L. C.; Chen, Z.; Forman, A. J.; Pinaud, B. A.; Benck, J. D.; Jaramillo, T. F., Modeling practical performance limits of photoelectrochemical water splitting based on the current state of materials research. *ChemSusChem* **2014,** *7* (5), 1372-1385.
9. Coridan, R. H.; Nielander, A. C.; Francis, S. A.; McDowell, M. T.; Dix, V.; Chatman, S. M.; Lewis, N. S., Methods for comparing the performance of energy-conversion systems for use in solar fuels and solar electricity generation. *Energy & Environmental Science* **2015,** *8* (10), 2886-2901.
10. Yang, Y.; Gu, J.; Young, J. L.; Miller, E. M.; Turner, J. A.; Neale, N. R.; Beard, M. C., Semiconductor interfacial carrier dynamics via photoinduced electric fields. *Science* **2015,** *350* (6264), 1061-1065.
11. Chen, X.; Pekarek, R. T.; Gu, J.; Zakutayev, A.; Hurst, K. E.; Neale, N. R.; Yang, Y.; Beard, M. C., Transient Evolution of the Built-in Field at Junctions of GaAs. *ACS Appl. Mater. Interfaces* **2020,** *12* (36), 40339-40346.
12. Zhang, C.; Fan, Y.; Huang, X.; Zhang, K. H. L.; Beard, M. C.; Yang, Y., Hot-carrier transfer at photocatalytic silicon/platinum interfaces. *The Journal of Chemical Physics* **2020,** *152* (14), 144705.
13. Chen, X.; Choing, S. N.; Aschaffenburg, D. J.; Pemmaraju, C. D.; Prendergast, D.; Cuk, T., The Formation Time of Ti–O• and Ti–O•–Ti Radicals at the n-$SrTiO_3$/Aqueous Interface during Photocatalytic Water Oxidation. *Journal of the American Chemical Society* **2017,** *139* (5), 1830-1841.

14. Selim, S.; Francàs, L.; García-Tecedor, M.; Corby, S.; Blackman, C.; Gimenez, S.; Durrant, J. R.; Kafizas, A., WO_3/$BiVO_4$: impact of charge separation at the timescale of water oxidation. *Chemical Science* **2019,** *10* (9), 2643-2652.
15. Moss, B.; Hegner, F. S.; Corby, S.; Selim, S.; Francàs, L.; López, N.; Giménez, S.; Galán-Mascarós, J.-R.; Durrant, J. R., Unraveling Charge Transfer in CoFe Prussian Blue Modified $BiVO_4$ Photoanodes. *ACS Energy Letters* **2019,** *4* (1), 337-342.
16. Warnan, J.; Willkomm, J.; Ng, J. N.; Godin, R.; Prantl, S.; Durrant, J. R.; Reisner, E., Solar H2 evolution in water with modified diketopyrrolopyrrole dyes immobilised on molecular Co and Ni catalyst-TiO_2 hybrids. *Chem Sci* **2017,** *8* (4), 3070-3079.
17. Willkomm, J.; Orchard, K. L.; Reynal, A.; Pastor, E.; Durrant, J. R.; Reisner, E., Dye-sensitised semiconductors modified with molecular catalysts for light-driven H_2 production. *Chem Soc Rev* **2016,** *45* (1), 9-23.
18. Ma, Y.; Kafizas, A.; Pendlebury, S. R.; Le Formal, F.; Durrant, J. R., Photoinduced Absorption Spectroscopy of CoPi on $BiVO_4$: The Function of CoPi during Water Oxidation. *Adv. Funct. Mater.* **2016,** *26* (27), 4951-4960.
19. Kafizas, A.; Wang, X.; Pendlebury, S. R.; Barnes, P.; Ling, M.; Sotelo-Vazquez, C.; Quesada-Cabrera, R.; Li, C.; Parkin, I. P.; Durrant, J. R., Where Do Photogenerated Holes Go in Anatase:Rutile TiO_2? A Transient Absorption Spectroscopy Study of Charge Transfer and Lifetime. *J. Phys. Chem. A* **2016,** *120* (5), 715-723.
20. Ma, Y.; Le Formal, F.; Kafizas, A.; Pendlebury, S. R.; Durrant, J. R., Efficient suppression of back electron/hole recombination in cobalt phosphate surface-modified undoped bismuth vanadate photoanodes. *J. Mater. Chem. A* **2015,** *3* (41), 20649-20657.
21. Le Formal, F.; Pastor, E.; Tilley, S. D.; Mesa, C. A.; Pendlebury, S. R.; Grätzel, M.; Durrant, J. R., Rate Law Analysis of Water Oxidation on a Hematite Surface. *Journal of the American Chemical Society* **2015,** *137* (20), 6629-6637.
22. Reynal, A.; Willkomm, J.; Muresan, N. M.; Lakadamyali, F.; Planells, M.; Reisner, E.; Durrant, J. R., Distance dependent charge separation and recombination in semiconductor/molecular catalyst systems for water splitting. *Chem Commun (Camb)* **2014,** *50* (84), 12768-71.
23. Le Formal, F.; Pendlebury, S. R.; Cornuz, M.; Tilley, S. D.; Grätzel, M.; Durrant, J. R., Back Electron–Hole Recombination in Hematite Photoanodes for Water Splitting. *Journal of the American Chemical Society* **2014,** *136* (6), 2564-2574.
24. Barroso, M.; Cowan, A. J.; Pendlebury, S. R.; Grätzel, M.; Klug, D. R.; Durrant, J. R., The Role of Cobalt Phosphate in Enhancing the Photocatalytic Activity of α-Fe_2O_3 toward Water Oxidation. *Journal of the American Chemical Society* **2011,** *133* (38), 14868-14871.
25. Bard, A. J.; Faulkner, L. R., *Electrochemical methods : fundamentals and applications*. 2nd ed.; Wiley: New York, 2001.
26. Boucher, D. G.; Kearney, K.; Ertekin, E.; Rose, M. J., Tuning p-Si(111) Photovoltage via Molecule|Semiconductor Electronic Coupling. *J Am Chem Soc* **2021,** *143* (6), 2567-2580.

27. Zhou, W.; Dong, C.-L.; Wang, Y.; Huang, Y.-C.; He, L.; Chang, H.-W.; Shen, S., Manipulating metal-oxygen local atomic structures in single-junctional p-Si/WO_3 photocathodes for efficient solar hydrogen generation. *Nano Research* **2020,** *14* (7), 2285-2293.
28. Jung, J. Y.; Yu, J. Y.; Lee, J. H., Dynamic Photoelectrochemical Device Using an Electrolyte-Permeable NiO_x/SiO_2/Si Photocathode with an Open-Circuit Potential of 0.75 V. *ACS Appl Mater Interfaces* **2018,** *10* (9), 7955-7962.
29. Zhou, X.; Liu, R.; Sun, K.; Papadantonakis, K. M.; Brunschwig, B. S.; Lewis, N. S., 570 mV photovoltage, stabilized n-Si/CoO_x heterojunction photoanodes fabricated using atomic layer deposition. *Energy & Environmental Science* **2016,** *9* (3), 892-897.
30. Seo, J.; Kim, H. J.; Pekarek, R. T.; Rose, M. J., Hybrid organic/inorganic band-edge modulation of p-Si(111) photoelectrodes: effects of R, metal oxide, and Pt on H_2 generation. *J Am Chem Soc* **2015,** *137* (9), 3173-6.
31. Qiu, J.; Zeng, G.; Ha, M.-A.; Ge, M.; Lin, Y.; Hettick, M.; Hou, B.; Alexandrova, A. N.; Javey, A.; Cronin, S. B., Artificial Photosynthesis on TiO_2-Passivated InP Nanopillars. *Nano Letters* **2015,** *15* (9), 6177-6181.
32. Zeng, G.; Qiu, J.; Li, Z.; Pavaskar, P.; Cronin, S. B., CO_2 Reduction to Methanol on TiO_2-Passivated GaP Photocatalysts. *ACS Catal.* **2014,** *4* (10), 3512-3516.
33. Qiu, J.; Zeng, G.; Pavaskar, P.; Li, Z.; Cronin, S. B., Plasmon-enhanced water splitting on TiO_2-passivated GaP photocatalysts. *Phys. Chem. Chem. Phys.* **2014,** *16* (7), 3115-3121.
34. Jellison, G. E., Optical functions of GaAs, GaP, and Ge determined by two-channel polarization modulation ellipsometry. *Optical Materials* **1992,** *1* (3), 151-160.
35. Shen, H.; Dutta, M., Franz–Keldysh oscillations in modulation spectroscopy. *Journal of Applied Physics* **1995,** *78* (4), 2151-2176.
36. Shen, H.; Pollak, F. H., Generalized Franz-Keldysh theory of electromodulation. *Physical Review B* **1990,** *42* (11), 7097.
37. Hall, D. J.; Hosea, T. J. C.; Lancefield, D.; T., T. W.; J., L. A. F.; G., B. E., Airy function analysis of Franz–Keldysh oscillations in the photoreflectance spectra of $In_{1-x}Ga_xAs_yP_{1-y}$ layers. *Journal of Applied Physics* **1997,** *82* (6), 3092-3099.
38. Pollak, F. H., Study of semiconductor surfaces and interfaces using electromodulation. *Surface and Interface Analysis* **2001,** *31* (10), 938-953.
39. Xu, Z.; Hou, B.; Zhao, F.; Suo, S.; Liu, Y.; Shi, H.; Cai, Z.; Hill, C. L.; Musaev, D. G.; Mecklenburg, M.; Cronin, S. B.; Lian, T., Direct *in situ* Measurement of Quantum Efficiencies of Charge Separation and Proton Reduction at TiO_2-Protected GaP Photocathodes. *J. Am. Chem. Soc.* **2023,** *145* (5), 2860-2869.
40. Kronik, L.; Shapira, Y., Surface photovoltage phenomena: theory, experiment, and applications. *Surface Science Reports* **1999,** *37* (1), 1-206.
41. Wright, M. R., *An introduction to aqueous electrolyte solutions*. John Wiley: Chichester, England ; Hoboken, NJ, 2007

7 Synergizing Electron and Heat Flows in Photocatalyst for Direct Conversion of Captured CO_2

Reproduced in part with permission from Choi, C[†]., Zhao, F. [†], Hart, J. L., Gao, Y., Menges, F., Rooney, C. L., Harmon, N. J., Shang, B., Xu, Z., Suo, S., Sam, Q., Cha, J. J., Lian, T; & Wang, H., Synergizing Electron and Heat Flows in Photocatalyst for Direct Conversion of Captured CO_2. *Angew. Chem. Int. Ed.* **2023,** e202302152 – Published by Wiley Online Library.

Author contribution: C.C. and H.W. conceived and designed the project; C.C. conducted materials synthesis and characterization, photocatalytic reactions, and *in situ* spectroscopic measurements. C.L.W. helped with electrochemical characterization. Y.G. performed COMSOL simulation. B.S. helped with photochemical reactions. F.Z. conducted TA spectroscopic analysis with supervision from T.L.; J.L.H. and Q.P.S. performed STEM imaging with supervision from J.J.C.; N.J.H. performed ICP-MS; C.C., F.Z. and H.W. wrote the manuscript; T.L. and H.W. supervised the project. C. C. and F. Z. share equal contributions. All the authors discussed the results and commented on the manuscript.

7.1. Introduction

The photochemical CO_2 reduction reaction is an emerging way to convert abundant and clean solar energy into chemical energy and simultaneously remedy the earth from increasing carbon emissions. Critical steps for photochemical CO_2 reduction include generation of electron-hole pairs, transfer of electrons to catalytically active sites, and catalytic CO_2 reduction.[1-3] To meet these requirements, a semiconductor material is needed to efficiently convert photons to electron-hole pairs under sunlight illumination; the photo-generated electrons should be quickly transferred to catalytic sites that have a suitable binding affinity for CO_2 and a sufficient reduction potential

to reduce CO_2. Among all semiconductors, CdS is a proper candidate with a bandgap in the visible region (~ 43% energy of the solar spectrum) and a sufficiently high conduction band minimum that suits CO_2 photoreduction.[4] While several structural modification approaches have been reported for improving the photochemical CO_2 reduction performance of CdS,[5-6] current CdS-based photocatalytic systems are still limited by fast electron-hole recombination, slow electron transfer to catalytic sites, and insufficient CO_2 reduction activity.[7] Ideally, an effective electron transfer component connecting the light absorber with a highly active CO_2 reduction catalyst would address these issues. However, realizing such a photocatalyst architecture is a notable challenge as it requires solving physical and chemical problems at multiple material interfaces.[7]

Practical photochemical CO_2 valorization will have to take CO_2 capture into consideration. Lewis base molecules like alkyl amines are well-known absorbents that can effectively capture CO_2 by forming carbamates.[8] However, regenerating CO_2 from carbamate solutions for CO_2 utilization usually requires extensive heating, which is energy-demanding and may produce toxic byproducts.[9] Direct conversion of a carbamate to yield CO_2 reduction products and simultaneously regenerate the amine would be an ideal approach to integrated CO_2 capture and utilization. However, these reactions are challenging because additional energy is required to break the C-N bond in the carbamate.[10-12] In consideration of this need, a smart design of CO_2 reduction photocatalyst materials might be to incorporate a component that can photothermally liberate or activate CO_2 from its carbamate form near the CO_2 reduction catalytic sites.

In this chapter, we developed a ternary hybrid photocatalyst material, consisting of CdS quantum dots (QDs) and cobalt phthalocyanine (CoPc) molecules selectively anchored on multiwalled carbon nanotubes (CNTs), that addresses all the aforementioned challenges. In this material architecture, CdS is the light absorber, CoPc is the CO_2 reduction catalyst with known

activity and selectivity for CO production like several other metal phthalocyanines and porphyrins,[13-17] and CNT serves as a charge transfer highway between CdS and CoPc. The intimate CdS/CNT and CNT/CoPc interfaces resulting from well-controlled material synthesis significantly accelerate charge carrier separation in the light absorber and electron transfer to the catalytic sites through the highly conductive CNTs. Our photocatalyst delivers a high CO production rate of 6.3 μmol h^{-1} (6.3 mmol g^{-1} h^{-1}) under visible light illumination. Remarkably, the photothermal effect of CNT enables local heating near the photocatalyst, which makes carbamate reactive. Taking advantage of this property, we successfully demonstrated direct photochemical production of CO from CO_2 captured by monoethanolamine (MEA) from air.

7.2. Materials and Methods

7.2.1. Materials

Cadmium oxide (≥ 99.99%), oleylamine (technical grade, 70%), oleic acid (technical grade, 90%), 1-octadecene (ODE, technical grade, 90%), *N,N*-dimethylformamide (DMF, anhydrous, 99.8%), cobalt(II) phthalocyanine (CoPc), triethanolamine (TEOA, ≥ 99.0%), and $KHCO_3$ (99.7%) were purchased from Sigma-Aldrich. n-hexane, methanol, and acetonitrile (≥ 99.6%) were purchased from Fisher Scientific. Multiwalled CNTs were purchased from C-Nano (product number FT 9100). CO_2 (USP medical grade) and Ar (99.999%) were purchased from Airgas. We used deionized water from a Millipore water purification system (18.2 MΩ cm at 25 °C) for all experiments. All purchased chemicals were used without further purification unless otherwise noted.

To prepare the CdS/CNT/CoPc, we start with the preparation of CNTs. Purchased multiwalled CNTs were purified by a two-step process. As-received CNTs were calcinated at 500 °C in air for 5 hours, and the calcined CNTs were put in a 5 wt.% HCl aqueous solution. The

mixture was sonicated for 30 min and then stirred overnight. We washed the CNTs with deionized water until pH neutral and collected them by freeze-drying. 383 mg of CdO in 3.9 mL of ODE and 3.9 mL of oleic acid was heated at 140 °C in an oil bath overnight under magnetic stirring at 500 rpm, after which the mixture turned into a transparent cadmium oleate precursor. We then added 40 mg of purified CNTs and 4 mL of 1 M sulfur in oleylamine to the prepared Cd precursor solution at 140 °C. After 2 hours of reaction, the mixture was cooled down in an ice bath. We collected the CdS/CNT product via centrifugation after washing it with hexane/ethanol and ethanol/methanol several times. To assemble CoPc on CdS/CNT, we dispersed the synthesized CdS/CNT (~ 80 mg) in a mixed solvent of 40 mL of DMF and 40 mL of methanol and sonicated the suspension for 1 hour. The CoPc/DMF dispersion (2 mg in 20 mL) was also sonicated for 1 hour. The two mixtures were merged and sonicated for another hour. The mixture was further stirred overnight. The product was collected via centrifugation after washing with DMF and water. Finally, the CdS/CNT/CoPc hybrid material was collected by freeze-drying. Unsupported CdS QDs were synthesized in the same way as CdS/CNT, except that no CNTs were added in the synthesis and the reaction temperature was 180 °C. CdS/CoPc was then prepared with a similar procedure as loading CoPc on CdS/CNT.

7.2.2. General Characterization Methods

Inductively coupled plasma–mass spectrometry (ICP–MS) was performed using an Agilent Technologies 7700 series instrument. Gas chromatography (GC) (MG #5, SRI Instruments) equipped with a flame ionization detector (with a methanizer) and a thermal conductivity detector was used to analyze gas products from photochemical CO_2 reduction. High-resolution STEM-HAADF images were acquired with a Cs probe-corrected Thermo Fisher Scientific Spectra 300 Kraken (S)TEM with an Extreme-Brightness Cold Field Emission Gun (X-CFEG). Data was

collected at 120 kV with a probe current of ~ 60 pA. Raman spectra were collected using a confocal Raman microscope with a 633 nm laser (LabRAM HR Evolution, Horiba Jobin Yvon). Ultraviolet photoelectron spectroscopy (UPS) data was obtained with a PHI VersaProbe II X-ray photoelectron spectrometer with low-energy photons (He I, 21.2 eV). The XRD measurements were carried out using a multipurpose thin-film X-ray diffractometer (D/Max 2500, Rigaku). UV-visible absorption spectroscopy was performed with a Shimadzu UV-2600 UV-visible spectrophotometer. Cyclic voltammetry was performed with a Bio-Logic VMP3 Multi Potentiostat. The counter electrode was a graphite rod from Sigma-Aldrich, and the reference electrode was a Ag/AgCl (0.1976 V vs SHE) electrode from Pine Research Instrumentation. The cathode and anode compartments were separated by an anion-exchange membrane (Selemion DSV).

7.2.3. Measuring work function and valence band maximum (VBM) with UPS

Before analyzing our samples, we analyzed a gold foil to verify the method and our operation (Figure A7.5a-c). Before measurement, 30 min of Ar sputtering was applied to remove surface contamination on the gold foil. A -5 V external bias was applied during the measurement to obtain the secondary electron cutoff (SEC). We used the MultiPack software to determine VBM and SEC. The equation below was used to obtain the work function value:[18]

$$e\emptyset_m = hv - (E_{K,max}^{meas} - E_{K,min}^{meas}) \quad (7.1)$$

$e\emptyset_m$: work function

hv: 21.22 eV (He I)

$E_{K,max}^{meas}$: VBM or the maximum kinetic energy of emitted electrons

$E_{K,min}^{meas}$: SEC or the minimum kinetic energy of emitted electrons

The measured work function of the gold foil was 5.1 eV with VBM at -5.088 eV and SEC at 10.996 eV (Figure A7.5a-c), which is consistent with the reported value.[19] For CNTs, the

measured VBM (-5.106 eV) and SEC (11.998 eV) provided a work function of 4.096 eV. For all work function measurements (Figure A7.5), a -5 V bias was applied. No external bias was applied for VBM measurements (Figure A7.6).

7.2.4. TA measurement conditions

Transient absorption (TA) spectroscopy setup is described in Chapter 2, section 2.1. In femtosecond experiments in this study, power density of 13.6 μJ cm^{-2} (400 nm) was used to excite CdS QDs (Figure 7.3c); power density of 201.6 μJ cm^{-2} (400 nm) was used to excite CdS/CNT, CdS/CNT+TEA, CdS/CNT/CoPc, and CdS/CNT/CoPc+CO_2+TEA samples; power densities of 201.6 (400 nm), 147.2 (550 nm) and 100.8 (800 nm) μJ cm^{-2} were used to excite samples in near-IR TA measurements to ensure the same photon flux. In nanosecond TA experiments, power densities of 60 μJ cm^{-2} (400 nm) and 700 μJ cm^{-2} (400 nm) were used to excite CdS QDs and CdS/CNT, respectively. Data collected from nanosecond and femtosecond TA measurements were stitched together by scaling the data at 3 ns to generate the results shown in Figure 7.3c. Although the power density used in the nanosecond TA measurements is above the single exciton region threshold, the results should not be affected by Auger recombination which occurs on the picosecond to sub-nanosecond timescale.[20-23] 1 mm cuvettes were used for all samples. A magnetic stirring condition of 1000 rpm was applied during both femtosecond and nanosecond experiments.

Samples for TA experiments were prepared by dispersing 1.8 mg of CdS QDs in 5 mL of toluene, 3 mg of CdS/CNT in 5 mL of toluene, 3.2 mg of CdS/CNT/CoPc in 5 mL of toluene, or 1.7 mg of CdS/CoPc in 5 mL of toluene. The CNT sample was prepared by suspending 1 mg of purified CNTs in 1 mL of ethanol with 10 μL of a 5 wt.% Nafion solution (Sigma-Aldrich). Control experiments with TEA were performed by replacing the pure toluene solvent with a mixed solvent containing 90% toluene and 10% TEA (vol%).

7.2.5. Photochemical CO_2 reduction measurements

Photochemical CO_2 reduction was carried out in a custom-designed gas-tight cylindrical quartz cell with a volume of 17 mL and an inner radius of 0.37 cm. 1 mg of CdS/CNT/CoPc was dispersed in 5 mL of TEOA-acetonitrile (1:4 volumetric ratio) via 30 min of sonication. The cell was connected to inlet and outlet gas lines. We purged CO_2 in the cell for 10 min and then kept the flow rate at 2 sccm. The outlet line was connected to the GC which sampled the gas every 10 min. For reactions using amine-captured CO_2, 1 mg of CdS/CNT/CoPc was dispersed in 5 mL of 0.2 M aqueous MEA in the reaction cell via 30 min of sonication. We purged CO_2 in the cell for 20 min and switched to Ar for 2 hours to remove residual CO_2. In the case of CO_2 captured from air, we purged air for 4 hours and then Ar for 2 hours. The cell was closed during the photochemical reaction. After 2 hours of reaction, we manually injected 1 mL of the gas in the cell into the GC using a syringe. We used three types of light sources in our experiments: a 150 W AM1.5G-filtered Xe lamp with 216 mW cm^{-2} beam power (ABET Technologies), a 405 nm LED with 47 mW cm^{-2} beam power (Thorlabs), and a 300 W Xe lamp with 766 mW cm^{-2} beam power (618 mW cm^{-2} with UV filter, Newport Corporation). The power of each light source was measured by a laser power meter (AI310 Astral). Except for reactions with LED, we immersed the cell in a 6.4 × 6.4 × 6.4 cm^3 quartz tank filled with water to cut off the IR spectrum and help stabilize the reaction temperature. Products (H_2 and CO) were quantified by the GC using calibration curves.

7.2.6. In situ Raman spectroscopy and in situ UV-visible spectroscopy

A custom-designed gas-tight quartz cell (5 mm diameter and ~ 8 cm height) was used for *in situ* Raman spectroscopy. In the experiment of reducing methyl viologen (MV^{2+}), 1 mg of CdS/CNT/CoPc was dispersed in 5 mL of TEOA-acetonitrile (1:4 volumetric ratio) via 30 min of sonication, and 9 mg of MV^{2+} was dissolved in another 5 mL of TEOA-acetonitrile (1:4 volumetric

ratio). The two mixtures were merged, and 0.45 mL of the merged dispersion was used in the cell. The reaction was under Ar atmosphere. In the experiment of reducing CO_2, we prepared 1 mg of CdS/CNT/CoPc dispersed in 5 mL of TEOA-acetonitrile (1:4 volumetric ratio) and used 0.45 mL of the mixture for reaction. A 633 nm laser was used for *in situ* Raman spectroscopy. For *in situ* UV-visible spectroscopy, we used a cuvette from Firefly Sci. 1 mg of CdS/CNT/CoPc was dispersed in 5 mL of TEOA-acetonitrile (1:4 volumetric ratio), and 3 mL of the mixture was used for the reaction. We used the 405 nm LED for all *in situ* spectroscopy experiments.

7.2.7. Modeling of CNT local heating

Based on our experiments shown in Figure A7.21, we built a model system comprising a CNT and a water body surrounding it using the heat transfer in solid and fluid method in the heat transfer module of COMSOL. The heat transfer in solid and liquid was calculated as:

$$Q_{solid} = \rho_s C_{p_s} \frac{\partial T}{\partial t} + \nabla \cdot q_s \tag{7.2}$$

$$Q_{liquid} = \rho_l C_{p_l} \frac{\partial T}{\partial t} + \rho_l C_{p_l} \mu \cdot \nabla T + \nabla \cdot q_l \tag{7.3}$$

$$q_s = -k_s \nabla T \tag{7.4}$$

$$q_l = -k_l \nabla T \tag{7.5}$$

where ρ_s is the density of CNT, ρ_l is the density of water, μ is the bulk viscosity of water, C_{p_s} and C_{p_l} are heat capacities of CNT and water, respectively, at constant pressure, k_s and k_l are thermal conductivities of CNT and water, respectively, $\frac{\partial T}{\partial t}$ is the change of temperature with respect to time, and ∇T is the temperature gradient.

The material properties of water were retrieved from COMSOL's Material Library while the properties of the CNT were set to be 1.7 g cm^{-3} for density and 2586 W m^{-1} K^{-1} for thermal conductivity.[24] The dimensions of the modeled CNT were chosen to be 20 μm in length and 50 nm

in diameter to mimic the CNTs used in the CdS/CNT/CoPc hybrid material. The volume ratio of the water body to the CNT was calculated to be 8.5×10^5 based on their densities and masses used in the experiment (150 g of water and 0.3 mg of CNTs). The CNT was set to be a boundary heat source while the water was selected to be a uniform heat source. The power of the water body was calculated based on the experimental data that illumination increased the temperature of the 150 g of water by 6 °C within the course of 1 hour. The introduction of 0.3 mg of CNTs was experimentally found to cause another 5 °C of temperature increase in the water during the 1 hour of illumination, based on which the power of the CNT was calculated. The simulated system was programed to initiate with a thermal equilibrium state at 20 °C and to terminate when the water body temperature reached 31.5 °C.

7.3. Results and Discussion

The CdS/CNT/CoPc ternary hybrid material was synthesized by firstly growing CdS QDs on multiwalled CNTs and subsequently assembling CoPc molecules on the uncovered CNT surfaces. We reacted cadmium (II) oleate with elemental sulfur in the presence of CNTs, oleic acid (OA) and oleylamine in octadecene at 140 °C to form CdS/CNT. The reaction temperature was controlled to be considerably lower than typical CdS QD syntheses (~ 250 °C) to allow for selective nucleation and growth of QDs on CNT surfaces.[25] OA served as a capping agent to control the size of CdS QDs. Transmission electron microscopy (TEM) characterization of CdS/CNT/CoPc revealed that nanoparticles with a narrow size distribution are selectively and uniformly anchored on CNT surfaces (Figure A7.1). Scanning transmission electron microscopy recorded with a high-angle annular dark-field detector (STEM-HAADF) clearly showed spherical nanoparticles with a diameter of ~ 5 nm on CNTs (Figure 7.1a). X-ray diffraction (XRD) confirmed the successful synthesis of CdS in the zinc blende phase (Figure 7.1b). The hybrid material shows

two absorption peaks in the UV-visible spectrum at 480 nm and 660 nm (Figure 7.1c), characteristic of CdS QDs and CoPc, respectively.[15, 26] Elemental mapping by electron energy loss spectroscopy (EELS) visualized CNTs and CdS QDs in the hybrid structure (Figure 7.1d-g). Notably, a layer of C is visible on the surface of the CdS QDs (red box in Figure 7.1e), which reflects the surface ligands. This OA capping layer may help suppress the toxicity of CdS as opposed to previous studies which mostly used uncapped CdS photocatalysts.[27-28]

CoPc molecules were assembled onto the uncovered CNT surfaces of CdS/CNT via non-covalent π-π interaction. High-resolution STEM-HAADF imaging of CdS/CNT/CoPc showed dispersion of high-contrast atoms (heavy metal atoms such as Co) on CNTs (Figure 7.1h). Energy dispersive X-ray (EDX) spectroscopy analysis confirmed the presence of Co element in CdS/CNT/CoPc but not in bare CNTs (Figure A7.2), which verifies the effective loading of CoPc. Inductively coupled plasma mass spectrometry (ICP-MS) revealed that the hybrid material contains approximately 70 wt% of CdS, 30 wt% of CNT, and 0.15 wt% of CoPc. These characterization results together delineate the structure of the CdS/CNT/CoPc ternary hybrid material as illustrated in Figure 7.1i.

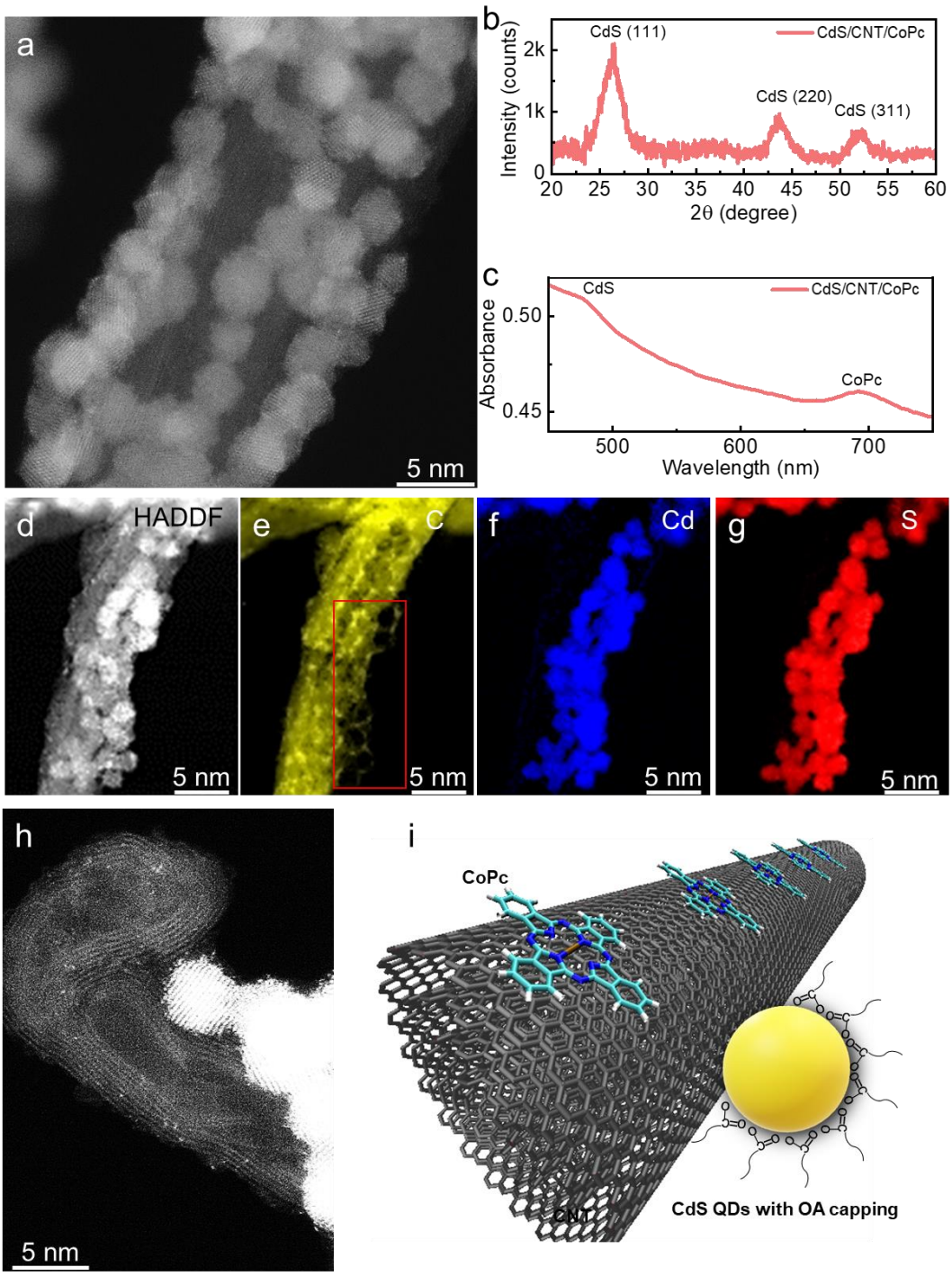

Figure 7.1. CdS/CNT/CoPc hybrid material. (a) STEM-HAADF image of CdS/CNT/CoPc. (b) XRD of CdS/CNT/CoPc. (c) UV-visible spectroscopy of CdS/CNT/CoPc. (d)-(g) STEM-HAADF

image and EELS elemental mapping of CdS/CNT/CoPc. (h) High-resolution STEM-HAADF image of CdS/CNT/CoPc. (i) Schematic illustration of CdS/CNT/CoPc structure.

Additional characterization was performed to understand the electronic structure of the ternary hybrid photocatalyst (Table A7.1). Cyclic voltammetry was used to determine the redox levels of CoPc and their positions with respect to the standard electrode potential of CO_2/CO (Figure A7.3). The first reduction level is 0.07 eV below CO_2/CO, and the second reduction is 0.5 eV higher (Figure 7.2). The energy gap corresponding to the Q band of CoPc was determined to be 1.78 eV from the Tauc plot (Figure A7.4). Ultraviolet photoelectron spectroscopy (UPS) was carried out to determine the work function of CNT as 4.09 eV (Figure A7.5) and the valence band maximum of CdS as 1.99 eV below the Fermi level of CNT (Figure A7.6). The band gap of the CdS QDs was measured from the Tauc plot to be 2.45 eV (Figure A7.7 and A7.8). These results allowed us to draw a wholistic energy band diagram of the CdS/CNT/CoPc ternary hybrid photocatalyst as shown in Figure 7.2. On the light absorber side, the conduction band of CdS QDs is high enough to generate electrons with sufficient reducing power for CO_2 conversion to CO. These electrons can be easily transferred to CNTs. On the co-catalyst side, CoPc needs to be doubly reduced to be active for reducing CO_2 to CO, which is consistent with the understanding from our prior electrocatalytic studies.[29] However, the second reduction energy level of CoPc is 0.26 eV higher than the Fermi level of CNTs, which indicates that electron accumulation in CNTs is required to further inject electrons into singly reduced CoPc.

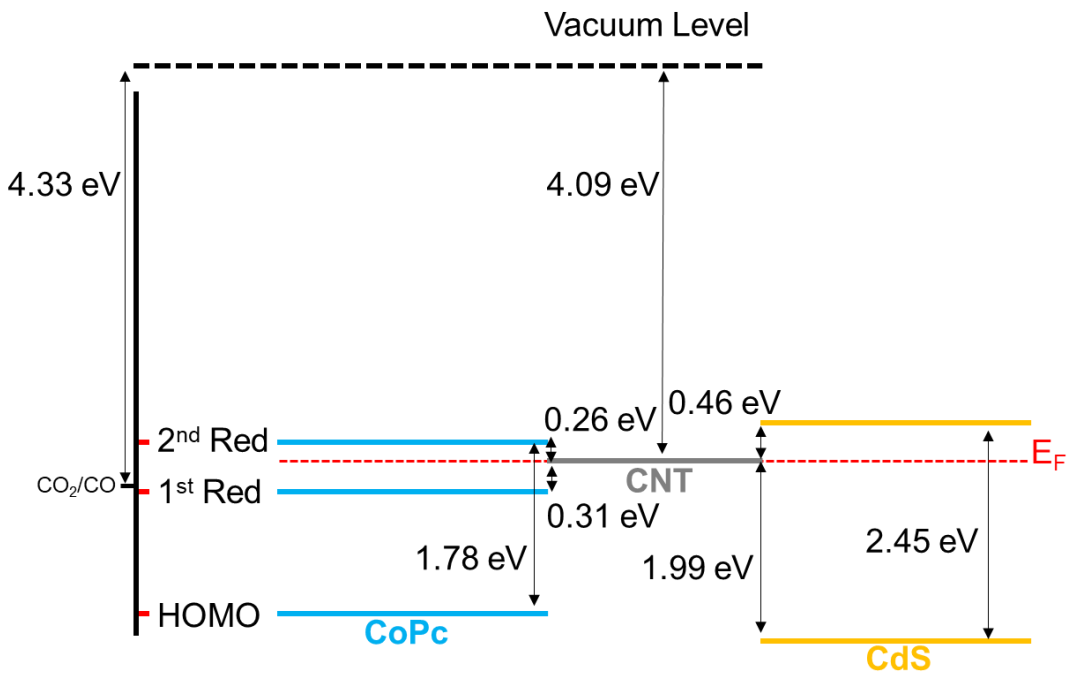

Figure 7.2. Electronic energy level diagram of CdS/CNT/CoPc.

Transient absorption (TA) spectroscopy was carried out to study the photo-induced charge separation process in the CdS/CNT/CoPc hybrid photocatalyst. Upon 400 nm excitation, CdS QDs, CdS/CNT and CdS/CNT/CoPc all exhibited a signal bleach centered at ~ 475 nm (Figure 7.3a, b, and Figure A7.9), which is related to the state-filling effect of the first exciton transition of CdS. As has been shown previously, the amplitude of the CdS exciton bleach can be directly related to the population of excited electrons at the CdS conduction band edge and can be used to follow the kinetics of electron-hole recombination and interfacial electron transfer.[30-31] This measurement was performed with power density within the single exciton region identified from the plot of maximum bleach signal recorded at 1 ps vs excitation power density (Figure A7.10) to avoid complication from multi-exciton Auger recombination in CdS QDs. CdS/CNT showed a higher single exciton threshold power density than CdS QDs, which is attributed to the absorption and

scattering by the CNTs that leads to decreased photon absorption of CdS under the same power density.

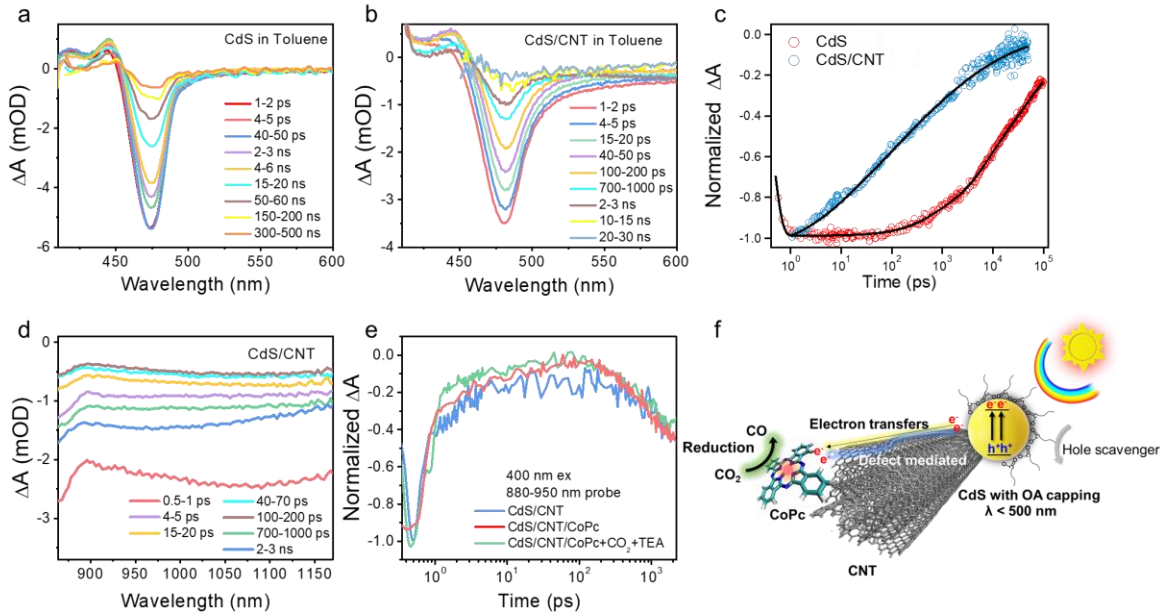

Figure 7.3. Electron transfer kinetics. TA spectra (400 nm excitation) probing CdS exciton bleach signal for (a) CdS QDs and (b) CdS/CNT at varied time delays. (c) Comparison of normalized exciton bleach signal decay between CdS/CNT and CdS QDs. Signal was averaged from 468 nm to 483 nm. Black curves are fitting results using Equations A7.1 and A7.2. (d) Near-IR TA spectra (400 nm excitation) probing CNT bleach signal for CdS/CNT. (e) CNT bleach kinetics of CdS/CNT and CdS/CNT/CoPc. Signal was averaged from 880 nm to 950 nm. (f) Proposed electron transfer pathway.

The exciton bleach signal of CdS/CNT showed a faster decay than free CdS QDs without CNT (Figure 7.3c), suggesting the transfer of excited electrons from CdS to CNT. The exciton bleach recovery kinetics of the CdS QDs can be fitted by a multi-exponential decay equation with an average lifetime of 168±24 ns (Table A7.2 and Equations A7.1, A7.3). This non-single-exponential decay of the exciton bleach signal has been attributed to the recombination of electrons

in the conduction band with holes in the trap states of CdS.[32] The exciton bleach kinetics of CdS/CNT can be best fitted by a stretched exponential decay function (Table A7.2 and Equation A7.2), which describes the kinetics of charge transfer from CdS to CNT via a dispersive transport model.[33-35] The fitting results are summarized in Table A7.2.

The dramatic difference in exciton average lifetime between CdS/CNT and CdS QDs reflects a ~ 37 times faster interfacial electron transfer rate in CdS/CNT than the electron-hole charge recombination rate within CdS. From the exciton bleach decay kinetics shown in Figure 7.3c, the electron transfer quantum yield QE_{ET} can be calculated to be 76.6 % using a previously proposed model (Equation A7.5).[36] The rapid electron transfer from CdS to CNT is also supported by our observation of no difference in decay kinetics within the first 5 ns when a hole scavenger, triethylamine (TEA), was introduced into the system (Figure A7.11a). CdS/CNT/CoPc showed the same exciton bleach kinetics as CdS/CNT without CoPc (Figure A7.11b). This indicates that the charge transfer from CNT to CoPc occurs on a much slower timescale and has no effects on the initial charge separation. It also rules out the possibility of direct electron transfer from CdS to CoPc molecules in the CdS/CNT/CoPc hybrid material. Thus, the observed fast exciton bleach signal decay for CdS/CNT is mainly attributed to the rapid electron transfer from CdS to CNT upon the excitation of CdS.

TA spectra in the near-IR region were used to characterize the arrival kinetics of electrons to CNT in the hybrid photocatalyst. Upon excitation, we observed a broad negative signal in the 870 – 1175 nm region for both CdS/CNT (Figure 7.3d) and pure CNTs (Figure A7.12a), which is assigned to the bleach of the M11 transition of metallic CNTs.[37-38] The wide size distribution of the CNTs is likely responsible for the broad signal. The decay kinetics of CNTs can be fitted by a single exponential function with a time constant of 171 ± 9 fs (Figure A7.12b), indicating fast

carrier relaxation due to electron-phonon scattering.[38-40] Interestingly, the bleach signal of CdS/CNT upon 400 nm excitation exhibits complex kinetics consisting of a decay component from 0 to 100 ps and then a gradual increase component from 100 ps to 2 ns (Figure 7.3d, e) in addition to the sub-picosecond decay observed for CNTs alone. This kinetics can be explained by the model proposed in Figure A7.13c and Equation A7.9. Briefly, the first term in Equation A7.9 describes the sub-picosecond decay component, which can be fitted with the same instantaneous rise and sub-picosecond decay time constants of the signal observed for pure CNTs and can be attributed to carrier dynamics resulted from the direct excitation of CNTs by 400 nm light. This assignment is further supported by the observation of the same fast decay kinetics in CdS/CNT excited by 800 nm light (Figure A7.13a), which selectively excites the CNT (and not the CdS) component. The second and third terms describe the kinetics of electron transfer from CdS QDs to the subpopulations of CNTs with and without electron traps, respectively. In CNTs with electron traps, due to an electron trapping time (0.14 ps) that is much faster than the interfacial electron transfer from CdS, the electron population (the bleach amplitude) grows on the electron trapping time scale and decays on the time scale of electron transfer, which accounts for the decay component on the sub-picosecond to 100 ps time scale in Figure 7.3e. In CNTs with negligible numbers of electron traps, the electron population grows with the electron transfer kinetics, which accounts for the bleach signal growth on the 100 ps to 2 ns time scale in Figure 7.3e. The details of the fitting model are described in Equation A7.9 and the fitting parameters are listed in Table A7.3. This model, with a clear physical meaning (Figure A7.13c) that is consistent with the experimentally measured energy levels (Figure 7.2), provides a satisfactory fit to the observed complicated kinetics (Figure A7.13a), which supports electron accumulation in the CNTs of CdS/CNT/CoPc under illumination (excitation of CdS). The accumulated electrons in CNT can raise its Fermi level and enable

electron transfer to the second reduction state of CoPc (Figure A7.13c and Figure 7.2). No difference in kinetics between CdS/CNT and CdS/CNT/CoPc was observed (Figure 7.3e) since the reduction of CoPc takes place on a much slower timescale. Adding TEA also made no difference (Figure 7.3e), indicating that no back recombination takes place between separated electrons in CNTs and holes in CdS within the 5 ns time range.

The photocatalytic performance of CdS/CNT/CoPc for CO_2 reduction was tested in acetonitrile with triethanolamine (TEOA) as the electron donor under the illumination of an AM1.5G-filtered 150 W Xe lamp (216 mW cm^{-2} beam power). The ternary hybrid photocatalyst exhibited a high CO production rate of 3.1 μmol h^{-1} (3.1 mmol g^{-1} h^{-1}) and a high CO/H_2 ratio of 93% (Figure 7.4a). Replacing Ar for CO_2 generated no CO (Figure 7.4a), and an isotope labeling experiment with $^{13}CO_2$ yielded ^{13}CO almost exclusively (Figure A7.14), both confirming that CO is indeed produced from CO_2 reduction. Controlled experiments with CdS/CNT and CNT/CoPc binary hybrids both produced no CO (Figure 7.4a), suggesting that both CdS and CoPc are critical components of the ternary photocatalyst. The result that CNT/CoPc has no photocatalytic activity rules out the possibility that CoPc molecules are excited to generate electrons for CO_2 reduction. Another binary material CdS/CoPc (Figure A7.7) showed a substantially lower CO production rate (0.1 μmol h^{-1}) compared to the ternary hybrid (Figure 7.4a), which reflects the critical role of CNT facilitating charge separation in CdS and electron transfer to the CoPc co-catalyst.

The intimate and abundant interface between CdS and CNT in the ternary hybrid, as rendered by the direct growth of CdS QDs on CNTs, is critical to the charge separation and transfer.[41-42] To test this hypothesis, we prepared another CdS/CNT/CoPc material by assembling CoPc molecules on pre-heated CdS/CNT. The pre-heating at 150 °C caused the CdS QDs to detach from the CNTs and sinter into larger particles, destroying the CdS/CNT interface (Figure A7.15a, b). The UV-

visible spectrum of this heated CdS/CNT/CoPc material features a ~ 40 nm redshift of the CdS absorption peak, consistent with CdS aggregation, and a CoPc absorption peak confirming effective loading of CoPc (Figure A7.15c). Notably, the CdS/CNT/CoPc material with aggregated CdS showed drastically lower CO_2 reduction photocatalytic activity than the original ternary hybrid (Figure 7.4a), verifying the vital role of the CdS/CNT interface in the ternary material system.

Photocatalytic CO_2 reduction performance of CdS/CNT/CoPc was also tested under visible light illumination. With a 405 nm LED (47 mW cm^{-2} beam power) light source, a high CO production rate of 2.9 μmol h^{-1} (2.9 mmol g^{-1} h^{-1}) was achieved and maintained for at least 5 hours (Figure 7.4b). The ~ 1 hour pre-activation time may be related to electron accumulation in CNTs for overcoming the 0.26 eV energy barrier between the 2nd reduction of CoPc and the CNT Fermi level (Figure 7.2) or to the multiple reductions of CoPc required for CO_2 activation.[15] When we replaced the light source to a UV-filtered 300 W Xe lamp (618 mW cm^{-2} beam power), the CO production rate increased to 6.3 μmol h^{-1} (6.3 mmol g^{-1} h^{-1}), marking one of the highest rates reported up to date under visible light at room temperature (Table A7.4).

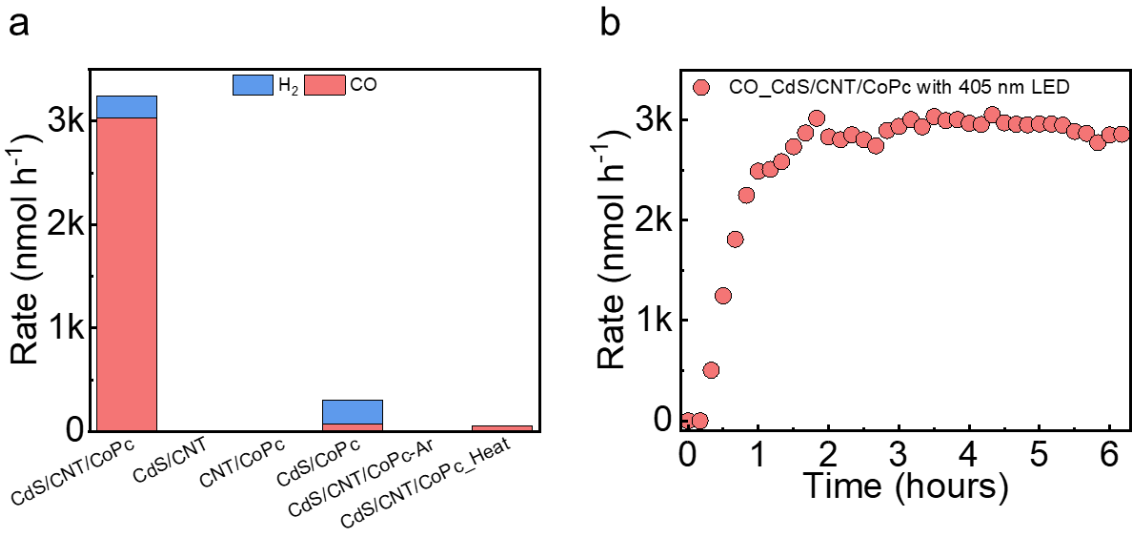

Figure 7.4. Photocatalytic CO_2 reduction performance measured in TEOA-acetonitrile (1:4). (a) Photocatalytic reaction rate of CdS/CNT/CoPc compared to CdS/CNT, CNT/CoPc, and CdS/CoPc under AM1.5G-filtered 150 W Xe lamp illumination (216 mW cm^{-2} beam power). (b) Long-term photocatalytic CO production rate of CdS/CNT/CoPc under 405 nm LED illumination (47 mW cm^{-2} beam power).

In situ Raman spectroscopy was conducted to identify CO_2 reduction active sites in the CdS/CNT/CoPc photocatalyst (Figure A7.16). In the first experiment, we used methyl viologen (MV^{2+}) as an electron acceptor.[43] Under 405 nm LED illumination, we observed MV^{2+} reduction to MV^{+} in the presence of CdS/CNT/CoPc but not with CdS/CNT (Figure 7.5a). This difference suggests that CoPc is the catalytically active site that transfers photo-generated electrons to oxidant molecules. In the second experiment, we performed photochemical CO_2 reduction with CdS/CNT/CoPc. Under illumination and CO_2 atmosphere, we observed Raman features at 590 cm^{-1}, 682 cm^{-1}, 749 cm^{-1}, and 1532 cm^{-1}, characteristic of $Co^{2+}Pc^{2-}$ (or $Co^{+}[HPc]^{-}$) molecules (Figure 7.5b).[44] All these Raman peaks disappeared after changing the gas atmosphere from CO_2 to Ar. This is caused by the reduction of CoPc, likely to $Co^{+}[H_2Pc]^{-}$, which bleaches the color of the molecule and consequently disrupts its resonance with the 633 nm Raman laser.[15] Notably, the CoPc peaks returned when Ar was again replaced by CO_2, indicating that $Co^{+}[H_2Pc]^{-}$ can quickly transfer electrons to CO_2 and is therefore the active species in the photochemical CO_2 reduction catalyzed by CdS/CNT/CoPc. This is consistent with our prior electrochemical CO_2 reduction study, which indicates CoPc needs to be reduced by two electrons before it can actively reduce CO_2 to CO.[29]

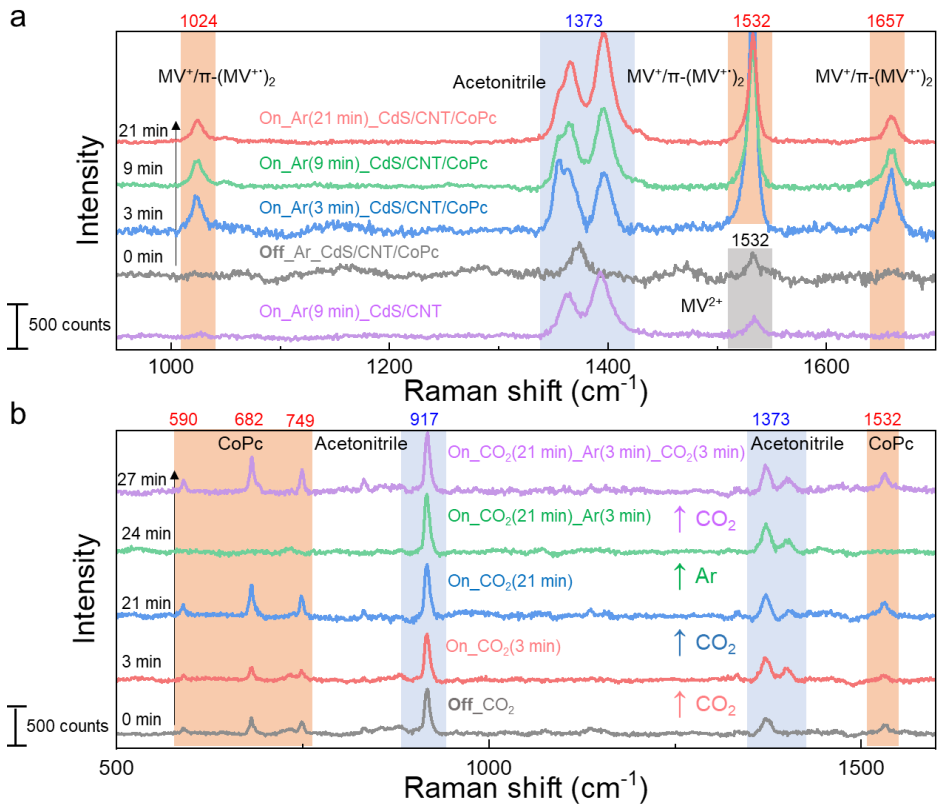

Figure 7.5. *In situ* Raman spectroscopy measurements to uncover catalytic sites and electron transfer. *In situ* Raman spectra of CdS/CNT/CoPc in TEOA-acetonitrile (1:4) under photochemical conditions (405 nm LED illumination) (a) with MV^{2+} or (b) CO_2 as electron acceptor.

The electron transfer from CoPc to CO_2 was further probed by *in situ* UV-visible spectroscopy with CdS/CNT/CoPc (Figure A7.17). Under Ar atmosphere without illumination, an absorption peak at 669 nm corresponding to $Co^{2+}Pc^{2-}$ was observed (Figure 7.6a).[15, 45-46] 30 min after turning on the 405 nm LED, the 669 nm peak disappeared, and two new peaks emerged at 660 nm and 698 nm, reflecting Co^{2+} reduction to Co^{+}.[15, 45-46] After 60 min of illumination, the 660 nm peak started to disappear, whereas the 698 nm one continued to grow, and two additional peaks started to emerge at 423 nm and 466 nm (Figure 7.6a). These changes suggest the second reduction of CoPc, likely from $Co^{+}[HPc]^{-}$ to $Co^{+}[H_2Pc]^{-}$ (reduction of the ligand).[15, 45-46] The approximately

1 hour of time needed to generate the CO_2-reduction-active $Co^+[H_2Pc]^-$ species matches well with the activation time of the aforementioned photochemical CO_2 reduction measurement (Figure 7.4b), which may be related to electron accumulation in the CNTs to overcome the 0.26 eV energy barrier shown in Figure 7.2.

We then conducted the experiment under CO_2 atmosphere. Interestingly, after the initial reduction, the CoPc molecular catalyst manifested a mixed state of $Co^+[HPc]^-$ and $Co^+[H_2Pc]^-$ with their ratio fluctuating in the following 2 hours (Figure 7.6b). This indicates the two redox states of CoPc involved in the catalytic cycle of CO_2 reduction: photo-generated electrons from CdS reduce CoPc to $Co^+[H_2Pc]^-$, which is subsequently oxidized by CO_2 to form $Co^+[HPc]^-$. To prove this conjecture, we first photo-reduced CdS/CNT/CoPc under Ar to form $Co^+[H_2Pc]^-$ and then dosed CO_2 into the system. CO_2 converted $Co^+[H_2Pc]^-$ to $Co^+[HPc]^-$ almost immediately (Figure 7.6c), which is consistent with the aforementioned *in situ* Raman results and confirms our hypothesis about the active form of CoPc and its electron transfer to CO_2 in the photochemical reaction.

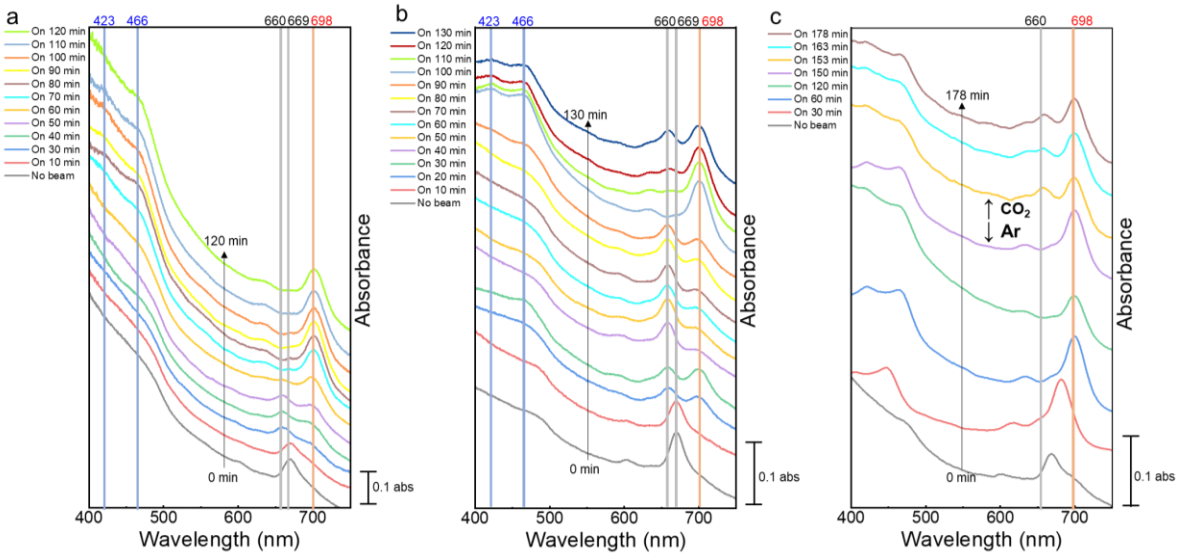

Figure 7.6. *In situ* UV-visible spectroscopy measurements to uncover catalytic sites and electron transfer. *In situ* UV-visible spectra of CdS/CNT/CoPc in TEOA-acetonitrile (1:4) under

photochemical conditions (405 nm LED illumination), (a) with Ar purging, (b) with CO_2 purging, and (c) with first Ar and then CO_2 purging.

An important aspect of CO_2 utilization is its integration with CO_2 capture. Amine solutions are widely used to absorb CO_2 by forming carbamates, but a considerable amount of energy, usually in the form of heat, is needed to release the captured CO_2 for valorization.[12] The black body characteristic of CNTs in our CdS/CNT/CoPc ternary hybrid photocatalyst enables it to absorb solar irradiation and generate heat, which may be used towards overcoming the energy barrier for releasing CO_2 from carbamate and realize the direct photochemical conversion of captured carbon emissions.[47] To this goal, we first carried out photochemical CO_2 reduction in 0.2 M aqueous MEA with our CdS/CNT/CoPc catalyst. The CO_2 in this MEA solution was captured from bubbling CO_2 gas through the solution, which yielded a carbamate concentration of ~ 6.8 mM (Figure A7.18). Under the illumination of a 300 W Xe lamp (766 mW cm^{-2} beam power), the reaction produced CO at a notable rate of 1.2 μmol h^{-1} together with 21 μmol h^{-1} of H_2 (Figure 7.7a). The H_2 production rate is inversely related with the carbamate concentration (Figure A7.19), which provides an opportunity to adjust the CO/H_2 ratio in the valuable syngas product. Controlled experiments without the CoPc co-catalyst, without the CdS/CNT/CoPc photocatalyst, or without captured CO_2 all showed background level CO production rates. Isotope labeling experiments with $^{13}CO_2$ confirmed ^{13}CO production from the carbamate source (Figure A7.20). To further push the performance of our system, we captured CO_2 from the ambient atmosphere using 0.2 M MEA, which yielded a carbamate concentration of ~ 2.2 mM (Figure A7.18). Remarkably, our CdS/CNT/CoPc hybrid catalyst effectively reduced carbamate photochemically to CO at a rate of 0.3 μmol h^{-1}, significantly higher than the background signal (Figure 7.7b). We observed that a considerable amount of heat was released by the CdS/CNT/CoPc photocatalyst during the

reactions (Figure A7.21). A simplified simulation with COMSOL estimated a local temperature of ~ 50 °C near the catalyst (Figure 7.7c). This value agrees with what was found necessary for carbamate solutions to be electrochemically reactive.[12] Therefore, the photothermal effect of CNT in our ternary hybrid photocatalyst provides local heating, without the need for additional energy input, to make carbamate reactive towards photochemical reduction (Figure 7.7d). To the best of our knowledge, this is the first demonstration of direct photochemical conversion of amine-captured CO_2 with no additional energy input, although more optimization is still needed to advance it towards practical application.

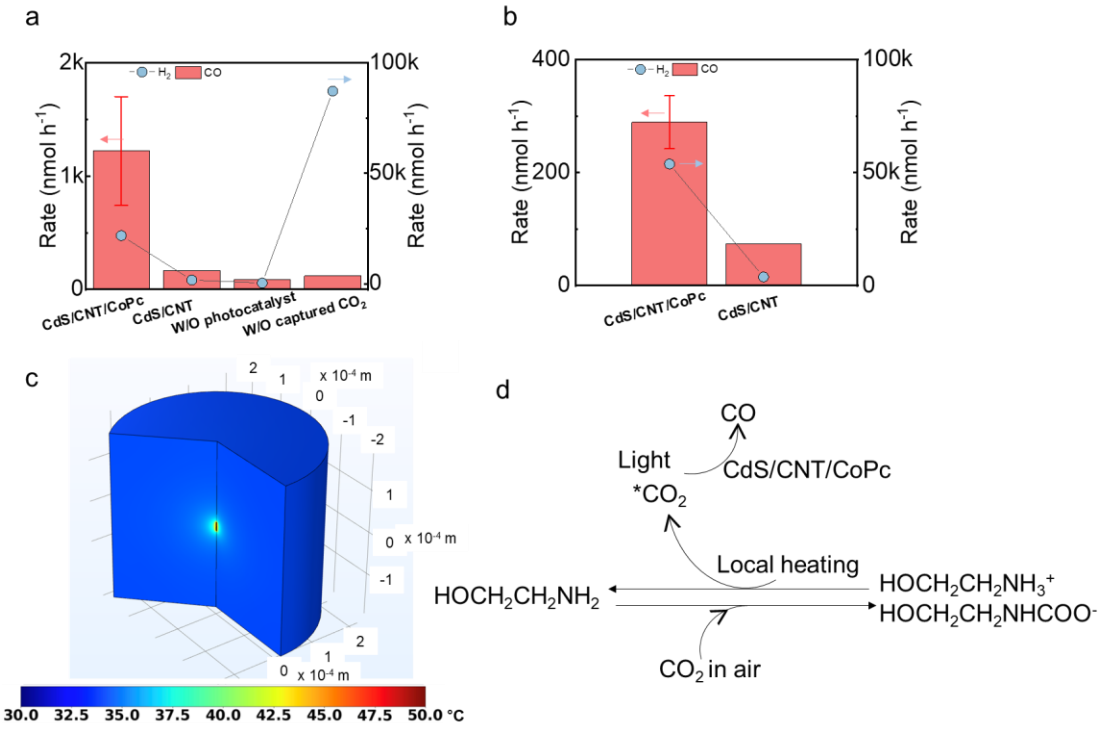

Figure 7.7. Photocatalytic conversion of captured CO_2. Photochemical CO and H_2 production from CO_2 captured by MEA solution (a) from a pure CO_2 source and (b) from air catalyzed by CdS/CNT/CoPc. (c) Modeling of local heating effect near CNT. (d) Proposed mechanism for direct photocatalytic reduction of MEA-captured CO_2.

7.4. Conclusion

This chapter develops a ternary CdS/CNT/CoPc hybrid photocatalyst towards utilizing solar energy for practical CO_2 valorization. CdS QDs in the hybrid material exhibit effective electron-hole pair generation under visible light irradiation. CNT with intimate CdS/CNT and CNT/CoPc interfaces rapidly transfers photogenerated electrons from CdS to CoPc which efficiently reduces CO_2 to CO. In addition, the photothermal effect of CNT in the hybrid catalyst structure enables direct photochemical conversion of amine-captured CO_2.

Appendix Chapter 7

Bleach decay kinetics fitting

The bleach decay kinetics in Figure 7.3c, Figure A7.12b, and Figure A7.13a (800 nm excitation data) were fitted with the following equations:

$$\Delta A(t) = \sum_{i=1}^{i} A_i \exp\left(-\frac{t}{\tau_{rec_i}}\right) \otimes G(\Delta t) \quad \text{(A7.1)}$$

$$\Delta A[CdS]_{CdS/CNT} = e^{-\left(\frac{t}{\tau_x}\right)^{\beta}} \quad \text{(A7.2)}$$

In Equation A7.1, $\otimes G(\Delta t)$ denotes convolution with the IRF, which is described by a Gaussian function with a full-width-at-half-max (FWHM) of 76 fs (Table A7.2). For CdS QDs, 4 decay components (i=4) are needed to adequately describe the kinetics (Figure 7.3c) and the fitting parameters are listed in Table A7.2. For the near-IR bleach decay of CNTs and of CdS/CNT under 800 nm excitation, a single exponential decay (i=1) is sufficient to describe the kinetics (Figure A7.12b and 14a). The CdS exciton bleach decay of CdS/CNT can be best fitted by a stretched exponential decay function (Equation A7.2) as shown in Figure 7.3c and the fitting parameters are listed in Table A7.2.

For multi-exponential and stretched exponential decay, their average lifetimes were calculated using Equations A7.3 and A7.4, respectively.

$$< \boldsymbol{\tau} > = \frac{\sum \boldsymbol{A_i \tau_i}}{\sum \boldsymbol{A_i}} \tag{A7.3}$$

$$< \boldsymbol{\tau} > = \frac{\boldsymbol{\tau_x}}{\boldsymbol{\beta}} \times \boldsymbol{\Gamma}\left(\frac{\boldsymbol{1}}{\boldsymbol{\beta}}\right) \tag{A7.4}$$

The electron transfer quantum yield QE_{ET} from CdS to CNT was calculated from the TA kinetics using Equation A7.5:

$$QE_{ET} = 1 + \int_0^\infty dt \frac{dS_{CdS}(t)}{dt} \frac{S_{CdS/CNT}(t)}{S_{CdS}(t)} \tag{A7.5}$$

where $S_{CdS}(t)$ and $S_{CdS/CNT}(t)$ represent the time-dependent survival probabilities of CdS conduction band electrons for CdS QDs and CdS/CNT, respectively. The survival probability at time t can be understood as the fraction of CdS electrons that remains in the conduction band at time t after being initially excited at time zero, where $S(t = 0) = 1$. In this model, two parallel processes are competing to consume the CdS conduction band electrons: recombination with trapped states in CdS and electron transfer from CdS to CNT.

Figure A7.13c depicts the key electron generation, separation, and recombination processes in the CdS/CNT/CoPc photocatalyst. The exciton bleach decay kinetics of CdS in CdS/CNT reflects the contributions of both electron-hole recombination in CdS (τ_{rec_i}) and electron transfer to CNT (τ_{et_j}). The heterogeneity in both processes gives rise to the stretched exponential decay shown in Figure 7.3c. However, to fit the kinetics of electron population change in the CNTs of CdS/CNT, we need to obtain the distributions of the electron transfer time constant τ_{et_j} and the probability B_j. Assuming CdS QDs on CNTs have the same properties (for example, trap state distribution) as free CdS QDs, we can write the Equation A7.6 to fit the bleach decay kinetics of CdS in CdS/CNT:

$$\Delta A_{CdS/CNT}(t) = \sum_{i=1,j=1}^{i=4,j=4} A_i B_j \exp\left(-\frac{t}{\tau_{rec_i}} - \frac{t}{\tau_{et_j}}\right) \otimes G(\Delta t) \quad \text{(A7.6)}$$

where τ_{rec_i} and A_i are the recombination time constant and its distribution probability obtained from the fitting results of CdS QDs summarized in Table A7.2. As shown in Figure A7.13b, this model provides a reasonable fit to the observed kinetics with the fitting parameters summarized in Table A7.3.

The electron concentration in the CNTs of CdS/CNT is determined by the time constants of electron transfer from CdS to CNT (τ_{et}), electron-phonon scattering (τ'_{rec}), electron trapping (τ_{trap}), electron transfer from CNT to CoPc (τ'_{et}), and recombination of separated electrons and holes (τ''_{rec}). From Figure 7.3e, we know τ'_{et} and τ''_{rec} are negligibly slow within the timescale we probe (0-5 ns). τ'_{rec}, which arises from the excitation of CNT itself, can be treated as an independent process. Therefore, the kinetics of electron concentration in the CNTs of CdS/CNT or CdS/CNT/CoPc is determined by the competition between τ_{et} and τ_{trap}, which is described by Equation A7.7:

$$[\mathrm{CNT}](t)_{i,j,h} = \sum C_h A_i B_j \frac{\tau_{rec_i}}{\tau_{rec_i}+\tau_{et_j}} \frac{\tau_{trap_h}}{\tau_{et_j}-\tau_{trap_h}} \left[\exp\left(-\frac{t}{\tau_{rec_i}} - \frac{t}{\tau_{et_j}}\right) - \exp\left(-\frac{t}{\tau_{trap_h}}\right)\right] \quad \text{(A7.7)}$$

where C_h is the amplitude of the CNT electron trapping component with time constant τ_{trap_h}, A_i, B_j, τ_{rec_i}, and τ_{et_j} are fitting parameters obtained from Figure 7.3c and Figure A7.13b using Equations A7.1 and A7.6.

By assuming that the CNT electron trapping rate distribution contains a fast (h=1) component and a slow one (h=2) and accounting for electrons generated directly from exciting the CNTs, the total electron concentration in CNT can be written as:

$$\Delta A[\mathrm{CNT}]_{CdS/CNT}(t) = \left[A_0 \exp\left(-\frac{t}{\tau'_{rec}}\right) + \sum_{i=1,j=1,h=1}^{i=4,j=4,h=2} [CNT](t)_{i,j,h}\right] \otimes G(\Delta t) \quad \text{(A7.8)}$$

By treating the second trapping component as infinitely slow (trap states are filled and $1/\tau_{trap_2} \rightarrow 0$), Equation A7.8 can be simplified to Equation A7.9:

$$\Delta A[CNT]_{CdS/CNT}(t) = \{A_0\, exp\left(-\frac{t}{\tau'_{rec}}\right) + \sum_{i=1,j=1}^{i=4,j=4} A_i B_j C_1 \frac{\tau_{rec_i}}{\tau_{rec_i}+\tau_{et_j}} \frac{\tau_{trap_1}}{\tau_{et_j}-\tau_{trap_1}} [\exp(-\frac{t}{\tau_{rec_i}} - \frac{t}{\tau_{et_j}}) - \exp(-\frac{t}{\tau_{trap_1}})] + \sum_{i=1,j=1}^{i=4,j=4} A_i B_j C_2 \left[1 - exp\left(-\frac{t}{\tau_{rec_i}} - \frac{t}{\tau_{et_j}}\right)\right]\} \otimes G(\Delta t) \qquad (A7.9)$$

We used Equation A7.9 to fit the CNT bleach kinetics of CdS/CNT shown in Figure 7.3e and Figure A7.13a, using only C_1, C_2 and τ_{trap_1} as independent fitting parameters. The fitting parameters are summarized in Table A7.3. This model can well fit the bleach kinetic decay from 0 to tens of ps, revealing that the slower decay (compared with pure CNTs) is due to the competition between electron transfer from CdS and ultrafast trapping within CNT. The model also captures the increase of the bleach signal after tens of ps, which is due to the electron transfer to CNTs with negligible numbers of traps. There is a noticeable deviation of the fit from the observed bleach growth kinetics. The difference may be attributed to the slightly different properties between CdS QDs grown on CNTs and free CdS QDs, which leads to errors in obtaining the electron transfer rate distribution using Equation A7.6. Nevertheless, our model (Figure A7.13c and Equation A7.9) can account for the complicated charge carrier kinetics observed for the CNTs in CdS/CNT (Figure 7.3e).

Supplementary Figures and Tables

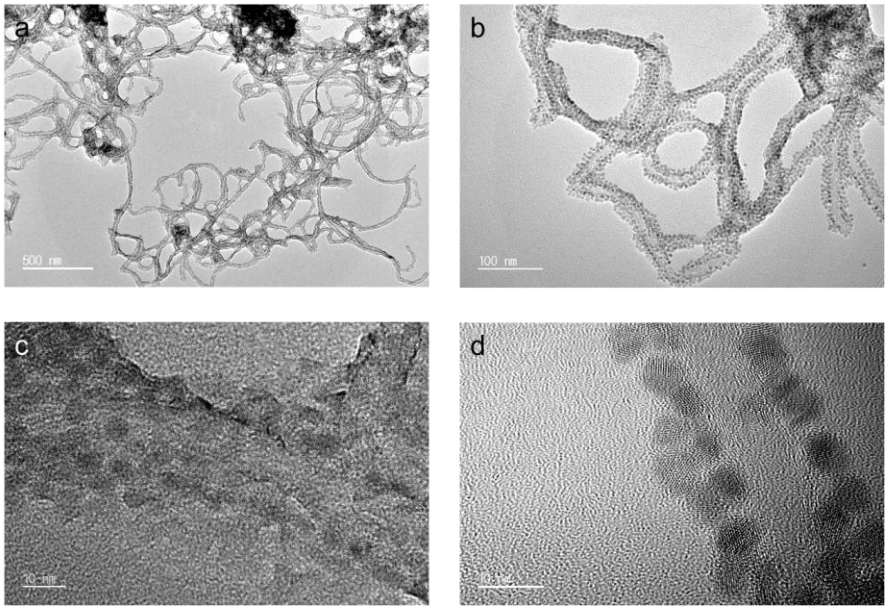

Figure A7.1. (a)-(d), TEM images of CdS/CNT/CoPc taken with different magnifications.

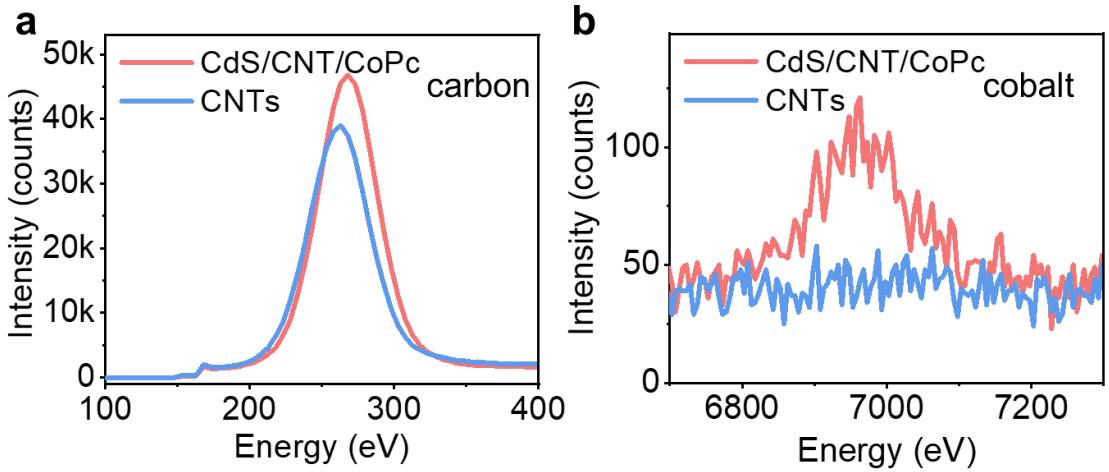

Figure A7.2. (a) Carbon and (b) Cobalt EDX spectrum of CdS/CNT/CoPc in comparison with that of bare CNTs.

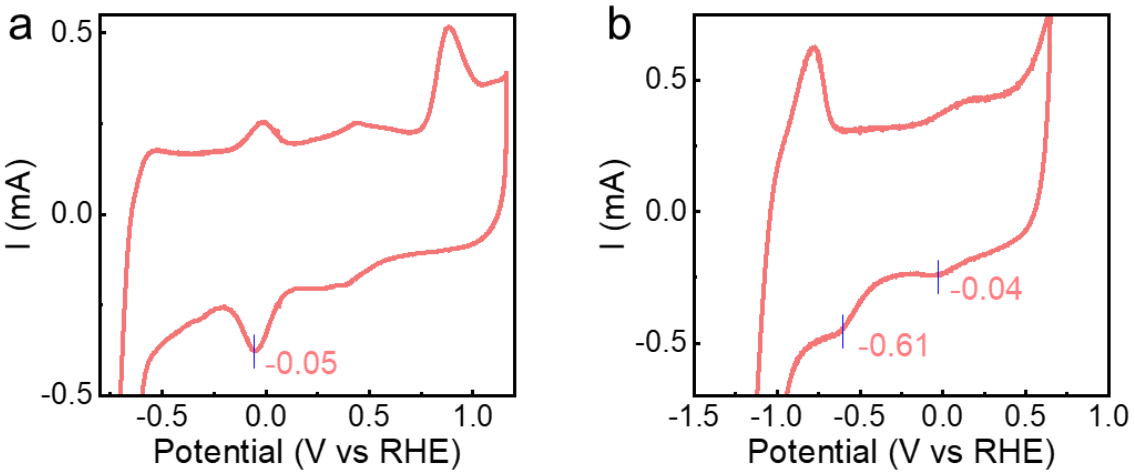

Figure A7.3. (a) Cyclic voltammograms of CNT/CoPc measured in CO_2-saturated 0.1 M aqueous $KHCO_3$ at 100 mV s^{-1}. (b) Cyclic voltammograms of CdS/CNT/CoPc measured in CO_2-saturated 0.1 M aqueous $KHCO_3$ at 100 mV s^{-1}. CNT/CoPc and CdS/CNT/CoPc show the first reduction peak of CoPc at similar electrode potentials, suggesting that CdS QDs have no effects on the reduction potential of CoPc. The standard electrode potential of CO_2 reduction to CO is -0.11 V vs RHE or 4.33 V below the vacuum level.[48]

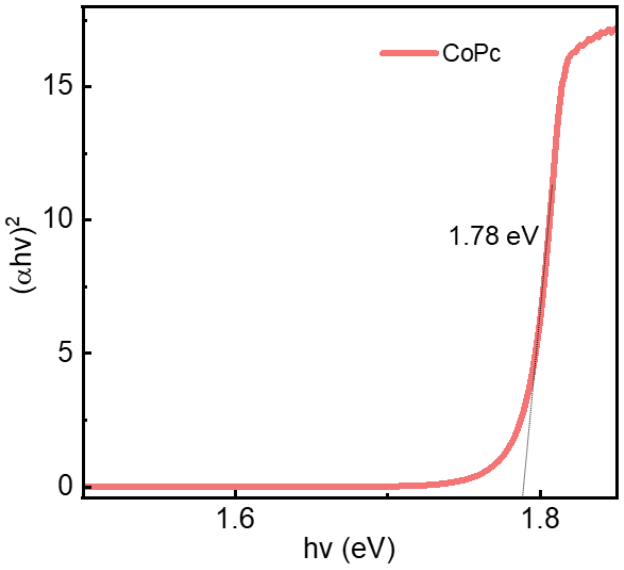

Figure A7.4. Determining orbital gap of CoPc from Tauc plot measured by UV-visible spectroscopy.

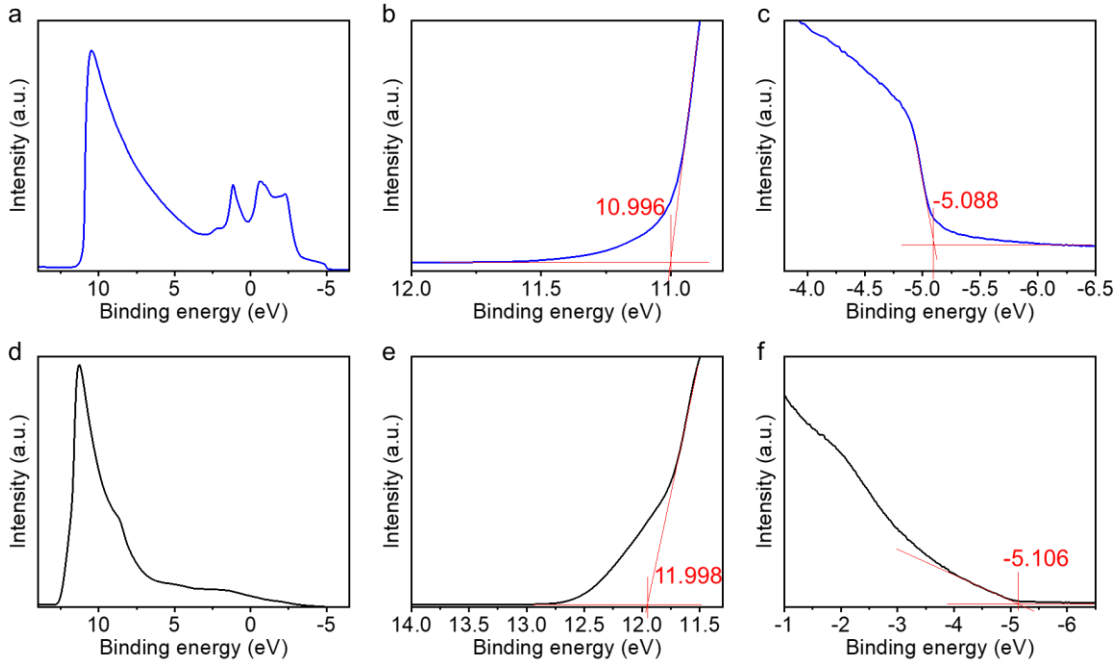

Figure A7.5. Determining work function of (a)-(c) gold standard, (d)-(f) CNT.

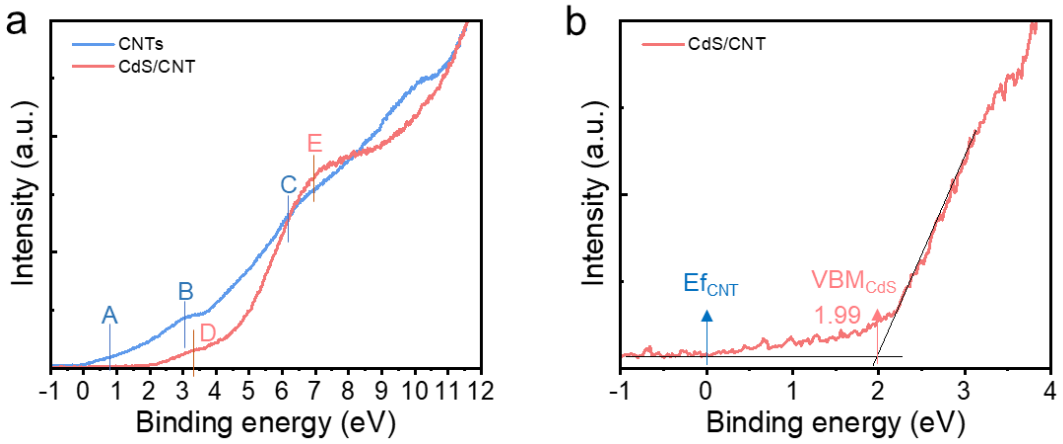

Figure A7.6. (a) Valence bands of CNTs and CdS/CNT measured by UPS. CNTs show the characteristic valence band features of multiwalled CNTs at 0.7 eV, 3 eV, and 6 eV (labeled as A, B, and C)[49]. CdS/CNT shows no clear CNT features but CdS valence band features from Cd 5s

and S 3p mixed orbitals at 3.5 eV and 6.9 eV (labeled as D and E)[50], which indicates that CdS (~70 wt.% in the material and covering most of the CNT surfaces) dominates the valence band structure probed by UPS. (b) Determination of valence band maximum (VBM) of CdS and Fermi energy (Ef) of CNT in CdS/CNT from the UPS result.

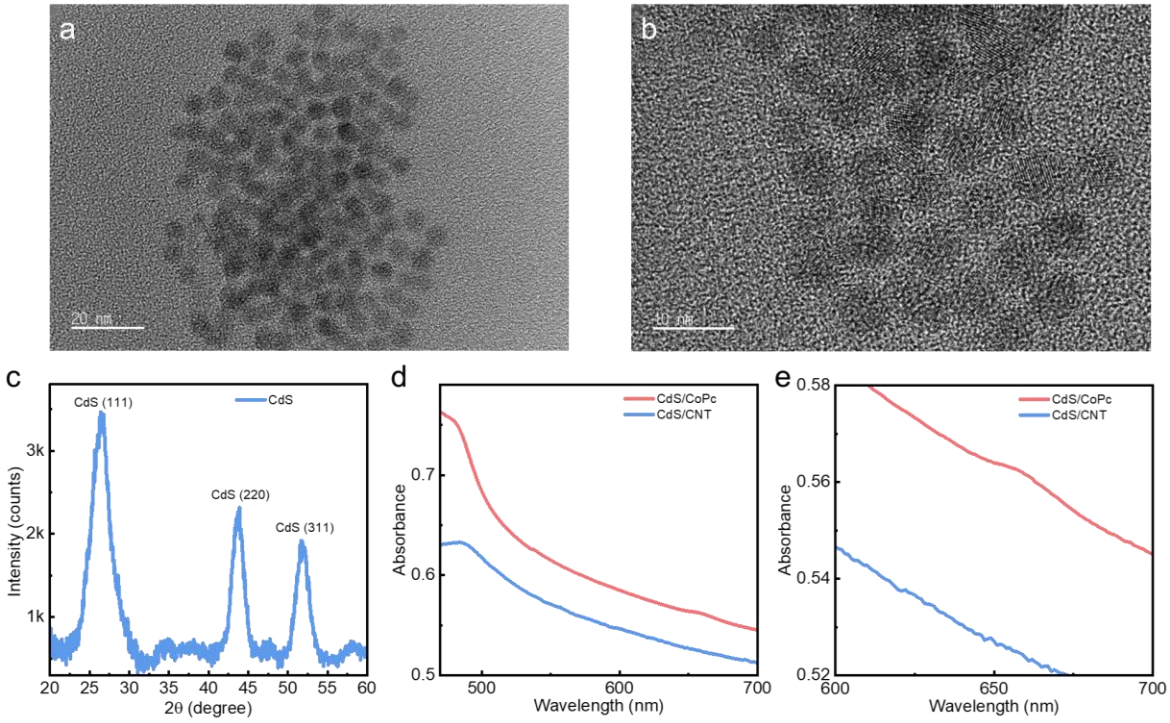

Figure A7.7. (a)-(b) TEM images of CdS taken with different magnifications. (c) XRD of CdS. (d)-(e) UV-visible spectroscopy of CdS/CoPc and CdS/CNT.

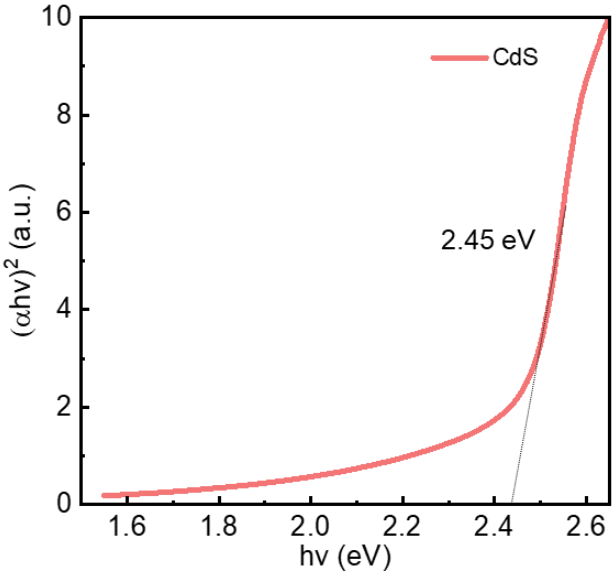

Figure A7.8. Determining band gap of CdS QDs from Tauc plot measured by UV-visible spectroscopy.

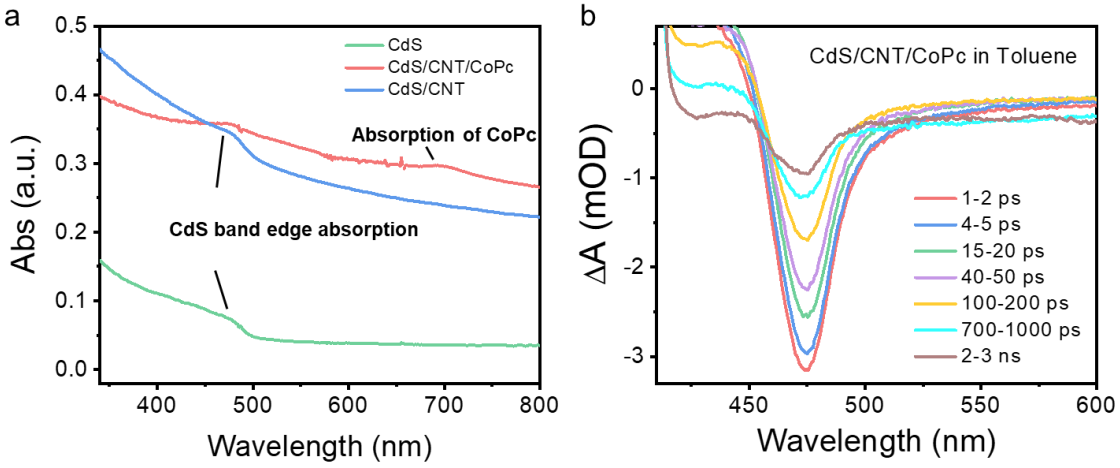

Figure A7.9. (a) UV-visible spectra of CdS, CdS/CNT, and CdS/CNT/CoPc in toluene. (b) TA spectra of CdS/CNT/CoPc. Pump beam was 400 nm. Probe signal was averaged from 468 nm to 483 nm.

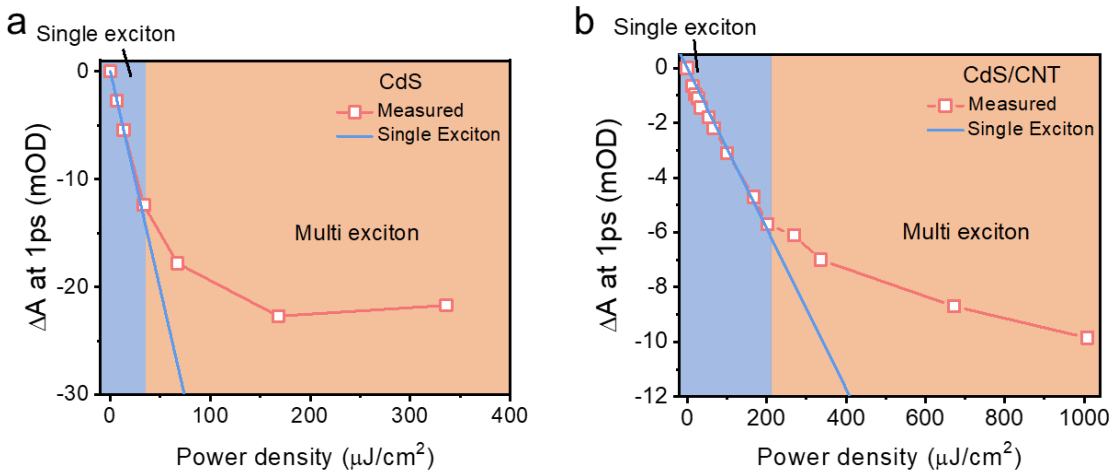

Figure A7.10. Maximum exciton bleach signal recorded at 1 ps time delay as a function of 400 nm excitation power density for (a) CdS QDs and (b) CdS/CNT.

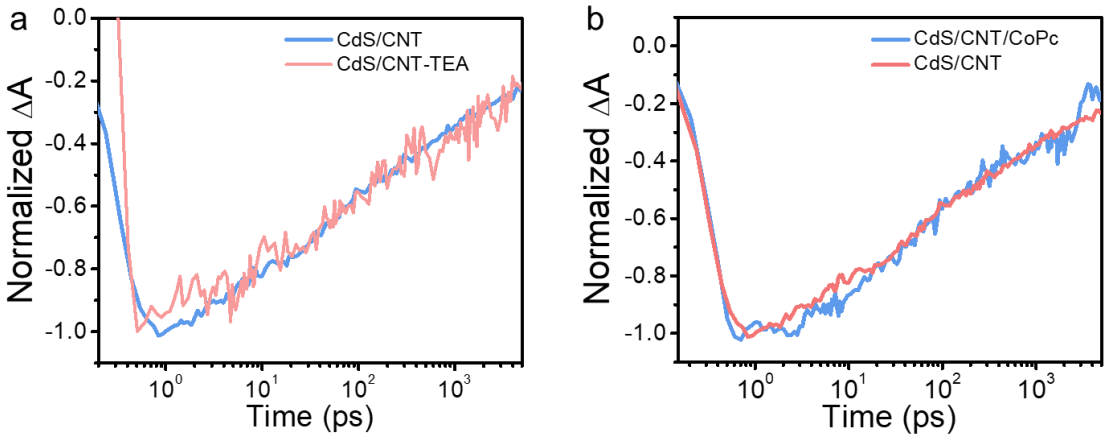

Figure A7.11. Comparison of CdS exciton bleach signal decay kinetics (a) between CdS/CNT and CdS/CNT with TEA, and (b) between CdS/CNT and CdS/CNT/CoPc. Pump beam was 400 nm. Probe signal was averaged from 468 nm to 483 nm.

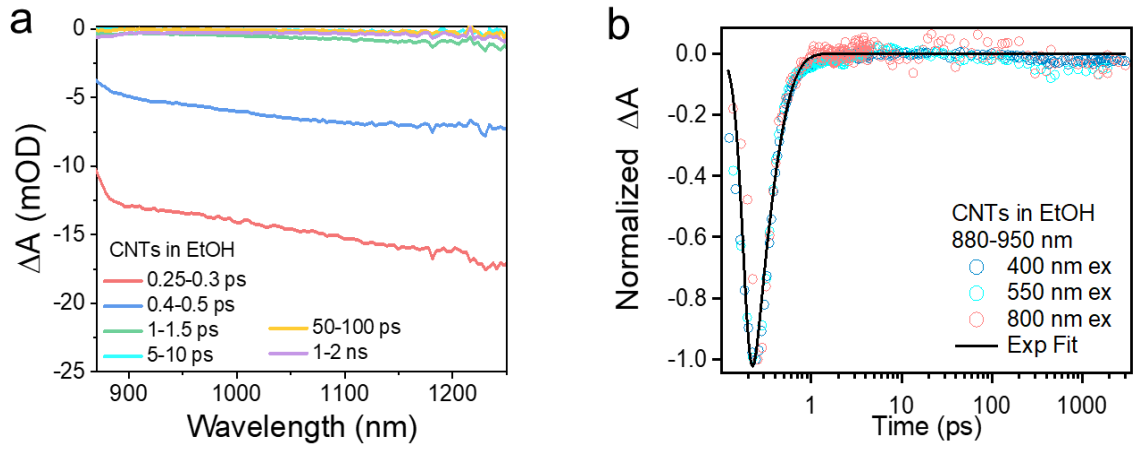

Figure A7.12. (a) Near-IR TA spectra of CNTs under 400 nm excitation. (b) CNTs bleach signal decay kinetics with varied excitation wavelength. Signal was averaged from 880 nm to 950 nm.

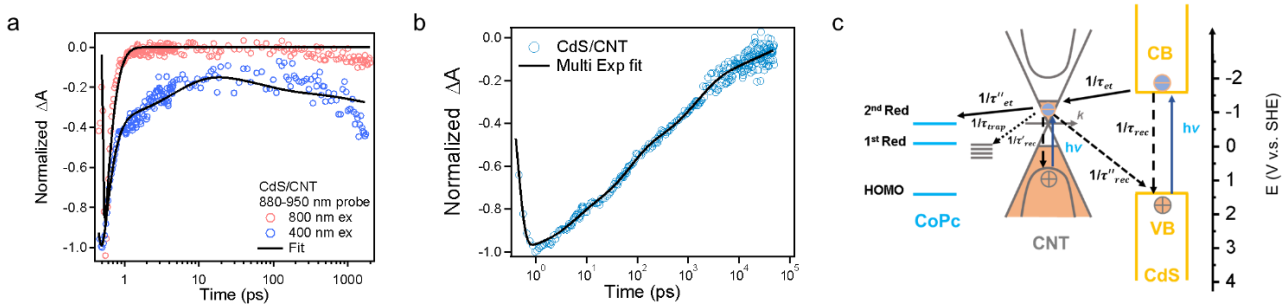

Figure A7.13. (a) CNT bleach signal decay kinetics of CdS/CNT under 400 and 800 nm pump excitation. The signal was averaged from 880 nm to 950 nm. (b) Fitting of CdS bleach decay kinetics of CdS/CNT (same data as Figure 7.3c) using model proposed in Equation A7.6. (c) Schematic of proposed charge transfer mechanism in CdS/CNT/CoPc.

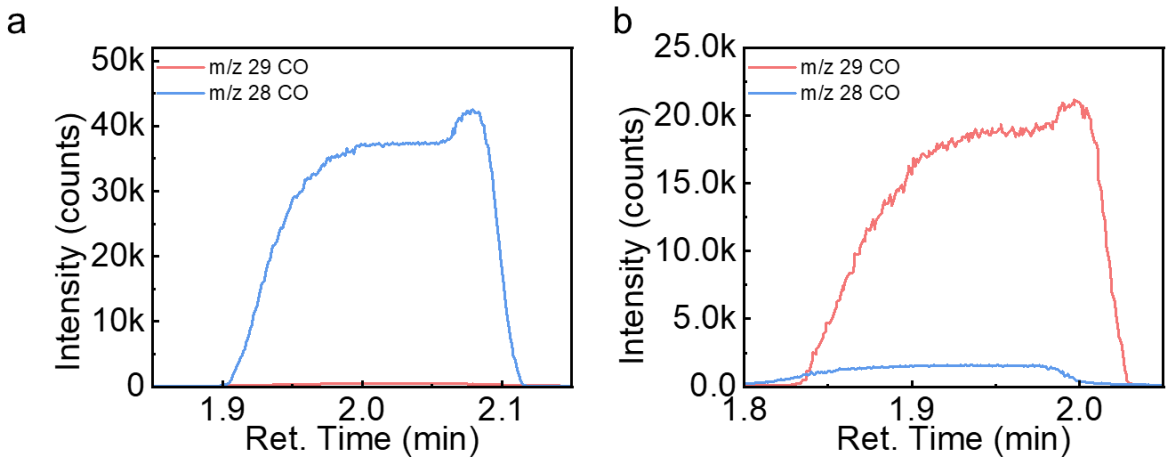

Figure A7.14. GC-MS analysis of CO produced from photochemical reduction reactions (a) with unlabelled CO_2 and (b) with $^{13}CO_2$ catalyzed by CdS/CNT/CoPc in TEOA-acetonitrile (1:4).

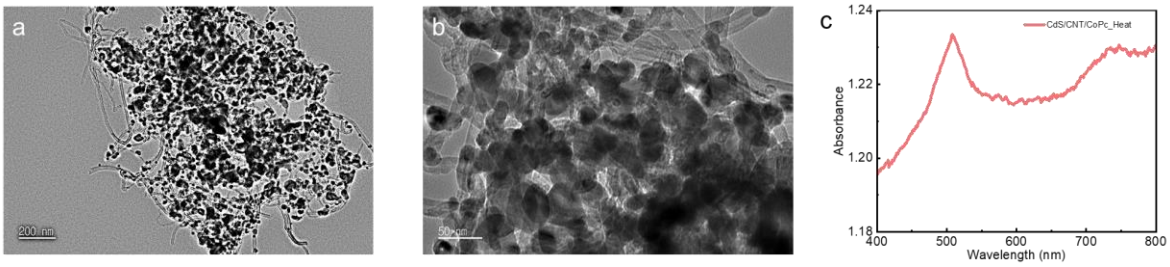

Figure A7.15. (a)-(b), TEM images of CdS/CNT after heat treatment at 150 °C for 1 hour. c, UV-visible absorption spectroscopy of CdS/CNT/CoPc control, whose CoPc was assembled on CdS/CNT after the CdS/CNT was heated at 150 °C for 1 hour under Ar and cooled down to room temperature.

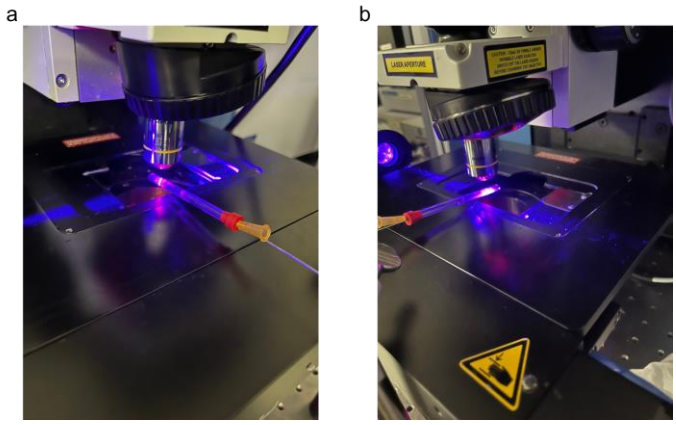

Figure A7.16. Photograph of *in situ* Raman spectroscopy setup.

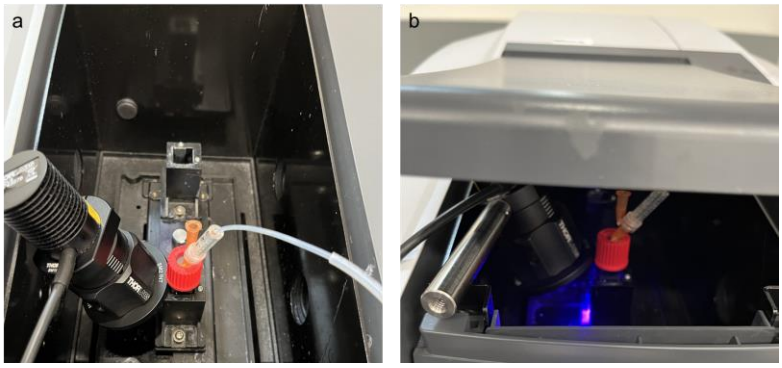

Figure A7.17. Photograph of *in situ* UV-visible spectroscopy setup.

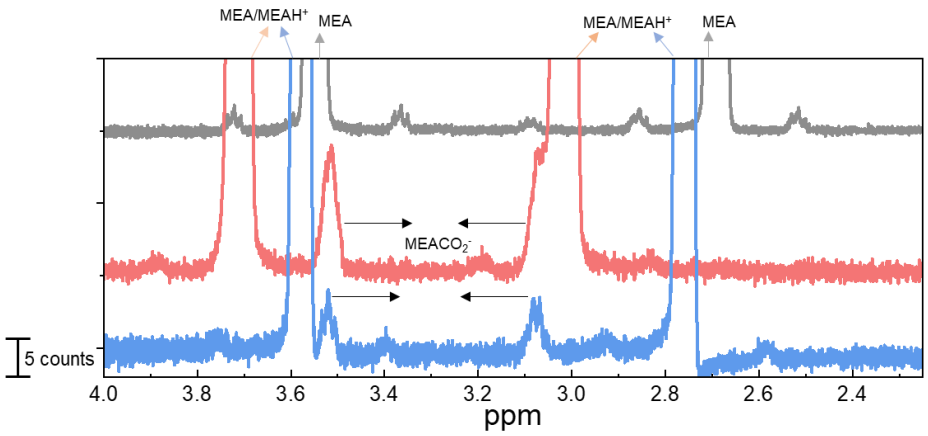

Figure A7.18. NMR spectra of MEA solution before and after CO_2 capturing. Red is from high-purity CO_2, and blue is from air. Dimethyl malonic acid was used as an internal standard to determine carbamate concentration.

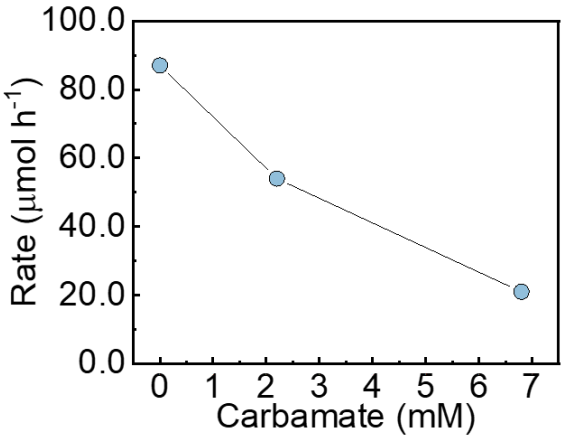

Figure A7.19. Correlation between carbamate concentration and H_2 production rate for photochemical reduction performed with MEA solutions.

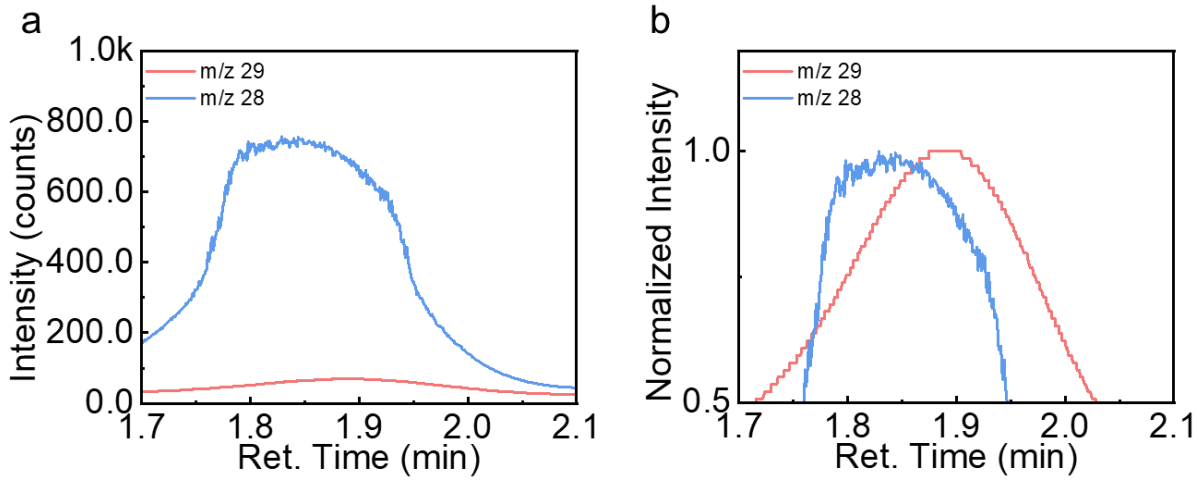

Figure A7.20. (a)-(b), GS-MS analysis of ^{13}CO produced from photochemical reduction of MEA-captured $^{13}CO_2$ catalyzed by CdS/CNT/CoPc. The m/z 28 signal is caused by N_2 as evidenced by its different retention time from CO (m/z 29).

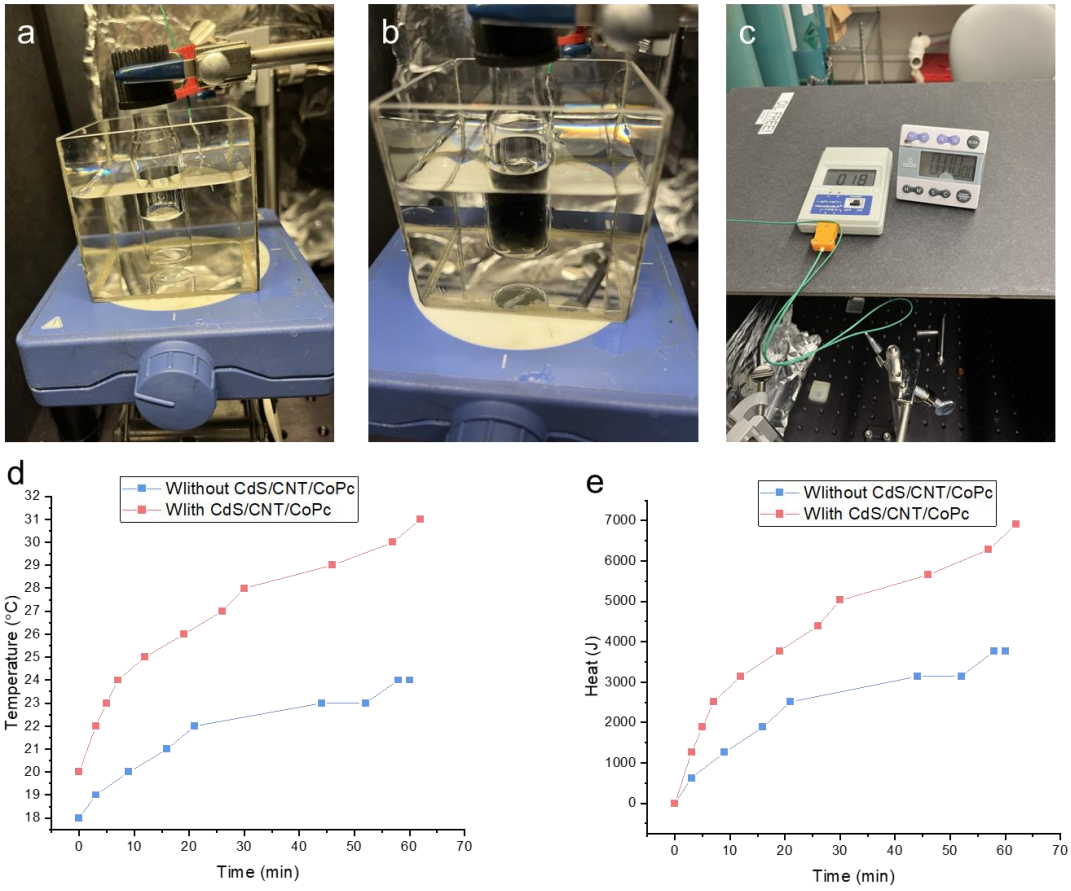

Figure A7.21. Illuminating 0.2 M aqueous MEA (a) without and (b) with CdS/CNT/CoPc (same conditions as photochemical reaction of captured CO_2). (c) Measuring water bath temperature. (d) Increasing water bath temperature as illumination proceeds. (e) Heat absorbed by water bath corresponding to its temperature increase.

Table A7.1. Methods used to determine the electronic band structure of CdS/CNT/CoPc.

	Energy level (eV)	Method

CoPc 2nd Reduction	3.83	2nd reduction peak of CdS/CNT/CoPc from cyclic voltammetry with respect to the standard electrode potential of CO_2/CO (Figure A7.3b)
CoPc 1st Reduction	4.40	1st reduction peak of CdS/CNT/CoPc from cyclic voltammetry with respect to the standard electrode potential of CO_2/CO (Figure A7.3b)
CoPc HOMO	5.61	1.78 eV below the 2nd reduction of CoPc, determined from the Tacu plot of CoPc (Figure A7.4)
Work function of CNTs	4.09	Measured by UPS (Figure A7.5)
E_{VB} of CdS QDs	1.99 below 4.09	Measured by UPS (Figure A7.6).
E_{CB} of CdS QDs	3.63	2.45 eV above E_{VB}, determined from the Tacu plot of CdS (Figure A7.8)

Table A7.2. Fitting parameters for bleach decay curves in Figure 7.3c.

Fitting parameters	ΔA(CdS QDs)	Fitting parameters	ΔA[CdS] (CdS/CNT)
τ_{rec1} (ns)	0.48 ± 0.19	τ(ps)	197±21
τ_{rec2} (ns)	6.1 ± 1.3	$<\tau>$ (ns)	4.5±0.5
τ_{rec3} (ns)	444 ± 6	$\tau_{50\%}$ (ps)	194

τ_{rec4} (ns)	668 ± 94	β	0.21±0.01
A_1	9.6±2.2%		
A_2	29.2±3.1%		
A_3	37.7±3.0%		
A_4	22.4±1.7%		
$< \tau >$	168±24		
IRF_FWHM (fs)	76		

Table A7.3. Fitting parameters for CdS bleach decay curves in Figure A7.13b and CNT bleach decay curves in Figure A7.13a using Equations A7.6 and A7.9, respectively.

Fitting parameters	ΔA[CdS](CdS/CNT)	Fitting parameters	ΔA[CNT](CdS/CNT)
τ_{et1} (ps)	4.9±2.8	τ_{trap1} (ps)	0.14±0.07
τ_{et2} (ps)	65.4±28.1	τ'_{rec} (ps)	0.17±0.01
τ_{et3} (ns)	1.7±0.7	C_1	-65.9±35.1 (99.3%)
τ_{et4} (ns)	132±131	C_2	-0.47±0.01 (0.7%)
B_1	16.7±6.2%	IRF_FWHM (fs)	76
B_2	30.0±5.9%		
B_3	28.8±4.3%		
B_4	24.5±4.3%		
IRF_FWHM (fs)	76		

Table A7.4. Comparison of photochemical CO_2 reduction performance of CdS/CNT/CoPc with other CdS or molecular co-catalyst systems reported in the literature.

Photocatalyst	Co-catalyst	Light source	Medium	Prod-ucts	CO%	Rate (μmol g^{-1} h^{-1})	Mass (mg)	Ref.
CdS/CNT/CoPc	CoPc	300 W Xe lamp, λ > 420 nm	Acetonitrile, TEOA	CO, H_2	>90	6259 (CO)	1	*This work*
CdS/CNT/CoPc	CoPc	AM1.5G 150 W Xe lamp	Acetonitrile, TEOA	CO, H_2	>93	3100 (CO)	1	*This work*
CN_x/CoPc-COOH	CoPc-COOH	AM1.5G 150 W Xe lamp	Acetonitrile, TEOA	CO, H_2	>98	1067 (CO)	3	*15*
Au/CdS hierarchical multi-cavity hollow particles	$Co(bpy)_3^{2+}$	300 W Xe lamp, λ > 400 nm	Acetonitrile, H_2O, TEOA	CO, H_2	70	3758 (CO)	4	*51*
$ZnIn_2S_4$-In_2O_3	$Co(bpy)_3^{2+}$	300 W Xe lamp, λ > 400 nm	Acetonitrile, H_2O, TEOA	CO, H_2	~79	3075 (CO)	4	52
CdS/BCN	$Co(bpy)_3^{2+}$	300 W Xe lamp, λ > 420 nm	Acetonitrile, H_2O, TEOA	CO, H_2	82	250 (CO)	50	5
Pt atom@$Zn_xCd_{1-x}S$/$Co(bpy)_3^{2+}$	$Co(bpy)_3^{2+}$	300 W Xe lamp, λ > 420 nm	Acetonitrile, H_2O, TEOA	CO, H_2	NA	75 μmol h^{-1}	8	53
mesoporous-CN_x-CoPPC	CoPPC	AM1.5G Xe lamp (1 sun, λ > 300 nm)	Acetonitrile,TEOA	NA	84	20.8 (CO)	2	54
CdS/UiO-bpy/Co	UiO-bpy/Co	300 W Xe lamp, λ > 420 nm	Acetonitrile,TEOA	CO, H_2	85	235 (CO)	10	55

CdS/Co-ZIF-9	Co-ZIF-9	300 W Xe lamp, $\lambda > 420$ nm	Acetonitrile, H_2O, TEOA	CO, H_2	82	2.4 (CO)	21	56
CdS/$[Ni(terpyS)_2]^{2+}$	$Ni(terpyS)_2^{2+}$	AM1.5G Xe lamp, $\lambda > 400$ nm	Acetonitrile, H_2O, TEOA	CO, H_2	92.2%	1 μmol	NA	*6*
CdS/$Co(bpy)_3Cl_2$	$Co(bpy)_3^{2+}$	50 W LED white visible light source	Acetonitrile, H_2O, TEOA	CO, H_2	67%	23 μmol	65	*57*
Amine-functionalized graphene/CdS	Ethylenediamine	300 W Xe lamp, $\lambda > 420$ nm	H_2O	CO, CH_4	93% for CH_4	~ 0.2 (CO) 2.84 (CH_4)	50	*58*

7.5. Reference

1. Xie, S.; Zhang, Q.; Liu, G.; Wang, Y., Photocatalytic and photoelectrocatalytic reduction of CO_2 using heterogeneous catalysts with controlled nanostructures. *Chemical Communications* **2016,** *52* (1), 35-59.
2. Sato, S.; Morikawa, T.; Saeki, S.; Kajino, T.; Motohiro, T., Visible-Light-Induced Selective CO_2 Reduction Utilizing a Ruthenium Complex Electrocatalyst Linked to a p-Type Nitrogen-Doped Ta_2O_5 Semiconductor. *Angewandte Chemie International Edition* **2010,** *49* (30), 5101-5105.
3. Kuriki, R.; Sekizawa, K.; Ishitani, O.; Maeda, K., Visible-Light-Driven CO_2 Reduction with Carbon Nitride: Enhancing the Activity of Ruthenium Catalysts. *Angewandte Chemie International Edition* **2015,** *54* (8), 2406-2409.
4. Cheng, L.; Xiang, Q.; Liao, Y.; Zhang, H., CdS-Based photocatalysts. *Energy & Environmental Science* **2018,** *11* (6), 1362-1391.
5. Zhou, M.; Wang, S.; Yang, P.; Huang, C.; Wang, X., Boron Carbon Nitride Semiconductors Decorated with CdS Nanoparticles for Photocatalytic Reduction of CO_2. *ACS Catalysis* **2018,** *8* (6), 4928-4936.
6. Kuehnel, M. F.; Orchard, K. L.; Dalle, K. E.; Reisner, E., Selective Photocatalytic CO_2 Reduction in Water through Anchoring of a Molecular Ni Catalyst on CdS Nanocrystals. *Journal of the American Chemical Society* **2017,** *139* (21), 7217-7223.
7. Yang, K.; Yang, Z.; Zhang, C.; Gu, Y.; Wei, J.; Li, Z.; Ma, C.; Yang, X.; Song, K.; Li, Y.; Fang, Q.; Zhou, J., Recent advances in CdS-based photocatalysts for CO_2 photocatalytic conversion. *Chemical Engineering Journal* **2021,** *418*, 129344.
8. Rochelle, G. T., Amine Scrubbing for CO_2 Capture. *Science* **2009,** *325* (5948), 1652-1654.
9. Haszeldine, R. S., Carbon Capture and Storage: How Green Can Black Be? *Science* **2009,** *325* (5948), 1647-1652.
10. Rheinhardt, J. H.; Singh, P.; Tarakeshwar, P.; Buttry, D. A., Electrochemical Capture and Release of Carbon Dioxide. *ACS Energy Letters* **2017,** *2* (2), 454-461.
11. Hwang, G. S.; Stowe, H. M.; Paek, E.; Manogaran, D., Reaction mechanisms of aqueous monoethanolamine with carbon dioxide: a combined quantum chemical and molecular dynamics study. *Physical Chemistry Chemical Physics* **2015,** *17* (2), 831-839.
12. Lee, G.; Li, Y. C.; Kim, J.-Y.; Peng, T.; Nam, D.-H.; Sedighian Rasouli, A.; Li, F.; Luo, M.; Ip, A. H.; Joo, Y.-C.; Sargent, E. H., Electrochemical upgrade of CO_2 from amine capture solution. *Nature Energy* **2021,** *6* (1), 46-53.
13. Liang, Z.; Wang, H.-Y.; Zheng, H.; Zhang, W.; Cao, R., Porphyrin-based frameworks for oxygen electrocatalysis and catalytic reduction of carbon dioxide. *Chemical Society Reviews* **2021,** *50* (4), 2540-2581.
14. Cao, R., Across the Board: Rui Cao on Electrocatalytic CO_2 Reduction. *ChemSusChem* **2022,** *15* (21), e202201788.
15. Shang, B.; Zhao, F.; Choi, C.; Jia, X.; Pauly, M.; Wu, Y.; Tao, Z.; Zhong, Y.; Harmon, N.; Maggard, P. A.; Lian, T.; Hazari, N.; Wang, H., Monolayer Molecular Functionalization Enabled

by Acid–Base Interaction for High-Performance Photochemical CO_2 Reduction. *ACS Energy Letters* **2022,** *7* (7), 2265-2272.
16. Wu, Y.; Liang, Y.; Wang, H., Heterogeneous Molecular Catalysts of Metal Phthalocyanines for Electrochemical CO2 Reduction Reactions. *Accounts of Chemical Research* **2021,** *54* (16), 3149-3159.
17. Lu, X.; Wu, Y.; Yuan, X.; Huang, L.; Wu, Z.; Xuan, J.; Wang, Y.; Wang, H., High-Performance Electrochemical CO_2 Reduction Cells Based on Non-noble Metal Catalysts. *ACS Energy Letters* **2018,** *3* (10), 2527-2532.
18. Helander, M. G.; Greiner, M. T.; Wang, Z. B.; Lu, Z. H., Pitfalls in measuring work function using photoelectron spectroscopy. *Applied Surface Science* **2010,** *256* (8), 2602-2605.
19. Ago, H.; Kugler, T.; Cacialli, F.; Salaneck, W. R.; Shaffer, M. S. P.; Windle, A. H.; Friend, R. H., Work Functions and Surface Functional Groups of Multiwall Carbon Nanotubes. *The Journal of Physical Chemistry B* **1999,** *103* (38), 8116-8121.
20. Liu, Y.; Cullen, D. A.; Lian, T., Slow Auger Recombination of Trapped Excitons Enables Efficient Multiple Electron Transfer in CdS–Pt Nanorod Heterostructures. *Journal of the American Chemical Society* **2021,** *143* (48), 20264-20273.
21. McGuire, J. A.; Joo, J.; Pietryga, J. M.; Schaller, R. D.; Klimov, V. I., New Aspects of Carrier Multiplication in Semiconductor Nanocrystals. *Accounts of Chemical Research* **2008,** *41* (12), 1810-1819.
22. Klimov, V. I.; McGuire, J. A.; Schaller, R. D.; Rupasov, V. I., Scaling of multiexciton lifetimes in semiconductor nanocrystals. *Physical Review B* **2008,** *77* (19).
23. Oron, D.; Kazes, M.; Banin, U., Multiexcitons in type-II colloidal semiconductor quantum dots. *Physical Review B* **2007,** *75* (3).
24. Han, Z.; Fina, A., Thermal conductivity of carbon nanotubes and their polymer nanocomposites: A review. *Progress in Polymer Science* **2011,** *36* (7), 914-944.
25. Huang, L.; Wang, X.; Yang, J.; Liu, G.; Han, J.; Li, C., Dual Cocatalysts Loaded Type I CdS/ZnS Core/Shell Nanocrystals as Effective and Stable Photocatalysts for H_2 Evolution. *The Journal of Physical Chemistry C* **2013,** *117* (22), 11584-11591.
26. Feng, Y.-X.; Wang, H.-J.; Wang, J.-W.; Zhang, W.; Zhang, M.; Lu, T.-B., Stand-Alone CdS Nanocrystals for Photocatalytic CO_2 Reduction with High Efficiency and Selectivity. *ACS Applied Materials & Interfaces* **2021,** *13* (22), 26573-26580.
27. Dubertret, B.; Skourides, P.; Norris, D. J.; Noireaux, V.; Brivanlou, A. H.; Libchaber, A., In Vivo Imaging of Quantum Dots Encapsulated in Phospholipid Micelles. *Science* **2002,** *298* (5599), 1759-1762.
28. Aldana, J.; Lavelle, N.; Wang, Y.; Peng, X., Size-Dependent Dissociation pH of Thiolate Ligands from Cadmium Chalcogenide Nanocrystals. *Journal of the American Chemical Society* **2005,** *127* (8), 2496-2504.
29. Zhang, X.; Wu, Z.; Zhang, X.; Li, L.; Li, Y.; Xu, H.; Li, X.; Yu, X.; Zhang, Z.; Liang, Y.; Wang, H., Highly selective and active CO_2 reduction electrocatalysts based on cobalt phthalocyanine/carbon nanotube hybrid structures. *Nature Communications* **2017,** *8* (1), 14675.

30. Wu, K.; Liu, Z.; Zhu, H.; Lian, T., Exciton Annihilation and Dissociation Dynamics in Group II–V Cd_3P_2 Quantum Dots. *The Journal of Physical Chemistry A* **2013,** *117* (29), 6362-6372.
31. Huang, J.; Stockwell, D.; Huang, Z.; Mohler, D. L.; Lian, T., Photoinduced Ultrafast Electron Transfer from CdSe Quantum Dots to Re-bipyridyl Complexes. *Journal of the American Chemical Society* **2008,** *130* (17), 5632-5633.
32. Wu, K.; Zhu, H.; Liu, Z.; Rodríguez-Córdoba, W.; Lian, T., Ultrafast Charge Separation and Long-Lived Charge Separated State in Photocatalytic CdS–Pt Nanorod Heterostructures. *Journal of the American Chemical Society* **2012,** *134* (25), 10337-10340.
33. Phillips, J. C., Stretched exponential relaxation in molecular and electronic glasses. *Reports on Progress in Physics* **1996,** *59* (9), 1133.
34. Nelson, J.; Haque, S. A.; Klug, D. R.; Durrant, J. R., Trap-limited recombination in dye-sensitized nanocrystalline metal oxide electrodes. *Physical Review B* **2001,** *63* (20).
35. Nelson, J.; Chandler, R. E., Random walk models of charge transfer and transport in dye sensitized systems. *Coordination Chemistry Reviews* **2004,** *248* (13), 1181-1194.
36. Utterback, J. K.; Wilker, M. B.; Mulder, D. W.; King, P. W.; Eaves, J. D.; Dukovic, G., Quantum Efficiency of Charge Transfer Competing against Nonexponential Processes: The Case of Electron Transfer from CdS Nanorods to Hydrogenase. *The Journal of Physical Chemistry C* **2019,** *123* (1), 886-896.
37. Lüer, L.; Lanzani, G.; Crochet, J.; Hertel, T.; Holt, J.; Vardeny, Z. V., Ultrafast dynamics in metallic and semiconducting carbon nanotubes. *Physical Review B* **2009,** *80* (20).
38. Koyama, T.; Shimizu, S.; Saito, T.; Miyata, Y.; Shinohara, H.; Nakamura, A., Ultrafast luminescence kinetics of metallic single-walled carbon nanotubes: Possible evidence for excitonic luminescence. *Physical Review B* **2012,** *85* (4).
39. Gao, B.; Hartland, G. V.; Huang, L., Transient Absorption Spectroscopy of Excitons in an Individual Suspended Metallic Carbon Nanotube. *The Journal of Physical Chemistry Letters* **2013,** *4* (18), 3050-3055.
40. Sun, D.; Wu, Z.-K.; Divin, C.; Li, X.; Berger, C.; De Heer, W. A.; First, P. N.; Norris, T. B., Ultrafast Relaxation of Excited Dirac Fermions in Epitaxial Graphene Using Optical Differential Transmission Spectroscopy. *Physical Review Letters* **2008,** *101* (15).
41. Wang, H.; Dai, H., Strongly coupled inorganic–nano-carbon hybrid materials for energy storage. *Chemical Society Reviews* **2013,** *42* (7), 3088-3113.
42. Liang, Y.; Li, Y.; Wang, H.; Dai, H., Strongly Coupled Inorganic/Nanocarbon Hybrid Materials for Advanced Electrocatalysis. *Journal of the American Chemical Society* **2013,** *135* (6), 2013-2036.
43. Sokołowski, K.; Huang, J.; Földes, T.; McCune, J. A.; Xu, D. D.; de Nijs, B.; Chikkaraddy, R.; Collins, S. M.; Rosta, E.; Baumberg, J. J.; Scherman, O. A., Nanoparticle surfactants for kinetically arrested photoactive assemblies to track light-induced electron transfer. *Nature Nanotechnology* **2021,** *16* (10), 1121-1129.

44. Jiang, S.; Chen, Z.; Chen, X.; Nguyen, D.; Mattei, M.; Goubert, G.; Van Duyne, R. P., Investigation of Cobalt Phthalocyanine at the Solid/Liquid Interface by Electrochemical Tip-Enhanced Raman Spectroscopy. *The Journal of Physical Chemistry C* **2019,** *123* (15), 9852-9859.
45. Uzunmehmetoğlu, H. Z.; Yenilmez, H. Y.; Kaya, K.; Koca, A.; Altındal, A.; Bayır, Z. A., Electrochemical, spectroelectrochemical, and dielectric properties of metallophthalocyanines bearing redox active cobalt and manganese metal centres. *Inorganica Chimica Acta* **2017,** *459*, 51-62.
46. Gök, A.; Orman, E. B.; Salan, Ü.; Özkaya, A. R.; Bulut, M., Synthesis, characterization and electrochemical properties of tetra 7-oxy-3-biphenylcoumarin substituted metal-free, zinc(II), cobalt(II) and indium(III) phthalocyanines. *Dyes and Pigments* **2016,** *133*, 311-323.
47. Mizuno, K.; Ishii, J.; Kishida, H.; Hayamizu, Y.; Yasuda, S.; Futaba, D. N.; Yumura, M.; Hata, K., A black body absorber from vertically aligned single-walled carbon nanotubes. *Proceedings of the National Academy of Sciences* **2009,** *106* (15), 6044-6047.
48. Cao, Y.; Chen, Q.; Shen, C.; He, L., Polyoxometalate-Based Catalysts for CO_2 Conversion. *Molecules* **2019,** *24* (11), 2069.
49. Bianconi, A.; Hagström, S. B. M.; Bachrach, R. Z., Photoemission studies of graphite high-energy conduction-band and valence-band states using soft-x-ray synchrotron radiation excitation. *Physical Review B* **1977,** *16* (12), 5543-5548.
50. Gansukh, M.; Li, Z.; Rodriguez, M. E.; Engberg, S.; Martinho, F. M. A.; Mariño, S. L.; Stamate, E.; Schou, J.; Hansen, O.; Canulescu, S., Energy band alignment at the heterointerface between CdS and Ag-alloyed CZTS. *Scientific Reports* **2020,** *10* (1), 18388.
51. Zhang, P.; Wang, S.; Guan, B. Y.; Lou, X. W., Fabrication of CdS hierarchical multi-cavity hollow particles for efficient visible light CO_2 reduction. *Energy & Environmental Science* **2019,** *12* (1), 164-168.
52. Wang, S.; Guan, B. Y.; Lou, X. W. D., Construction of $ZnIn_2S_4$–In_2O_3 Hierarchical Tubular Heterostructures for Efficient CO_2 Photoreduction. *Journal of the American Chemical Society* **2018,** *140* (15), 5037-5040.
53. Zeng, R.; Lian, K.; Su, B.; Lu, L.; Lin, J.; Tang, D.; Lin, S.; Wang, X., Versatile Synthesis of Hollow Metal Sulfides via Reverse Cation Exchange Reactions for Photocatalytic CO_2 Reduction. *Angewandte Chemie International Edition* **2021,** *60* (47), 25055-25062.
54. Roy, S.; Reisner, E., Visible-Light-Driven CO_2 Reduction by Mesoporous Carbon Nitride Modified with Polymeric Cobalt Phthalocyanine. *Angewandte Chemie International Edition* **2019,** *58* (35), 12180-12184.
55. Chen, C.; Wu, T.; Wu, H.; Liu, H.; Qian, Q.; Liu, Z.; Yang, G.; Han, B., Highly effective photoreduction of CO_2 to CO promoted by integration of CdS with molecular redox catalysts through metal–organic frameworks. *Chemical Science* **2018,** *9* (47), 8890-8894.
56. Wang, S.; Wang, X., Photocatalytic CO_2 reduction by CdS promoted with a zeolitic imidazolate framework. *Applied Catalysis B: Environmental* **2015,** *162*, 494-500.
57. Lin, J.; Li, Y., The influence of inorganic anions on photocatalytic CO_2 reduction. *Catalysis Science & Technology* **2020,** *10* (4), 959-966.

58. Cho, K. M.; Kim, K. H.; Park, K.; Kim, C.; Kim, S.; Al-Saggaf, A.; Gereige, I.; Jung, H.-T., Amine-Functionalized Graphene/CdS Composite for Photocatalytic Reduction of CO_2. *ACS Catalysis* **2017,** *7* (10), 7064-7069.

8 Enhanced Methanol Production from Photoelectrochemical CO_2 Reduction via Interface and Microenvironment Tailoring

This chapter is reproduced in part of an unpublished manuscript with permission from Shang, B.[†], Zhao, F. [†], Sa, S., Gao, Y., Sheehan, C., Jeon, S., Li, J., Rooney, C. L., Leitner, O., Xiao, L., Fan, H., Elimelech, M., Wang, L. Meyer, G. J., Stach, E. A., Mallouk, T. E., Lian, T*; & Wang, H.*, Enhanced Methanol Production from Photoelectrochemical CO_2 Reduction via Interface and Microenvironment Tailoring. *Under Review*.

Author contribution: B.S. and H.W. conceived and designed the project; B.S. conducted materials synthesis, photocatalytic reactions, and product analysis. S.C. performed COMSOL simulation. F.Z., and S.S. conducted *in situ* Raman spectroscopic analysis and with supervision from T.L.; F. Z. conducted the Raman data analysis. B.S., F.Z. T. L. and H.W. wrote the manuscript; T.L. and H.W. supervised the project. B. S. and F. Z. share equal contributions. All the authors discussed the results and commented on the manuscript.

8.1. Introduction

The reduction of carbon dioxide (CO_2) into liquid fuels with renewable energy represents a promising solution to combat greenhouse gas emissions.[1] Photoelectrocatalysis has emerged as an efficient method to harness solar energy and facilitate CO_2 electroreduction at low applied voltages.[2-5] In a typical photoelectrocatalytic (PEC) CO_2 reduction process, a semiconductor absorbs light to generate excited electrons, which are transferred by a catalyst to CO_2. Among the various semiconductor materials investigated, Si-based photocathodes have garnered attention due to their cost-effectiveness and relatively well-understood chemical properties.[6-7] Molecular catalysts, particularly transition metal complexes, are viable options for catalyzing the CO_2

reduction reaction, offering high selectivity and tunable catalytic properties.[8-10] Previous studies have achieved successful CO_2 reduction to CO and formate using Si-based photocathodes combined with molecular catalysts.[6, 11-12] However, achieving efficient and stable PEC CO_2 reduction to deeply reduced liquid fuels remains a challenge.[13-14]

In the prior work, a TiO_2-coated planar p-type Si substrate was integrated via a molecular linker with a cobalt phthalocyanine (CoPc)/graphene oxide (GO) hybrid catalyst.[14] Although this photocathode demonstrated the ability to achieve six-electron reduction of CO_2 to methanol with a Faradaic efficiency (FE) of 8%, the current density and stability were limited, likely due to the relatively low catalytic performance of GO/CoPc and its weak interaction between the Si substrate. To improve the PEC performance, successful integration of a better catalyst on Si is desired, which entails to solve several challenges including stabilizing the catalyst layer on the Si surface through linking or assembly, designing an efficient catalyst loading method for optimal light transmission, passivating the native Si surface to prevent the competing hydrogen evolution reaction (HER), providing a large enough thermodynamic driving force in solution for interfacial charge transfer, and creating a hydrophobic local environment to tailor the reaction selectivity towards methanol. Therefore, it is critical to control the interface between the Si substrate and the molecular catalyst and its microenvironment.[15]

In this chapter, we report the achievement of PEC CO_2 reduction with over 20% FE, a remarkable partial photocurrent density of 3.4 mA cm^{-2}, and a high turnover frequency (TOF) of 1.5 s^{-1} for methanol. This stands as the highest performance reported to date for any molecular catalyst-based photoelectrode. The enhancement in performance was realized by designing the semiconductor/catalyst interface and tailoring the electrode microenvironment, which plays a critical role in optimizing the CO_2 reduction to methanol cascade. We fabricated the p-type Si

substrate surface into an array of micropillars, which enabled effective integration of an amine-substituted CoPc/carbon nanotube (CNT/CoPc-NH_2) catalyst without sacrificing light absorption as well as improved retention of the key CO intermediate. This Si micropillar array (SMA) photoelectrode yielded a 1.6-fold increase in total current density and a 1.5-fold increase in $FE_{methanol}$ compared to the prior planar Si electrode with the GO/CoPc catalyst. We further implemented a superhydrophobic carbon fluoride (CF_x) coating on the SMA substrate to enhance the conversion of the gaseous reactant and intermediate. This microenvironment led to another 2-fold increase in $FE_{methanol}$ and more remarkably, an additional 7-fold increase in the methanol partial current density. *In situ* Raman Spectroscopy revealed ~300 mV of photovoltage from SMA and observed the transition from adaptive to buried semiconductor/catalyst junctions with negative applied potential, further deepening our mechanistic understanding of the SMA-CNT/CoPc-NH_2 interface.

8.2. Material and Methods

8.2.1. Materials

Si wafers (3 inch diameter, p-doped with B, 1-10 Ω cm; 1 inch diameter, n-degenerately doped with As, 0.001-0.005 Ω cm) were purchased from University Wafers Inc.. CoPc-NH_2 (99%) was purchased from PorphyChem. CNTs were purchased from C-Nano (product number FT 9100). *N*,*N*-dimethylformamide (DMF, 99%), ethanol (98%), Nafion solution (5 wt.% in alcohol), dimethylsulfoxide (DMSO, 99.9%), and D_2O were purchased from Sigma-Aldrich. $KHCO_3$ (99%) was purchased from Fisher Scientific. CO_2 (99.9%), C_4F_8, and SF_6 were purchased from Airgas.

8.2.2. Preparation of catalyst ink

Pre-purified[8] CNTs and CoPc-NH_2 were first dispersed in DMF (1 mg mL^{-1}, and 0.1 mg mL^{-1}, respectively), and ultrasonicated for 30 min. 30 mL of the CNT and 15 mL of the CoPc-NH_2

dispersions were mixed together and ultrasonicated for another 30 min. The resulting mixture was then stirred vigorously for 12 h. After that, the mixture was filtered through a Nylon membrane (0.2 μm pore size), washed with DMF and water, re-dispersed in water, and then freeze-dried. The obtained powder was then dispersed in ethanol at a concentration of 1 mg mL^{-1}. 15 wt.% Nafion (relative to the mass of the CNT/CoPc-NH_2 catalyst) was added, followed by ultrasonication for at least 30 min to achieve a homogenous catalyst ink. The as-made CNT/CoPc-NH_2 ink was then stored in air for future use.

8.2.3. Fabrication of SMA-CF_x

A p-type Si wafer was first spin-coated with hexamethyldisilazane (HMDS) and an AZ 1505 photoresist. A photo-lithography mask featuring a square array of 3 μm-diameter holes with a pitch of 10 μm was applied to the coated wafer, and the masked wafer was exposed using a SUSS MJB4 mask aligner. The exposed wafer was developed using an AZ 400K developer and dried using nitrogen gas. 100 nm of Al was then evaporated by e-beam onto the wafer to serve as a hard mask for etching. After the Al deposition, the whole wafer was immersed into acetone to remove the remaining photoresist and Al on the photoresist, leaving behind an array of Al disks (3 μm in diameter) with a pitch of 10 μm. Next, the wafer was transferred into an Oxford PlasmaPro 100 RIE chamber. An SF_6 (etching reagent) and C_4F_8 (protection reagent) alternating plasma was applied for 60 cycles to create the 18 μm-tall pillars. Different pillar heights can be achieved by controlling the cycle number. A hydrophobic CF_x layer was finally deposited onto the created pillars using a C_4F_8 plasma for 15 s without breaking the vacuum.

8.2.4. Fabrication of photocathode

Firstly, an SMA-CF_x wafer was cut into 1 cm × 1 cm pieces using a diamond pen. Then 10 μL of the prepared CNT/CoPc-NH_2 ink was drop-casted onto an SMA-CF_x piece with mild

nitrogen gas blowing, and this operation was repeated 10 times. Next, the SMA-CNT/CoPc-NH_2 piece was cut into two 0.5 cm × 1 cm pieces. A tiny drop (~1 μL) of In-Ga eutectic was transferred onto the back of the 0.5 cm^2 piece and rubbed into the substrate by scratching using a diamond pen. Finally, the back-scratched piece was connected to an aluminum electrical wire using a silver conductive paste and a copper tape. The back and edges of the as-made photocathode was then sealed with a vacuum wax (Apiezon Wax W).

8.2.5. PEC measurement

All PEC measurements were carried out in 0.1 M $KHCO_3$ aqueous electrolyte using a custom-made H-cell. CO_2 was continuously purged into the cell with a flow rate of 20 sccm. A carbon rod and saturated Ag/AgCl were used as the counter and reference electrodes, respectively. A 300 W Xe lamp (Newport) was used as the light source. A 400 nm cut-off filter (Thorlabs) was used to filter the UV spectrum. The illumination power was measured by a photodiode to be around 150 mW cm^{-2}. Before constant-potential photoelectrolysis the photocathode was pre-conditioned under -0.5 V for 10 mins to obtain a stable current The gas products were detected using an online GC system, which injects 1 mL of the outlet gas every 10 min for measuring the CO and H_2 concentration. After each 30 min of electrolysis, 0.45 mL of the electrolyte was taken out of the H-cell using a syringe without letting the electrode expose to air. 50 μL of D_2O containing 10 mM DMSO as internal standard was added to the sample and transferred into an NMR tube for measuring the methanol concentration.

8.2.6. Characterization

SEM images were taken using a Hitachi SU8230 scanning electron microscope. FIB cutting was conducted using a Thermo Fisher Helios G4 SEM/FIB system. XPS was measured using a PHI VersaProbe II Scanning XPS Microprobe instrument. The height of the pillars was

measured using a Zygo 3D Optical Profiler. STEM images were obtained using a JEOL NEOARM transmission electron microscope at 200 kV with a high-angle annular dark field detector. EDS mapping was performed with a 4 cm camera length, a 6C probe size, and a 40 μm condenser aperture, yielding approximately 62.5 pA probe current and a convergence angle of approximately 27 mrad.

In situ Raman experiments were carried out with a home-built Raman system as described in Chapter 2 section 2.3. A Ne light was used for calibration in the 700 to 2100 cm^{-1} Raman shift spectral window before measurement. A quartz electrochemical cell (Gaoss Union, C012) was used for *in situ* Raman measurement, with a Ag/AgCl reference electrode and a Pt mesh counter electrode. The 632.8 nm laser with a power of 13.7 mW was used as both the excitation source and Raman probe. The linear sweep voltammetry analysis under Raman collection condition was conducted using a CHI 660E potentiostat. The scan rate was set to be 1.667 mV/s to match the Raman collection window (30 s accumulation per spectrum, 0.05 V interval). Before *in situ* Raman measurement, electrodes were pre-conditioned under -0.5 V for 10 mins under 150 mW cm^{-2} Xe lamp illumination.

8.2.7. Numerical Modeling

Numerical modeling was performed with the use of COMSOL Multiphysics® Version 5.6. A 3-dimensional model consisting of a 4-pillar lattice was chosen to represent the pillared surface most accurately. This geometry was compared to a completely flat surface. The model utilized the software's transport of dilute species module to monitor the concentration of CO within the model domain. Symmetry constraints were applied to the four side walls of the domain and a concentration constraint of 0 M CO was applied to the top barrier to represent the transition to bulk. A stationary study was performed to determine local CO concentration.

For the pillared structure, a CO flux value of 4.11×10^{-4} mol s^{-1} m^{-2} was added to the side walls and top of each pillar. This value was chosen based on the molar production of both CO and methanol, as it was assumed that all produced methanol proceeded through a CO intermediate. A no flux constraint was applied on the very bottom of the pillars, as SEM images showed limited catalyst deposition on the sidewalls and top. For the flat surface, the same flux condition was applied to the entire electrode surface.

8.3. Results and Discussion

The SMA structure with a pillar diameter of 3 μm, a pillar height of 18 μm, and a pitch of 10 μm was fabricated through photolithography and dry etching (Figure 8.1a, A8.1). Following the etching step, a thin CF_x layer was coated on SMA using an octafluorocyclobutane (C_4F_8) plasma. Subsequently, the CNT/CoPc-NH_2 catalyst was drop-casted onto the SMA-CF_x substrate (Figure 8.1b). Due to the hydrophobic nature of the SMA-CF_x surface, the CNT/CoPc-NH_2 catalyst exhibits a preference for adhering to the Si pillars rather than the flat Si basal plane (Figure 8.1c-e). This distinct assembly pattern allows for circumventing the high optical density issue of the CNT-based catalyst and facilitating efficient light absorption by the Si substrate (Figure A8.2).

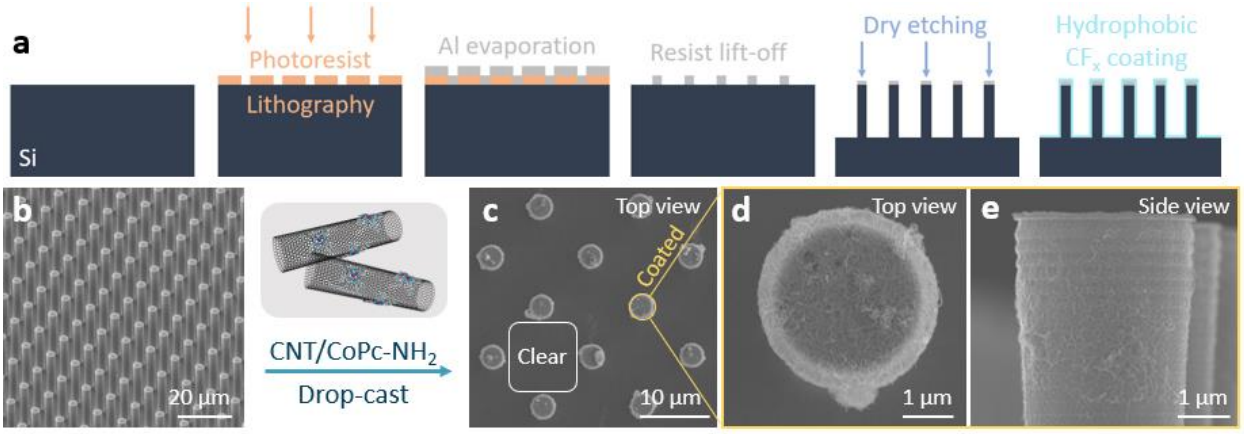

Figure 8.1. (a) SMA fabrication and CF_x coating. (b) SEM image of SMA-CF_x. (c) SEM image of SMA-CF_x coated with CNT/CoPc-NH_2 catalyst. (d-e) Top-view and side-view SEM images of a single SMA-CF_x pillar coated with CNT/CoPc-NH_2.

To directly probe how the quasi-Fermi level of CNT/CoPc-NH_2 catalysts changes with potential under light illumination, the SMA-CF_x-CNT/CoPc-NH_2 photoelectrode was characterized by *in situ* Raman spectroscopy using 632.8 nm He-Ne laser serving as both Raman probe and illumination source with recorded Raman spectra shown in Figure 8.2a. Potential was applied through a linear sweep voltammetry (LSV) scan from 0.625 to -0.375 V (Figure 2b) vs the reversible hydrogen electrode (RHE, all potentials in this work are referenced to RHE unless otherwise stated) at the same time of Raman spectrum acquisition. From the Raman spectra, resonance Raman features of CoPc-NH_2 were observed at 755, 1458, and 1543 cm^{-1} (red shade in Figure 8.2a).[16-18] The peaks at 1334, 1585, and 1617 cm^{-1} correspond to CNT's D, G^-, and G^+ bands (gray shade in Figure 8.2a), respectively.[19-20] Our initial focus was to monitor the resonant Raman peaks of CoPc-NH_2 as a function of applied potential, whose intensity will drop upon one-electron reduction of the CoPc-NH_2 molecule.[16-17] As the applied potential is polarized toward the negative direction, the CoPc-NH_2 peaks start to decrease in intensity at 0.3 V, and the decrease levels off after the potential reaches 0 V (Figure 8.2c). This change suggests that the CoPc-NH_2 molecules undergo one-electron reduction in the potential range from 0.3 to 0 V. Consistently, a photoelectrochemical reduction wave that reaches its peak current at 0.05 V can be observed in the same potential range of the LSV diagram (Figure 8.2b). The new peak appearing at 746 cm^{-1} (green shade in Figure 8.2a, Figure A8.3) is attributed to reduced CoPc-NH_2. In a control experiment, we studied the electrochemical reduction of CoPc-NH_2/CNT deposited on a degenerately doped n-type SMA-CF_x (n^+-SMA-CF_x) substrate (Figure A8.4). The resonant Raman peaks of CoPc-NH_2

do not reach their lowest intensity until about -0.3 V, which, in comparison with the corresponding SMA-CF_x-CNT/CoPc-NH_2 results (Figure 8.2c), enables us to discern a 300 mV of photovoltage, i.e., quasi-Fermi-level splitting, for the p-type SMA electrode.

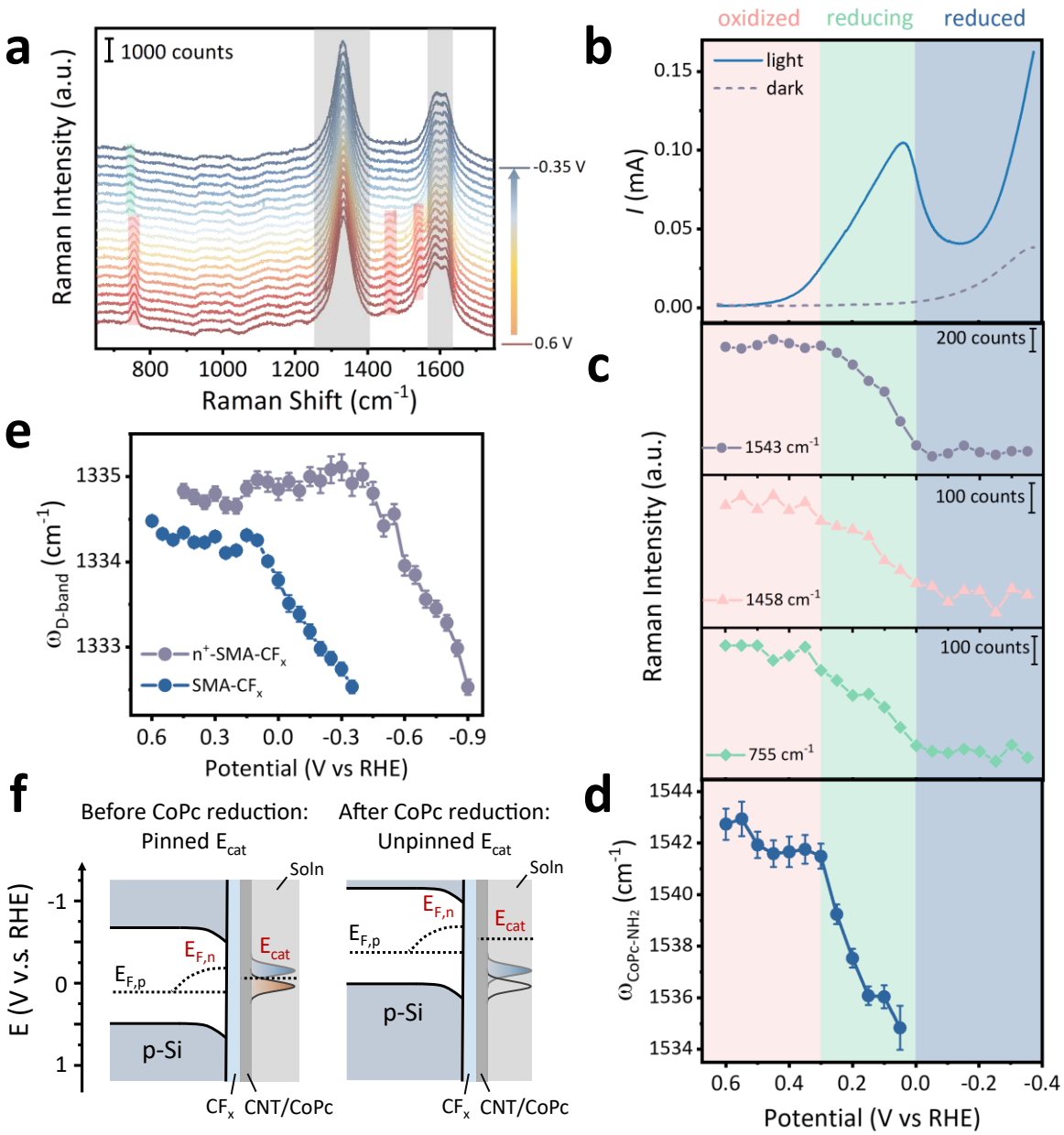

Figure 8.2. (a) *In situ* Raman spectra of CNT/CoPc-NH_2 on SMA-CF_x from 0.625 V to -0.375 V under 632 nm illumination. (b) LSV curve of SMA-CF_x-CNT/CoPc-NH_2 during *in situ* Raman

measurement under illumination or in dark conditions. (c) One-electron reduction of CoPc-NH_2 tracked by changes in resonance Raman intensity. Potential-dependent Raman vibrational frequencies of (d) CoPc-NH_2 1543 cm^{-1} peak and (e) CNT D band. (f) Proposed band diagram at SMA-CF_x-CNT/CoPc-NH_2-solution interfaces. The electrode was tested after pre-conditioning the electrode at -0.5 V for 10 min under 150 mW cm^{-2} Xe lamp irradiation. The red, blue, and green shaded potential region in (b), (c), and (d) indicate the potential range of oxidized, one-electron-reduced, and mixed of oxidized and one-electron-reduced CoPc-NH_2, species, respectively, determined from Raman intensity change in (c).

Further details about the CNT/CoPc-NH_2 catalyst can be obtained through fitting of the CNT D, G^+, and G^- bands as well as the 1458 and 1543 cm^{-1} peaks of CoPc-NH_2 (Figure A8.5). The frequency of the CoPc-NH_2 1543cm^{-1} peak ($\omega_{CoPc\text{-}NH2}$) exhibits intriguing potential-dependent behavior. It remains unchanged at potentials above 0.3 V and continuously decreases with increasingly reducing potential in the 0.3-0 V region (Figure 8.2d). This phenomenon signifies the change in the molecule's electrochemical potential when potential is more negative than 0.3 V. The $\omega_{CoPc\text{-}NH2}$ shift with applied potential can be attributed to the stark effect or electro-inductive effect on oxidized CoPc-NH_2 molecule.[21-23] Out of the three observed vibrational modes of CoPc-NH_2, the 1543 cm^{-1} peak, assigned to the C_α-N_β-C_α bridging bond displacement, is the only one that demonstrates a significant potential-dependent frequency shift. This may be attributed to the macrocycle plane's rotation along the C_α-N_β-C_α bridge that generates a dipole moment perpendicular to the CNT surface.[23] The other two modes, however, mainly generate dipole moments within the molecular plane.[18, 24]

The frequency of the CNT D band ($\omega_{D\text{-}band}$) has been shown to be sensitive to the Fermi level of the material and can be used as a reporter of chemical and electrochemcial doping.[20, 25-26]

Interestingly, $\omega_{D\text{-band}}$ shows a potential-dependent behavior similar to the 1543 cm^{-1} peak of CoPc-NH_2. As the applied potential is swept cathodically from 0.625 V to -0.375 V, $\omega_{D\text{-band}}$ remains constant until 0.1 V and then decreases (Figure 8.2e). We attribute this to the shift of CNT quasi-Fermi-level at 0.1V for CNT/CoPc-NH_2 on SMA-CF_x under photoelectrochemical conditions. For CNT/CoPc-NH_2 on n^+-SMA-CF_x, a similar potential-dependent $\omega_{D\text{-band}}$ trend is observed, but the onset of $\omega_{D\text{-band}}$ frequency shift occurs at -0.3 V (grey trace in Figure 8.2e). It is worth noting that although the shift of $\omega_{D\text{-band}}$ reports the change of CNT Fermi level, it is difficult to establish a universal calibration curve that relates the $\omega_{D\text{-band}}$ value to the Fermi level (Figure A8.6 and Table A8.1) because the D band frequency are not only sensitive to the electric field but also to solution microenvironment factors such as chemisorption of electrolyte ions and local pH changes.[25, 27-28]

Based on the above analysis, we propose the following properties for the SMA-CF_x-CNT/CoPc-NH_2-solution junction. As summarized in Figure 8.2f, the potentiostat controls the hole Fermi-level of Silicon ($E_{F,p}$); the quasi-Fermi-level of electrons ($E_{F,n}$) arises upon photogeneration and separation of electrons; Fermi-level of CNT and the attached CoPc-NH_2 molecules equilibrate with each other, denoted as E_{cat}. From the Silicon flat-band potential to 0.1 V (left panel of Figure 8.2f), E_{cat} is pinned by the one-electron redox potential on CoPc-NH_2, which means that the applied potential mainly drops on the semiconductor side, providing the electric field needed to separate the photogenerated charge carriers and generating a ~300 mV photovoltage to reduce the CoPc-NH_2 molecules. When the applied potential becomes more negative than 0.1 V (right panel of Figure 8.2f), E_{cat} is unpinned as molecules are being reduced. In this potential region, the semiconductor band bending and the height of the semiconductor-catalyst barrier remain constant, irrespective of the applied potential. The applied potential change ($\Delta E_{F,p}$) directly shifts E_{cat} towards more negative potential. The junction properties in terms of pinned and unpinned E_{cat} is

also known as ‘adaptive’ to ‘buried’ junction, respectively, from previous literatures.[29-32] The formation of the buried junction results in an electrostatic potential drop across the solution double layer, facilitating a suitable microenvironment for methanol production at more negative potentials. This scenario also implies efficient electron tunneling from SMA to CNT/CoPc-NH_2 even without direct contact.

The performance of the fabricated photoelectrode for PEC CO_2 reduction was evaluated using an H-cell with a quartz window under the illumination of an Xe lamp (150 mW cm^{-2}, 400 nm cutoff), as depicted in Figure 8.3a. All constant-potential photoelectrolysis experiments were conducted after pre-conditioning the electrode at -0.5 V for 10 mins. The current increases and then stabilizes during the pre-conditioning (Figure A8.11), which is possibly due to the dissolution of the insulating native oxide layer on Si. *In situ* Raman spectroscopy measurement of fresh SMA-CF_x-CNT/CoPc observes CoPc-NH_2 reduction and CNT electron doping similar to that on the pre-conditioned photoelectrode but at more cathodic potentials (Figure A8.7). By comparing the CoPc-NH_2 reduction potential and $\omega_{D\text{-band}}$ turning potential between these two conditions, we found that the pre-conditioning could reduce about 200 mV of the interfacial potential loss, probably by reducing the silicon surface oxide or surface states and thus decreasing the interfacial resistance. Under -0.7 V applied potential, the SMA-CF_x-CNT/CoPc-NH_2 photocathode delivers a methanol FE of 21% and a CO FE of 37%, accompanied by a total photocurrent of 16.6 mA cm^{-2} (Figure 8.3b). About 350 mV photovoltage was gained from the Si substrate, which matches the results from the in-situ Raman (Figure 8.2c, Figures A8.4, A8.10). The stability of SMA-CF_x-CNT/CoPc-NH_2 was evaluated under the constant-current mode with a photocurrent of 15 mA cm^{-2} (Figure 8.3c). In the first 20 min, the applied potential drops continuously, which is similar to the activation observed in the pre-conditioning step under the constant-potential mode. After that, a stable FE of

~20% for methanol is achieved and maintained for 2 h. Subsequently, $FE_{methanol}$ decreases to 6%, accompanied by an increase in the partial current density of H_2, which may be attributed to the exposure of the Si surface to the electrolyte.

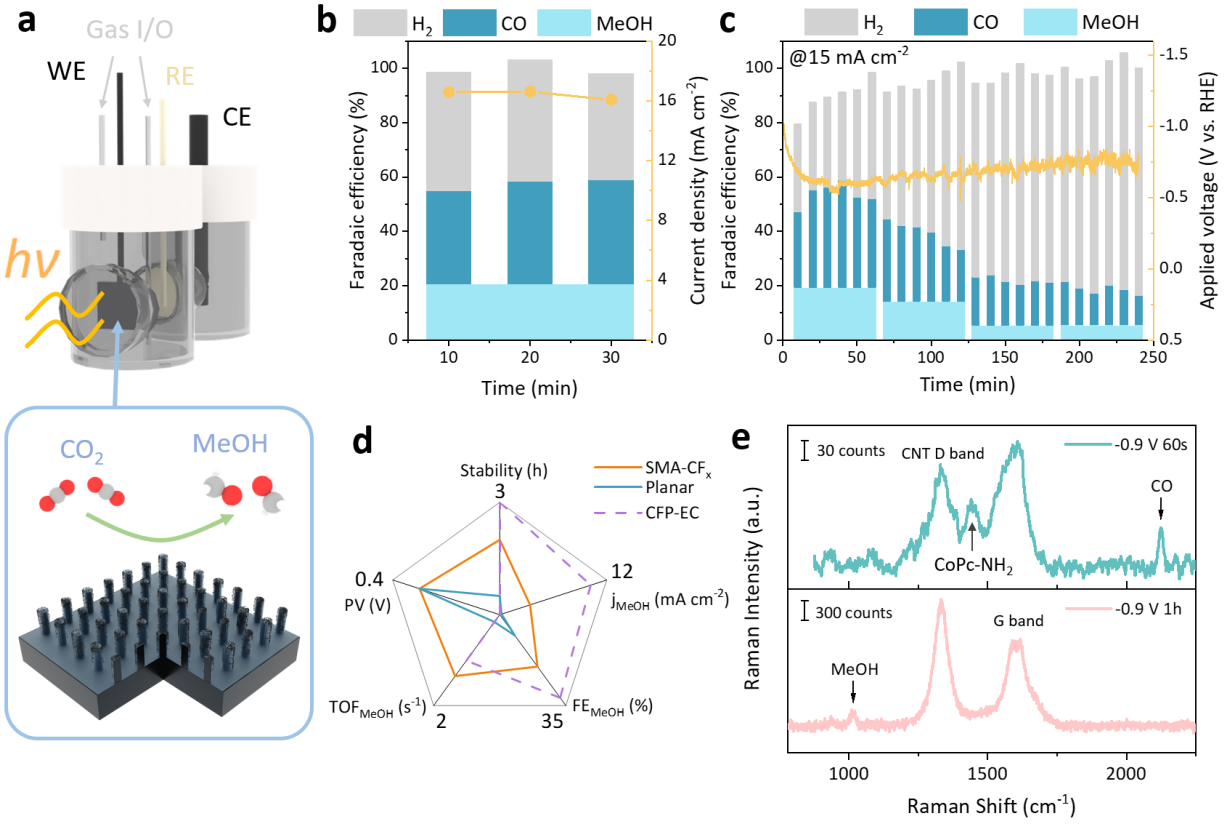

Figure 8.3. PEC CO_2 reduction performance of SMA-CF_x-CNT/CoPc-NH_2 in 0.1 M aqueous $KHCO_3$ under illumination. (a) PEC cell structure. (b) Total photocurrent and product distribution at -0.7 V as a function of time. Methanol concentration was measured after the 30 min reaction and is assumed to be constant within the time window. (c) Stability test at constant photocurrent of 15 mA cm^{-2}. (d) Performance comparison with GO/CoPc-functionalized planar Si (under illumination), and CNT/CoPc-NH_2 deposited on carbon fiber paper (CFP, electrolysis without illumination). (e) *In situ* Raman measurements at -0.9 V at 60 s (top) and 1 hr (bottom), showing generated CO and methanol.

Comparison of performance for CO_2 reduction to methanol, in terms of stability, partial current density, FE, TOF, and photovoltage, is made between different CoPc-based (photo)electrodes (Figure 8.3d). The SMA-CF_x-CNT/CoPc-NH_2 photoelectrode has the best overall performance. It exhibits a similar photovoltage of ~350 mV (Figure A8.10) but 3, 17, and 4 times higher FE, methanol production rate, and stable operation time, respectively, than our prior generation of photoelectrodes based on planar Si and the GO/CoPc catalyst.[14] Compared with the state-of-the-art electrode of CNT/CoPc-NH_2 deposited on CFP (Figure A8.9), the SMA-CF_x-CNT/CoPc-NH_2 photoelectrode has the advantage of improved overpotential because of the photovoltage, but obtains about 66% and 33% of the FE and partial current density, respectively (Figure 8.3d).[8] The lower methanol selectivity and production rate may be attributed to lower catalyst loading (0.1 mg cm^{-2} on SMA versus 0.4 mg cm^{-2} on CFP) and less effective CO_2 mass transport (the hydrophobic CFP substrate resembles a gas diffusion electrode in CO_2 electrocatalysis). Both are limitations that need to be solved in future work to further improve the PEC performance. Interestingly, the TOF for methanol production on SMA-CF_x-CNT/CoPc-NH_2 reaches approximately 1.5 s^{-1}, which is comparable to that achieved with CNT/CoPc-NH_2-catalyzed electrolysis (1.0 s^{-1}) if the catalyst loading difference is taken into consideration. This observation suggests that the CO_2-to-methanol catalytic processes on the SMA-based photoelectrode and CFP-based electrode likely go through the same mechanism.

CO_2 reduction intermediates and products are also detected by Raman spectroscopy as shown in Figure 8.3e. Under -0.9 V applied potential for 60 s, a peak at 2120 cm^{-1} evolves (pink, lower panel), confirming the formation of free CO bubbles on the surface.[33] A peak at 1015 cm^{-1} appears after 1 hour of product accumulation under light illumination (green, upper panel). This peak is assigned to methanol C-O stretching frequency,[34] confirming the generation of methanol

product (also see methanol calibration in Figure A8.8). 2120 cm^{-1} CO stretching peak is not detected in this spectrum, likely because loosely bound CO bubble detach from the electrode, which did not generate enough Raman signal.

The improved methanol production performance of the SMA-CF_x-CNT/CoPc-NH_2 photoelectrode is a result of the micropillar array structure and the CF_x coating. The SMA-CNT/CoPc-NH_2 photoelectrode (without CF_x coating) shows 1.5 times the FE and 2.3 times the partial current density of the planar Si-GO/CoPc electrode (Figure 8.4a). We hypothesize that micropillar array can help retain CO, the key reaction intermediate on the CO_2-to-methanol pathway that desorbs from the CoPc catalytic site,[35] and thus enhance its further reduction to generate methanol. This hypothesis is supported by our simulation results which show that the micropillar array structure can generate over 1.5 times the local CO concentration compared to the planar surface (Figure A8.18). In this simulation, a Si array with the same morphology was created in COMSO Multiphysics, a CO flux derived from the experimental partial current for CO and methanol was added to the planar Si, the sidewall, and top of the pillars. This hypothesis is further supported by the experimental observation that the height and pitch of the micropillar array influence methanol selectivity and photocurrent. Considerably lower $FE_{methanol}$ and slightly lower total current density are observed for SMA with a shorter pillar height of 7 μm (Figure A8.12a, b). This may be due to reduced CO trapping capability and lower electrode surface area. A larger pillar height of 36 μm does not seem to affect methanol production much but significantly increase the HER rate likely because of a larger area of exposed Si surface (Figure A8.12c, d).[7, 14, 36] For a similar reason, a smaller pitch of 8 μm also elevates H_2 evolution (Figure A8.12a, c).

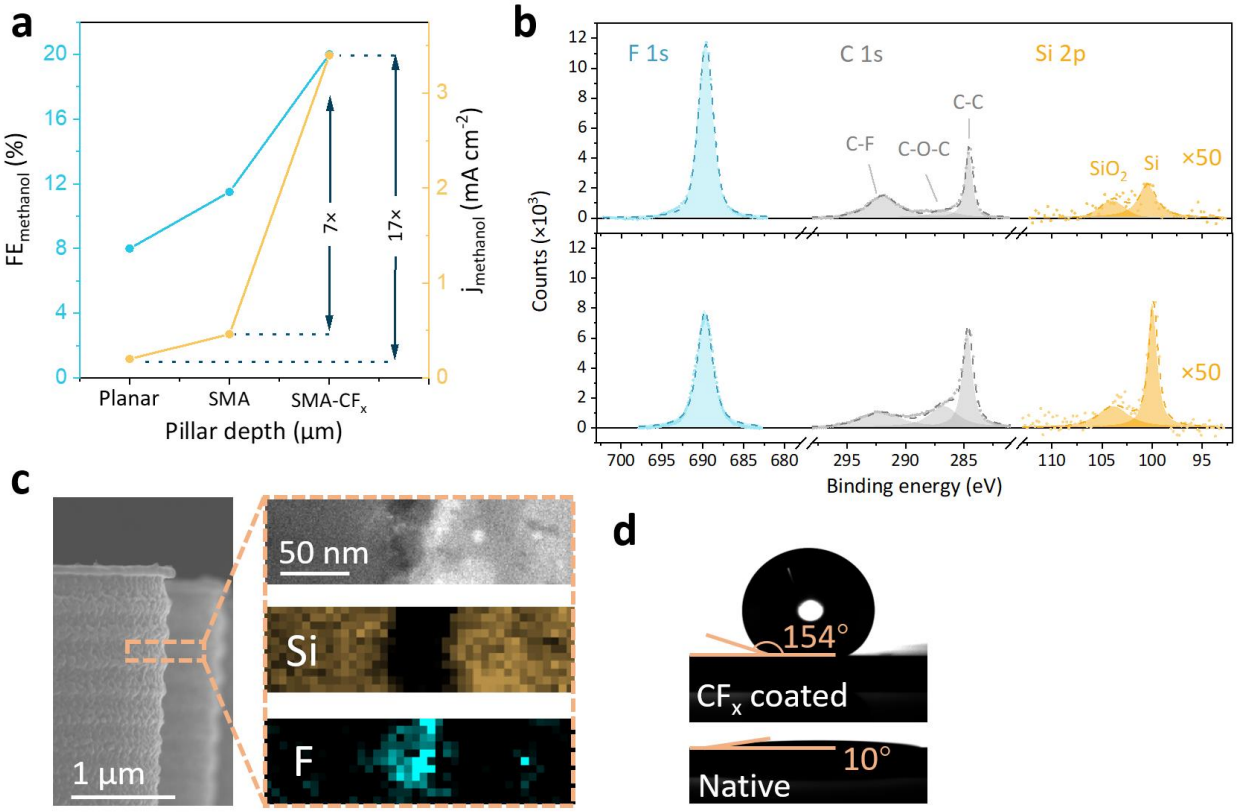

Figure 8.4. (a) Comparison of methanol selectivity and partial current density between SMA-CF_x-CNT/CoPc-NH_2 (noted as SMA-CF_x), SMA-CNT/CoPc-NH_2 (noted as SMA), and planar Si-TiO_2-GO/CoPc (noted as Planar). (b) XPS spectra of SMA-CF_x-CNT/CoPc-NH_2 before (upper panel) and after (lower panel) 4 h of PEC CO_2 reduction under 15 mA cm^{-2}. (c) SEM image of the side wall of a single Si pillar (left), and STEM-EDS mapping of the boxed area. (d) Contact angle measurements on SMA-CF_x and SMA.

The CF_x coating is also key to the enhanced PEC performance. X-ray photoelectron spectroscopy (XPS) successfully detected F and C bonded to F together with little Si (Figure 8.4b, upper panel), confirming the presence of CF_x on the photoelectrode surface. To characterize the thickness and uniformity of the CF_x layer, we used focused ion beam to slice a thin layer (approximately 100 nm thick) off a pillar, as illustrated in Figure 8.4c and S14. Scanning transmission electron microscopy (STEM) and energy-dispersive X-ray spectroscopy (EDS) were

performed on the slice. A continuous F-containing layer with an average thickness of ~40 nm was observed (Figure 8.4c, Figure A8.19), suggesting that a CF_x layer of the same thickness effectively covers the Si surface. With this coating, the SMA-CF_x substrate exhibits an ultrahigh contact angle of 154° with water, while the CF_x-free SMA (native oxide surface) shows a low contact angle of only 10° (Figure 8.4d). Incorporation of CF_x into the SMA-CNT/CoPc-NH_2 structure increases CO_2 reduction current by 4 times and $FE_{methanol}$ by 1.8 times, leading to a 7-fold increase in methanol production rate (Figure 8.4a, Figure A8.12a). In a control experiment, a SMA-TiO_2-CNT/CoPc-NH_2 photoelectrode exhibits a lower photocurrent (~7 mA cm^{-2}), a lower methanol FE (14%), and a much higher H_2 FE (71%) than SMA-CF_x-CNT/CoPc-NH_2 (Figure A8.16). This comparison reflects the roles of the hydrophobic CF_x layer. It can facilitate CO_2 mass transport, enhance CO retention, and suppress electrolyte penetration into the interspace of the micropillars, leading to improved CO_2 reduction to methanol and suppressed H_2 evolution.[37]

As the methanol production performance of the SMA-CF_x-CNT/CoPc-NH_2 photoelectrode starts to decay after 2 h of operation (Figure 8.3c), we further examined a used photoelectrode (after 4 h of PEC test) to understand the deactivation. Compared to the fresh photoelectrode, the deactivated photoelectrode has considerably less F and more Si on the surface as revealed by XPS (Figure 8.4b, Table A8.2), indicating that the CF_x coating layer has degraded after the long-term PEC test. This change in surface composition can explain the observed deactivation behavior. The degradation of the CF_x layer leads to lowered surface hydrophobicity, which lessens CO_2 reduction to methanol. On the other hand, the newly exposed Si surface facilitates HER.[7, 14, 36] We note that suppressing HER on Si photoelectrodes, especially during long-term operation, remains challenging. It is limited by the tradeoff between catalyst coverage/loading and light absorption as

well as the durability of the surface passivation/protection layer under reaction conditions, which we will try to address in future work.

8.4. Conclusion

In conclusion, the study in this chapter successfully showcases the effectiveness of microenvironment and interface tailoring on Si-based CO_2 reduction photocathodes, leading to a remarkable FE of over 20% for methanol production with record-high current density. The unique Si-catalyst buried junction allows a beneficial thermodynamic driving force for CO_2 to methanol reduction on the catalyst. The incorporation of the micropillar array structure and the superhydrophobic coating plays a crucial role in enhancing retention of the CO intermediate, consequently improving the selectivity towards the deeply reduced methanol product. This work pioneers a route for microenvironment tailoring on semiconductor surfaces and establishes a new benchmark for PEC CO_2 reduction to liquid fuels using molecular catalysts. The insights gained from this research hold promise for driving further developments in the quest for sustainable and efficient utilization of carbon emissions.

Appendix Chapter 8

Supplementary Results

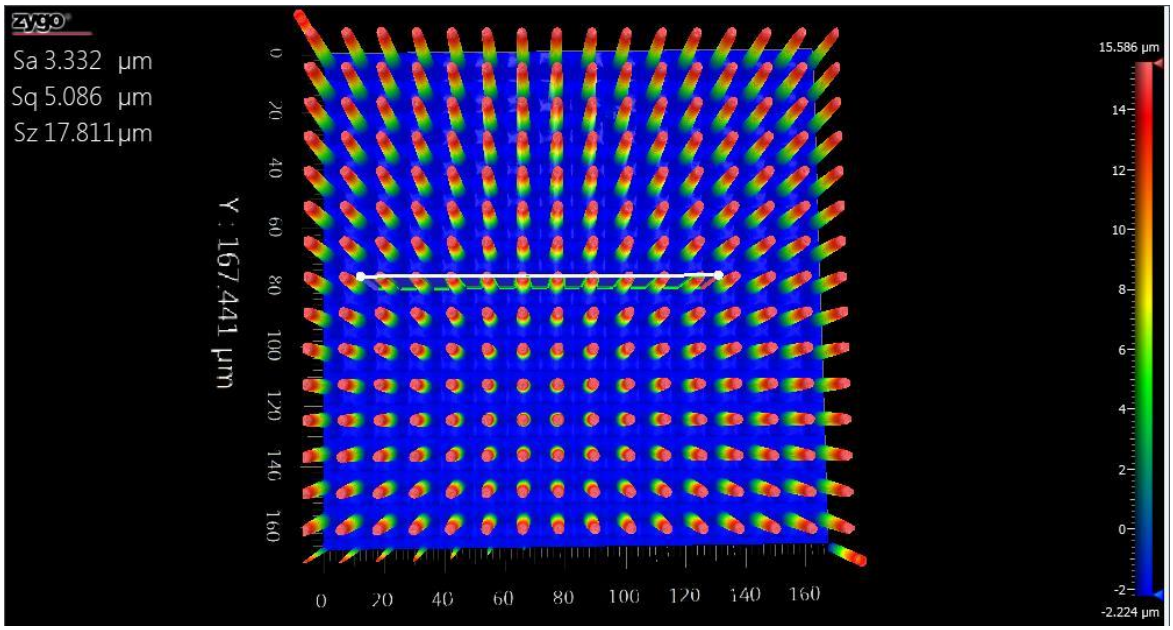

Figure A8.1. Three-dimensional image of SMA obtained by optical profiler.

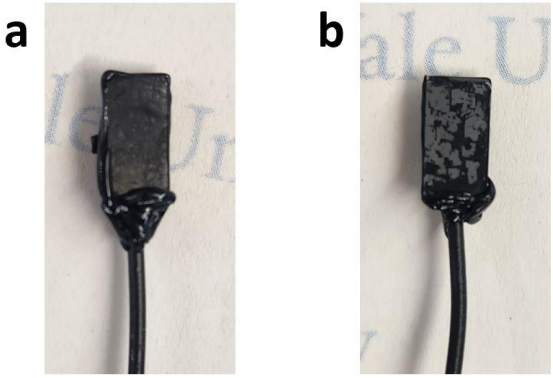

Figure A8.2. Picture of SMA-CF_x photoelectrode with uniformly coated (a) and self-clustered (b) CNT/CoPc-NH_2 layer. The self-clustered assembly of CNT/CoPc-NH_2 on SMA-CF_x enabled light transmission.

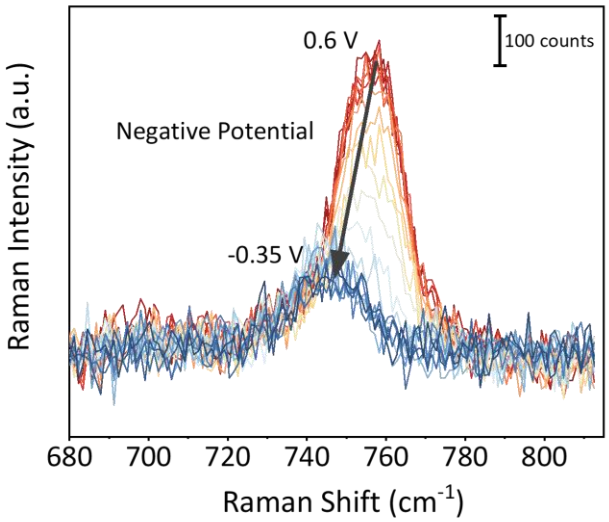

Figure A8.3. *In situ* Raman spectra of CoPc-NH_2 755 cm^{-1} peak on a pre-conditioned SMA-CF_x electrode after background subtraction.

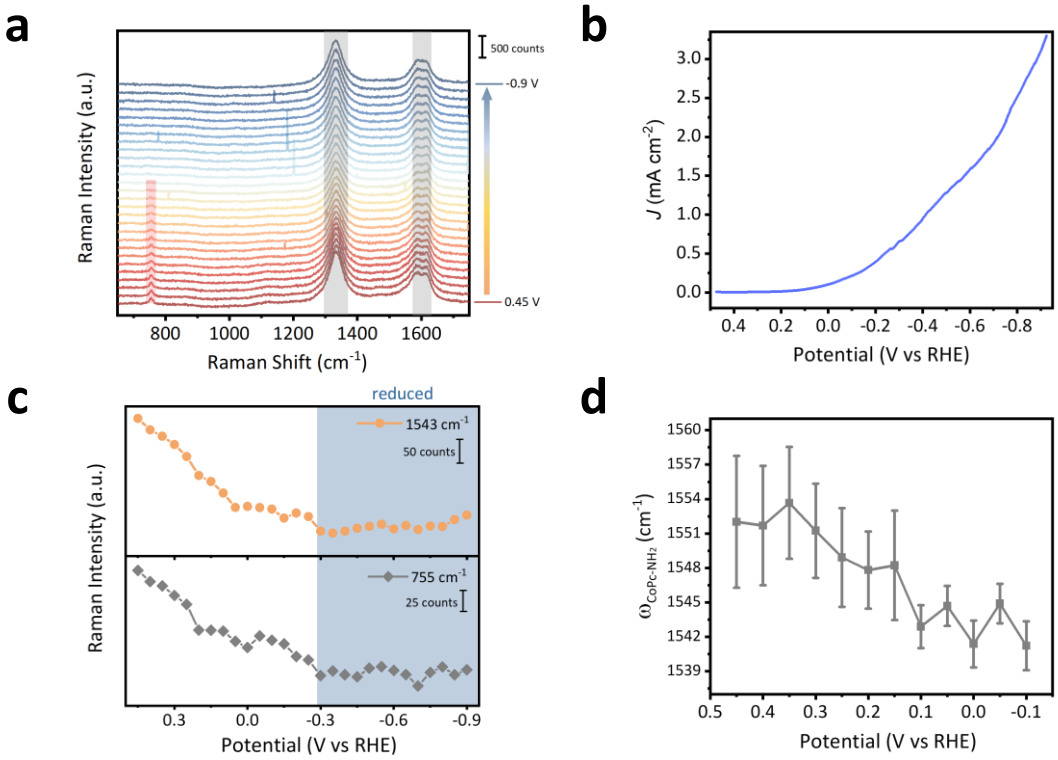

Figure A8.4. (a) *In situ* Raman spectra of CNT/CoPc-NH_2 on n^+-SMA-CF_x from 0.475 V to -0.925 V. (b) LSV diagram of n^+-SMA-CF_x-CNT/CoPc-NH_2 during *in situ* Raman measurement. (c) One-electron reduction of CoPc-NH_2 tracked by changes in resonance Raman intensity at 755 cm^{-1} and 1543 cm^{-1}. (d) Potential-dependent Raman frequency of CoPc-NH_2 1543 cm^{-1} peak.

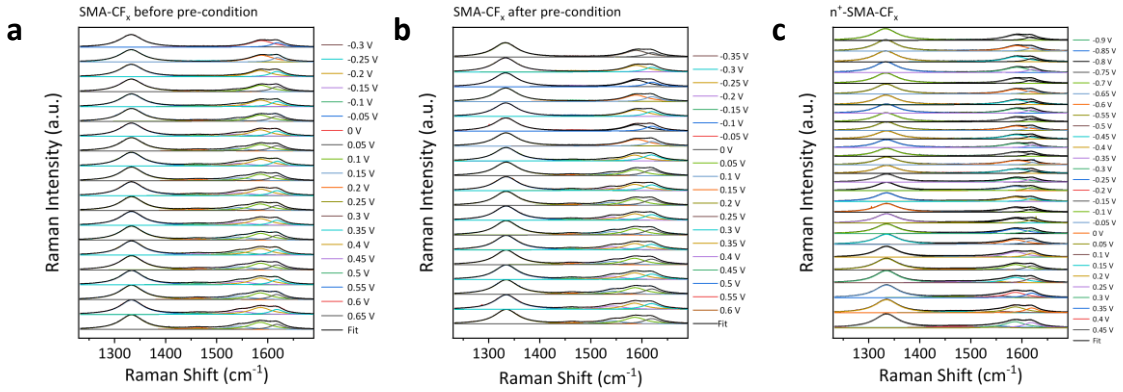

Figure A8.5. Peak analyses of CNT/CoPc-NH_2 from 1233 cm^{-1} to 1800 cm^{-1} on SMA-CF_x (a) before, (b) after pre-condition, and (c) on n^+-SMA-CF_x electrode. Five Lorentz multipeak fittings were used for spectra before CoPc reduction, and three Lorentz multipeak fittings are used for spectra after CoPc reduction. All peak analysis were conducted after background subtraction.

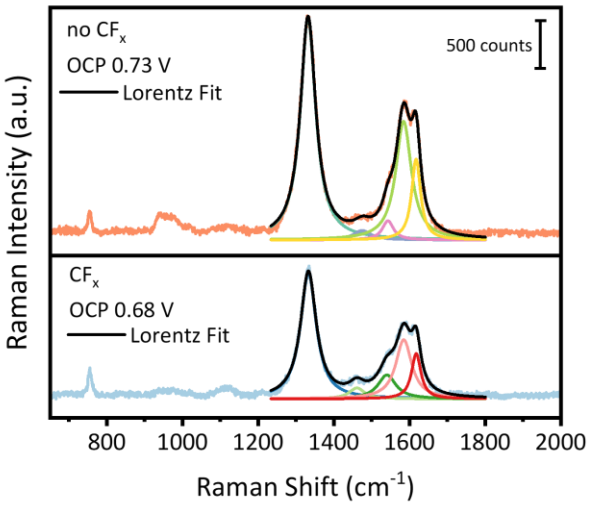

Figure A8.6. Raman spectra of SMA-CNT/CoPc-NH_2 electrode with (lower panel) and without CF_x under open circuit potential in 0.1 M $KHCO_3$ (pH 6.8). Peak position of CNT D band and CoPc-NH_2 are extracted by five Lorentz multipeak fittings and summarized in Table A8.1. The fitting results suggest that the trend between $\omega_{D\text{-band}}$ on two electrodes and their OCP do not agree with the trend between 1543 cm^{-1} CoPc-NH_2 peak frequency and their OCP (decreased ω with more negative potential), suggesting absolute $\omega_{D\text{-band}}$ position does not reflect accurate CNT Fermi-level.

Table A8.1. Raman analysis of CNT/CoPc-NH_2 loaded on SMA with and without CF_x.

	CF_x	**No CF_x**
OCP (V vs RHE)	0.68	0.73
$\omega_{CNT\text{-}D\ band}$ (cm^{-1})	1332.7 ± 0.1	1331.8 ± 0.07
$\omega_{CoPc\text{-}NH2}$ (cm^{-1})	1540.4 ± 1.7	1542.9 ± 1.2

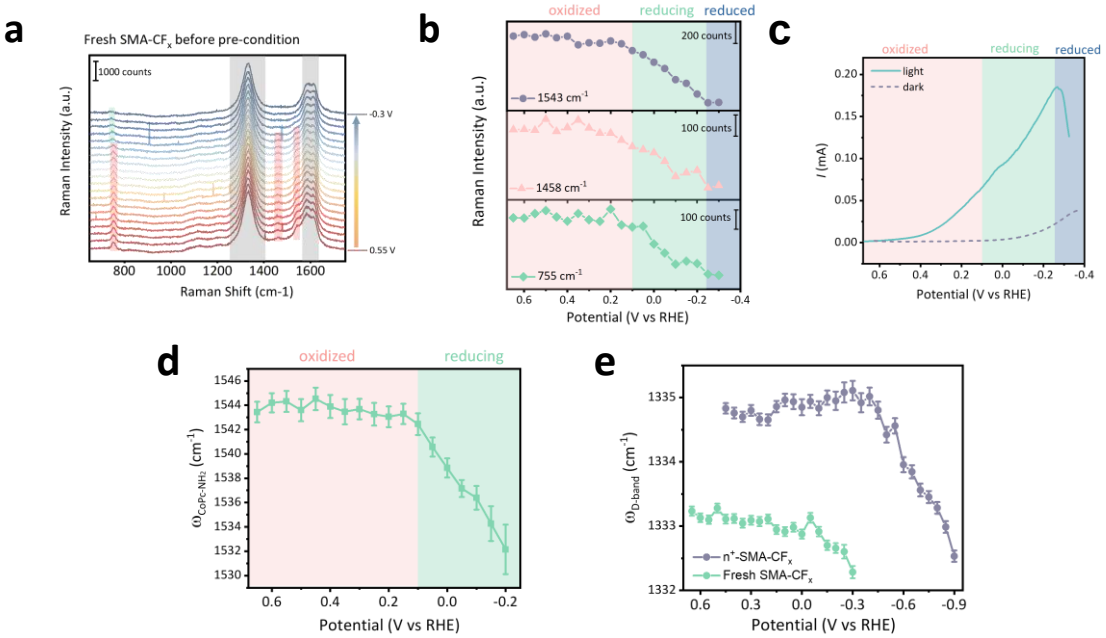

Figure A8.7. (a) *In situ* Raman spectra of CNT/CoPc-NH_2 on SMA-CF_x without pre-conditioning from 0.675 V to -0.325 V. (b) One-electron reduction of CoPc-NH_2 tracked by change in resonance

Raman intensity. (c) LSV curve of SMA-CF_x-CNT/CoPc-NH_2 during *in situ* Raman measurement. (d-e) Potential-dependent Raman vibrational frequencies of (d) CoPc-NH_2 1543 cm^{-1} peak and (e) CNT D band.

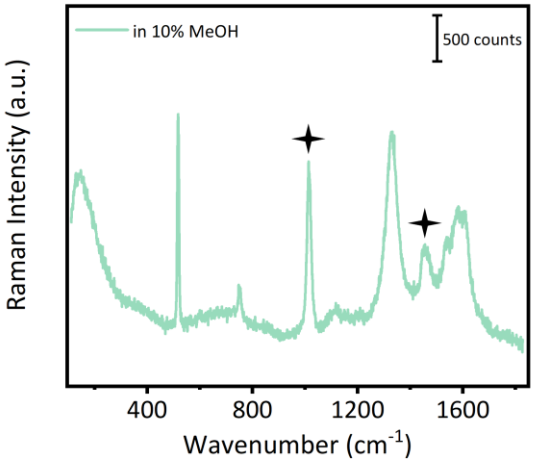

Figure A8.8. Calibration of methanol peaks by measuring the SMA-CF_x-CNT/CoPc-NH_2 in 0.1 M $KHCO_3$ solution containing 10% (v/v%) methanol with no applied bias. The methanol peaks are indicated by the stars.

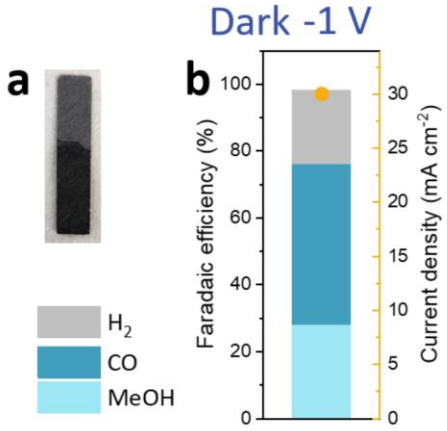

Figure A8.9. Photo of a CFP-CNT/CoPc-NH_2 electrode (a), and the electrocatalytic CO_2 reduction performance under dark (b).

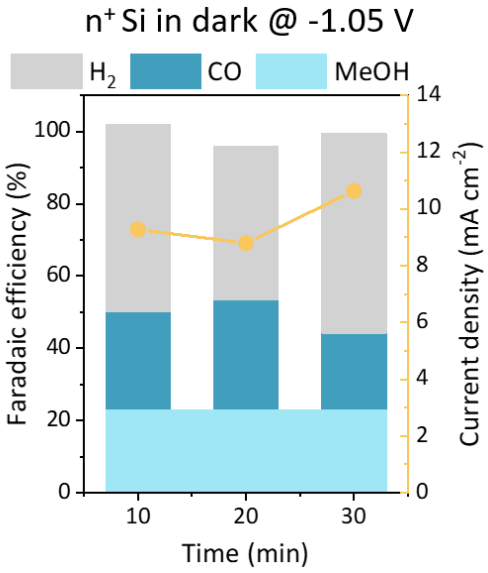

Figure A8.10. Electrocatalytic performance of n-degenerately doped n^+-SMA-CF_x-CNT/CoPc-NH_2 under -1.05 V applied voltage and dark.

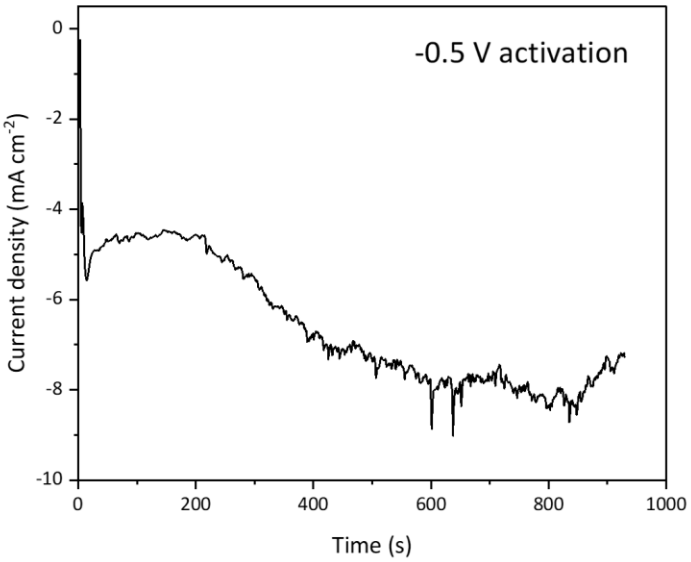

Figure A8.11. Activation current curve of the SMA-CF_x-CNT/CoPc-NH_2 under -0.5 V applied potential (and all other same condition as PEC) before constant potential electrolysis.

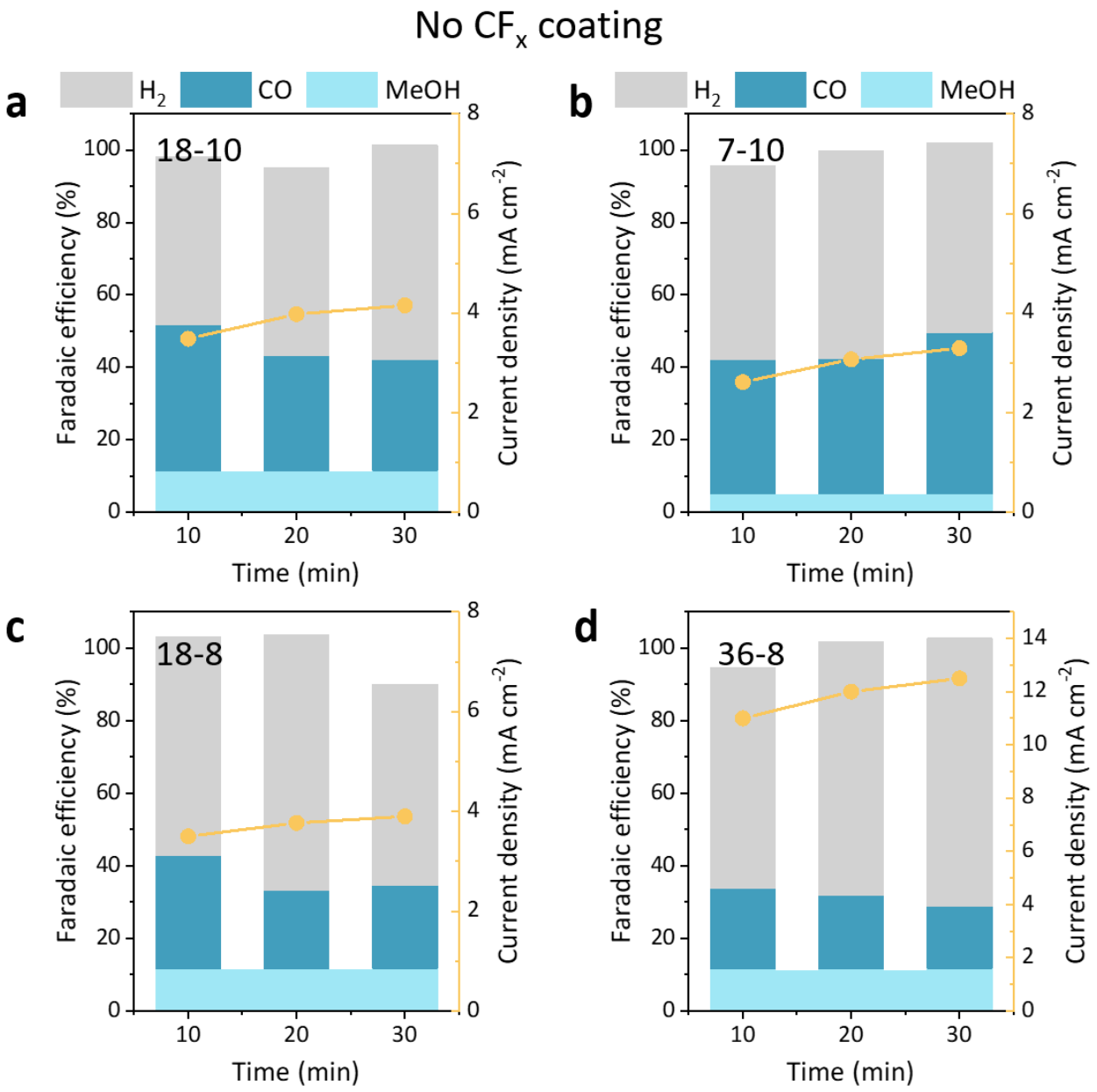

Figure A8.12. PEC performance of SMA-CNT/CoPc-NH_2 without CF_x coating. The top-left corner indicates the pillars height and pitch (H-P). Electrodes were cleaned with HF before drop casting catalyst to remove the insulating native oxide.

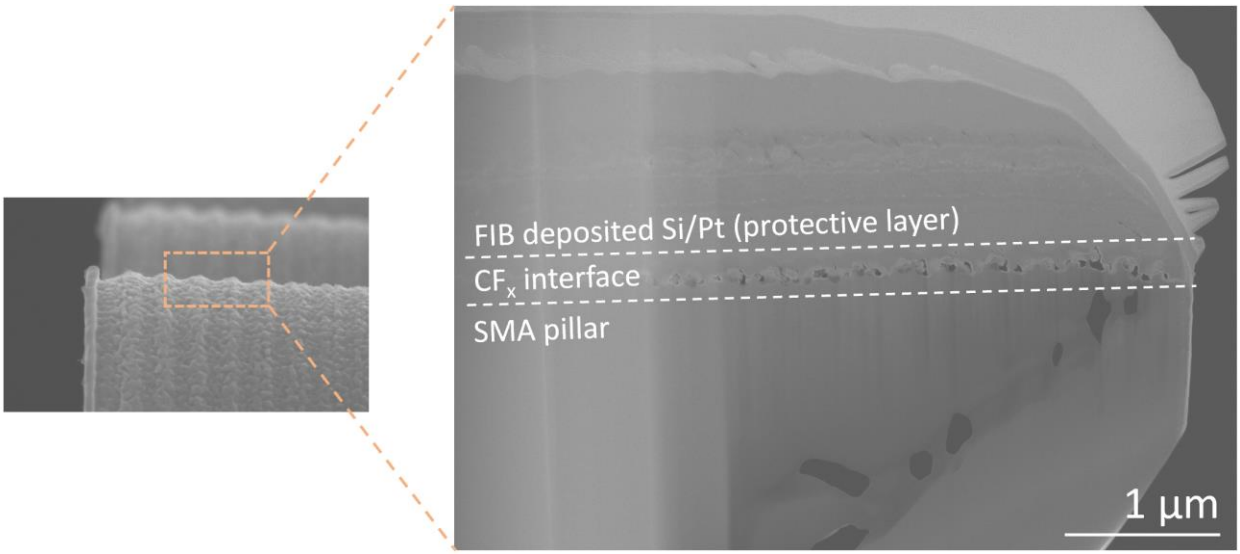

Figure A8.13. SEM image of the FIB-cut Si pillar sidewall cross-section.

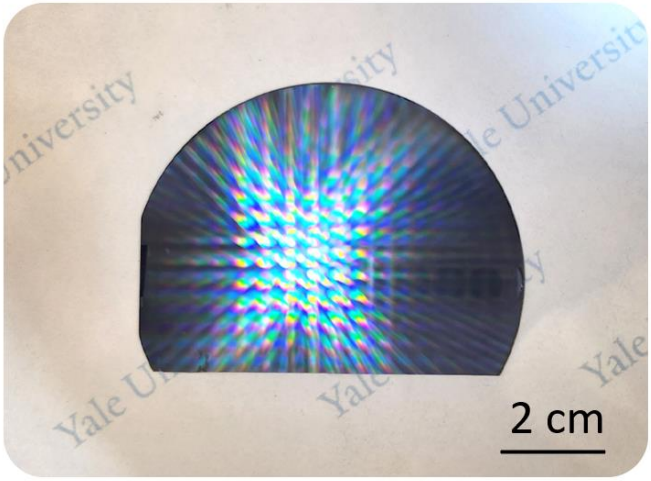

Figure A8.14. Photo of a 3-inch wafer fabricated with SMA pattern.

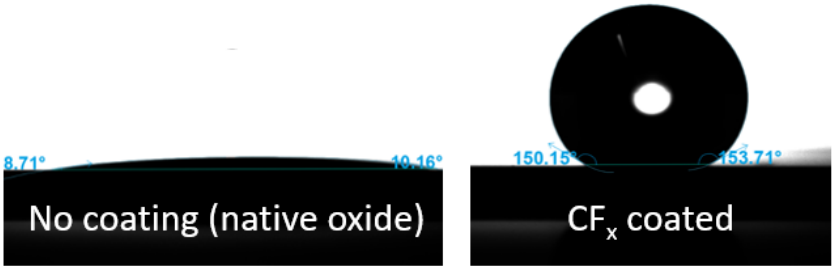

Figure A8.15. Contact angle analysis of the SMA without CF_x coating (left) and with CF_x coating (right).

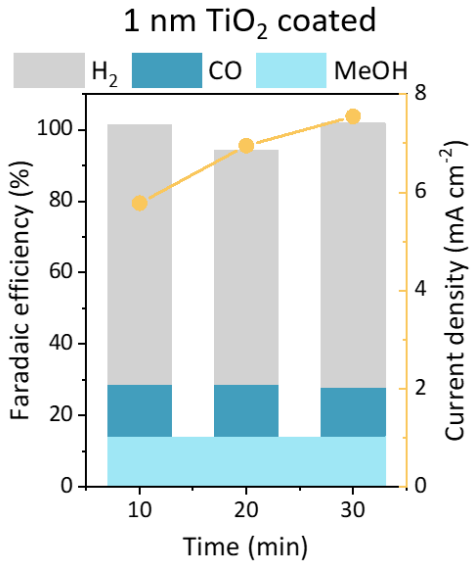

Figure A8.16. SMA-CF_x-CNT/CoPc-NH_2 with 1 nm TiO_2 passivation layer under the same testing condition.

Table A8.2. XPS atomic percent of different elements before and after 4 hours stability test.

Element	Co	F	Si	C	N	O
Before (%)	0.05	44.01	0.31	48.61	0.79	6.23
After (%)	0.04	22.79	0.82	71.12	0.36	4.87

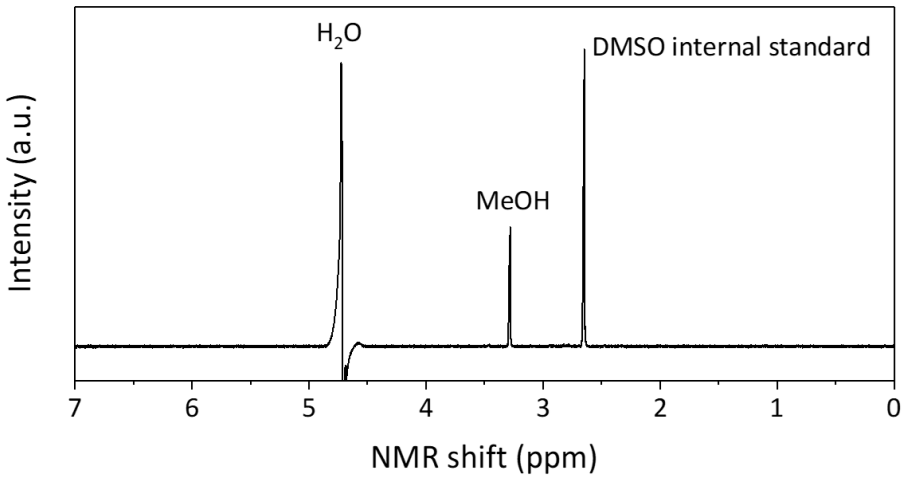

Figure A8.17. NMR spectrum of electrolyte after PEC. 1 mM DMSO was added to the solution as an internal standard.

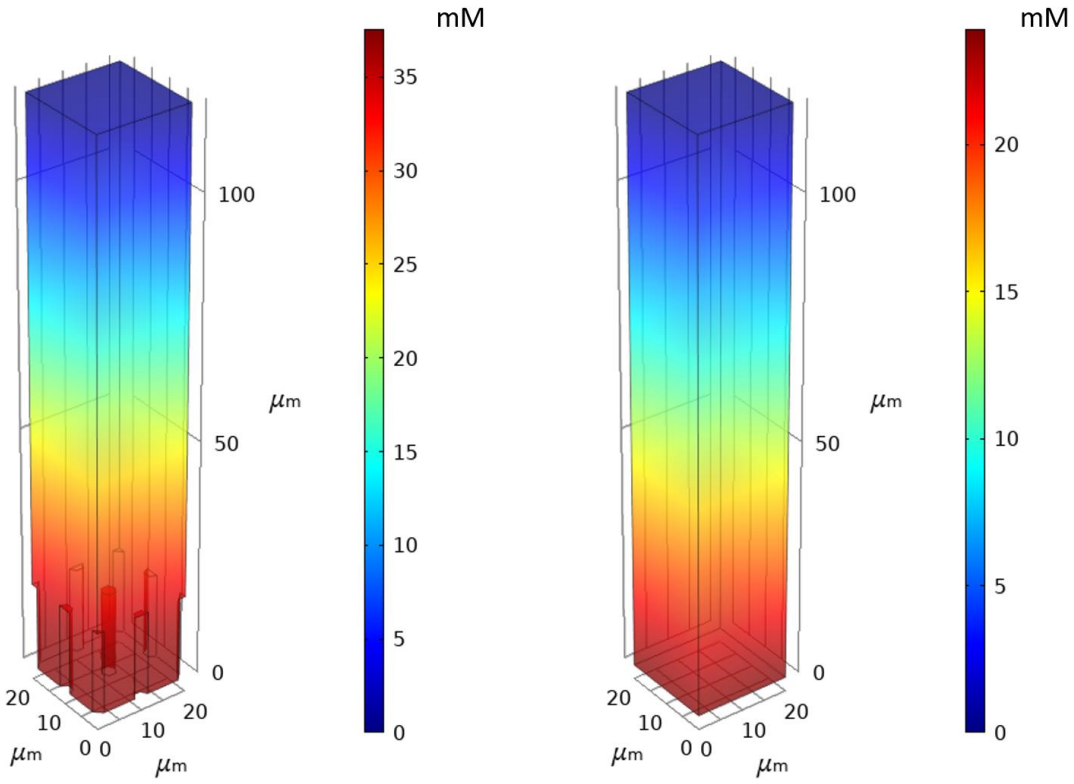

Figure A8.18. Simulation of the local CO concentration on SMA structure (left) and planar Si (right).

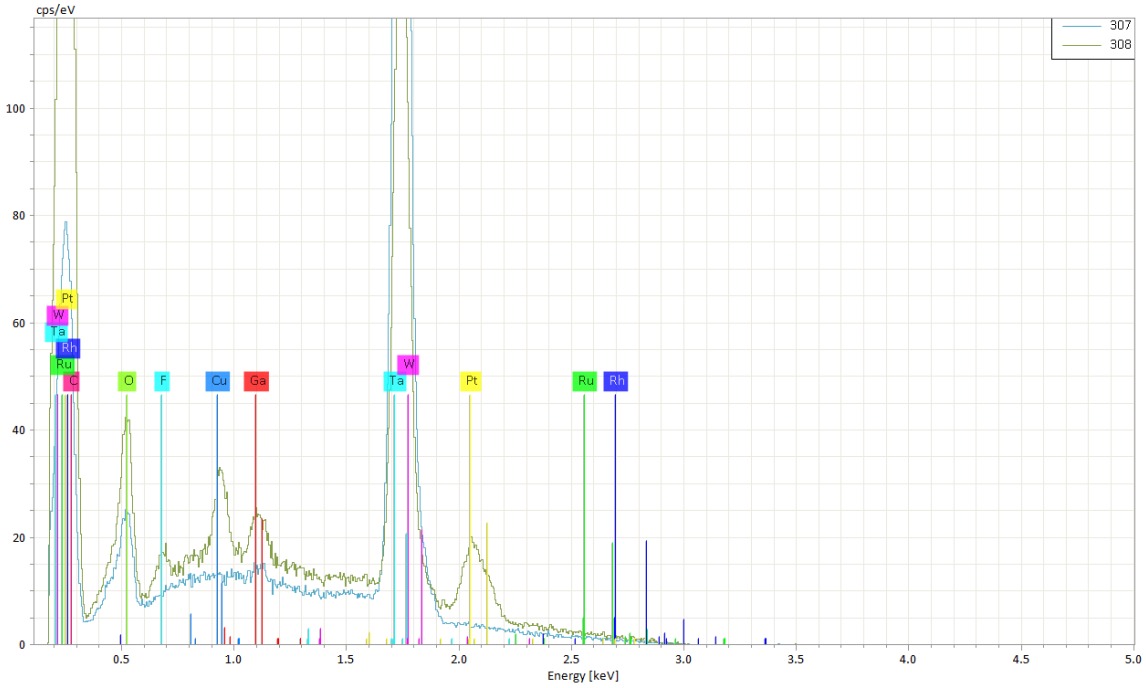

Figure A8.19. EDS spectrum of the Si-CF_x interface (green) and bulk Si (blue). The other elements (Pt, Ga) are from the FIB-deposited protective layer.

8.5. References

1. Jordaan, S. M.; Wang, C., Electrocatalytic conversion of carbon dioxide for the Paris goals. *Nature Catalysis* **2021,** *4* (11), 915-920.
2. Kondratenko, E. V.; Mul, G.; Baltrusaitis, J.; Larrazábal, G. O.; Pérez-Ramírez, J., Status and perspectives of CO_2 conversion into fuels and chemicals by catalytic, photocatalytic and electrocatalytic processes. *Energy & environmental science* **2013,** *6* (11), 3112-3135.
3. Bhattacharjee, S.; Rahaman, M.; Andrei, V.; Miller, M.; Rodríguez-Jiménez, S.; Lam, E.; Pornrungroj, C.; Reisner, E., Photoelectrochemical CO_2-to-fuel conversion with simultaneous plastic reforming. *Nature Synthesis* **2023,** *2* (2), 182-192.
4. Shan, B.; Vanka, S.; Li, T.-T.; Troian-Gautier, L.; Brennaman, M. K.; Mi, Z.; Meyer, T. J., Binary molecular-semiconductor p–n junctions for photoelectrocatalytic CO_2 reduction. *Nat. Energy* **2019,** *4* (4), 290-299.
5. Rahaman, M.; Andrei, V.; Wright, D.; Lam, E.; Pornrungroj, C.; Bhattacharjee, S.; Pichler, C. M.; Greer, H. F.; Baumberg, J. J.; Reisner, E., Solar-driven liquid multi-carbon fuel production using a standalone perovskite–BiVO4 artificial leaf. *Nature Energy* **2023,** *8* (6), 629-638.
6. Leung, J. J.; Warnan, J.; Ly, K. H.; Heidary, N.; Nam, D. H.; Kuehnel, M. F.; Reisner, E., Solar-driven reduction of aqueous CO_2 with a cobalt bis(terpyridine)-based photocathode. *Nature Catalysis* **2019,** *2* (4), 354-365.
7. Roh, I.; Yu, S.; Lin, C. K.; Louisia, S.; Cestellos Blanco, S.; Yang, P., Photoelectrochemical CO_2 Reduction toward Multicarbon Products with Silicon Nanowire Photocathodes Interfaced with Copper Nanoparticles. *Journal of the American Chemical Society* **2022,** *144* (18), 8002-8006.
8. Wu, Y.; Jiang, Z.; Lu, X.; Liang, Y.; Wang, H., Domino electroreduction of CO_2 to methanol on a molecular catalyst. *Nature* **2019,** *575* (7784), 639-642.
9. Zhang, X.; Wu, Z.; Zhang, X.; Li, L.; Li, Y.; Xu, H.; Li, X.; Yu, X.; Zhang, Z.; Liang, Y.; Wang, H., Highly selective and active CO_2 reduction electrocatalysts based on cobalt phthalocyanine/carbon nanotube hybrid structures. *Nature Communications* **2017,** *8* (1), 14675.
10. Shang, B.; Zhao, F.; Choi, C.; Jia, X.; Pauly, M.; Wu, Y.; Tao, Z.; Zhong, Y.; Harmon, N.; Maggard, P. A.; Lian, T.; Hazari, N.; Wang, H., Monolayer Molecular Functionalization Enabled by Acid–Base Interaction for High-Performance Photochemical CO_2 Reduction. *ACS Energy Letters* **2022,** *7* (7), 2265-2272.
11. Nandal, N.; Jain, S. L., A review on progress and perspective of molecular catalysis in photoelectrochemical reduction of CO_2. *Coordin Chem Rev* **2022,** *451*, 214271.
12. Chang, X.; Wang, T.; Yang, P.; Zhang, G.; Gong, J., The Development of Cocatalysts for Photoelectrochemical CO_2 Reduction. *Advanced Materials* **2019,** *31* (31), 1804710.
13. Wen, Z.; Xu, S.; Zhu, Y.; Liu, G.; Gao, H.; Sun, L.; Li, F., Aqueous CO_2 Reduction on Si Photocathodes Functionalized by Cobalt Molecular Catalysts/Carbon Nanotubes. *Angewandte Chemie International Edition* **2022,** *61*, e202201086.
14. Shang, B.; Rooney, C. L.; Gallagher, D. J.; Wang, B. T.; Krayev, A.; Shema, H.; Leitner, O.; Harmon, N. J.; Xiao, L.; Sheehan, C.; Bottum, S. R.; Gross, E.; Cahoon, J. F.; Mallouk, T. E.;

Wang, H., Aqueous Photoelectrochemical CO_2 Reduction to CO and Methanol over a Silicon Photocathode Functionalized with a Cobalt Phthalocyanine Molecular Catalyst. *Angewandte Chemie International Edition* **2023,** *62* (4), e202215213.
15. Yao, T.; An, X.; Han, H.; Chen, J. Q.; Li, C., Photoelectrocatalytic Materials for Solar Water Splitting. *Adv. Energy Mater.* **2018,** *8* (21), 1800210.
16. Choi, C.; Zhao, F.; Hart, J. L.; Gao, Y.; Menges, F.; Rooney, C. L.; Harmon, N. J.; Shang, B.; Xu, Z.; Suo, S.; Sam, Q.; Cha, J. J.; Lian, T.; Wang, H., Synergizing Electron and Heat Flows in Photocatalyst for Direct Conversion of Captured CO2. *Angew. Chem. Int. Ed.* **2023**.
17. Jiang, S.; Chen, Z.; Chen, X.; Nguyen, D.; Mattei, M.; Goubert, G.; Van Duyne, R. P., Investigation of Cobalt Phthalocyanine at the Solid/Liquid Interface by Electrochemical Tip-Enhanced Raman Spectroscopy. *The Journal of Physical Chemistry C* **2019,** *123* (15), 9852-9859.
18. Liu, Z.; Chen, Z.-X.; Jin, B.; Zhang, X., Theoretical studies on the structures and vibrational spectra of Ni, Pd, and Pt phthalocyanines. *Vibrational Spectroscopy* **2011,** *56* (2), 210-218.
19. Dresselhaus, M. S.; Dresselhaus, G.; Saito, R.; Jorio, A., Raman spectroscopy of carbon nanotubes. *Physics Reports* **2005,** *409* (2), 47-99.
20. Filho, A. G. S.; Jorio, A.; Ge, G. S.; Dresselhaus, G.; Saito, R.; Dresselhaus, M. S., Raman spectroscopy for probing chemically/physically induced phenomena in carbon nanotubes. *Nanotechnology* **2003,** *14* (10), 1130.
21. Clark, M. L.; Ge, A.; Videla, P. E.; Rudshteyn, B.; Miller, C. J.; Song, J.; Batista, V. S.; Lian, T.; Kubiak, C. P., CO_2 Reduction Catalysts on Gold Electrode Surfaces Influenced by Large Electric Fields. *J. Am. Chem. Soc.* **2018,** *140* (50), 17643-17655.
22. Heo, J.; Ahn, H.; Won, J.; Son, J. G.; Shon, H. K.; Lee, T. G.; Han, S. W.; Baik, M.-H., Electro-inductive effect: Electrodes as functional groups with tunable electronic properties. *Science* **2020,** *370* (6513), 214-219.
23. Shi, H.; Zhao, B.; Ma, J.; Bronson Jr, M. J.; Cai, Z.; Chen, J.; Wang, Y.; Cronin, M.; Jensen, L.; Cronin, S. B., Measuring Local Electric Fields and Local Charge Densities at Electrode Surfaces Using Graphene-Enhanced Raman Spectroscopy (GERS)-Based Stark-Shifts. *ACS Applied Materials & Interfaces* **2019,** *11* (39), 36252-36258.
24. Basova, T. V.; Kiselev, V. G.; Schuster, B.-E.; Peisert, H.; Chassã©, T., Experimental and theoretical investigation of vibrational spectra of copper phthalocyanine: polarized single-crystal Raman spectra, isotope effect and DFT calculations. *Journal of Raman Spectroscopy* **2009,** *40* (12), 2080-2087.
25. Ott, A.; Verzhbitskiy, I. A.; Clough, J.; Eckmann, A.; Georgiou, T.; Casiraghi, C., Tunable D peak in gated graphene. *Nano Research* **2014,** *7* (3), 338-344.
26. Liu, J.; Li, Q.; Zou, Y.; Qian, Q.; Jin, Y.; Li, G.; Jiang, K.; Fan, S., The Dependence of Graphene Raman D-band on Carrier Density. *Nano Lett.* **2013,** *13* (12), 6170-6175.
27. Fu, W.; Nef, C.; Knopfmacher, O.; Tarasov, A.; Weiss, M.; Calame, M.; Schönenberger, C., Graphene Transistors Are Insensitive to pH Changes in Solution. *Nano Lett.* **2011,** *11* (9), 3597-3600.

28. Ang, P. K.; Chen, W.; Wee, A. T. S.; Loh, K. P., Solution-Gated Epitaxial Graphene as pH Sensor. *J. Am. Chem. Soc.* **2008,** *130* (44), 14392-14393.
29. Lin, F.; Boettcher, S. W., Adaptive semiconductor/electrocatalyst junctions in water-splitting photoanodes. *Nat. Mater.* **2014,** *13* (1), 81-86.
30. Nellist, M. R.; Laskowski, F. A. L.; Lin, F.; Mills, T. J.; Boettcher, S. W., Semiconductor–Electrocatalyst Interfaces: Theory, Experiment, and Applications in Photoelectrochemical Water Splitting. *Acc. Chem. Res.* **2016,** *49* (4), 733-740.
31. Lin, F.; Bachman, B. F.; Boettcher, S. W., Impact of Electrocatalyst Activity and Ion Permeability on Water-Splitting Photoanodes. *J. Phys. Chem. Lett.* **2015,** *6* (13), 2427-2433.
32. Mills, T. J.; Lin, F.; Boettcher, S. W., Theory and Simulations of Electrocatalyst-Coated Semiconductor Electrodes for Solar Water Splitting. *Physical Review Letters* **2014,** *112* (14).
33. Thibault, F.; Martinez, R. Z.; Domenech, J. L.; Bermejo, D.; Bouanich, J.-P., Raman and infrared linewidths of CO in Ar. *J. Chem. Phys.* **2002,** *117* (6), 2523-2531.
34. Hickstein, D. D.; Goldfarbmuren, R.; Darrah, J.; Erickson, L.; Johnson, L. A., Rapid, accurate, and precise concentration measurements of a methanol-water mixture using Raman spectroscopy. *OSA Continuum* **2018,** *1* (3), 1097-1110.
35. Wu, Y.; Liang, Y.; Wang, H., Heterogeneous Molecular Catalysts of Metal Phthalocyanines for Electrochemical CO_2 Reduction Reactions. *Accounts of Chemical Research* **2021,** *54* (16), 3149-3159.
36. Kempler, P. A.; Richter, M. H.; Cheng, W.-H.; Brunschwig, B. S.; Lewis, N. S., Si Microwire-Array Photocathodes Decorated with Cu Allow CO_2 Reduction with Minimal Parasitic Absorption of Sunlight. *ACS Energy Letters* **2020,** *5* (8), 2528-2534.
37. Wakerley, D.; Lamaison, S.; Ozanam, F.; Menguy, N.; Mercier, D.; Marcus, P.; Fontecave, M.; Mougel, V., Bio-inspired hydrophobicity promotes CO_2 reduction on a Cu surface. *Nature Materials* **2019,** *18* (11), 1222-1227.

9 Conclusions and Outlook

In chapter 3, we developed an *in-situ* bias-dependent Second Harmonic Generation (SHG) technique to investigate the potential drop at the semiconductor electrode and solution double layer side. We noticed that on anisotropic single crystal TiO_2/electrolyte junction, TiO_2 azimuthal angle and light polarization impact both the relative phase and amplitude between the bias-independent and bias-dependent non-linear susceptibility. This will affect the accuracy of using quadratic response minimum potential V_{min} to predict the semiconductor flatband potential $V_{fb.}$ The most accurate prediction is found with azimuthal angle $\Phi = 0^o$ and sp polarization, where the cross term between bias-independent and bias-dependent term vanished. We verify the correlation between V_{min} and through a pH-dependent experiment. This study underscores the importance of considering the anisotropic angle when we conduct bias-dependent SHG experiment to extract the semiconductor flatband potential. In the following chapter 4, we conduct our light-induced OER reaction on TiO_2 and study the electric field induced Second Harmonic Generation (EFISH) under the $\Phi = 0^o$ and sp polarization. We achieve *operando* measurement of the band edge unpinning or light-induced Fermi-level pinning effect under illumination conditions through EFISH. Chang of built-in potential ΔV_{bi} can be directly correlated with surface hole accumulation at the surface states. The surface hole accumulation indicates the rate-determining water oxidation species on TiO_2 photoelectrode. Kinetic isotope experiments suggest that proton-coupled electron transfer step (PCET) is the rate-determining elementary step on TiO_2 electrolyte in pH 7 solution. Further control experiments observed that tunning of solution microenvironment will mitigate the built-in potential change, with solution anions specifically adsorbed on the surface and compensate the charge. As a non-invasive, electric field sensitive, *in situ* and potentially time-resolved techniques, we believe that SHG can be a promising technique to study the interfacial electric field distribution

across the semiconductor/electrolyte junction, for example, light-induced Fermi-level pinning. Preliminary attempted have been conducted on a Si/TiO_2 photocathode and hematite photoanode materials, which will be more ideal for EFISH study due to their isotropic surface that give rise to negligible $\chi^{(2)}$ term.

In chapter 5, we synthesize a hybrid photoanode material TiO_2-**Co$_9$POM** by functionalizing $Na_8K_8[Co_9(H_2O)_6(OH)_3(HPO_4)_2(PW_9O_{34})_3]\cdot 49H_2O$ (**Co$_9$POM**), a type of polyoxometalate water oxidization catalyst, on nanoporous TiO_2 photoanode through a cationic linkage 3-aminopropyltrimethoxysilane (APS). In pH 2 acidic condition, we achieve a three-fold photocurrent enhancement of TiO_2-**Co$_9$POM** photocurrent compared to pure TiO_2. Structural integrity can be maintained upon a stability test confirmed by Raman and XPS experiments. We applied various photoelectrochemical (PEC) characterizations on TiO_2-**Co$_9$POM** and TiO_2 to understand the performance enhancement mechanism. We believe that application of highly charged **Co$_9$POM** catalyst on TiO_2 surface will modify its band edge, increasing the band bending that favors that charge separation. Combing the transient absorption in visible range and mid-IR range, we unambiguously rule out the function of **Co$_9$POM** acts as hole collector and active water oxidation center on TiO_2. We also found that TiO_2-**Co$_9$POM** to be a highly coupled system with tungsten states of **Co$_9$POM** can achieve electron interchange with TiO_2 conduction band. In this work, we characterize the catalytic effect of **Co$_9$POM** on TiO_2 photoanode with comprehensive characterization methods. With combination of PEC characterization and transient absorption spectroscopy, this routine can be further applied to study catalyst effect on other hybrid photocatalytic system.

In chapter 6, we characterize a photocathode material GaP/TiO_2 using nanosecond *in situ* transient reflectance spectroscopy (TRS). Several sequential events have been observed on

GaP/TiO_2 after its initial charge separation across the *p-n* junction. We observed Franz-Keldysh effect (FKO) of GaP/TiO_2, where its signal provides a direct probe of photogenerated charge carriers at the *p-n* junction interface. By studying the decay of the separated charge carrier on GaP/TiO_2, we observed a faster carrier decay in a higher electrolyte concentration, which relates to the potentiostat response that removes the photogenerated holes. The potentiostat response time depends on the electrolyte concentration. The removal rate is essential to suppress the interfacial recombination, which further affects the HER efficiency, which is further verified by directly measuring the GaP/TiO_2 IPCE in solution with different electrolyte concentrations. Through TRS investigation of GaP/TiO_2 system, we showed a time-resolved picture of processes closely related to photocatalysis on a semiconductor photocathode. This underscores the important role of the solution electrolyte concentration and the potentiostat's response to the overall IPCE, further deepening the mechanistic understanding of semiconductor/electrolyte junction.

In chapter 7 and chapter 8, we focus our characterizations on photo(electro)chemical CO_2 reduction process using two types of hybrid photo(electro)catalytic materials. In chapter 7, we develop a ternary CdS/CNT/CoPc hybrid photocatalyst by directly growing CdS on multiwall carbon nanotubes and further anchor CO_2 reduction catalyst CoPc on CNTs via π-π interaction. An efficient CO_2 to CO conversion is achieved upon light illumination. Transient absorption in visible and near-IR region is used to investigate the charge carrier dynamics of this hybrid catalyst. We observed a rapid electron transfer from CdS to CNTs with its rate 37 times faster than recombination rate. We also observed electron accumulation on CNTs, building up it Fermi-level to achieve following CoPc reduction process. In addition to the rapid electron transfer, the photothermal effect of CNT in the hybrid catalyst structure enables direct photochemical conversion of amine-captured CO_2. In chapter 7, we believe one of the reason why CO is the only

CO_2 reduction product is that only a limited Fermi-level on CNT can be achieved due to the limited CdS conduction band edge position and limited electron accumulation. Thus, we turn to a photoelectrode with junction electric field can be tuned by applying potential. In chapter 8, we developed a Silicon-based Silicon micropillar arrays (SMA) photocathode modified with CNT/CoPc-NH_2 CO_2 reduction catalyst, showing a remarkable over 20% CO_2 to methanol reduction Faraday efficiency with record-high current density. We use *in situ* Raman to investigate the junction properties. A photovoltage of around 300 mV is observed on silicon, we also find that the Fermi-level of CNT and catalyst will be unpinned upon one-electron reduction of CoPc-NH_2 molecules and shift with more negative applied potential. This allows a beneficial thermodynamic driving force for CO_2 to methanol reduction on the catalyst. The incorporation of the micropillar array structure and the superhydrophobic coating also plays a crucial role in enhancing retention of the CO intermediate, consequently improving the selectivity towards the deeply reduced methanol product. This work pioneers a route for tailoring the microenvironment on semiconductor surfaces to enhance the overall CO_2 reduction performance. The insights gained from this study can be further applied to photo(electro)chemical CO_2 reduction materials.